

2012

Development of a high performance protective barrier utilising non-composite steel-concrete-steel panels

Sih Ying Kong
University of Wollongong

Recommended Citation

Kong, Sih Ying, Development of a high performance protective barrier utilising non-composite steel-concrete-steel panels, Doctor of Philosophy thesis, School of Civil, Mining and Environmental Engineering, University of Wollongong, 2012. <http://ro.uow.edu.au/theses/3573>

UNIVERSITY OF WOLLONGONG

COPYRIGHT WARNING

You may print or download ONE copy of this document for the purpose of your own research or study. The University does not authorise you to copy, communicate or otherwise make available electronically to any other person any copyright material contained on this site. You are reminded of the following:

Copyright owners are entitled to take legal action against persons who infringe their copyright. A reproduction of material that is protected by copyright may be a copyright infringement. A court may impose penalties and award damages in relation to offences and infringements relating to copyright material. Higher penalties may apply, and higher damages may be awarded, for offences and infringements involving the conversion of material into digital or electronic form.

**DEVELOPMENT OF A HIGH PERFORMANCE
PROTECTIVE BARRIER UTILISING NON-
COMPOSITE STEEL-CONCRETE-STEEL
PANELS**

A Thesis Submitted in Fulfilment of
the Requirements for the Award of the Degree of

Doctor of Philosophy

From

UNIVERSITY OF WOLLONGONG

by

SIH YING KONG

BEng (Hons), MSc (Structural)

School of Civil, Mining and Environmental Engineering,
Faculty of Engineering.

2012

@ COPYRIGHT 2012
BY
SIH YING KONG
ALL RIGHTS RESERVED

CERTIFICATION

I, Sih Ying Kong, declare that this thesis, submitted in fulfilment of the requirements for the award of Doctor of Philosophy, in the School of Civil, Mining and Environmental Engineering, Faculty of Engineering, University of Wollongong, is wholly my own work unless otherwise referenced or acknowledged. The document has not been submitted for qualification at any other academic institution.

Sih Ying Kong

30 January 2012

TABLE OF CONTENTS

CERTIFICATION	ii
TABLE OF CONTENTS	iii
LIST OF FIGURES	x
LIST OF TABLES	xxiv
NOMENCLATURES	xxvii
ABSTRACT	xxix
ACKNOWLEDGMENTS	xxxii
PUBLICATION LIST	xxxiii
CHAPTER 1 INTRODUCTION	1
1. 1 Statement of problem.....	2
1. 2 Research objectives	4
1. 3 Scope of research.....	5
1. 4 Organisation of thesis	5
CHAPTER 2 LITERATURE REVIEW	8
2. 1 Effectiveness of protective walls in reducing blast loading	9
2. 2 Types of blast barriers	11
2.2.1 Earth-filled wall.....	12
2.2.2 Reinforced concrete wall	13
2.2.3 Concrete-sand-concrete wall.....	15
2.2.4 Steel-concrete-steel structures.....	17
2.2.4.1 Adler blast wall.....	20
2. 3 Blast loading characterisation	21
2.3.1 Detonation process of high explosives	21
2.3.2 Blast wave interactions with structures	23
2.3.3 Computational Fluid Dynamics (CFD) analysis	24

2. 4	Impact loading characterisation	27
2. 5	Material characterisation.....	29
2.5.1	Characteristics of high performance steel.....	29
2.5.2	Material properties under dynamic loading	32
2. 6	Structural response to blast and impact loading.....	35
2.6.1	Single degree of freedom (SDOF) system.....	35
2.6.2	Structural response under blast loading	37
2.6.3	Structural response under impact loading.....	38
2.6.4	Deformation limits for structural members.....	39
CHAPTER 3 TENSILE MEMBRANE MECHANISM.....		42
3. 1	Young (1959)	49
3. 2	Jones (1973).....	52
3. 3	Hodge Jr. (1974).....	53
3. 4	Izzuddin (2005)	57
3. 5	Summary.....	60
CHAPTER 4 MEDIUM STRAIN RATE TESTING ON Grade 304 STAINLESS STEEL.....		61
4. 1	Introduction of strain rate effects	61
4. 2	Literature review of strain rate effects on stainless steel.....	61
4. 3	Cowper-Symonds equation.....	65
4. 4	Design of IFWI test rig.....	65
4. 5	Experimental procedure.....	68
4. 6	Determination of strain rate	70
4. 7	Experimental results	70
4.7.1	Results from Instron universal testing machine	70
4.7.2	Results from IFWI test rig	73
4. 8	Comparison of experimental results with existing Cowper-Symonds coefficients	78
4. 9	Derivation of Cowper-Symonds coefficients.....	79
4. 10	Conclusions.....	81
CHAPTER 5 STATIC TESTING OF AXIALLY RESTRAINED NON-COMPOSITE STEEL-CONCRETE-STEEL PANELS		82

5. 1	Concept of axially restrained non-composite SCS panels	82
5. 2	Description of reduced scale SCS panels	83
5.2.1	Lightweight concrete preparation.....	86
5. 3	Experimental programme	88
5.3.1	Material testing.....	88
5.3.1.1	Unconfined concrete compressive tests	88
5.3.1.2	Steel tensile coupon tests.....	89
5.3.2	Push-out test.....	89
5.3.3	Simply supported non-composite SCS panel under static four-point bending	91
5.3.4	Static three-point bending test on axially restrained non-composite SCS panels	92
5. 4	Experimental results for material testing and push-out tests	95
5. 5	Test results of SCS panels	99
5.5.1	Simply supported non-composite SCS panel.....	99
5.5.2	Control panel.....	101
5.5.3	Lightweight core panel	105
5.5.4	Reinforced core panel.....	108
5.5.5	Improved bonding panel.....	111
5.5.6	Fully enclosed panel.....	112
5.5.7	Stainless steel panel.....	115
5.5.8	Summary and discussion on panel results	117
5. 6	Conclusions.....	121

CHAPTER 6 DEVELOPMENT OF STATIC RESISTANCE FUNCTION

FOR NON-COMPOSITE SCS PANELS.....123

6. 1	Flexural response of SCS panels	123
6.1.1	Flexural load capacity of SCS panels with natural interaction	123
6.1.1.1	Flexural load capacity of non-composite SCS panels (with natural interaction): non-reinforced concrete core.....	125
6.1.1.2	Flexural load capacity of non-composite SCS panels (with natural interaction): reinforced concrete core.....	127
6.1.1.3	Flexural stiffness of non-composite SCS panels (with natural interaction).....	128

6.1.1.4	Comparison between experimental and theoretical flexural load capacity of non-composite SCS panels (with natural interaction).....	130
6.1.2	Flexural load capacity of SCS panels with partial shear connection....	133
6.1.3	Flexural load capacity of fully enclosed SCS panels	136
6.2	Tensile Membrane resistance of SCS panels	139
6.2.1	Analysis of SCS panels with mild steel faceplates.....	141
6.2.2	Analysis of SCS panel with stainless steel faceplates	141
6.2.3	Determination of stiffness of the axial restraint support	142
6.2.4	Comparison between theoretical and experimental results.....	144
6.3	Static resistance function for axially restrained SCS panels.....	148
6.3.1	Axially restrained non-composite SCS panels.....	148
6.3.2	Axially restrained SCS panels with partial shear connection	150
6.4	Conclusions.....	152

CHAPTER 7 IMPACT TESTING OF AXIALLY RESTRAINED NON-COMPOSITE SCS PANELS.....154

7.1	Experimental program	154
7.1.1	Unconfined concrete compressive test	154
7.1.2	Impact testing of axially restrained SCS panels.....	155
7.2	Experimental results	159
7.2.1	Concrete compressive strength.....	159
7.2.2	Response of axially restrained SCS panels under impact loading condition.....	160
7.2.2.1	Control panel	160
7.2.2.2	Increased impact energy panel	164
7.2.2.3	Lightweight core panel.....	167
7.2.2.4	Panel with bracing elements.....	169
7.2.2.5	Reinforced core panel and Double reinforced core panel.....	171
7.2.2.6	Stainless steel panel	175
7.2.2.7	Improved bonding panel.....	177
7.2.2.8	Fully enclosed panel	179
7.3	Analysis of impact test results of axially restrained SCS panels	181
7.3.1	Control panel versus Increased impact energy panel	181
7.3.2	Lightweight core panel	184

7.3.3	Stainless steel panel	185
7.3.4	Panel with bracing elements.....	187
7.3.5	Reinforced core panel and Double reinforced core panel.....	188
7.3.6	Improved bonding panel	189
7.3.7	Fully enclosed panel	191
7.4	Theoretical prediction of maximum displacement of axially restrained SCS panels subjected to impact loading	192
7.5	Conclusions	194

CHAPTER 8 FINITE ELEMENT MODELLING OF AXIALLY RESTRAINED SCS PANELS UNDER IMPACT LOADING196

8.1	Introduction to LS-Dyna.....	196
8.2	Numerical model description	197
8.2.1	Boundary conditions	198
8.2.2	Contact surfaces	199
8.2.3	Material models	200
8.2.3.1	Steel material model	200
8.2.3.2	Concrete material model	201
8.2.4	Element erosion.....	205
8.3	Calibration of FE model	206
8.3.1	Mesh convergence study.....	206
8.3.2	Support conditions.....	208
8.3.2.1	Spacing between keyed inserts and UC sections	208
8.3.2.2	Bolt connection between UC section and I-beam.....	209
8.3.3	Separation of steel faceplates from concrete core	210
8.3.4	Shell element formulations	212
8.3.5	Dynamic coefficient of friction between the steel faceplates and the concrete core.....	213
8.3.6	Concrete material models	213
8.3.6.1	Concrete material model CSCM (Mat. 159)	214
8.3.6.2	Concrete material model 72R3	217
8.3.7	Hourglass energy of the concrete core.....	219
8.3.8	Strain rate effects of materials.....	222
8.3.8.1	Strain rate effects of concrete	222

8.3.8.2	Strain rate effects of mild steel.....	224
8. 4	Simulation results and discussion	227
8.4.1	Control panel.....	227
8.4.2	Increased impact energy panel	229
8.4.3	Stainless steel panel.....	230
8.4.4	Lightweight core panel	231
8.4.5	Reinforced core panel and Double reinforced core panel.....	232
8.4.6	Panel with bracing elements.....	235
8.4.7	Improved bonding panel	237
8.4.8	Fully enclosed panel	238
8. 5	Conclusions.....	240

CHAPTER 9 RESPONSE OF AXIALLY RESTRAINED NON-COMPOSITE SCS PANELS SUBJECTED TO BLAST LOADING.....242

9. 1	Introduction to the catcher system.....	243
9.1.1	Analytical model for the thin steel sheet catcher system.....	244
9.1.2	Improved analytical model for non-composite SCS panels.....	247
9. 2	Response of fully fixed non-composite SCS panels subjected to uniform blast impulse	248
9.2.1	Parametric study 1: Effects of increased blast loading on the response of non-composite SCS panels	250
9.2.2	Parametric study 2: Effects of the rear faceplate thickness on the response of non-composite SCS panels.....	254
9.2.3	Parametric study 3: Effects of the concrete core thickness on the response of non-composite SCS panels.....	257
9.2.4	Summary for the response of non-composite SCS panels under fixed support condition.....	260
9. 3	Response of full scale protective barrier under non-uniform blast pressure	261
9.3.1	Design of the post.....	261
9.3.2	FE modelling	262
9.3.3	FE results for the barrier with 200 mm thick non-composite SCS panels supported by posts.....	264

9.3.3.1	Effects of increased thickness of non-composite SCS panels on barrier performance	271
9.3.3.2	Summary for the non-composite SCS panels supported by posts	274
9.3.4	Theoretical analysis for non-composite SCS panels supported by posts	275
9.3.5	Two degrees of freedom (2DOF) system for the barrier	278
9.4	Comparison between the prototype barrier with non-composite SCS panel and the cantilever concrete blast wall	286
9.5	Conclusions.....	291

CHAPTER 10 CONCLUSIONS AND SUGGESTIONS FOR FUTURE

WORKS 293

10.1	Strain rate effects for stainless steel Grade 304	293
10.2	Static testing of axially restrained non-composite SCS panels.....	294
10.3	Impact testing of axially restrained non-composite SCS panels.....	295
10.4	Response of non-composite SCS panels subjected to blast loading	295

REFERENCES297

APPENDIX A: DRAWINGS OF THE INSTRUMENTED FALLING

WEIGHT IMPACT (IFWI) TEST RIG308

LIST OF FIGURES

Figure 2.1: Interaction between the blast pressure and protective wall with the blast environment behind the wall. (Remennikov and Rose, 2007).....	9
Figure 2.2: Peak scaled impulse versus scaled standoff distance at $h= 600\text{mm}$. (Rose et al. 1997)	11
Figure 2.3: A protective barrier constructed using Hesco Bastions. (Crawford and Lan, 2006).....	12
Figure 2.4: Cantilever reinforced concrete blast wall with lacing reinforcement. (U.S. Department of the Army, 1990).....	14
Figure 2.5: Pre-cast concrete blast walls ‘Texas’ (smaller in size) and ‘Alaskan’. (Smith, 2010)	14
Figure 2.6: Blast barriers consist of two reinforced concrete panels and a sand infill. (U.S. Department of the Army, 1990).....	16
Figure 2.7: (a) Bi-steel panel before concrete casting (Hulton, 2010), (b) J-hook panel before concrete casting (Liew and Soheli, 2009)	17
Figure 2.8: Bi-steel wall subjected to detonation of two tonnes of high explosives at 2 m standoff distance (a) before the test and (b) after the test. (Hulton, 2010)..	18
Figure 2.9: Redline 2 wall. (Hulton, 2010)	19
Figure 2.10: Deformation of Adler blast wall after subjected to close-in detonation of high explosive. (Crawford and Lan, 2006).....	20
Figure 2.11: (a) SCS panel and the keyed connection used to connect the steel post to the panel, (b) steel posts penetrate into the ground to support the barrier. (reproduced from Crawford and Lan , 2006).....	21
Figure 2.12: Typical pressure-time profile for the blast wave in free air.	22
Figure 2.13: Simulation of the blast wave interaction with the blast wall using Air3D.	26
Figure 2.14: Hard impact and soft impact. (Eibl, 1988)	27
Figure 2.15: FE model of Ford 800 obtained from the National Crash Analysis Centre. (www.ncac.gwu.edu)	29
Figure 2.16: Typical stress-strain curves for mild steel, high strength steel and stainless steel.....	30

Figure 2.17: Strain rate effects on material properties of mild steel. (Blazynski, 1987)	34
.....	
Figure 2.18: Single degree of freedom (SDOF) system.....	35
Figure 2.19: Non-dimensionalised pressure-impulse diagram for SDOF elastic system (reproduced from Cormie et al. 2009).....	36
Figure 2.20: The shear cone angle decreases as the impact velocity increases (Eibl, 1988).....	38
Figure 2.21: Reinforced concrete responses under impact loading. (Bangash, 1993)	39
Figure 3.1: The force and moment distribution in the fix supported plate under a uniformly distributed load.	42
Figure 3.2: (a) Deformation of the fixed end beam subjected to a concentrated load at mid-span, (b) the force and moment equilibrium in the beam. (reproduced from Campbell and Charlton, 1972).....	45
Figure 3.3: Load-displacement relationship for the fixed end beam after formation of plastic hinges using rigid plastic analysis.....	46
Figure 3.4: Flow rule relationship for the rectangular section subjected to bending moment and axial load.	47
Figure 3.5: Stress distribution and movement of the axis of rotation of a plastic hinge under increased displacement. (reproduced from Campbell and Charlton, 1972).....	47
Figure 3.6: Load-displacement relationship for the clamped long rectangular plate subjected to a uniformly distributed load (reproduced from Young, 1959).....	51
Figure 3.7: The beam with rectangular cross section pin supported by the rig (reproduced from Hodge Jr., 1974).....	54
Figure 3.8: Transient and plastic membrane load-displacement relationship for a beam restrained with various axial stiffness at the supports.	57
Figure 3.9: (a) A simply supported steel beam with elastic axial restraints at the supports, (b) simplified flow rule between the bending moment and the axial force.....	57
Figure 3.10: Elasto-plastic responses of the axially restrained steel beam.	58
Figure 4.1: Front view of the instrumented falling weight impact (IFWI) test rig developed at the University of Wollongong.....	66
Figure 4.2: Von Mises stress contour plot for the test rig under impact.....	67

Figure 4.3: Full experimental set up for medium strain rate tests.	68
Figure 4.4: Geometry of a cylindrical specimen.	69
Figure 4.5: Engineering stress-strain curves for Grade 304 stainless steel at a strain rate of 0.002 s^{-1}	71
Figure 4.6: Engineering stress-strain curves for Grade 304 stainless steel at a strain rate of 1 s^{-1}	72
Figure 4.7: Processed load and strain time histories for the specimen 3 tested using the IFWI test rig under a drop height of 500 mm.	74
Figure 4.8: Initial elastic-plastic stress strain curves for stainless steel specimens under 500 mm drop height.....	75
Figure 4.9: Engineering stress-strain curves for Grade 304 stainless steel at a strain rate of about 90 s^{-1}	76
Figure 4.10: Engineering stress-strain curves for Grade 304 stainless steel at a strain rate of about 300 s^{-1}	76
Figure 4.11: Engineering stress-strain curves for Grade 304 stainless steel at a strain rate of about 600 s^{-1}	77
Figure 4.12: Comparison between the experimental yield stress and the theoretical dynamic yield stress predicted by the existing Cowper-Symonds coefficients..	78
Figure 4.13: Comparison between the experimental ultimate tensile strength and the theoretical dynamic ultimate tensile strength predicted by the existing Cowper-Symonds coefficients.	79
Figure 4.14: Curve fitting to obtain new Cowper-Symonds coefficients for the yield stress for Grade 304 stainless steel.	80
Figure 4.15: Curve fitting to obtain new Cowper-Symonds coefficients for the ultimate tensile strength for Grade 304 stainless steel.	80
Figure 5.1: Geometry and dimension of the non-composite SCS panel used in this study.	83
Figure 5.2: (a) two layers of 4@50 mm wire meshes inserted into the mild steel shell, (b) a layer of 3@25 mm wire mesh tack welded to the mild steel shell.	86
Figure 5.3: Welding of steel end cap to form a fully enclosed panel before testing. .	86
Figure 5.4: BST lightweight aggregates (polystyrene beads) being poured into concrete mix.....	88

Figure 5.5: Unconfined concrete compressive test using the Instron Universal testing machine for normal weight concrete at the University of Western Sydney.	89
Figure 5.6: Geometry and dimension of a tensile coupon.	89
Figure 5.7: Geometry and dimension of a push out specimen.	90
Figure 5.8: Push out test set up.....	91
Figure 5.9: Experimental setup for a simply supported non-composite SCS panel under static four-point bending conducted at the University of Wollongong. ...	92
Figure 5.10: Axial restraint support components used in the experimental setup for static three-point bending test.	93
Figure 5.11: Geometry and dimension of a key insert.....	93
Figure 5.12: The experimental setup for static three-point bending test at the University of Western Sydney using the dynamic actuator test frame.	94
Figure 5.13: Instrumentation on axially restrained SCS panels under static three-point bending test.	95
Figure 5.14: The laser displacement gauge used to record the displacement.	95
Figure 5.15: Shear failure of concrete cylinders under unconfined concrete compressive test (a) normal weight concrete, (b) lightweight concrete.....	96
Figure 5.16: Engineering stress-strain curves for mild steel.....	97
Figure 5.17: Engineering stress-strain curves for stainless steel.....	97
Figure 5.18: Tensile fracture of mild steel and stainless steel coupons.....	98
Figure 5.19: Load-displacement curves obtained from the push-out tests.....	99
Figure 5.20: Load-displacement relationship for the simply supported non-composite SCS panel under static four-point bending test.	100
Figure 5.21: Welding fracture failure at the joint between the bottom faceplate and one of the end plates for the simply supported non-composite SCS panel under four-point bending test.	100
Figure 5.22: Total applied load versus centre deformation of the bottom faceplate of the simply supported non-composite SCS panel.	101
Figure 5.23: Load-displacement relationship for the Control panel (CP).....	102
Figure 5.24: Separation of the bottom steel faceplate from the concrete core during the flexural response of the Control panel.....	102
Figure 5.25: Applied load versus strain deformation of the steel faceplates at various locations of the Control panel.....	103

Figure 5.26: Applied load versus in-plane displacement of the axial restraint supports.....	104
Figure 5.27: The flared end of the Control panel being pulled out from the keyed connection.....	105
Figure 5.28: Load-displacement curve of the Lightweight core panel (LP) compared to the load-displacement relationship of the Control panel (CP).....	106
Figure 5.29: Applied load versus strain deformation curves of steel faceplates at various locations of the Lightweight core panel.....	107
Figure 5.30: Crushing of lightweight concrete and buckling of steel end plate for the Lightweight core panel.....	107
Figure 5.31: Load-displacement curve of the Reinforced core panel (RP) compared to the load-displacement relationship of the Control panel (CP).....	109
Figure 5.32: Applied load versus strain deformation curves of steel faceplates at various locations of the Reinforced core panel.....	109
Figure 5.33: Welding fracture failure at the joint between the bottom faceplate and the end plate of the Reinforced core panel.....	110
Figure 5.34: Load-displacement curve of the Improved bonding panel (IBP) compared to the load-displacement relationship of the Control panel (CP). ...	112
Figure 5.35: Applied load versus strain deformation curves of the steel faceplates at various locations of the Improved bonding panel.....	112
Figure 5.36: Load-displacement curve of the Fully enclosed panel (ECP) compared to the load-displacement relationship of the Control panel (CP).....	114
Figure 5.37: Applied load versus strain deformation curves of the steel faceplates at various positions of the Fully enclosed panel.....	114
Figure 5.38: Deformation observed in the Fully enclosed panel, (a) buckling of top faceplate adjacent to the loading point, (b) fracture of the end cap and failure of weld between the end cap and steel faceplates.....	115
Figure 5.39: Load-displacement curve of the Stainless steel panel (SP) compared to the load-displacement relationship of the Control panel (CP).....	116
Figure 5.40: Applied load versus strain deformation curves of steel faceplates at various locations of the Stainless steel panel.....	117
Figure 6.1: Strength ratio versus shear span ratio for the steel concrete composite slab under natural interaction. (Jeong, 2008).....	124

Figure 6.2: Definition of the shear span and effective depth of the panel cross section.....	125
Figure 6.3: Cross section analysis for fully composite SCS panels with a non-reinforced concrete core at the ultimate moment capacity.	126
Figure 6.4: Cross section analysis for fully composite SCS panels with a reinforced concrete core at the ultimate moment capacity.....	128
Figure 6.5: Comparison between predicted and experimental flexural response of the Control panel (CP).	131
Figure 6.6: Comparison between predicted and experimental flexural response of the Lightweight core panel (LP).....	132
Figure 6.7: Comparison between predicted and experimental flexural response of the Stainless steel panel (SP).....	132
Figure 6.8: Comparison between predicted and experimental flexural response of the Reinforced core panel (RP).	133
Figure 6.9: Cross section analysis for SCS panels with partial shear connection. ...	133
Figure 6.10: Comparison between predicted and experimental flexural response of the Improved bonding panel (IBP).....	136
Figure 6.11: Strain and stress distribution in the Fully enclosed panel at the ultimate moment capacity.	137
Figure 6.12: Comparison between theoretical and experimental flexural response of the Fully enclosed panel (ECP).....	139
Figure 6.13: Free body diagram of the panel at a large displacement.	143
Figure 6.14: Load-displacement relationship for the axial restraint supports.....	144
Figure 6.15: Comparison between theoretical and experimental membrane resistance of the Control panel (CP).	145
Figure 6.16: Comparison between theoretical and experimental membrane resistance of the Stainless steel panel (SP).....	145
Figure 6.17: Comparison between theoretical and experimental membrane resistance of the Lightweight core panel (LP).	146
Figure 6.18: Comparison between theoretical and experimental membrane resistance of the Reinforced core panel (RP).....	146
Figure 6.19: Comparison between theoretical and experimental membrane resistance of the Improved bonding panel (IBP).	147

Figure 6.20: Comparison between theoretical and experimental membrane resistance of the Fully enclosed panel (ECP).	147
Figure 6.21: Static resistance function of the Control panel (CP).	150
Figure 6.22: Static resistance function of the Improved bonding panel (IBP).	151
Figure 7.1: The concrete cylinders have been capped with high strength plaster before the unconfined concrete compressive test is conducted.	155
Figure 7.2: The high capacity drop hammer impact apparatus at the University of Wollongong.	156
Figure 7.3: The experimental setup for axially restrained SCS panels subjected to a drop mass impact.	156
Figure 7.4: Separation of the steel faceplates from the concrete core for the Control panel prior to the impact test.	159
Figure 7.5: Impact load and displacement time histories of the Control panel (CP).	161
Figure 7.6: Impact load and strain time histories of the Control panel (CP).	162
Figure 7.7: Impact load-displacement relationship of the Control panel (CP) subjected to mid-span impact.	163
Figure 7.8: Damage on the Control panel observed after the impact test, (a) indentation on the top steel faceplate, (b) extensive damage of concrete core at mid-span, (c) wide crack at the support and buckling of steel end plate.	164
Figure 7.9: A comparison of impact load-displacement relationship between the Increased impact energy panel (4mP) and Control panel (CP).	165
Figure 7.10: Impact load and strain time histories of the Increased impact energy panel (4mP).	166
Figure 7.11: Damage on the Increased impact energy panel, (a) a partial fracture of the top faceplate, (b) buckling of the end plate.	166
Figure 7.12: A comparison of impact load-displacement relationship between the Lightweight core panel (LP) and Control panel (CP).	167
Figure 7.13: Impact load and strain time histories of the Lightweight core panel (LP).	168
Figure 7.14: Damage of the Lightweight core panel: (a) buckling of the end plate, (b) extensive cracking on the concrete along the span.	169

Figure 7.15: A comparison of impact load-displacement relationship between the Panel with bracing elements (BP) and Control panel (CP).	170
Figure 7.16: Impact load and strain time histories of the Panel with bracing elements (BP).	170
Figure 7.17: Damage of concrete for the Panel with bracing elements.	171
Figure 7.18: A comparison of impact load-displacement relationship between the Reinforced core panel (RP), Double reinforced core panel (DRP) and Control panel (CP).	173
Figure 7.19: Impact load and strain time histories of the Reinforced core panel (RP).	173
Figure 7.20: Impact load and strain time histories of the Double reinforced core panel (DRP).	174
Figure 7.21: Damage on the Reinforced core panel: (a) cracking of concrete at flared zone, (b) crushing and cracking of concrete at mid-span, (c) buckling of top layer of wire mesh at mid-span.	174
Figure 7.22: A comparison of impact load-displacement relationship between the Stainless steel panel (SP) and Control panel (CP).	176
Figure 7.23: Impact load and strain time histories of the Stainless steel panel (SP).	176
Figure 7.24: A comparison of impact load-displacement relationship between the Improved bonding panel (IBP) and Control panel (CP).	178
Figure 7.25: Impact load and strain time histories of the Improved bonding panel (IBP).	178
Figure 7.26: Separation of wire meshes from the steel faceplates on the Improved bonding panel.	179
Figure 7.27: A comparison of impact load-displacement relationships between the Fully enclosed panel (ECP) and Control panel (CP).	180
Figure 7.28: Impact load and strain time histories of the Fully enclosed panel (ECP).	180
Figure 7.29: Damage on the Fully enclosed panel: (a) buckling of the end cap and indentation of the top faceplate, (b) failure of the welding between the steel faceplates and end cap.	181

Figure 7.30: A comparison between the quasi-static and impact load-displacement relationships of the Control panel (CP), and the theoretical static resistance function.....	182
Figure 7.31: A comparison between the impact load-displacement relationship of the Increased impact energy panel (4mP), the static load-displacement relationship for the Control panel (CP), and the theoretical static resistance function.....	184
Figure 7.32: A comparison of the quasi-static and impact load-displacement relationship of the Lightweight core panel (LP), and the theoretical static resistance function.....	185
Figure 7.33: A comparison of the quasi-static and impact load-displacement relationships of the Stainless steel panel (SP), and the theoretical static resistance function.....	186
Figure 7.34: The impact load-displacement relationship of the Panel with bracing elements (BP), the quasi-static load-displacement relationship of the Control panel (CP), and the theoretical static resistance function.....	188
Figure 7.35: A comparison between the impact load-displacement relationships of the Reinforced core panel (RP) and Double reinforced core panel (DRP) with the static load-displacement relationship for the Reinforced core panel (RP), and the theoretical static resistance function.....	189
Figure 7.36: A comparison of the quasi-static and impact load-displacement relationships of the Improved bonding panel (IBP), and the theoretical static resistance function.....	190
Figure 7.37: A comparison of the quasi-static and impact load-displacement relationships of the Fully enclosed panel (ECP), and the theoretical static resistance function.....	191
Figure 8.1: FE model for axially restrained SCS panels subjected to a drop mass impact at mid-span (quarter model).	198
Figure 8.2: Schematic of the shear failure surface and the cap surface in the material model CSCM. (reproduced from FHWA, 2007a)	202
Figure 8.3: Numerically generated stress-strain relationships for concrete infill using a single element simulation.	205
Figure 8.4: The FE model of a simply support non-composite SCS panel with a mesh size of 10 mm used in the mesh convergence study.	207

Figure 8.5: Load time histories of FE models with different spacing between the keyed inserts and the UC sections compared to the experimental result of the Control panel (CP).	209
Figure 8.6: Load time histories of FE models with different clearance spacing in the bolt connection compared to the experimental result of the Control panel (CP).	210
Figure 8.7: Separation of the steel faceplates from the concrete core in the FE model.	211
Figure 8.8: Load time histories of FE models with and without separation between the steel faceplates and the concrete core compared to the experimental result of the Control panel (CP).....	211
Figure 8.9: Load time histories of FE models with different types of shell element formulations compared to the experimental result of the Control panel (CP)..	212
Figure 8.10: Load time histories of FE models with different values of dynamic coefficient of friction between the steel faceplates and the concrete core compared to the experimental result of the Control panel (CP).	213
Figure 8.11: Load time histories of FE models using the material model CSCM with different values of erosion coefficients compared to the experimental result of the Control panel (CP).....	215
Figure 8.12: Damage contour plot of the concrete core using the material model CSCM (Mat. 159) with an erosion coefficient of 0.9 (no erosion).....	216
Figure 8.13: Damage contour plot of the concrete core using the material model CSCM (Mat. 159) with an erosion coefficient of 1.	216
Figure 8.14: Damage contour plot of the concrete core using the material model CSCM (Mat. 159) with an erosion coefficient of 1.2.....	217
Figure 8.15: Load time histories of the FE models using the concrete material model Damage Release III compared to the experimental result of the Control panel (CP).	218
Figure 8.16: Damage contour plot of the concrete core for the FE model using the concrete material model Damage Release III.....	219
Figure 8.17: Damage contour plot of the concrete core for the FE model using combined material models of CSCM 159 and Damage Release III.	219

Figure 8.18: Damage contour plot and mesh distortion of the concrete core for the FE model using the default hourglass control formulation (HG type 1).	221
Figure 8.19: Damage contour plot of the concrete core for the FE model using the hourglass control formulation type 5.	221
Figure 8.20: Load time histories of FE models using different types of hourglass control formulations for the concrete core compared to the experimental result of the Control panel (CP).	222
Figure 8.21: Load time histories of FE models with and without the strain rate effects of the concrete compared to the experimental result of the Control panel (CP).	224
Figure 8.22: Damage contour plot of the concrete core at 0.012 s for the FE model using the material model CSCM considering the strain rate effect of the concrete.....	224
Figure 8.23: Load time histories of FE models with and without the strain rate effects of the mild steel compared to the experimental result of the Control panel (CP).	226
Figure 8.24: Von Mises stress contour plot on the faceplates for the FE model ignoring the strain rate effects of mild steel at the peak tensile membrane resistance (a) top faceplates and (b) bottom faceplates.....	226
Figure 8.25: Von Mises stress contour plot of the faceplates for the FE model considering the strain rate effects of the mild steel at the peak tensile membrane resistance (a) top faceplate and (b) bottom faceplate.....	227
Figure 8.26: A comparison between experimental and predicted results for the Control panel (CP) (a) load time histories, (b) displacement time histories. ...	228
Figure 8.27: Damage contour plot for the concrete core of the FE model for the Control panel.....	228
Figure 8.28: Von Mises stress contour plot on the top faceplate of the FE model of the Control panel.....	229
Figure 8.29: A comparison between experimental and predicted results for the Increased impact energy panel (4mP) (a) load time histories, (b) displacement time histories.....	230

Figure 8.30: A comparison between the experimental and predicted results for the Stainless steel panel (SP) (a) load time histories, (b) displacement time histories.	231
Figure 8.31: A comparison between the experimental and predicted results for the Lightweight core panel (LP) (a) load time histories, (b) displacement time histories.....	232
Figure 8.32: A comparison between experimental and predicted results for the Reinforced core panel (RP) (a) load time histories, (b) displacement time histories.....	233
Figure 8.33: A comparison between experimental and predicted results for the Double reinforced core panel (DRP) (a) load time histories, (b) displacement time histories.....	234
Figure 8.34: Damage contour plot for the concrete core of the FE model for the Reinforced core panel.....	234
Figure 8.35: Deformation and axial force distribution in the wire meshes of the FE model for the Reinforced core panel.....	235
Figure 8.36: A comparison between experimental and predicted results for the Panel with bracing elements (BP) (a) load time histories, (b) displacement time histories.....	236
Figure 8.37: Von Mises stress contour plot on the top faceplate for the FE model of the Panel with bracing elements.	236
Figure 8.38: A comparison between experimental and predicted results for the Improved bonding panel (IBP) (a) load time histories, (b) displacement time histories.....	238
Figure 8.39: Damage contour plot of the concrete core for the FE model of the Improved bonding panel.....	238
Figure 8.40: A comparison between experimental and predicted results for the Fully enclosed panel (ECP) (a) load time histories, (b) displacement time histories.	240
Figure 9.1: Masonry wall retrofitted by the thin steel sheet catcher system. (Crawford et al. 2009).....	243
Figure 9.2: Assumed bilinear stress-strain curve for the steel used in the thin sheet catcher system.....	244

Figure 9.3: Triangular deformed shape of the steel sheet.	246
Figure 9.4: Geometry and dimension (in mm) of a full scale non-composite SCS panel.	248
Figure 9.5: Deformation profile of a non-composite SCS panel subjected to blast loading of 250 kg TNT at a 5 m standoff distance: (a) at 0.005 s, (b) at 0.01 s and (c) at the maximum displacement.	251
Figure 9.6: A comparison between the maximum displacement of the rear faceplate predicted by the FE models and the analytical models under increased blast loading conditions.	254
Figure 9.7: A comparison between the maximum displacement of the rear faceplate predicted by the FE models and the analytical models for the SCS panels with increased rear faceplate thickness.	256
Figure 9.8: A comparison between the maximum displacement of the rear faceplate predicted by the FE models and analytical models for the SCS panels with increased concrete core thickness.	259
Figure 9.9: (a) Connection details between the non-composite SCS panel and the post, (b) geometry and dimension of the post.	262
Figure 9.10: FE model of the barrier consists of non-composite SCS panels and posts (a) top view, (b) isometric view.	264
Figure 9.11: The response of a protective barrier with 200 mm thick non-composite SCS panels supported by mild steel posts under the blast loading of 500 kg TNT at a 5 m standoff distance.	265
Figure 9.12: Fracture of the mild steel post at the base when the barrier was subjected to blast loading of 750 kg TNT at a standoff distance of 5 m.	267
Figure 9.13: Fracture of the mild steel rear faceplate at the flared ends when the barrier supported by high strength steel posts was subjected to blast loading of 1000 kg TNT at a standoff distance of 5 m.	270
Figure 9.14: (a) The panels and the post of the barrier, (b) simplification of the barrier system into two degrees of freedom system, (c) determination of the velocity of panel.	279
Figure 9.15: Static resistance functions: (a) the rear faceplate with a reduced plastic membrane response, (b) the elasto-plastic response of the post.	282

Figure 9.16: Displacement time histories of the middle panel and the post for the barrier supported by mild steel post under 250 kg TNT at a 5 m standoff distance, (a) FE simulation results and (b) two degrees of freedom system (2DOF).285

Figure 9.17: Reinforcement detail in the concrete blast wall designed to resist blast loading of 250 kg TNT at a 5 m standoff distance.....289

LIST OF TABLES

Table 2.1:Dynamic increase factors (DIF) for steel and concrete. (Cormie et al., 2009).....	33
Table 2.2:Deformation limits for different types of structures. (Cormie et al., 2009)40	
Table 4.1: Chemical composition of Grade 304 stainless steel used in this study.	68
Table 4.2: Experimental program of 304 stainless steel under quasi-static and medium strain rates.	69
Table 4.3: Summary of the 0.2% proof stress and the ultimate tensile strength of 304 stainless steel specimens tested using Instron universal tester.	72
Table 4.4: Summary of experimental results obtained from the IFWI test rig.	75
Table 4.5: Proposed Cowper-Symonds coefficients for stainless steel Grade 304 used in this study.....	81
Table 5.1: Details description for the SCS panels used in the static test.	84
Table 5.2: Mix proportions for one cubic meter of BST concrete with various densities. (BST concrete information sheet number 3.2).....	87
Table 5.3: Mix proportions for 0.12 m ³ lightweight concrete.....	87
Table 5.4: Unconfined concrete compressive strength of normal weight concrete and lightweight concrete used in the static test.	96
Table 5.5: Yield stress and ultimate tensile strength for mild steel and stainless steel.	98
Table 5.6: Summary of experimental results of non-composite SCS panel under static loading conditions.	118
Table 7.1: Detailed description of the SCS panels used in the impact test.....	157
Table 7.2: Concrete compressive strength for the concrete infill in the SCS panels.	160
Table 7.3: Comparison between experimental and theoretical maximum displacement and tensile membrane resistance.....	193
Table 8.1: Summary of the mesh convergence study.	208
Table 8.2: Hourglass energy in the concrete core.....	221

Table 9.1: Blast loading for various detonation scenarios obtained from ATBLAST.	250
Table 9.2: Maximum displacement of the rear faceplate and the hourglass energy ratio of the concrete core under various blast loading conditions.	252
Table 9.3: Strain energy partition in the non-composite SCS panel under increased blast loading condition.	252
Table 9.4: A comparison between the maximum displacement of the rear faceplate predicted by the FE models and the results of analytical models under increased blast loading conditions.....	253
Table 9.5: FE results for non-composite SCS panels with increased thickness of the rear faceplate.....	255
Table 9.6: Strain energy partition in non-composite SCS panels with increased thickness of the rear faceplate.....	255
Table 9.7: A comparison between the maximum displacement of the rear faceplate from the simulation results and the theoretical predictions for the SCS panels with increased rear faceplate thickness.	257
Table 9.8: FE results for non-composite SCS panels with increased concrete core thickness.	258
Table 9.9: Strain energy partition in the non-composite SCS panel with increased concrete core thickness.....	258
Table 9.10: A comparison between the maximum displacement of the rear faceplate from the simulation results and the theoretical predictions for the SCS panels with increased concrete core thickness.	260
Table 9.11: Deformation of the barrier with 200 mm thick SCS panels supported by mild steel posts under various blast loading conditions.	267
Table 9.12: Energy transferred from the SCS panels to the posts for 200 mm thick SCS panels supported by mild steel posts.	268
Table 9.13: Deformation of the barrier with 200 mm thick SCS panels supported by high strength steel posts under various blast loading conditions.....	269
Table 9.14: Energy transferred from the SCS panels to the posts for 200 mm thick SCS panels supported by high strength steel posts.	271
Table 9.15: Deformation of the barrier with 300 mm thick non-composite SCS panels supported by mild steel posts under various blast loading conditions.	272

Table 9.16: Energy transferred from the SCS panels to the posts for the barrier with 300 mm thick SCS panels supported by mild steel posts.....	272
Table 9.17: Deformation of the barrier with 300 mm thick SCS panels supported by high strength steel posts under various blast loading conditions.....	273
Table 9.18: Energy transferred from the SCS panels to the posts for the barrier with 300 mm thick SCS panels supported by high strength steel posts.....	274
Table 9.19: Equivalent uniform impulse on each components of the barrier determined using the Conwep program under various blast loading conditions.	276
Table 9.20: Theoretical maximum displacement of 200 mm thick non-composite SCS panel compared to the simulation results of the middle panel supported by steel posts under various blast loading conditions.	277
Table 9.21: Theoretical maximum displacement of 300 mm thick non-composite SCS panel compared to the simulation results of the middle panel supported by steel posts under various blast loading conditions.	277
Table 9.22: Velocity of the concrete core and rear faceplate upon contact under various blast loading conditions.....	280
Table 9.23: Properties of mild steel post and high strength steel post.....	282
Table 9.24: A comparison between the maximum deformation of the barrier predicted by the FE models and two degrees of freedom (2DOF) system.....	284
Table 9.25: Comparison between the concrete blast wall and the barrier composed of non-composite SCS panels supported by mild steel posts under blast loading of 250 kg TNT at 5 m standoff distance.	290

NOMENCLATURES

A	is the area
a	is the acceleration
B	is the width of a cross section
C	is the axial compressive force
C_D	is the drag coefficient
D	is the flexural rigidity of the plate or Cowper-Symonds coefficient
d	is the scalar damage parameter or diameter
d_e	is the effective depth of a cross section
E	is the Young's modulus or energy
F	is the force
F_f	is the shear failure surface
F_c	is the hardening cap
f_c	is the unconfined compressive strength of concrete
H	is the thickness of the plate or concrete core
I	is the second moment of area or reflected blast impulse
J	is the stress invariant
K	is the axial stiffness of the test rig or flexural stiffness of the panel
k	is the dimensionless rig constant
k_e	is the ratio of support displacement (Δ) to the elastic extension of the middle surface of the plate
L	is the length between supports
M	is the moment or mass
M_o	is the plastic moment capacity
m	is the bending moment parameter or mass per unit area
n	is the ratio of the modulus of elasticity
P	is the concentrated load
P_o	is the plastic flexural collapse load
p	is the force parameter or pressure
q	is the uniformly applied load or Cowper-Symonds coefficient
q_o	is the uniform collapse load of the plate

R	is the distance from the centre of a spherical charge in meters
$R(x)$	is the resistance function
R_m	is the dynamic ultimate load capacity
X_E	is the elastic displacement limit
X_m	is the maximum displacement
x	is the distance from the support
T	is the axial tensile force
T_o	is the axial yield force of the cross section
t	is the axial force parameter or time
V	is the volume
W	is the charge mass expressed in kilograms of TNT
Z	is the scaled distance
z	is the position of the neutral axis
\ddot{x}	is the acceleration
α	is the coefficient
δ	is the displacement
v	is the velocity
η	is the strain energy per unit volume
θ	is the support rotation
τ	is the shear resistance per unit area
ρ_s	is the shear span ratio
ε	is the strain
$\dot{\varepsilon}$	is the strain rate
Δ	is the in-plane displacement at the supports
$\dot{\theta}$	is the rate of rotation of adjacent sections
$\dot{\varepsilon}$	is the rate of extension of centriodal fibre
λ	is the extension of the plate
σ	is the stress
ν	is the Poisson ratio
μ	is the membrane stress parameter
K	is the Rubin three invariants reduction factor

DEVELOPMENT OF A HIGH PERFORMANCE PROTECTIVE BARRIER UTILISING NON-COMPOSITE STEEL-CONCRETE-STEEL PANELS

Sih Ying Kong

A thesis for Doctor of Philosophy

School of Civil, Mining and Environmental Engineering, Faculty of Engineering,
University of Wollongong

ABSTRACT

This study investigates the response of axially restrained non-composite steel-concrete-steel (SCS) panels under static, impact and blast loading conditions. This type of panels shows promising economic and technological characteristics as protective barriers for critical infrastructure protection. Axially restrained non-composite SCS panels have high strength and ductility, which enable them to withstand extreme loading such as impact and blast. The concrete core mass provides inertial characteristics which are beneficial for resisting impulsive loads. The primary resisting mechanism in this type of panels is based on dissipation of imparted energy by axial stretching of the steel faceplates (membrane resistance) and crushing of the concrete core. No hazardous projectiles will be generated since the concrete core is confined by the steel faceplates. The overall cost of construction is reduced by not providing shear connectors between the steel faceplates.

Comprehensive experimental investigations have been carried out on axially restrained non-composite SCS panels under static and impact loading conditions. The experimental results have demonstrated that the panel resistance combines the flexural resistance at the initial stage, followed by the tensile membrane resistance of the steel faceplates under large deformation. The tensile membrane resistance of steel faceplates at large deformation could be significantly higher than the flexural capacity of non-composite SCS panels, and it is the main energy dissipation mechanism in this type of panels. The static resistance function of axially restrained non-composite SCS panels has been derived from the results of quasi-static monotonic loading tests. The finite element (FE) modelling techniques for the non-

composite SCS panels have been developed and validated against the impact test results of the panels.

Using the validated FE modelling techniques, the response of axially restrained non-composite SCS panels subjected to blast loading has been investigated. It is observed that the response of non-composite SCS panels under blast loading can be simulated by simplified model of the thin steel sheet catcher systems. During blast loading, the front faceplate is separated from the concrete core and bounces back before the panel reaches its maximum displacement. Therefore, the energy dissipation by the front faceplate can be neglected, while the rear faceplate dissipates about 80% of the kinetic energy in the panel through membrane stretching. A simplified engineering-level model of the panel has been proposed that considers only the rear faceplate as a catcher system for resisting the impulse delivered by the fragmented concrete core.

The response of a barrier composed of non-composite SCS panels and steel posts subjected to blast loading has been studied using numerical simulations. It is found that a certain amount of kinetic energy in the panels is transferred and dissipated by the steel posts due to panel-post interaction. The failure modes observed from the simulations are bending failure of the posts and fracture failure of the rear faceplate of the non-composite SCS panel. From the comparison between the response of a reinforced concrete blast wall and the barrier utilising non-composite SCS panels, it is found that the barrier with non-composite SCS panels could reduce the wall thickness by about 60% when similar amount of steel is used in the construction of both walls. Therefore, the barrier utilising non-composite SCS panels is an economical alternative to the reinforced concrete blast walls in resisting close-range detonation of high explosives.

As part of this study, an instrumented falling weight impact (IFWI) test rig is developed to investigate medium strain rate effects on stainless steel. The test results of the stainless steel specimens in this study are significantly lower than the theoretical prediction using the existing Cowper-Symonds coefficients. From comprehensive literature reviews, it is found that the stress level, prior work hardening, heat treatment condition and microstructure of the stainless steel will

affect the strain rate effects. Therefore, the Cowper-Symonds coefficients should be used with care. Improved Cowper-Symonds coefficients have been proposed for the stainless steel Grade 304 used in this study.

ACKNOWLEDGMENTS

First of all, the author would like to thank his supervisor, Associate Professor Alex Remennikov for his guidance and invaluable support throughout the course of this research. The author is extremely grateful to Associate Professor Alex Remennikov for his contribution of ideas and constructive criticism that has led to the completion of this study.

The author would like to express his sincere appreciation to Professor Brian Uy of the University of Western Sydney for his comments and suggestions, and also providing financial support for the experiments carried out at the University of Western Sydney. The author would like to thank technical officers from the University of Wollongong and University of Western Sydney for their assistance in the experiments, namely Alan Grant, Ian Bridge, Ritchie MacLean, Cameron Nielsen, Robert Marshall and Daniel Gallaty.

The author would like to express his gratitude to the Australia Research Council (ARC) for his PhD scholarship and financing this research project. My sincere appreciation also goes to all my colleagues and friends, Dr. Lip Teh, Jie Yang, Khay Wai See, Nadeesha Dhamarsiri, Vo-Trong Nguyen, Zhenyu Zhang, Thirukumaran Sivanathan and Ni Jing whose support and friendship contributed to the successful completion of this research.

The author would like to thank his wonderful wife, Jeannie Wong Hsiu Ding, for her support, encouragement and patience. The author is deeply grateful for the continuous moral support from his family, which motivated him during the course of his candidature.

PUBLICATION LIST

Journal papers

Remennikov, A.M., Kong, S.Y. and Uy, B. (2011). "The Response of Foam- and Concrete-Filled Square Steel Tubes under Low Velocity Impact Loading." *Journal of Performance of Constructed Facilities (ASCE)* 25 (5), pp. 373-381.

Kong, S.Y., Remennikov, A.M., Uy, B. (2012). "Numerical simulation of the response of non-composite steel-concrete-steel sandwich panels to impact loading". *Australian Journal of Structural Engineering* Vol 12, No. 3.

Conference papers

Remennikov, A.M, Kong, S.Y., Uy, B. (2009). "Response of rigid polyurethane foam-filled steel hollow columns under low velocity impact". 8th International Conference on Shock & Impact Loads on Structures, 2-4 December 2009, Adelaide, Australia.

Remennikov, A.M, Kong, S.Y., Uy, B. (2009). "Simulation of impulsive loading on columns using an inflatable airbag technique". 8th International Conference on Shock & Impact Loads on Structures, 2-4 December 2009, Adelaide, Australia.

Remennikov, A.M, Kong, S.Y., Uy, B. (2010). "Static and dynamic behaviour of non-composite steel-concrete-steel protective panels under large deformation". 4th International Conference on Steel & Composite Structures, 21-23 July 2010, Sydney Australia.

Remennikov, A.M, Kong, S.Y., Uy, B. (2010). "Impact resistance of non-composite axially restrained steel-concrete-steel sandwich panels". *Australasian Structural Engineering* 2010, 8-12 August 2010, Sydney, Australia.

Kong, S.Y., Remennikov, A.M., Uy, B. (2010). "Numerical simulation of high-performance SCS panels under static and impact loading conditions". *Proceedings of the 21st Australian Conference on the Mechanics of Structures and Materials*, 7-10 December, Melbourne, Australia.

Kong, S.Y., Remennikov, A.M., Uy, B. (2010). “The effect of medium strain rates on the mechanical properties of high performance steels”. Proceedings of the 21st Australian Conference on the Mechanics of Structures and Materials, 7-10 December, Melbourne, Australia.

Remennikov, A.M, Kong, S.Y., Uy, B. (2011). “A High-Performance Protective Barrier Utilizing Non-Composite Steel-Concrete-Steel Sandwich Panels.” International Symposium on Interaction of the Effects of Munitions with Structures, 19-23 September 2011, Seattle, USA.

CHAPTER 1

INTRODUCTION

In recent years, car bombs have been widely used by terrorists to attack government buildings, important landmarks and critical infrastructure facilities. The Vehicle Borne Improvised Explosive Device (VBIED) is an effective weapon because it can be detonated at close proximity to a target, producing high pressure loads and large amount of flying debris that cause severe damage to personnel and buildings. The Australian embassy bombing on the 9th of September 2004 in Jakarta, Indonesia, was an example of a vehicle-based bomb attack on Australian critical infrastructure facility. The terrorist attack on the Alfred P. Murrah Federal building in Oklahoma, United States, in 1995 killed 168 people and destroyed one-third of the building.

With the consideration of car bombings and accidental vehicle impacts on critical infrastructures, there is an increasing need to develop a cost-effective solution for protecting these facilities. The Australian Government defines critical infrastructure as facilities that, if destroyed, degraded or rendered unavailable for an extended period, would significantly affect the social or economic well-being of the nation. These include buildings, bridges and offshore structures.

Buildings and infrastructure facilities can be incorporated with hardening designs such as wrapping with different types of fibres, polymers or steel sheets to increase the robustness of the structures. These hardening techniques can be very expensive and the appearance of a hardened structure is likely to be intrusive. An alternative method of protection is to construct a perimeter wall which increases the standoff distance between targeted structures and the bomb. This effectively reduces the blast pressure on the buildings and the occupants. When a vehicle bomb is detonated adjacent to the protective wall, the wall protects the targeted structures behind it by reflecting the blast pressure back towards the explosive source. The wall also provides anti-ram protection against vehicle impact.

Steel-concrete-steel (SCS) panels are an effective means of protecting structures against extreme impact and blast loading due to their high strength and ductility characteristics. According to Hulton (2010), the application of SCS panels could significantly reduce the wall thickness required to prevent breaching and spalling failure compared to reinforced concrete blast walls. In conventional SCS panels, shear connectors are provided to transfer shear stress at the concrete-steel interface. Crawford and Lan (2006) presented the design philosophy of non-composite SCS panels to resist blast loading, where the rear faceplate dissipated the energy through tensile membrane action. Non-composite SCS panels have high energy absorption capability, and promising economic and technological advantages.

The SCS panels can utilise high performance steel such as stainless steel as it exhibits improved strength, corrosion resistance and energy absorption capacity compared to mild steel. According to Gardner (2005), the ductility for common austenitic stainless steel grades is approximately 40–60% compared to around 20-30% for mild steel. These characteristics show that stainless steel is a potential candidate in the construction of steel-concrete-steel protective barriers to resist close-range detonation of high explosives. Furthermore, profiled stainless steel sheets have been used effectively to contain hydrocarbon explosions in the oil and gas industry (Langdon and Schleyer, 2005 a & b, and Langdon and Schleyer, 2006).

1.1 Statement of problem

The design guidelines for a reinforced concrete blast wall to resist close-in detonation of high explosives are provided by TM5-1300 (U.S. Department of the Army, 1990). The disadvantages of using a reinforced concrete blast wall are the spalling of concrete cover during blast loading, enormous wall thickness and complicated construction process. The blast wave could cause spalling of the concrete cover, thus producing high-velocity fragments that might cause more damage to personnel or structures behind the blast wall than the blast pressure itself. To resist large vehicle bombs at close range, the thickness of concrete walls required is likely to be more than 500 mm and their application in an urban environment might be limited due to space constraint.

The use of lacing reinforcement to maintain the structural integrity of reinforced concrete blast walls when subjected to close-in detonations is not feasible due to difficulties in construction and limited access to skilled labour required for this type of construction. Some of the commercial blast walls address these issues by utilising simple construction techniques such as Hesco Basket and Defencell (Smith, 2010). These barriers resist the blast loading through inertial effects, therefore a very thick wall is required and their appearance is likely to be very intrusive in urban settings.

Over the past years, research in steel-concrete-steel sandwich panels have been focused on the development of shear connections between the concrete infill and steel plates to achieve full or partial composite action, and increase the flexural capacity of the panels. The use of shear connectors, such as friction-welded steel bars in Bi-steel panels and J-hook connectors, require a high level of technical skill and high construction cost. In addition, the benefits of membrane resistance of the steel plates are not considered in the design. Shanmugam and Kumar (2005) showed that steel-concrete-steel panels are capable of developing tensile membrane resistance at large displacements under static loading.

Crawford and Lan (2006) presented the design philosophy for axially restrained SCS panels without shear connectors to resist blast loading. The advantages of this non-composite SCS panel are high energy absorption capability, and improved economic and technological characteristics. The mass of concrete core is used to provide inertial characteristics, and the imparted energy is dissipated by axial stretching of the steel faceplates (membrane action) and crushing of the concrete core. Based on a comprehensive literature review, it is found that there are no detailed studies addressing analytical and experimental investigation of this type of non-composite SCS panel.

Physical testing of a prototype protective barrier under vehicle impact and blast loadings involves significant amount of resources, a high cost and is time consuming. Therefore, most studies on structural performance under blast loadings are carried out using non-linear transient dynamic finite element (FE) softwares. The FE modelling techniques are available for SCS panels under static loading condition

(Shanmugam et al. 2002 and Foundoukus and Chapman 2008). However, there is a lack of open literature on the FE modelling techniques for non-composite SCS panels under impact and blast loading conditions. The FE modelling of non-composite SCS panels under extreme loading events is challenging due to difficulties in modelling the non-linear behaviour of concrete and concrete-steel interaction under these loading conditions.

Material properties under high strain rate are required in the design of structures subjected to impact and blast loading. The strain rate effect on the strength of steels is considered by using Cowper-Symonds coefficients. The existing Cowper-Symonds coefficients for stainless steel were derived based on the stainless steel with a yield stress of about 200 MPa in 1978. Literature reviews suggest that differences in stress level, prior work hardening, heat treatment condition and microstructure could affect the mechanical properties under increased strain rates. As this study is concerned with the performance of high performance steels under extreme loading conditions, the Cowper-Symonds coefficients of stainless steel will be revised to take into account the significant improvements made in the yield strength of recent grades of stainless steels.

1.2 Research objectives

This project aims to utilise the benefits associated with high performance steels and infill materials to reduce the vulnerability of building and infrastructures to extreme events using a cost-effective protective barrier. The specific objectives of this study are as follows:

- (a) To utilise the benefits of high performance steel (high strength steel and stainless steel) and infill materials in developing high performance blast resistant barriers;
- (b) To determine the material properties of stainless steel under medium strain rates;
- (c) To utilise a novel structural form for protective barrier structures to resist close-range detonation of high explosives;
- (d) To determine the response of non-composite SCS panels under static, impact and blast loading conditions;
- (e) To develop three-dimensional finite element modelling techniques for the non-composite SCS panels under impact and blast loading conditions;

- (f) To develop the design recommendations for protective panels under impact and blast loading.

1.3 Scope of research

The material properties of stainless steel under medium strain rates will be determined by using the instrumented falling weight impact (IFWI) test rig developed at the University of Wollongong. Based on the experimental results, new Cowper-Symonds coefficients for stainless steel used in this study will be proposed. Suitable structural form and connection details for the high capacity anti-ram and blast barriers utilising high performance steels (stainless steel and high strength steel) and infill materials will be identified, followed by the experimental testing of the scaled barrier models under static and impact loading conditions. The static test results of scaled models of non-composite SCS panels will be used to construct the static resistance function, while the experiment results from impact testing will be used to calibrate the finite element (FE) model. Using the validated FE modelling techniques, a full scale FE model of the barrier will be generated to carry out a parametric study for blast loading conditions. Based on the simulation results, recommendations for analysis and design of protective barriers utilising non-composite SCS panels will be developed.

1.4 Organisation of thesis

This thesis has 10 chapters, followed by references. The content of each chapter is briefly described.

Chapter 1 contains an introduction, statement of problem, research objectives and scope of this research.

Chapter 2 gives a survey of literature on a wide range of topics related to this research, including 1) effectiveness of blast wall in protecting targeted structures from vehicle bombs, 2) types of blast wall, 3) blast and impact loading characterisation, 4) material properties under high strain rate and 5) the response of structure components under impact and blast loading conditions.

Chapter 3 presents a comprehensive review on analytical models for the membrane resistance of the steel plate under fixed and semi-rigid support conditions.

Chapter 4 discusses the derivation of existing Cowper-Symonds coefficients for stainless steel Grade 304, followed by the experimental testing of stainless steel specimens under high strain rate loading. The experimental results of the stainless steel specimens are compared to the existing Cowper-Symonds coefficients.

Chapter 5 presents the static testing of scaled models of non-composite SCS panels. The panels are supported by axial restraint supports to restrain the in-plane movement of panels during the tests. The load-displacement relationship of the axially restrained non-composite SCS panels under quasi-static loading is developed. A comprehensive parameter study is carried out to investigate the effects of different infill materials, application of stainless steel and degree of interaction between the concrete core and steel faceplates on the static behaviour of the panels.

Chapter 6 shows the derivation of the static resistance function for axially restrained non-composite SCS panels.

Chapter 7 investigates the response of axially restrained non-composite SCS panels under impact loading condition. The experimental program includes investigations on the effects of different infill materials, application of stainless steel and degree of interaction between the concrete core and steel faceplates on the impact behaviour of panels. The impact test results are compared to the static test results to identify the differences in the response of panels under static and impact loading conditions. The static resistance function is used to predict the impact response of the panels and the theoretical results are compared to the impact test results.

Chapter 8 presents three dimensional finite element (FE) modelling techniques for the axially restrained non-composite SCS panels under impact loading condition. These modelling techniques are verified against the impact test results of the panels.

Chapter 9 investigates the response of non-composite SCS panels under blast loading condition using the validated FE modelling techniques. Firstly, the response of non-composite SCS panels under fixed support condition is studied. Then, the response of the barrier structure composed of non-composite SCS panels and steel posts are investigated. The analytical model for the thin steel sheet catcher system is adapted to predict the response of non-composite SCS panels subjected to blast loading. Two degrees of freedom system is developed for the barrier structure composed of non-composite panels and steel posts. The response of the barrier is compared to the response of the reinforced concrete blast wall under the same blast loading condition.

Chapter 10 presents the conclusions and recommendations for future research.

CHAPTER 2

LITERATURE REVIEW

Blast pressure generated from VBIEDS (Vehicle-Based Improvised Explosive Devices) can cause loss of life and catastrophic collapse of buildings or infrastructure facilities. The terrorist attack on the Alfred P. Murrah Federal building in the United States in 1995 killed 168 people and destroyed a third of the building. Buildings or infrastructures can incorporate hardening techniques to structural members such as wrapping with FRP (fibre-reinforced polymers) or jacketing with steel plates to increase the robustness of the structures. These hardening techniques could be expensive and the appearance of the hardened structure is likely to be intrusive. An alternative method of protection is to construct a perimeter wall which increases the standoff distance between the targeted structures and the bomb, which effectively reduces the blast pressure on the buildings and the occupants (Smith, 2010). When a vehicle bomb is detonated adjacent to the protective wall, the wall protects the targeted structures behind it by reflecting the blast pressure back towards the explosive source. The blast wave interaction with the blast wall is shown in Figure 2.1. The process of blast pressure-wall interaction (reflection and diffraction of blast pressure) leads to significant reduction of blast pressure behind the wall compared to the situation where the wall is not provided. The wall also provides anti-ram protection against the vehicle impact.

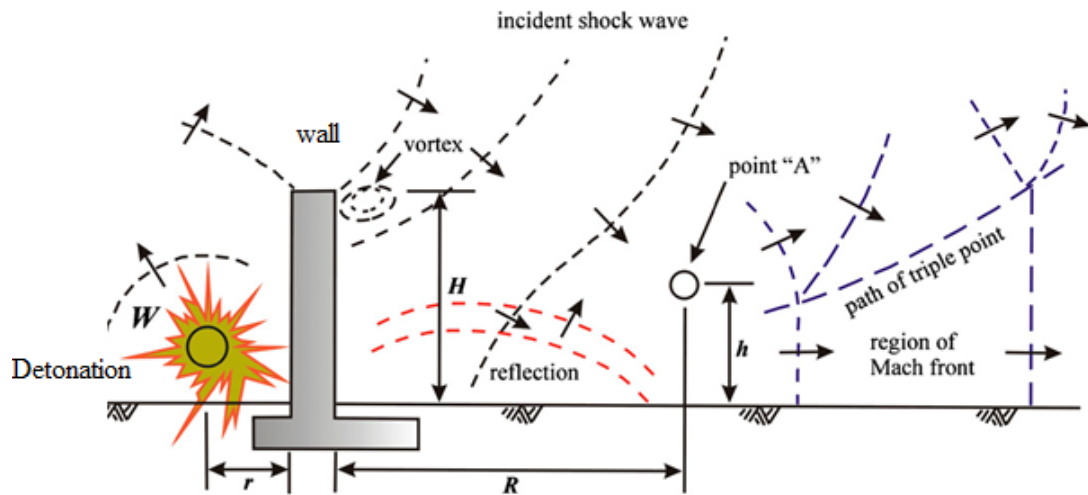


Figure 2.1: Interaction between the blast pressure and protective wall with the blast environment behind the wall. (Remennikov and Rose, 2007)

2.1 Effectiveness of protective walls in reducing blast loading

Beyer (1986) conducted small-scale blast tests to quantify the blast pressure parameters behind the blast wall (protective wall) such as the peak overpressure, blast impulse and blast load duration. It showed that the blast pressure parameters at a certain point behind the protective wall were influenced by the mass of explosive charge, distance of charge from the wall, elevation of charge above the ground and the height of the wall. Generally, the peak overpressure and blast impulse behind the wall was reduced compared to the situation where there was no wall at all. The study described the important blast wave-wall interactions, including diffraction of the blast wave over the wall, reflection of the blast wave from the ground and formation of Mach Stem behind the wall as shown in Figure 2.1.

Rose et al. (1995) conducted blast testing on a one-tenth scale rigid steel wall to measure the blast environment behind a vertical blast wall caused by detonation of high explosives. The vertical wall was constructed from a 20 mm thick steel plate, with the height and width of 300 mm and 2100 mm, respectively. The pressure-time histories were measured in the grid, which was located up to 6 wall heights and up to 3 wall heights above the ground behind the wall. The results showed that the blast

pressure and impulse for distance up to 6 wall heights behind the wall could be reduced up to 60% of those without a wall.

Rose et al. (1997) carried out further research to investigate the effects of different heights of burst and standoff distances between the charge and the wall on the blast environment behind the wall. The peak overpressure and the peak impulse were plotted in the “scaled space” that allowed a wide range of different threat scenarios to be represented. Figure 2.2 shows the curves for the peak scaled impulse versus the scaled distance behind the wall measured at a height, $h = 600$ mm. W (in Figure 2.2) is the mass of charge, R is the distance behind the wall, r is the standoff distance of the charge from the wall, z is the height of charge from the ground, and h is the height of measurement points. It shows that the peak blast impulse behind the wall decreases as the distance behind the blast wall increases. Therefore, the distance between the wall and the protected structure should be optimized in the design stage to obtain the highest level of protection.

Rose et al. (1998) investigated the effectiveness of barriers with limited robustness for blast protection. Walls were constructed from a range of materials, including sand, wood, ice, water and expanded foam plastic. The experimental results showed that these types of walls suffered severe damage (partial failure) after the test. The significant finding of this research is that walls with limited robustness are as effective as rigid blast walls in reducing the blast impulse behind the wall. However, it is important to note that the partial failure of the walls does produce high velocity secondary fragments that could cause damage to structures behind it or injury to personnel.

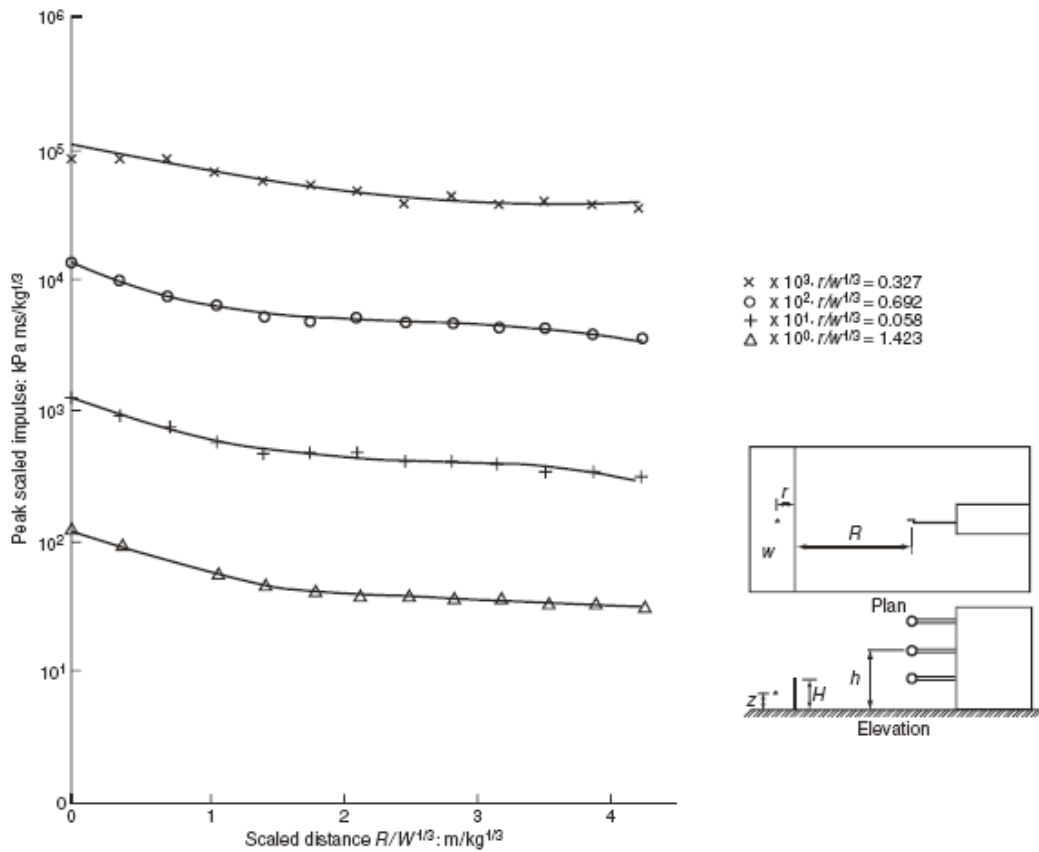


Figure 2.2: Peak scaled impulse versus scaled standoff distance at $h= 600\text{mm}$. (Rose et al. 1997)

2.2 Types of blast barriers

Smith (2010) and Hulton (2010) presented extensive reviews on the design of different types of blast walls used in military and civilian applications. The blast barrier can be categorised into simple earth-filled walls, to more sophisticated reinforced concrete walls and composite walls. The composite walls can be divided into concrete-sand-concrete and steel-concrete-steel wall. The design of composite concrete-sand-concrete walls is provided in TM5-1300 (U.S. Department of the Army, 1990).

The steel-concrete-steel (SCS) composite walls consist of a thick concrete core confined by two relatively thin steel faceplates. Crawford and Lan (2006) presented details of a new design concept of SCS sandwich wall without shear connectors connecting the steel plates to the concrete core. The robustness of the SCS panel

without shear connectors has been verified under detonation of a large amount of high explosives by Crawford and Lan (2006).

2.2.1 Earth-filled wall

Earth-filled wall is easy to build, and is relatively cheap compared to other types of blast barriers. It relies on the inertial effect of the soil infill to resist the blast or impact loading. Therefore, enormous wall thickness is usually required (1-2 metres). Its application in the urban environment is limited due to its thickness and aesthetic aspect. Sand-bag walls are commonly used in military expeditions. Two examples of earth-filled walls developed using geotextile are the Hesco Bastions and the Defencell (Smith, 2010). The Hesco Bastions are steel wire gabions, lined with geotextile and then filled with soil, sand or rubble. The Defencell is a grid formed by geotextile and filled with sand. Both Hesco Bastion and Defencell can be stacked to build a wall of desired height, as exemplified by the Hesco Bastion in Figure 2.3. The Houston Barricade is made of high density polythene construction filled with granular ballast. It is portable and several units can be interconnected to form a blast wall. Crawford and Lan (2006) described the use of corrugated steel sheets to form cells of width ranging 1-2.5 m that are then filled with sand. The system is called Metalith and a simple pinning mechanism is used to attach the sheets together.



Figure 2.3: A protective barrier constructed using Hesco Bastions. (Crawford and Lan, 2006)

2.2.2 Reinforced concrete wall

According to Hulton (2010), extensive research had been conducted in the United States on reinforced concrete structures for protection against nuclear threats and their use as explosives storages. TM5-1300 (U.S. Department of the Army, 1990) provides the design specifications for reinforced concrete blast walls to resist close-in detonation of high explosives. Lacing reinforcement is provided in the reinforced concrete blast wall to maintain its structural integrity under large deformation as shown in Figure 2.4. Localised high pressure concentrations due to close-in detonations can produce punching failure on blast walls. With the lacing reinforcement, the punching failure can be prevented, and the localised high shear stress due to close-in detonation of high explosives is spread out to a greater area of the wall. The disadvantages of using the lacing reinforcement are its complicated construction process and high construction cost.

The resistance of reinforced concrete blast walls should be determined based on the ultimate moment capacity for various possible cross-section types, ultimate shear capacity as well as ultimate direct shear and punching shear capacity. Design of reinforced concrete blast walls under various support conditions is presented in the TM5-1300 (U.S. Department of the Army, 1990). Cormie et al. (2009) described the design of a cantilever reinforced concrete blast wall subjected to impulsive and quasi-static loading using the equivalent single degree of freedom (SDOF) system. Commercially available precast concrete blast walls, “Alaska” and “Texas” barriers are shown in Figure 2.5. According to Smith (2010), “Texas” and “Alaskan” barriers have been widely deployed in Baghdad and Afghanistan to protect military and civilian facilities.

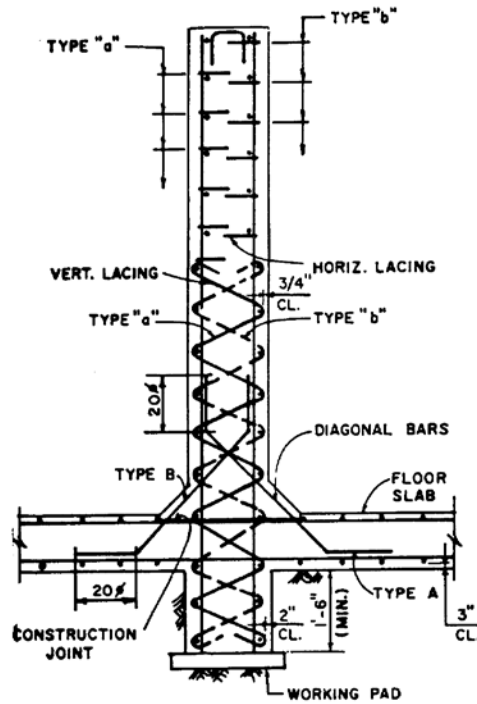


Figure 2.4: Cantilever reinforced concrete blast wall with lacing reinforcement. (U.S. Department of the Army, 1990)



Figure 2.5: Pre-cast concrete blast walls 'Texas' (smaller in size) and 'Alaskan'. (Smith, 2010)

The concrete in the reinforced concrete structures will shatter under strong impact or blast loading, producing high speed secondary fragments which are hazardous to the building and its occupants. Cavill and Rebstroff (2006), Coughlin et al. (2010) and Nili and Afroughsabet (2010) showed that the ductility and toughness of the concrete could be increased by adding steel fibres into the concrete mix. Wu et al. (2009), Ngo et al. (2007) and Farnam et al. (2010) showed that the performance of concrete under blast loading could be improved significantly by using FRP and CFRP. Zhang et al. (2005) and Dancygier et al. (2007) showed that the high strength concrete performed better under impact loading conditions compared to the normal strength concrete. Millard et al. (2010) conducted experimental study on ultra high performance fibre-reinforced concrete and proposed a new dynamic increase factor for the flexural tensile strength of this concrete. Nystrom and Gylltoft (2011) conducted a numerical study on the steel fibre-reinforced concrete and concluded that the scabbing crater could be reduced and prevented by using fibre-reinforced concrete.

2.2.3 Concrete-sand-concrete wall

The TM5-1300 (U.S. Department of the Army, 1990) provides the guidelines for designing composite panels composed of two reinforced concrete panels separated by a sand filled cavity as shown in Figure 2.6. They are normally used to resist close-in detonation of large amount of high explosives. These structures are designed for incipient failure, and if the support rotation is limited to 4 degrees or less, single-leg stirrups can be used to replace the lacing reinforcement.

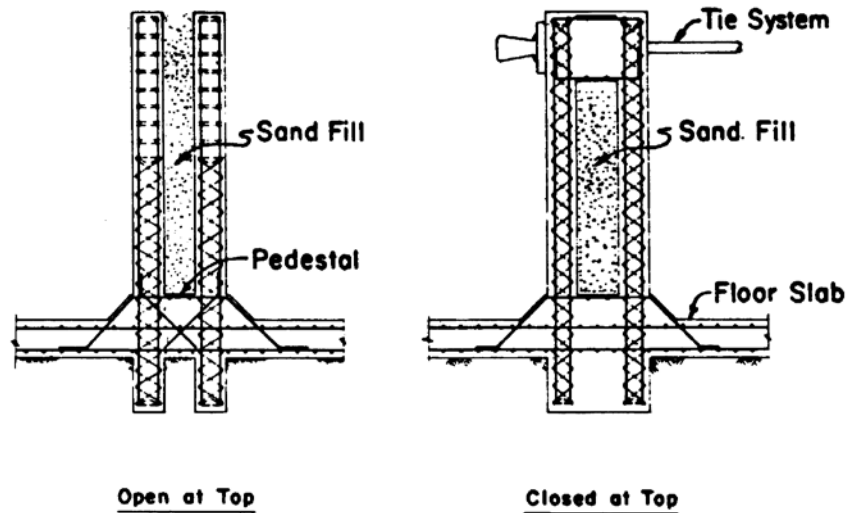


Figure 2.6: Blast barriers consist of two reinforced concrete panels and a sand infill. (U.S. Department of the Army, 1990)

The blast resistance mechanisms of the concrete-sand-concrete composite structures are:

- (a) the strength and ductility of the concrete panels
- (b) blast attenuating ability of the sand infill, including increased mass of the composite panel, increased distance travelled by the blast wave due to sand-infill (blast wave dispersion), and the energy absorbed by displacement and compression of sand particles.

The higher the initial density of sand, the lower amount of energy will be absorbed. For the sand with a density around 1600 kgm^{-3} , the deflection magnitude of the front panel is approximately the same as the rear panel. While for the sand with a density of 1360 kgm^{-3} , the magnitude of deflection for the rear panel is significantly less than the front panel. This is due to the sand with lower density has more voids, therefore, more room for the movement of sand particles. The sand movement allows large deflection at the front panel before the near solid state of sand occurs and pushes the rear panel in the direction of the blast loading.

2.2.4 Steel-concrete-steel structures

Composite steel-concrete-steel (SCS) or double skin composite structures consist of a concrete core connected to two steel faceplates using mechanical shear connectors. This form of construction was originally conceived during the initial design stage for the Convy river submerged tube tunnel in UK (Narayanan, 1994) and has been used in building cores, gravity seawalls, nuclear structures and defence structures.

Shear resistance at the steel and concrete interfaces is vital in determining the flexural capacity of the SCS panels. The flexural capacity of SCS panels increases as the degree of shear connection increases. The SCS panels can achieve the maximum flexural capacity when the shear connection provided is sufficient to achieve full composite action. Mechanical shear connectors currently used to achieve composite action in SCS panels are headed studs, friction-welded bars and J-hooks. Oduyemi and Wright (1989), Wright et al. (1991) and Shanmugam and Kumar (2005) carried out experimental investigations on the response of SCS structural members with headed shear studs subjected to static loading. Corus UK has developed Bi-steel panels with transverse steel bars that are friction-welded to both steel faceplates simultaneously as shown in Figure 2.7 (a). Xie et al. (2007) conducted static tests on the Bi-steel panels and developed analytical equations to predict the bending response of the panels. Liew and Soheli (2009) presented double J-hook connectors to interlock the steel faceplates, as shown in Figure 2.7 (b).

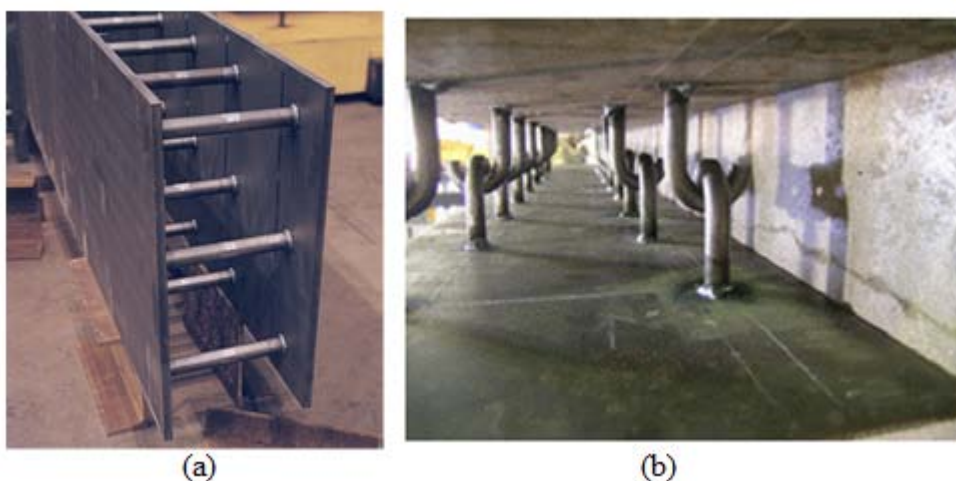


Figure 2.7: (a) Bi-steel panel before concrete casting (Hulton, 2010), (b) J-hook panel before concrete casting (Liew and Soheli, 2009)

SCS panels are effective in protecting structures against extreme impact and blast loading because of its high strength and ductility characteristics. Young and Coyle (2002) showed that Bi-steel panels were able to withstand in-contact and close-in detonations of high explosives. The required wall thickness to prevent breach and spalling could be significantly reduced compared to reinforced concrete blast walls. Hulton (2010) showed that the full scale barrier made of 300 mm thick Bi-steel panels could withstand the explosion of 2 tonnes of high explosives at a range of 2 metres. Figure 2.8 illustrates the experimental set up and the deformation of the Bi-steel wall after subjected to the blast loading. According to Hulton (2010), the Redline 2 blast wall is a steel-concrete-steel wall that is more effective in resisting blast loading than an equivalent Bi-steel wall (in terms of thickness). The steel faceplates of the Redline 2 wall are connected by steel hoops. The Redline 2 wall is shown in Figure 2.9. Liew et al. (2009) performed low-velocity impact tests on the J-hook panels filled with lightweight concrete. The results showed that the J-hook panels resisted the impact loading by flexural resistance, and the maximum displacement of the panels was reduced with a higher number of shear connectors.

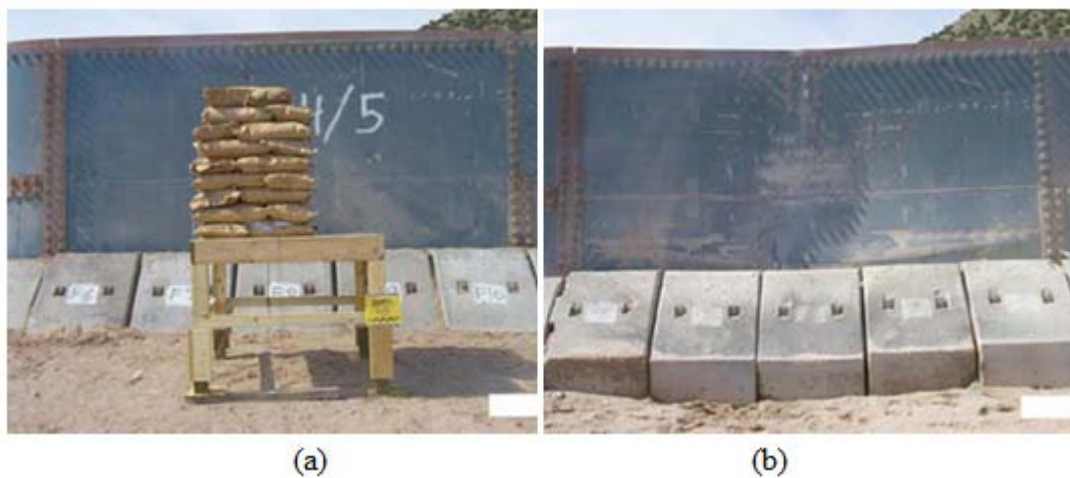


Figure 2.8: Bi-steel wall subjected to detonation of two tonnes of high explosives at 2 m standoff distance (a) before the test and (b) after the test. (Hulton, 2010)



Figure 2.9: Redline 2 wall. (Hulton, 2010)

So far, very limited research has been carried out on SCS panels without using the abovementioned shear connectors. Heng et al. (1995) carried out an experimental study on fully enclosed SCS panels under static and blast loading conditions, and no other means of shear connectors was used in these panels. The model blast test results showed that this type of panels could provide expedient construction and high level of protection. Lan et al. (2005) carried out further studies on the fully enclosed SCS panels, and the results showed that these panels were able to withstand very large blast pressures. Crawford and Lan (2006) presented the design philosophy of non-composite SCS panels to resist blast loadings and these design concepts had been verified by experimental results. Figure 2.10 shows the deformation of non-composite SCS panel of the Adler blast wall after subjected to close-in detonation of large amount of high explosives. The rear faceplate dissipated the energy through tensile membrane action and it confined the concrete core to minimize the hazardous debris due to damage of concrete core.



Figure 2.10: Deformation of Adler blast wall after subjected to close-in detonation of high explosive. (Crawford and Lan, 2006)

2.2.4.1 Adler blast wall

Adler blast wall is composed of non-composite SCS panels supported by steel posts (Crawford and Lan, 2006). Non-composite SCS panels have high energy absorption capability and promising economic and technological characteristics. The concrete core mass provides inertial effects which are beneficial in resisting the impulsive loading. Imparted energy is dissipated by axially stretching of the steel faceplates (membrane action) and crushing of the concrete core. No hazardous projectiles will be generated since the concrete core is confined by the steel faceplates. The overall cost of construction is reduced by not providing shear connectors between the faceplates.

Three major components in this protective barrier are: 1) the SCS panel without shear connectors, 2) the flared end connections, and 3) steel posts acting as effective supporting structures. Simple keyed connections are used to connect the panels to the steel posts. The keyed connections have sufficient axial and rotational stiffness, and it provides the axial restraint to enable tensile membrane action in the panels that undergo large deformation. The steel posts are penetrated into the soil, therefore, the impact or blast energy will be dissipated through the bending of the steel posts and deformation of soil. The prototype barrier is shown in Figure 2.11.

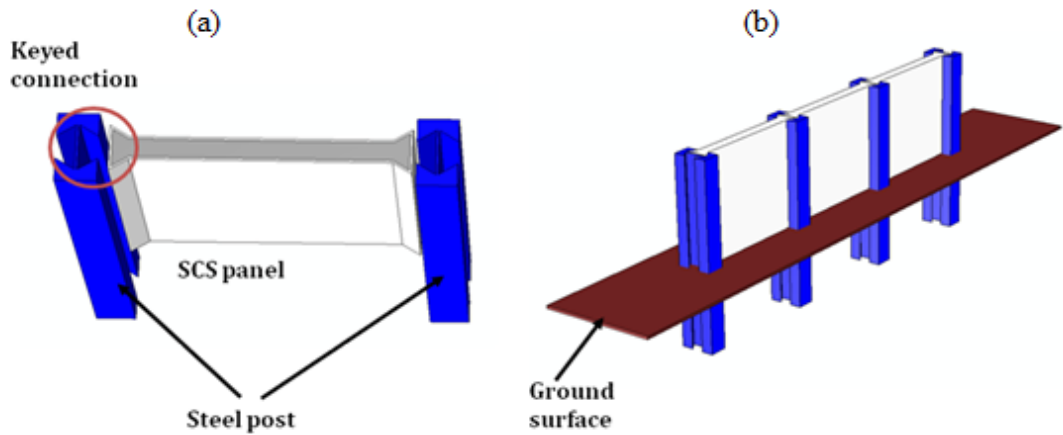


Figure 2.11: (a) SCS panel and the keyed connection used to connect the steel post to the panel, (b) steel posts penetrate into the ground to support the barrier. (reproduced from Crawford and Lan , 2006)

Based on the comprehensive literature review, it was found that there were no studies addressing detailed analytical and experimental investigations of non-composite SCS sandwich panels with axially restrained connections. Preliminary results of axially restrained non-composite SCS panels subjected to impact loading reported by Remennikov et al. (2010 a, b) showed that the panels developed high resistance through membrane action in the steel plates at large displacement.

2.3 Blast loading characterisation

2.3.1 Detonation process of high explosives

According to Ngo et al. (2007) and Cormie et al. (2009), when a high explosive is detonated, it releases hot gas of very high pressure. The temperature of the hot gas is in the range of 3000-4000°C and the pressure is in the range of 10-30 GPa. The hot gas expands at a speed higher than the speed of sound, and this causes a thin layer of air in front of the hot gas to become highly compressed to form a blast wave. The blast wave contains most of the energy released from the detonation of high explosives and the pressure at the blast wave front is called the peak static overpressure. The peak static overpressure decreases as the blast wave moves outward from the source of explosion. Overexpansion of the hot gas causes the pressure behind the blast wave to drop below atmospheric pressure. In this negative phase, the air will flow towards the source of explosion to achieve equilibrium.

The static blast overpressure-time profile for a point located at a distance from the explosion source is shown in Figure 2.12. When the blast wave arrives at time t_a , the pressure at that point increases instantaneously to the peak static overpressure (p_s). After reaching the peak static overpressure, the pressure at that point decreases non-linearly as time increases, where the pressure drops below atmospheric pressure (p_o) before it achieving equilibrium with atmospheric pressure. The portion of the blast pressure profile above the atmospheric pressure is called the positive phase and that below the atmospheric pressure is called the negative phase. The peak pressure in the negative phase is significantly lower than the peak pressure at the positive phase. The specific impulse is the area underneath the pressure-time curve for the positive phase duration.

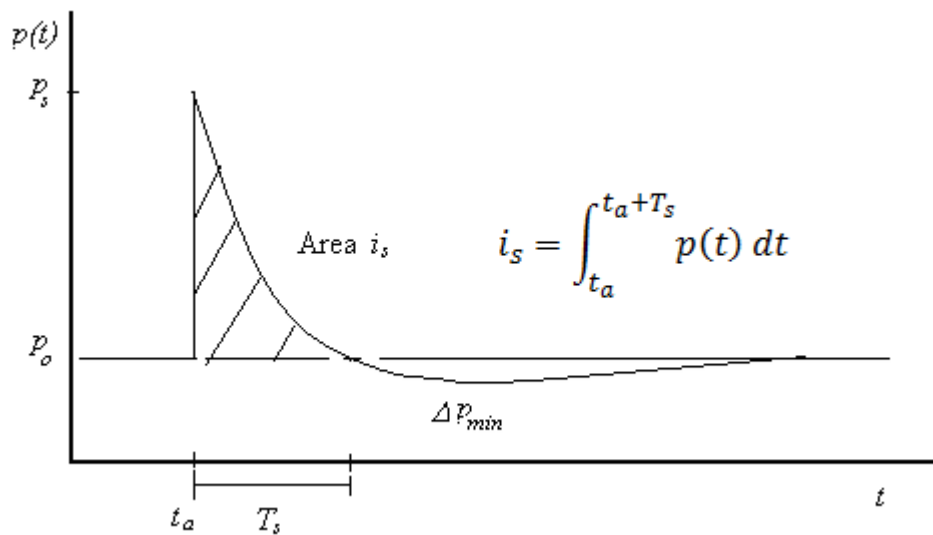


Figure 2.12: Typical pressure-time profile for the blast wave in free air.

According to Ritzel (2009), another important feature that can be observed physically is the flames surrounding the high explosive immediately after detonation. The flames or so-called “fireball” expands from the source of explosion simultaneously with the blast wave for a certain distance, the expansion stops after the maximum diameter of the fireball is reached. Four blast regimes are defined based on the distance from the charge in terms of the maximum radius of fireball (R_{fb}), namely (1) detonics regime, (2) near-field regime, (3) mid-field regime, and (4) far-field regime. In the detonics regime, the charge is in direct or near-contact with the measurement point ($<0.1 R_{fb}$). Blast pressure profiles in this regime can only be

predicted by using hydrocode or computational fluid dynamic (CFD) modelling, since little experimental data have been published.

For the near-field regime, the distance between the measurement point from the charge is less than R_{fb} . The distance between the explosion source and the measuring point for the mid-field regime is less than 10 times of R_{fb} , while the distance for the far-field regime is greater than 10 times of R_{fb} . The peak static overpressure (p_s) in the near-field regime and in the medium to far-field regime based on spherical blast can be determined from the analysis of Brode (1955).

$$p_s = \frac{6.7}{Z^3} + 1 \text{ bar} \quad (\text{near field, } p_s > 10 \text{ bar})$$

$$p_s = \frac{0.975}{Z} + \frac{1.455}{Z^2} + \frac{5.85}{Z^3} - 0.019 \text{ bar} \quad (\text{medium to far field, } 0.1 < p_s < 10 \text{ bar}) \quad (2.1)$$

where Z is the scaled distance given by $Z = R/W^{1/3}$, R is the distance from the centre of a spherical charge in meters and W is the charge mass expressed in kilograms of TNT. For the charge made of high explosives other than TNT, a conversion factor must be used to convert its mass into TNT equivalent mass. Conversion factors for a number of high explosives are shown in Table 3.1 in Cormie et al. (2009).

The air behind the blast wave moves outward from the source of explosion at a lower velocity than the blast wave. The dynamic pressure due to the air velocity is given by:

$$q_s = \frac{5p_s^2}{2(p_s + 7p_0)} \quad (2.2)$$

2.3.2 Blast wave interactions with structures

When a blast wave encounters a rigid obstacle in the perpendicular direction of wave propagation, the blast wave will reflect from it and diffract around it as shown in Figure 2.1. Reflection of the blast wave from the obstacle causes the over-pressure to locally increase above the incident pressure. The reflected pressure in the near to far-field regimes is given by,

$$p_r = 2p_s \left[\frac{7p_o + 4p_s}{7p_o + p_s} \right] \quad (2.3)$$

where p_s is the peak static overpressure and p_o is the atmospheric pressure. When the angle of incidence between the blast wave and the reflecting surface exceeds about 40° , the Mach reflection process occurs where the reflected blast wave combines with the incidence blast wave to form a blast wave with a higher peak static overpressure. This phenomenon can be observed when the charge is detonated at a certain height from the ground, or when the explosion occurs inside a confined structure. It can also be observed behind the blast wall when the blast wave diffracts over the wall as shown in Figure 2.1.

Ngo et al. (2007) discussed that the reflected overpressure profile can be idealized into an equivalent triangular pulse with the peak reflected over-pressure p_r and the equivalent pulse duration, t_e to determine the reflected impulse on the structures,

$$i_r = \frac{1}{2} p_r t_e \quad (2.4)$$

As an alternative to determining blast parameters such as the peak static overpressure, peak reflected overpressure and the specific reflected impulse using the formulae described above, they can be determined from the design charts presented in Figure 3.3, Figure 3.5, Figure 3.6 and Figure 3.7 in Cormie et al. (2009).

The drag force exerted on the front and rear faces of the building structure due to the dynamic pressure is given by,

$$F_D = C_D \times q_s(t) \times A \quad (2.5)$$

where C_D is the drag coefficient that depends on the target geometry, $q_s(t)$ is the dynamic pressure and A is the area loaded by the dynamic pressure.

2.3.3 Computational Fluid Dynamics (CFD) analysis

Existing analytical and empirical methods to predict the air blast pressure in the near-field to far-field regime are based on derivations of bare spherical high explosives. However, Ritzel (2009) pointed out that these methods are not applicable for charges with different shapes if accurate blast wave parameters are needed. For example, widely used cylindrical charges produce much stronger side-blasts than an equivalent

spherical charge, and this effect can persist to great distances. In addition, these empirical equations cannot predict the blast pressure parameters in the detonics regime.

Local terrain or environment has significant effect on the blast pressure parameters. In the built-up environment, the blast wave profile is significantly different from the blast wave profile in an unconfined environment. A small-scale experiment by Smith et al. (2001) investigated the effects of city street configurations on the blast environment. The results showed that the “channelling” effects can enhance the blast loading up to 3 or 4 times. Rose et al. (2002) carried out experimental and numerical investigations on the effects of the confinement of city streets on the positive and negative blast wave impulses. The results showed that the positive phase impulse was significantly enhanced, depending on the width of the street and the height of the building.

Due to the complexity and cost of the explosion testing, computational fluid dynamic (CFD) computer programs, such as LS-DYNA, AUTODYN and Air3D are widely used to simulate the blast loading in complex environments. The idealization of high explosive detonation process in Air3D (Rose, 2003) will be briefly described. The high explosives are modelled as highly compressed air with an evenly distributed, constant internal energy equal to the chemical energy of the high explosives. During the simulation, the highly compressed air generates a compressive shock wave representing the blast wave that propagates outwards. The dominant features such as the profiles of pressure, density and velocity of the air are similar to the actual detonation of high explosives. Figure 2.13 shows the interaction of the blast wave and the blast wall when a 1000 kg spherical TNT charge was detonated at a 5 m standoff distance.

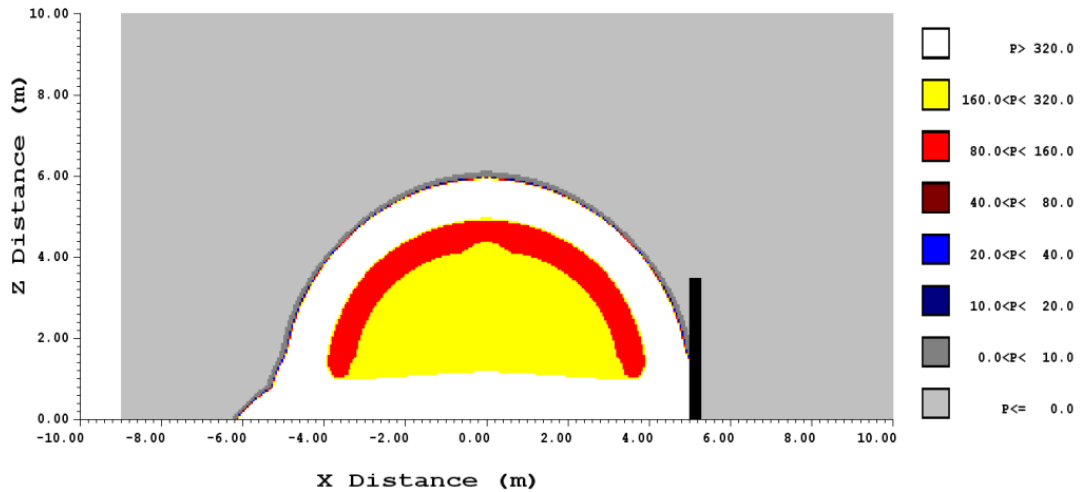


Figure 2.13: Simulation of the blast wave interaction with the blast wall using Air3D.

Chapman et al. (1995) conducted a comprehensive parametric study using AUTODYN2D. The simulation results correlated well with the experimental blast reflected overpressure in simple and complex geometrical situations. Lu et al. (2003) carried out a study on the detonation using the high explosive model in the commercial software LS-DYNA, and the simulation results were compared to the experimental data and the empirical results from ConWep. It was observed that LS-DYNA had a tendency to underestimate the overpressure and impulse in the mid-field and far-field regime. Borgers and Vantomme (2006) showed that AUTODYN could be used to model a spherical detonation accurately, and the blast wave parameters caused by the detonating cord were investigated. Remennikov and Rose (2005) used Air3D to investigate the blast effects on a building in a typical urban terrain.

Remennikov and Rose (2007) used an artificial neural network (ANN) to predict the blast environment behind a blast wall. The main advantage of ANN is its ability to predict the effectiveness of a blast wall configuration within very short period of time compared to the numerical CFD simulation, which requires a long computational time. Zhou and Hao (2008) used AUTODYN3D to investigate the blast loading on the structures behind the blast wall. The simulation results were used to derive pseudo-analytical formulae that could be used to estimate the reflected pressure-time history on a rigid wall behind the blast wall. Børvik et al. (2009) showed that CFD analysis could be coupled with the finite element analysis. It is a hybrid technique

that combined the advantages of both methods to have a full coupling between the blast waves and the deformation of the structure. The application of this hybrid technique is in the preliminary stage and more research is required to verify its application.

2.4 Impact loading characterisation

Impact events occur in a wide variety of circumstances and can cause severe damage to critical infrastructures, for an example, when a heavy vehicle crashes into a bridge pier. Eibl (1988) classified the impact phenomena into two groups, soft impact and hard impact. For the hard impact, the striking body is more rigid than the resisting structure and the kinetic energy of the striker, to a large extent, is absorbed by deformation of the struck body as shown in Figure 2.14. Local failure mode of the structure such as punching shear failure should be considered in addition to its global bending deformation. Soft impact implies vehicle or soft missiles striking a relatively rigid structure. The kinetic energy of the striking body is completely dissipated by deformation of the striking body, while the resisting structures can be assumed rigid and remains undeformed.

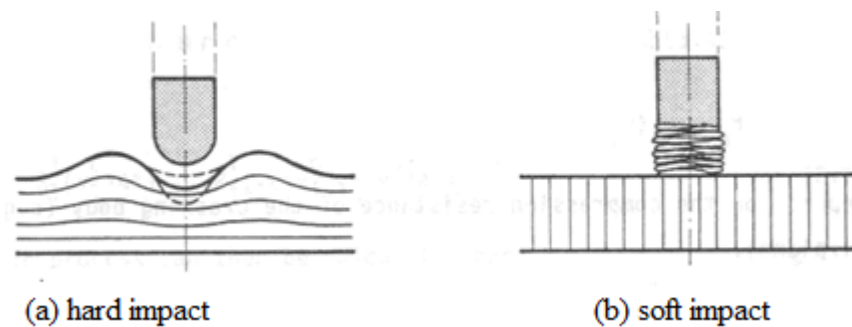


Figure 2.14: Hard impact and soft impact. (Eibl, 1988)

Jones (1989) showed that the response of a steel beam subjected to the impact of a heavy rigid impactor can be analysed using the conservation of energy equation, where the kinetic energy from the impactor is dissipated through strain energy in the beam.

$$4M_o\theta = \frac{mv_o^2}{2} \quad (2.6)$$

where M_o is the moment capacity of the steel beam, θ is the support rotation, m and v_o is the mass and velocity of the impactor, respectively.

The effects of the shape of striking body were discussed by Eibl (1988). For the hemispherical nose striker, it required up to approximately 30% more velocity to perforate a reinforced concrete barrier than a flat-faced striker having the same mass and diameter. For the conical- or chisel-nosed strikers, they also needed to possess a greater velocity of approximately 15% more than a flat-faced striker to perforate a reinforced concrete barrier.

According to Li et al. (2005), the penetration depth, x_p of reinforced concrete structures struck by hard missiles can be estimated using the Army Corps of Engineers (ACE) empirical formula, given by:

$$\frac{x_p}{d} = \frac{3.5 \times 10^{-4}}{\sqrt{f_c}} \left(\frac{M}{d^3} \right) d^{0.215} v_o^{1.5} + 0.5 \quad (2.7)$$

where d is the diameter of projectile, M is the mass of projectile, f_c is the unconfined compressive strength of concrete and v_o is the impacting velocity of projectile. Based on the penetration depth given above, the formulae for perforation (e), and scabbing limits (h_s), are given by,

$$\begin{aligned} \frac{e}{d} &= 1.32 + 1.24 \frac{x_p}{d} \quad \text{for } 1.35 < \frac{x_p}{d} < 13.5 \text{ or } 3 < \frac{e}{d} < 18 \\ \frac{h_s}{d} &= 2.12 + 1.36 \frac{x_p}{d} \quad \text{for } 0.65 < \frac{x_p}{d} < 11.75 \text{ or } 3 < \frac{h_s}{d} < 18 \end{aligned} \quad (2.8)$$

Terry and Tholen (2006) proposed using Newton's second law to predict the equivalent static design force for the vehicle impact scenario based on the deceleration of the vehicle during the impact.

$$F = Ma \quad (2.9)$$

where M is the mass of the vehicle, and a is the deceleration of the vehicle during impact. However, it is difficult to determine the equivalent static design force for a specific crash scenario because the deceleration from literature ranges from 157 ms^{-2} to 980 ms^{-2} .

The investigation of vehicle crash scenarios are either carried out by full scale crash testing or by using non-linear finite element transient analysis programs such as LS-DYNA. The National Crash Analysis Centre (NCAC) has developed a wide range of vehicle FE models to perform vehicle crash simulations using LS-DYNA. Figure 2.15 shows the FE model of a Ford 800 single unit truck obtained from the NCAC website. Ren and Vesenjok (2005) investigated the performance of a W-beam barrier under vehicle impact using both LS-DYNA and full scale crash testing. The simulation results correlated well with the experimental results. Lan et al. (2006) used LS-DYNA to investigate a frontal impact scenario of bollard by a 6800 kg truck model at speeds of 48.3, 64.4 and 80.5 km/h. Itoh et al. (2007) analysed the performance of a rigid concrete barrier subject to an angular impact of a 20000 kg truck using LS-DYNA.

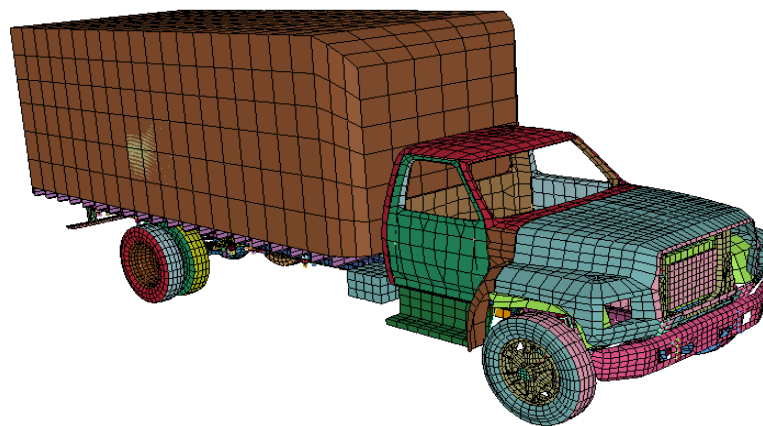


Figure 2.15: FE model of Ford 800 obtained from the National Crash Analysis Centre. (www.ncac.gwu.edu)

2.5 Material characterisation

2.5.1 Characteristics of high performance steel

High performance steels (HPSs) are steels which exhibit improved strength, corrosion resistance and energy absorption capacity compared to mild steel. These enhanced properties, compared to conventional steels, may give HPSs protective properties against extreme loads that occur in events such as explosions, earthquakes, fire, hurricanes and accidental impact. Such events are severe for buildings, bridges and other infrastructures, and need innovative structural engineering solutions.

In 1994, a cooperative research program was carried out between the Federal Highway Administration (FHWA), the U.S. Navy and the American Iron and Steel Institute (AISI) to develop high performance steels for bridges. These steels exhibit better corrosion resistance, higher toughness and improved weldability, thus reducing the need for maintenance and increased workability. Two types of HPSs are the high strength steel (HSS) and stainless steel (SS). High strength steel is produced by a quenching and tempering process, and typically has a nominal yield stress of about 700MPa. Stainless steel displays much more defined non-linear characteristics than mild steel, with 0.2% proof stress in the range of 450MPa and maximum stress typically about 600MPa. Typical modulus of elasticity for both steels is 200 GPa. Figure 2.16 shows both steels exhibiting higher strengths than mild steel and potential increased energy absorption under impact and blast loading when the structures under the same displacement.

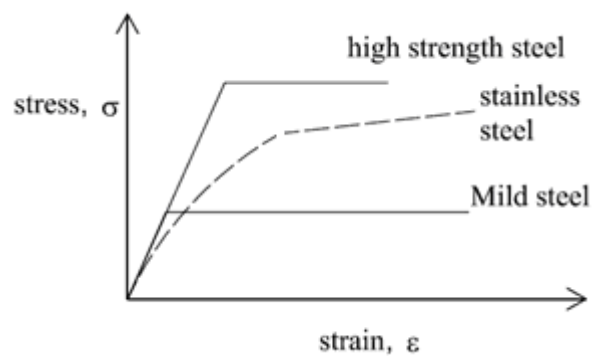


Figure 2.16: Typical stress-strain curves for mild steel, high strength steel and stainless steel.

Stainless steel is a steel alloy which contains minimum 11% of chromium by mass. The chromium reacts with the oxygen to form a passive film of chromium oxide, and protects the steel from corrosion. The application of stainless steel in the design of structures can reduce maintenance cost during its life circle due to corrosion resistance characteristic. According to Gardner (2005), the ductility (strain at fracture) for the common austenitic stainless steel grades is approximately 40–60% compared to around 20-30% for mild steel. The ductility level of stainless steel depends upon the material composition, heat treatment and the degree of cold-work that the section has been subjected to, with reduced ductility for increasing cold-work.

Rasmussen (2001) presented a full range stress-strain relationship to predict the non-linear behaviour of stainless steel after yielding. The full range stress-strain relationship for stainless steel is given by,

$$\varepsilon = \begin{cases} \frac{\sigma}{E_o} + 0.002 \left(\frac{\sigma}{\sigma_{0.2}} \right)^n & \text{for } \sigma \leq \sigma_{0.2} \\ \frac{\sigma - \sigma_{0.2}}{E_{0.2}} + \varepsilon_u \left(\frac{\sigma - \sigma_{0.2}}{\sigma_u - \sigma_{0.2}} \right)^m + \varepsilon_{0.2} & \text{for } \sigma > \sigma_{0.2} \end{cases} \quad (2.10)$$

where ε is the strain, σ is the stress, E_o is the elastic Young's modulus, σ_u is the ultimate tensile strength, $\sigma_{0.2}$ is 0.2% proof stress. The m , n and $E_{0.2}$ are given by,

$$\begin{aligned} m &= 1 + 3.5 \frac{\sigma_{0.2}}{\sigma_u} \\ n &= \frac{\ln(20)}{\ln(\sigma_{0.2} / \sigma_{0.01})} \\ E_{0.2} &= \frac{E_o}{(1 + 0.002n/e)} \end{aligned} \quad (2.11)$$

Mursi and Uy (2004) conducted research on high strength steel box columns filled with concrete while numerical investigations of stainless steel concrete-filled columns under static loading has been carried out by Roufegarinejad et al. (2004). Both studies showed that the strength of HPSs concrete filled columns is significantly higher than the strength predicted by Eurocode 4.

Uy (2008) and Baddoo (2008) showed that stainless steel have been used in the construction of high-rise buildings, bridges and landmark structures around the world. Pérez-Quiroz et al. (2008) showed that stainless steel reinforcement offered superior corrosion resistance in an aggressive environment. The design of structural stainless steel can be carried out in accordance to Design Manual for Structural Stainless Steel Third Edition (2006). This design manual also includes cold worked austenitic stainless steel sheets, fire resistance and fatigue designs.

Several studies investigated the application of stainless steel in resisting dynamic loading. Research by Louca et al. (2004) has considered the application of stainless steel plates for containing hydrocarbon explosions on offshore structures. Di Sarno et

al. (2003) assessed the feasibility of applying stainless steel in the seismic design of regular and irregular framed structures. Schleyer et al. (2007) tested a 1/4 scaled profiled stainless steel blast panels with welded angle connections at the top and bottom using a shock tube (blast simulator). The experimental results showed that large permanent deformations were observed on the panels and the connection details could significantly influence the response and the resistance of panels under extreme pressure loading.

Initial tests by Uy (2006) had shown that the concrete-filled steel tubes had high impact resistance and high ductility when they were subjected to a drop mass impact at mid-span. Uy and Remennikov (2007) indicated that the dynamic moment capacity of hollow and concrete filled stainless steel columns under transverse impact loading increased by up to 42% of the capacity associated with static loading. Yousuf et al. (2009) conducted experiments on compact hollow and concrete filled stainless steel sections and the increase in dynamic moment capacity was discussed. Remennikov et al. (2009) and Remennikov et al. (2011) conducted impact tests on rigid polyurethane foam-filled stainless steel columns and showed the effectiveness of using rigid polyurethane foam as an infill material in hollow structural elements for increasing their impact and blast resistance. Remennikov et al. (2009 b) investigated the resistance of small scale hollow and sand-filled stainless steel rectangular sections subjected to quasi-static loading using the air-bag technique.

2.5.2 Material properties under dynamic loading

According to Harding et al. (1960), most metals and alloys show a significant change in their mechanical properties under increased rates of strain. The strain rate for structures under impact loading is in the range of $0.1-200 \text{ s}^{-1}$, while the strain rate exceeds 200 s^{-1} for structures subjected to the blast loading conditions. According to Zobotkin et al. (2003), instrumented falling weight impact (IFWI) testers were normally used to obtain material properties under medium strain rate ($0.1-200 \text{ s}^{-1}$) while a split Hopkinson pressure bar could be used to obtain material properties under a higher strain rate.

The TM5-1300 (U.S. Department of the Army, 1990) outlines several important characteristics of mild steel under a high strain rate compared to static loading conditions. The yield stress of mild steel increases significantly under high strain rate loading, while the ultimate tensile strength is not as sensitive to the strain rate. The modulus of elasticity generally remains insensitive to the rate of loading, while the elongation at rupture remains the same or is slightly reduced. Cormie et al. (2009) presented dynamic increase factors (DIF) to account for the strength increment of steel and concrete in the design of structures against extreme loads. The dynamic increase factor for concrete and steel depend on the type of loading on the structures as shown in Table 2.1. Different sets of dynamic increase factors are used for yield stress and ultimate strength of steel because their strain rate sensitivities are different under high strain rate.

Table 2.1: Dynamic increase factors (DIF) for steel and concrete. (Cormie et al., 2009)

Loading type	DIF Steel		DIF Concrete
	Yield stress	Ultimate strength	Compressive strength
Bending	1.2	1.05	1.25
Shear	1.2	1.05	1.00
Compression	1.1	-	1.15

The dynamic increase factors presented above assume that the strength enhancement of steel and concrete is independent of the strain rate. In reality, the strength of these materials increases with the increase of strain rate. Figure 2.17 shows that the yield stress of mild steel increases as the strain rate increases. For steel, the dynamic yield stress or ultimate tensile strength under a specific strain rate can be determined using the Cowper-Symonds equation. The relationship between the dynamic stress of a material to the strain rate is given by,

$$\sigma_d = \sigma_s \left[1 + \left(\frac{\dot{\epsilon}}{D} \right)^{1/q} \right] \quad (2.12)$$

where σ_d is the dynamic stress or strength, σ_s is the static stress or strength, $\dot{\epsilon}$ is the strain rate, D and q are the Cowper-Symonds coefficients. Jones (1989) presented the Cowper-Symonds coefficients for yield stress of mild steel as 40.4 (D) and 5 (q). The

Cowper-Symonds coefficients for stainless steel will be discussed in details in Chapter 4.

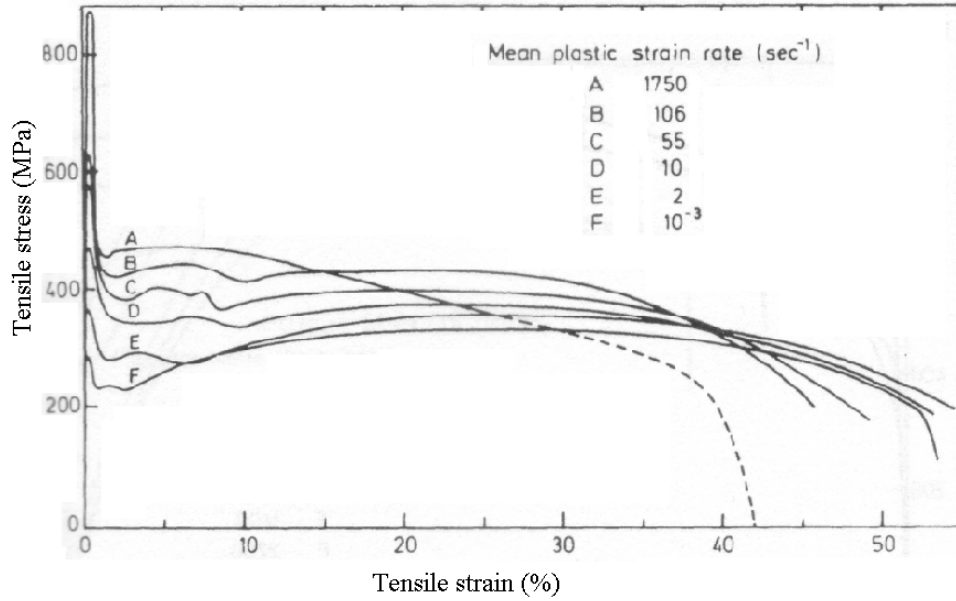


Figure 2.17: Strain rate effects on material properties of mild steel. (Blazynski, 1987)

Dynamic increase factor for concrete at a specific strain rate can be estimated in accordance to the CEB model code (1993). For concrete under compression, the dynamic increase factor is given by,

$$\begin{aligned}
 DIF_{conc_comp} &= \left(\frac{\dot{\epsilon}}{\dot{\epsilon}_s} \right)^{1.026\alpha_s} && \text{for } \dot{\epsilon} \leq 30 \text{ s}^{-1} \\
 &= \gamma_s \left(\frac{\dot{\epsilon}}{\dot{\epsilon}_s} \right)^{1/3} && \text{for } \dot{\epsilon} > 30 \text{ s}^{-1}
 \end{aligned} \tag{2.13}$$

where $\dot{\epsilon}$ is the strain rate in the range of 30×10^{-6} to 300 s^{-1} , $\dot{\epsilon}_s$ is the static strain rate of 30×10^{-6} . The parameter α_s and γ_s is given by,

$$\begin{aligned}
 \alpha_s &= \frac{1}{(5 + 9f'_c / 10 \text{ MPa})} \\
 \log \gamma_s &= 6.15\alpha_s - 2
 \end{aligned} \tag{2.14}$$

where f'_c is the static compressive strength. The dynamic increase factor for concrete in tension is given by,

$$DIF_{conc_tension} = \left(\frac{\dot{\epsilon}}{\dot{\epsilon}_s} \right)^{1.016\delta} \quad \text{for } \dot{\epsilon} \leq 30 \text{ s}^{-1} \quad \delta = \frac{1}{(10 + 6f'_c / 10 \text{ MPa})}$$

$$= \beta \left(\frac{\dot{\varepsilon}}{\dot{\varepsilon}_s} \right)^{1/3} \quad \text{for } \dot{\varepsilon} > 30\text{s}^{-1} \quad \log \beta = 7.11\delta - 2.33 \quad (2.15)$$

Malvar and Ross (1998) conducted extensive review on the experimental data of concrete in tension under various strain rates. It was found that their data differed from the CEB recommendation. Therefore, an alternate formulation was proposed for concrete in tension under various strain rates.

2.6 Structural response to blast and impact loading

2.6.1 Single degree of freedom (SDOF) system

The single degree of freedom (SDOF) system was introduced by Biggs (1964) to analyse the dynamic responses of structures. The structure is idealized as an equivalent lumped mass (M_e) supported by a spring with a stiffness k_e . The system is subjected to a transient load as shown in Figure 2.18 and the damping effect of the structure is ignored.

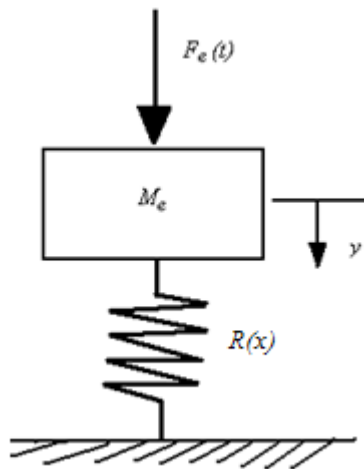


Figure 2.18: Single degree of freedom (SDOF) system.

The equation of motion for the un-damped elastic SDOF system is,

$$M_e \ddot{x} + R_e(x) = F_e(t) \quad (2.16)$$

where \ddot{x} is the acceleration of the equivalent mass. The equivalent mass (M_e), equivalent resistance function ($R_e(x)$) and equivalent transient load can be obtained using transformation factors.

$$K_M M\ddot{x} + K_s R(x) = K_L F(t) \quad (2.17)$$

where K_M is the mass transformation factor, K_s is the stiffness transformation factor, K_L is the load transformation factor and $R(x)$ is the resistance function. The stiffness transformation factor is equal to the load transformation factor, therefore the equation above can be simplified as,

$$K_{LM} M\ddot{x} + R(x) = F(t) \quad (2.18)$$

The transformation factors depend on the types of loading and the support conditions. These transformation factors are presented in Appendix A by Cormie et al. (2009).

The pressure-impulse ($P-I$) diagram can be derived from the SDOF system to assess the damage level of a structure component under a combination of load-impulse. When a structure subjected to a combination of pressure and impulse that fall on the lower left quadrant of the solid line curve in Figure 2.19, it will experience no or minor damage. Otherwise, the structure will suffer severe damage. Shi et al. (2008) derived the $P-I$ diagram for reinforced concrete columns, while Mutalib and Hao (2010) derived the $P-I$ diagram for FRP strengthened RC columns based on the LS-Dyna simulation results.

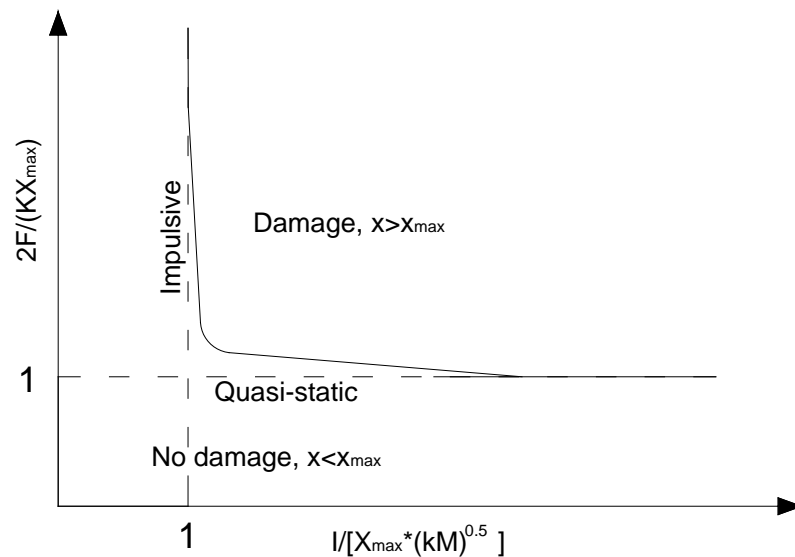


Figure 2.19: Non-dimensionalised pressure-impulse diagram for SDOF elastic system (reproduced from Cormie et al. 2009).

For reinforced concrete structures subjected to impulsive loading, when the support rotation is limited to less than 5° , the structures resist the loading by flexural resistance. The response of the structures can be predicted using equilibrium of kinetic energy from the blast loading to the strain energy due to flexural response in the structures.

$$\frac{I^2 A^2}{2K_{LM}M} = \frac{P_o X_E}{2} + P_o (X_m - X_E) \quad (2.19)$$

where A is the surface area of the structures in contact with the blast wave, P_o is the maximum flexural capacity, X_E is the elastic limit of displacement and X_m is the maximum displacement.

2.6.2 Structural response under blast loading

The response of the structures subjected to the blast loading depends on the natural period of vibration of the structure, T , and the positive phase duration of the blast loading, t_d . Based on the idealised elastic single degree of freedom (SDOF) system (Cormie et al. 2009), the structural response can be classified into 3 regimes, namely impulsive, dynamic and quasi-static response. The ratio of natural period of structures to the positive phase duration of the blast loading for each response regimes is given by,

$$\begin{aligned} \frac{t_d}{T} < 0.1 & \quad \text{Impulsive} \\ 0.1 < \frac{t_d}{T} < 10 & \quad \text{Dynamic} \\ 10 < \frac{t_d}{T} & \quad \text{Quasi-static} \end{aligned} \quad (2.20)$$

In the impulsive regime, the positive phase of the blast loading, t_d , is much shorter than the natural period of the structures, T , which means that the maximum displacement of the structures occur after the blast loading decay to zero. This is normally the case for buildings and blast walls, where their large mass causes their natural period of vibration to be significantly longer than the positive phase duration of blast loading. In this loading regime, the structures obtain kinetic energy from the impulse of the blast wave. The kinetic energy from the blast impulse is given by,

$$K.E. = \frac{I^2}{2m} \quad (2.21)$$

where I is the blast impulse and m is the mass per unit area of the structures. The kinetic energy is dissipated through development of strain energy in the structures.

For dynamic regime, t_d is approximately the same with the duration of T . When the positive phase of the blast loading is long compared to the natural period of the structure, its response falls into the quasi-static regime. The quasi-static regime could happen during a hydrocarbon explosion or when large amount of high explosives are detonated at a long distance.

2.6.3 Structural response under impact loading

Under impact loading condition, the responses of structures are mainly influenced by the mass of the projectile, the impact velocities, and types of projectile. For impact velocities up to 10 ms^{-1} , the failure modes are generally the same as the static failure modes, except there is an increased tendency for local damage or shear failure to occur. Eibl (1988) showed that with increased impact velocity, the shear cone angle would decrease as shown in Figure 2.20, and punching shear failure would occur if the velocity was sufficient for the striker to penetrate the structures.

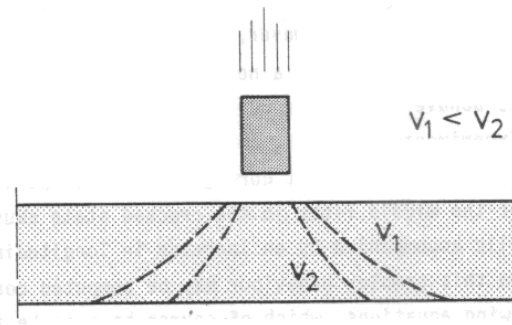


Figure 2.20: The shear cone angle decreases as the impact velocity increases (Eibl, 1988).

Bangash (1993) classified the failure modes of the reinforced concrete structures under impact loading into local and global failure modes. The local failures are penetration, perforation, scabbing and spalling while the global failures consist of global bending, shear and membrane action as shown in Figure 2.21.

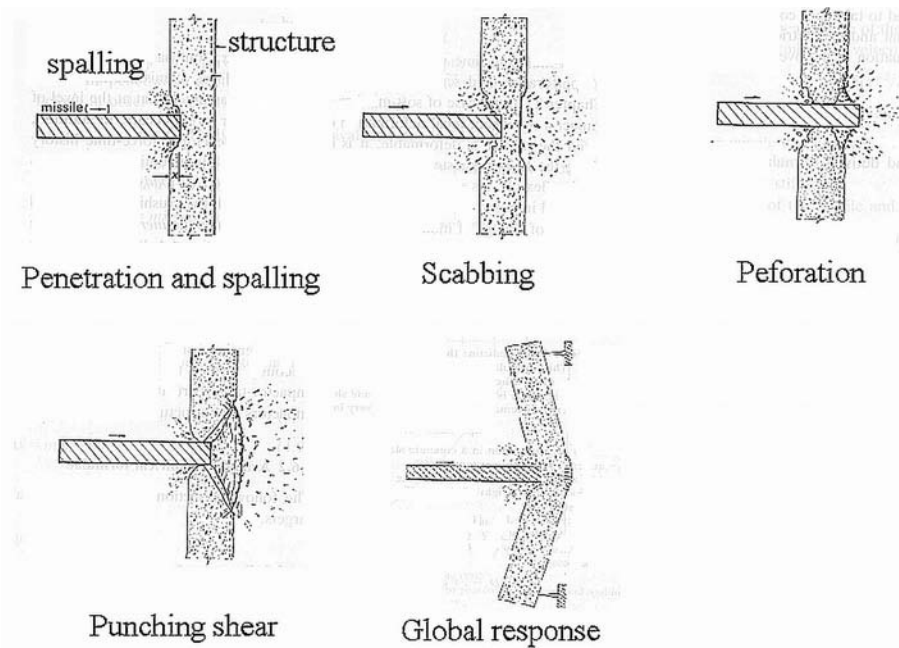


Figure 2.21: Reinforced concrete responses under impact loading. (Bangash, 1993)

Jones (1989) examined the dynamic plastic response of the fully clamped beam struck at mid span by a rigid mass and a cantilever beam struck by a mass at the tip. Rigid-perfectly plastic material properties were applied in the analysis. The responses of the fully clamped beam subjected to the impact of heavy and light strikers at mid-span were presented. Jones (1995) further simplified the analysis of fully clamped beam problem by using quasi-static analysis for impact velocities up to 12 ms^{-1} .

2.6.4 Deformation limits for structural members

Under extreme loading events, a structural element develops strain energy through elastic or plastic deformation to dissipate the kinetic energy from the blast or impact loading. The limit of the deformation or deflection of a structural element is controlled by the protection level required in the design. Structures under protection category 1 are designed to protect personnel and equipment in the facilities from blast pressures and primary fragments. It should not generate secondary fragments due to spalling of concrete under blast loading. For protection category 2, the structures are allowed to undergo large plastic deformation, without forming collapse

mechanism in the structural elements. Damage level of a structure is specified by using the support rotation, θ , and the deformation limits for different types of structures are presented in Table 2.2.

Table 2.2: Deformation limits for different types of structures. (Cormie et al., 2009)

	Category 1 deformation limit ($^{\circ}$)	Category 2 deformation limit ($^{\circ}$)
Structural steel beam and plates	2	12
Reinforced concrete beams and slabs	2	4
Steel-concrete-steel composite	2	5

For the reinforced concrete structures, the deformation limit for protection category 2 is limited to 4° support rotation under normal circumstances. When sufficient axial restraint is provided to restrain the in-plane movement of reinforced concrete structures, tensile membrane action will develop in the reinforcement at large displacement, and the deformation limit is increased to 8° support rotation. Membrane resistance in steel structural members and reinforced concrete elements is normally considered in the design of protective structures to withstand extreme loading conditions. Det Norske Veritas (2010) provides the design recommendations for membrane resistance in structural steel members, while TM5-1300 (U.S. Department of the Army, 1990) provides design guideline for reinforced concrete elements. A review on the analytical solutions for membrane resistance will be provided in the next chapter.

It is important for a structural element to have sufficient ductility to deform and dissipate blast or impact energy. Connections or joints between the structural elements should be carefully detailed so that the structures do not fail prematurely, because of shear failure or local instability. Krauthammer (1999) showed that structural connection details are vital in designing blast-resistant structures, and the connection details based on static design considerations might not be sufficient to resist extreme loading events associated with explosive loads. It is important to provide sufficient ductility in both structures and connections, so that the structural

elements meet the concept “fail-save”, which means the structures fail without causing catastrophic damage.

CHAPTER 3

TENSILE MEMBRANE MECHANISM

Axially restrained steel structural members such as beams and plates demonstrate higher load resistance than their plastic flexural collapse loads due to the development of axial tensile force in these members under moderate to large deflection. The load carrying mechanism due to the development of the axial tensile forces in the steel members is called tensile membrane resistance. According to Clarkson (1956), a fully fixed plate resists lateral pressure entirely by the flexural resistance for deflection up to about 20 percent of the plate thickness. As the displacement exceeds about 70 percent of the plate thickness, the strength is mainly controlled by the tensile membrane mechanism.

In 1910, von Karman derived differential equations for the elastic behaviour of initially flat plates by taking membrane stresses (axial tensile force) into account. Timoshenko and Krieger (1959) presented theoretical solutions for a strip of infinitely long elastic steel plate with an aspect ratio of zero by including the effects of membrane stress. Figure 3.1 shows the free body diagram of a fully fixed plate subjected to a uniformly distributed load. The plate develops an axial tensile force (T) due to the membrane stretching under moderate to large deformation.

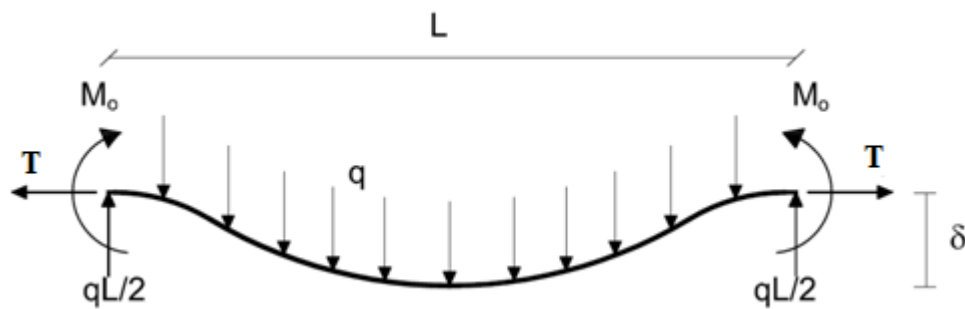


Figure 3.1: The force and moment distribution in the fix supported plate under a uniformly distributed load.

From the moment equilibrium of the plate shown in Figure 3.1,

$$M(x) = \frac{q(Lx - x^2)}{2} - T\delta(x) + M_o \quad (3.1)$$

where $M(x)$ is the bending moment at distance x from the left support, q is the uniformly distributed load, T is the axial force of the member, $\delta(x)$ is the displacement of the plate at x , and M_o is the plastic moment capacity of the plate. The moment-curvature relationship for the plate under uniaxial plane strain conditions is given by,

$$D \frac{d^2 \delta(x)}{dx^2} = -M(x) \quad (3.2)$$

The flexural rigidity (D) of the plate is,

$$D = \frac{EH^3}{12(1-\nu^2)} \quad (3.3)$$

where E is the Young's modulus, H is the thickness of the plate, ν is the Poisson's ratio. By combining Eq.3.1 and Eq. 3.2, the relationship between the curvature, the axial force, the applied load and the moment capacity of the section is given by,

$$\frac{d^2 \delta(x)}{dx^2} + \frac{T\delta(x)}{D} = \frac{q(Lx - x^2)}{2D} + \frac{M_o}{D} \quad (3.4)$$

Eq.3.4 can be solved to obtain the load-displacement relationship by introducing the boundary conditions of the plate:

$$\begin{aligned} \frac{d\delta}{dx} &= 0 & \text{at } x = 0, \quad x = L \\ \delta &= 0 & \text{at } x = 0 \end{aligned} \quad (3.5)$$

Then, the displacement of the plate at a distance x from the left support is given as,

$$\delta(x) = \frac{qL^4 \{ \cosh[\mu(1 - 2x/L)] / \cosh \mu - 1 \}}{16\mu^3 D \tanh \mu} + \frac{qL^2(L-x)x}{8\mu^2 D} \quad (3.6)$$

where the membrane stress parameter, μ is given as,

$$\mu = \sqrt{\frac{TL^2}{4D}} \quad (3.7)$$

If the deflection of the plate is small compared to the total length of the plate (L), the axial force of the member can be simplified as,

$$T = \frac{\lambda EH}{L(1-\nu^2)} \quad (3.8)$$

where λ is the extension of the plate at the centriodal axis. To determine the displacement of the plate using Eq. 3.6, the membrane stress parameter (μ) must be solve in advance. The membrane stress parameter can be solved by trial and error using the equation below.

$$\frac{E^2 H^8}{(1-\nu^2)^2 q^2 L^8} = -\frac{81}{16\mu^7 \tanh \mu} - \frac{27}{16\mu^6 \sinh^2 \mu} + \frac{27}{4\mu^8} + \frac{9}{8\mu^6} \quad (3.9)$$

The closed-form solution presented by Timoshenko and Krieger (1959) is limited to elastic behaviour of the plate. The application of plastic membrane action as a load resistance mechanism was first investigated both theoretically and experimentally for naval architecture by Clarkson (1956) and Young (1959), in order to take advantage of the considerable reserve strength in steel plates loaded beyond the elastic limit. Haythornthwaite (1956) conducted an experimental and theoretical study on the plastic membrane resistance of a rectangular steel beam section, while Ronalds (1990) studied asymmetrical I-sections.

Park (1964) showed that reinforced concrete slabs with edges restrained against in-plane movement developed tensile membrane action at large deflection due to the development of axial tensile force in the reinforcement. Park's study had significantly contributed towards the design of protective reinforced concrete structures, where tensile membrane action under large deformation was adopted in the TM5-1300 (U.S. Department of the Army, 1990) design standard to resist extreme loading conditions. According to Park (1964), the tensile membrane resistance for the one way slab subjected to a uniformly distributed load is proportional to the mid-span displacement as below:

$$q = \frac{8T_o \delta}{L^2} \quad (3.10)$$

where T_o is the axial yield force of the reinforcement, δ is the displacement at mid-span, and L is the length of the slab.

The application of tensile membrane resistance in protective structures was recently carried out by several researchers. Dinan (2005) investigated application of tensile membrane resistance in steel stud walls and presented experimental and analytical results. Izzuddin (2005) presented a simplified explicit model for axially restrained steel beams subjected to extreme loading under ambient and elevated temperatures. Crawford and Lan (2006) investigated the application of tensile membrane action in steel-concrete-steel panels for designing a blast barrier.

Campbell and Charlton (1972) discussed post-yield behaviours of a mild steel beam of rectangular cross section with fixed end supports subjected to a concentrated load at mid-span as shown in Figure 3.2. Their derivation of the post-yield response of the steel beam was similar to Haythornthwaite (1956). The beam was assumed to have rigid perfectly plastic material properties.

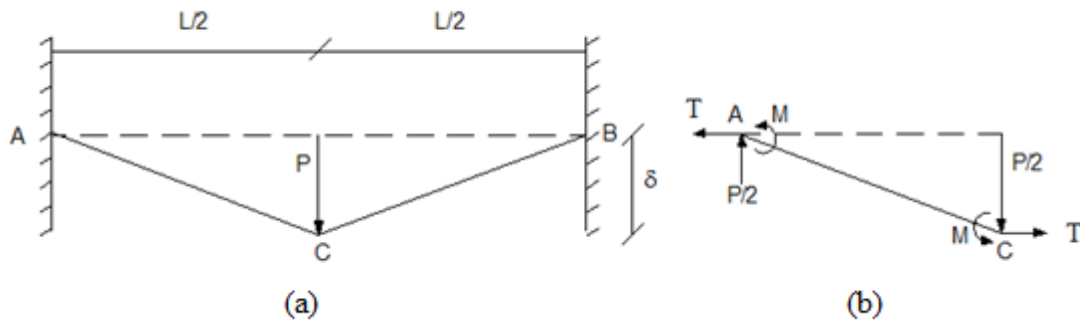


Figure 3.2: (a) Deformation of the fixed end beam subjected to a concentrated load at mid-span, (b) the force and moment equilibrium in the beam. (reproduced from Campbell and Charlton, 1972)

After formation of plastic hinges in the beam due to the bending moment, the tensile membrane resistance can be divided into two stages as shown in Figure 3.3. The first stage is transient membrane resistance, characterised by the non-linear load-displacement relationship, where the applied load is resisted by a corresponding increase in both the mid-span displacement and the axial tensile force. The second stage starts after the beam reaches the tensile yield force of the cross section and becomes a plastic membrane. The applied load is resisted by an increase in the mid-span displacement of the beam with the load-displacement relationship remaining linear.

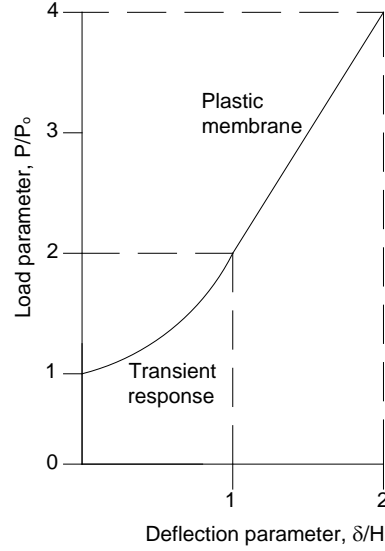


Figure 3.3: Load-displacement relationship for the fixed end beam after formation of plastic hinges using rigid plastic analysis.

The load-displacement relationship for the transient and plastic membranes can be predicted using Eq. 3.11:

$$\begin{aligned}
 p &= 1 + (\delta/H)^2 & \text{if } \delta/H \leq 1 & \text{(transient membrane)} \\
 p &= 2(\delta/H) & \text{if } \delta/H > 1 & \text{(plastic membrane)}
 \end{aligned}
 \tag{3.11}$$

where the load parameter $p = P/P_o$, P is the applied concentrated load, P_o is the plastic flexural collapse load ($P_o = 8M_o/L$ for fixed end beam), δ is the mid-span displacement, H is the depth of the beam. Moment capacity of the steel plate or beam with rectangular cross section is, $M_o = BH^2 \sigma_y /4$, where B and H is the width and height of the cross section, respectively.

The response of the transient membrane can be derived based on the basic relationship for plasticity (flow rule) under combined bending and axial load (Haythornthwaite, 1956):

$$t^2 + m = 1 \tag{3.12}$$

The axial force parameter, t , is given by,

$$t = \frac{T}{T_o} = \frac{\sigma}{\sigma_y} \tag{3.13}$$

where T is the axial tensile force in the cross section, T_o is the axial yield force of the cross section, σ is the axial stress, σ_y is the yield stress, m is the bending moment

parameter, $m = M/M_o$. The flow rule is illustrated in Figure 3.4, it shows the proportion of the maximum bending moment and the maximum tensile force required to induce the yielding in the cross section. When t is zero, the cross section yields due to the bending moment, while the section fully yields due to the tensile force if m is zero.

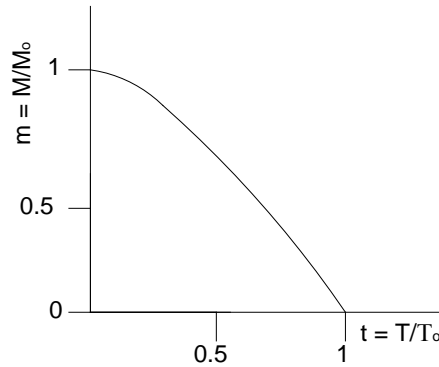


Figure 3.4: Flow rule relationship for the rectangular section subjected to bending moment and axial load.

During the transient membrane response, the axis of rotation in the plastic hinge shifts away from the centroid of the cross section as the displacement increases, as shown in Figure 3.5. As a consequence, the plastic hinge has to allow for the rotation and axial separation of adjoining sections. The shift of the axis of rotation causes an unbalanced stress distribution and therefore, an axial tensile force develops in the cross section. When the axis of rotation of the plastic hinge reaches the outermost top fibre and the whole cross section yields in tension, the beam turns into a plastic membrane.

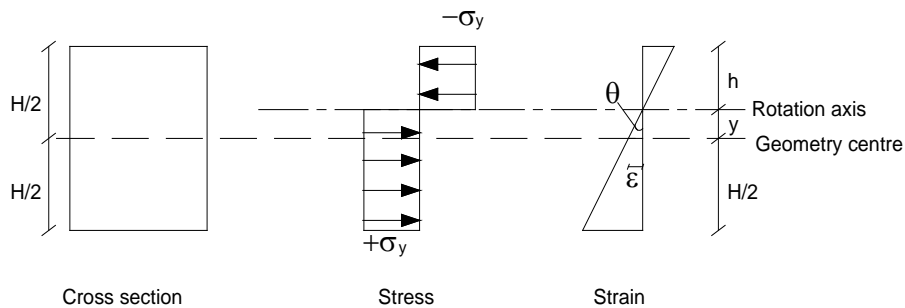


Figure 3.5: Stress distribution and movement of the axis of rotation of a plastic hinge under increased displacement. (reproduced from Campbell and Charlton, 1972)

By considering moment equilibrium of the beam in Figure 3.2,

$$P = \frac{4}{L}(2M_o + T\delta) \quad (3.14)$$

By dividing Eq. 3.14 by the plastic collapse load (P_o), we have,

$$p = 1 - t^2 + 2\frac{\delta}{H}t \quad (3.15)$$

During the transient membrane response, the axial force parameter, t , is related to the flow rule by,

$$t = \frac{\sigma}{\sigma_y} = \frac{2}{H} \frac{\dot{\epsilon}}{\dot{\theta}} \quad (3.16)$$

where $\dot{\epsilon}$ is the rate of extension of centriodal fibre and $\dot{\theta}$ is the rate of rotation of adjacent sections. The extension of centriodal fibre and the rotation of adjacent sections are illustrated in Figure 3.5. The rate of extension of centriodal fibre ($\dot{\epsilon}$) and the rate of rotation of adjacent sections were given by Campbell and Charlton (1972),

$$\begin{aligned} \dot{\epsilon} &= \frac{1}{L/2} \\ \dot{\theta} &= \frac{\delta}{L} \end{aligned} \quad (3.17)$$

Therefore, the axial force parameter (t) during the transient membrane response can be simplified into,

$$t = \frac{2}{H} \frac{\dot{\epsilon}}{\dot{\theta}} = \frac{\delta}{H} \quad (3.18)$$

and the transient membrane response is expressed as,

$$\begin{aligned} p &= 1 - t^2 + 2\frac{\delta}{H}t \\ &= 1 - \left(\frac{\delta}{H}\right)^2 + 2\frac{\delta}{H}\left(\frac{\delta}{H}\right) \quad \text{for } \frac{\delta}{H} \leq 1 \\ &= 1 + \left(\frac{\delta}{H}\right)^2 \end{aligned} \quad (3.19)$$

For the plastic membrane response, substitute $t=1$ into Eq.3.15, we have,

$$p = 2 \frac{\delta}{H} \quad \text{for } \frac{\delta}{H} \geq 1 \quad (3.20)$$

The discussion so far has focused on beams or plates supported by fully fixed end restraints, where no in-plane displacement of the supports will occur during tensile membrane resistance. The stiffness of axial restraints has significant effect on the development of tensile membrane resistance. Young (1959), Jones (1973), Hodge Jr. (1974) and Izzuddin (2005) showed that for semi-rigid supports, the axial restraints move with the induced axial force, causing the member to become a plastic membrane at a larger mid-span displacement compared to rigid support. When the axial stiffness of the supports is very low, the resistance of the member approaches to the member with simply supported conditions, where no tensile membrane resistance can be observed. All the derivations show that only the transient membrane response will be affected by support rigidity while the response of the plastic membrane is independent of the support rigidity.

3.1 Young (1959)

Young (1959) derived analytical solutions of the plate clamped at four edges subjected to a uniformly distributed load. The plate was assumed to be sufficiently long and could be simplified into the one way plate. The elastic behaviour of the plate was analysed based on the analytical solutions presented by Timoshenko and Krieger (1959). Formation of the plastic hinge at mid-span was determined using elasto-plastic analysis. The response after plastic hinges formation due to bending was analysed using the rigid-plastic analysis. The effect of biaxial yield stress of the plate is considered by using the Poisson's ratio of 0.5 for steel after yielding in the analysis:

$$\sigma_p = \frac{\sigma_y}{(1 - \nu_p + \nu_p^2)^{1/2}} = 1.156\sigma_y \quad (3.21)$$

where σ_p is the biaxial yield stress, σ_y is the uniaxial yield stress and ν_p is the Poisson's ratio (0.5).

During the transient membrane response, the load-displacement relationship is influenced by the axial force parameter, σ/σ_p and mid-span displacement:

$$\frac{q}{q_o} = 1 - \left(\frac{\sigma}{\sigma_p}\right)^2 + 2\left(\frac{\sigma}{\sigma_p}\right)\left(\frac{\delta}{H}\right) \quad \text{for } t = \sigma/\sigma_p < 1 \quad (3.22)$$

where q is the uniformly distributed load, q_o is the uniform collapse load of the plate under bending with rotationally fixed support, $q_o = 8(2M_o)/L^2$. δ is the mid-span displacement and H is the depth of the plate. The axial force parameter is a function of the non-dimensional plate parameter, F_{yo} :

$$\frac{\sigma}{\sigma_p} = \frac{8(\delta/H)^2}{F_{yo} + 24(\delta/H)} \quad (3.23)$$

The non-dimensional plate parameter is,

$$F_{yo} = \frac{HL^2\sigma_p}{4D} \quad (3.24)$$

where D is the flexural rigidity of the plate given as,

$$D = \frac{EH^3}{12(1-\nu_p^2)} \quad (3.25)$$

For the plastic membrane response, the load increases proportionally with the mid-span displacement:

$$\frac{q}{q_o} = \frac{2\delta}{H} \quad t = \sigma/\sigma_p = 1 \quad (3.26)$$

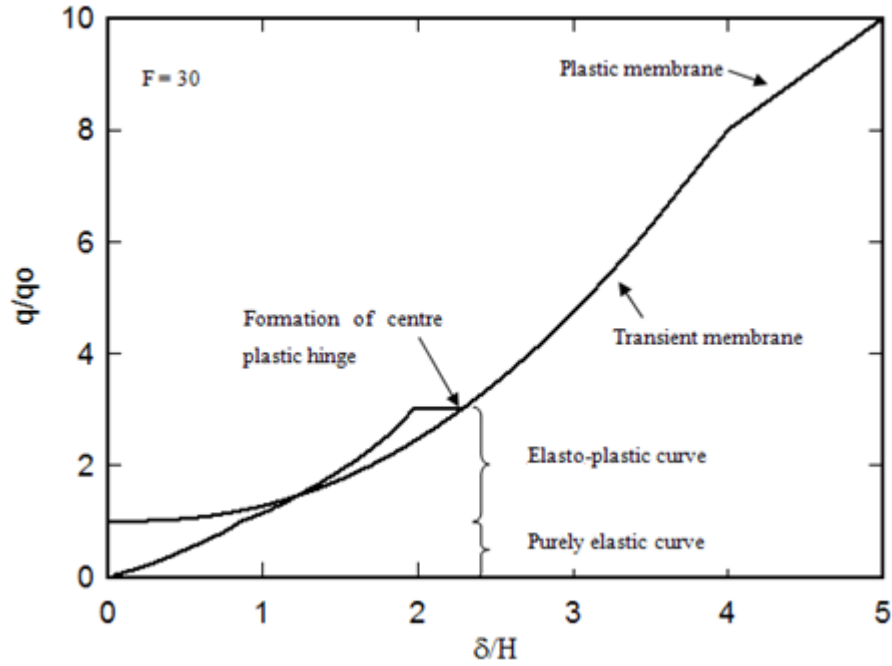


Figure 3.6: Load-displacement relationship for the clamped long rectangular plate subjected to a uniformly distributed load (reproduced from Young, 1959).

The effect of axial restraint stiffness is considered by introducing an edge elasticity coefficient (k_e) during the transient membrane response:

$$\frac{q}{q_o} = 1 - \left(\frac{\sigma}{\sigma_p}\right)^2 + 2\left(\frac{\sigma}{\sigma_p}\right)\left(\frac{\delta}{H}\right) \quad \text{for } t = \sigma/\sigma_p < 1$$

$$\frac{\sigma}{\sigma_p} = \frac{8(\delta/H)^2}{F_{yo}(1+k_e) + 24(\delta/H)} \quad (3.27)$$

where k_e is a ratio of support displacement (Δ) to the elastic extension at the middle surface of the plate. The value of the edge elasticity coefficient, k_e , ranges from zero to infinity. When the coefficient is zero, the plate is fully restrained while the edge elasticity coefficient of infinity means that the plate is simply supported. When the axial restraint stiffness is low, the plate will undergo larger displacement before it becomes a plastic membrane compared to the fully restrained plate. The plastic membrane response ($t = \sigma/\sigma_p = 1$) is not influenced by the axial restraint stiffness.

3.2 Jones (1973)

Jones (1973) analysed the effects of in-plane movement of axial restraint supports on the tensile membrane resistance of the beam with rectangular cross section. The analysis was carried out with the assumption that the steel beam has rigid plastic material properties. Two types of support conditions considered were the rotational free and rotational fixed supports with semi-rigid axial restraint. The loading conditions included a concentrated load at mid-span and a uniformly distributed load. The response was divided into two stages, namely the transient membrane response and the plastic membrane response. It was assumed that the in-plane displacement at the supports (Δ) was proportional to the square of the maximum transverse displacement ($\Delta = 2\beta\delta^2/L$). The axial stiffness coefficient (β) ranges from -0.5 to 0, where -0.5 represents no axial restraint, while 0 is rigid axial restraint.

The transient membrane response and the plastic membrane response of a rotational free beam under a point load at mid-span are,

$$\begin{aligned} p_{ro_free} &= 1 + 4(1 - 4\beta^2)(\delta/H)^2 & \delta/H \leq 1/[2(1+2\beta)] \\ p_{ro_free} &= 4(\delta/H) & \delta/H > 1/[2(1+2\beta)] \end{aligned} \quad (3.28)$$

For a rotationally fixed beam supported by the semi-rigid axial restraints and subjected to a point load at mid-span, the transient and plastic membrane responses are as below:

$$\begin{aligned} p &= 1 + (1 - 4\beta^2)(\delta/H)^2 & \delta/H \leq 1/(1+2\beta) \\ p &= 2(\delta/H) & \delta/H > 1/(1+2\beta) \end{aligned} \quad (3.29)$$

The transient membrane response and the plastic membrane response of the rotational free beam subjected to a uniformly distributed load are,

$$\begin{aligned} \frac{q}{q_{o_free}} &= 1 + 4(1 - 4\beta^2)(\delta/H)^2 & \delta/H \leq 1/[2(1+2\beta)] \\ \frac{q}{q_{o_free}} &= 4(\delta/H) & \delta/H > 1/[2(1+2\beta)] \end{aligned} \quad (3.30)$$

For a rotationally fixed beam supported by the semi-rigid axial restraints and subjected to a uniformly distributed load, the transient and plastic membrane responses are,

$$\begin{aligned} \frac{q}{q_o} &= 1 + (1 - 4\beta^2)(\delta/H)^2 & \delta/H \leq 1/(1+2\beta) \\ \frac{q}{q_o} &= 2(\delta/H) & \delta/H > 1/(1+2\beta) \end{aligned} \quad (3.31)$$

where q_o is the uniform collapse load of the plate due to bending with rotationally fixed support, $q_o = 8(2M_o)/L^2$. q_{o_free} is the uniform collapse load of the plate due to bending with rotationally free support, $q_{o_free} = 8M_o/L^2$. These analytical solutions show that the stiffness of axial restraint only affects the response of transient membrane, even though the loading and support conditions changed.

3.3 Hodge Jr. (1974)

Hodge Jr. (1974) improved Jones' (1973) work by considering the in-plane displacement of the supports as a function of the axial stiffness of the support. Hodge Jr. (1974) derived the response of a rectangular cross-section beam, pin-supported by axial restraints and subjected to a concentrated load at mid-span as shown in Figure 3.7. The thickness of the beam is H and the width is denoted as B . The steel beam was assumed to have rigid perfectly plastic material properties. The axial restraint was assumed to be purely elastic and the horizontal reaction force (F) in the restraint due to the displacement can be determined as:

$$F = K\Delta \quad (3.32)$$

where K is the axial stiffness of the test rig, and Δ is the support displacement. The axial stiffness can be determined either by an analysis of the restraint or by the experiment.

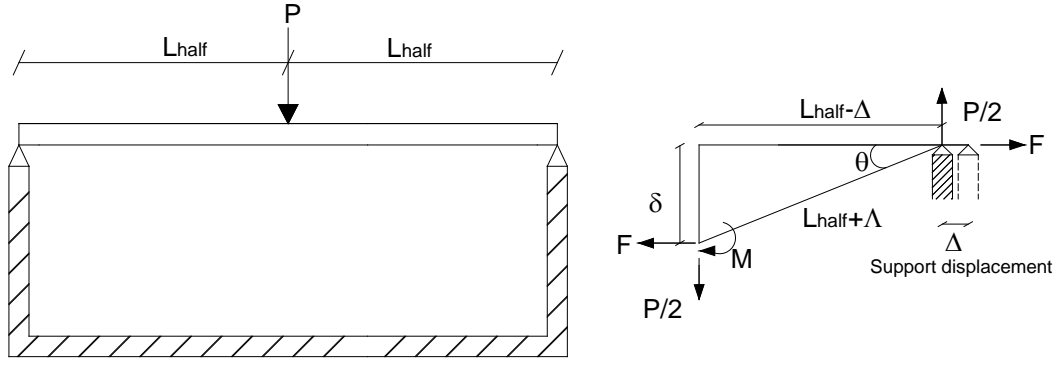


Figure 3.7: The beam with rectangular cross section pin supported by the rig (reproduced from Hodge Jr., 1974).

The response of the beam is derived based on the basic relationships for plasticity under combined bending and axial load,

$$t^2 + m = 1 \quad (3.33)$$

where t is the axial force parameter, $t = T/T_o$, T is the axial tensile force, T_o is the axial yield force, m is the bending moment parameter, $m = M/M_o$, $M_o = BH^2 \sigma_y / 4$. As shown in Figure 3.7, the extension (Λ) of the beam, and the rotation (θ) of the yield hinge are defined by,

$$\delta^2 + (L_{half} - \Delta)^2 = (L_{half} + \Lambda)^2$$

$$\tan \theta = \frac{\delta}{L_{half} - \Delta} \quad (3.34)$$

The analysis is carried out in terms of small parameter,

$$h = \frac{H_{half}}{L_{half}} = \frac{H}{L} \quad (3.35)$$

The dimensionless kinematic quantities are defined as,

$$w = \frac{\delta}{H_{half}} = \frac{2\delta}{H} \quad u = \frac{\Delta L_{half}}{H_{half}^2} = \frac{2\Delta L}{H^2} \quad \lambda = \frac{\Lambda T_o}{M_o} \quad (3.36)$$

where δ is the mid-span displacement, H_{half} is half of the depth of the beam, H is the depth of the beam.

Eq.3.34 can be written in the form of dimensionless quantities,

$$\lambda = h \left[(w^2 - 2u) + h^2 w^2 (u - w^2 / 4) + O(h^4) \right] \quad (3.37)$$

$$\theta = hw \left[1 + h^2 (u - w^2 / 3 + O(h^4)) \right]$$

From the static equilibrium of the moment and the axial force in Figure 3.7,

$$M = \frac{P(L_{half} - \Delta)}{2} - F\delta \quad (3.38)$$

$$T = F \cos \theta + \frac{P \sin \theta}{2}$$

By introducing the parameters,

$$f = \frac{F}{T_o} = \frac{F}{BH\sigma_y} \quad p_{ro_free} = \frac{PL}{4M_o} \quad (3.39)$$

Eq.3.37 can be written as:

$$m = p_{ro_free} - 2wf - h^2 p_{ro_free} u \quad (3.40)$$

$$t = \cos \theta (f + 0.5h p_{ro_free} \tan \theta)$$

Dimensionless rig constant, k , can be determined from,

$$f = ku$$

$$k = f / u \quad (3.41)$$

$$k = \frac{hK}{2\sigma_y B}$$

Substitute Eq. 3.41 into Eq. 3.40,

$$m = p_{ro_free} - 2wf - h^2 p_{ro_free} f / k \quad (3.42)$$

$$t = f + 0.5h^2 w (p_{ro_free} - fw) + O(h^4)$$

To simplify the solution, terms with parameter h higher than 2 degree in Eq.2.42 are ignored and, therefore, it gives,

$$m = p_{ro_free} - 2wf \quad t = f \quad (3.43)$$

When $t < 1$, t is related to the flow rule by,

$$\dot{\lambda} = 2t\dot{\theta} \quad (3.44)$$

Eq. 3.44 is solved by using Eq. 3.37 and Eq.3.41 to obtain,

$$kw - \frac{dt}{dw} = kt$$

$$t = \frac{(kw - dt/dw)}{k} \quad (3.45)$$

$$t = \frac{e^{-kw} + kw - 1}{k}$$

By combining Eq.3.45 and Eq.3.43,

$$p_{ro_free} = 1 + 2wt - t^2 \quad (3.46)$$

When $t = 1$, $m = 0$ and Eq. 3.42 can be simplified as,

$$p_{ro_free} = 2w \quad (3.47)$$

Therefore the overall responses of the beam after yielding using the rigid plastic analysis are:

if $t < 1$

$$t = \frac{e^{-kw} + kw - 1}{k} = \frac{e^{-2k\delta/H} + 2k\delta/H - 1}{k}$$

$$p_{ro_free} = 1 + 2wt - t^2 = 1 + 4t\delta/H - t^2$$

$$\text{else } p_{ro_free} = 2w = \frac{4\delta}{H} \quad (3.48)$$

Eq.3.48 shows that the stiffness of axial restraints only affects the transient membrane response of the beam while it has no effects once the beam becomes a plastic membrane. The effect of the stiffness of axial restraint on the transient membrane response of the beam is plotted in Figure 3.8. With the rigid support, the beam becomes a plastic membrane when the displacement parameter (δ/H) is less than 0.5. When the stiffness of axial restraint decreases, the beam undergoes larger mid-span displacement before it turns into a plastic membrane.

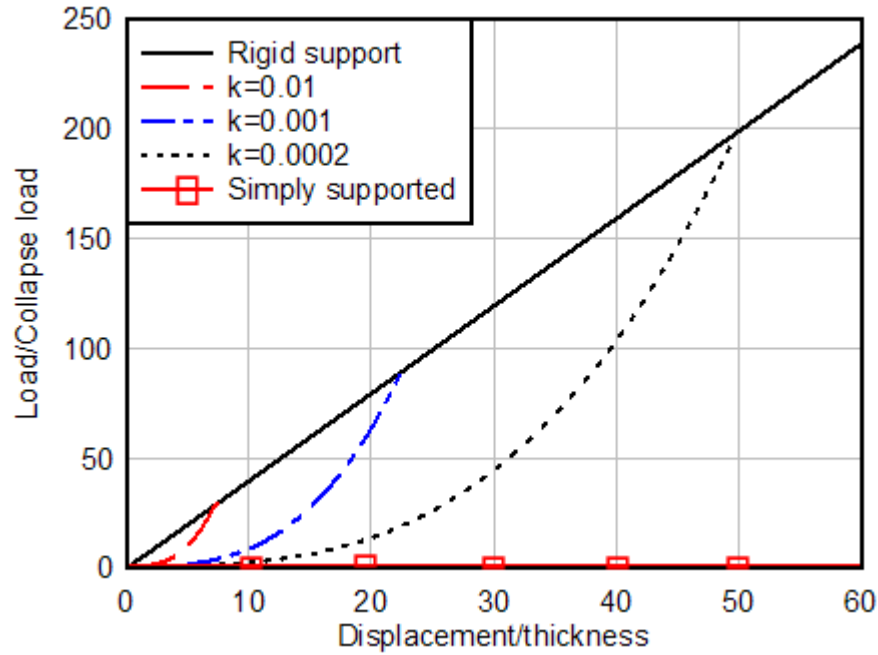


Figure 3.8: Transient and plastic membrane load-displacement relationship for a beam restrained with various axial stiffness at the supports.

3.4 Izzuddin (2005)

Izzuddin (2005) presented a simplified theoretical model for the axially restrained steel beam subjected to a point load at mid-span or a uniformly distributed load. The elastic axial restraint was applied to the ends of the beam at the centroidal axis position as shown in Figure 3.9 (a), and the beam was assumed to behave elastic-perfectly plastic. The interaction between bending moment and axial load during the transient membrane response was simplified into a linear curve with a slope of r_p as shown in Figure 3.9 (b). The temperature was assumed uniform over the beam length and the cross section depth.

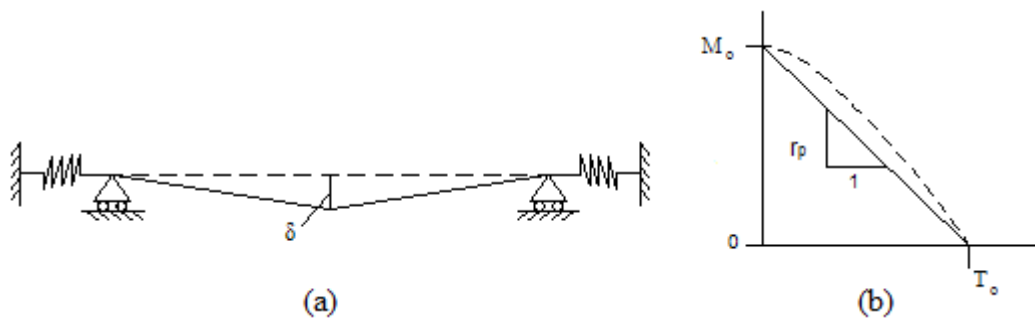


Figure 3.9: (a) A simply supported steel beam with elastic axial restraints at the supports, (b) simplified flow rule between the bending moment and the axial force.

The response of the beam can be divided into four stages: (1) initial elastic flexural response, (2) plastic bending response, (3) transient membrane response and (4) plastic membrane response as illustrated in Figure 3.10.

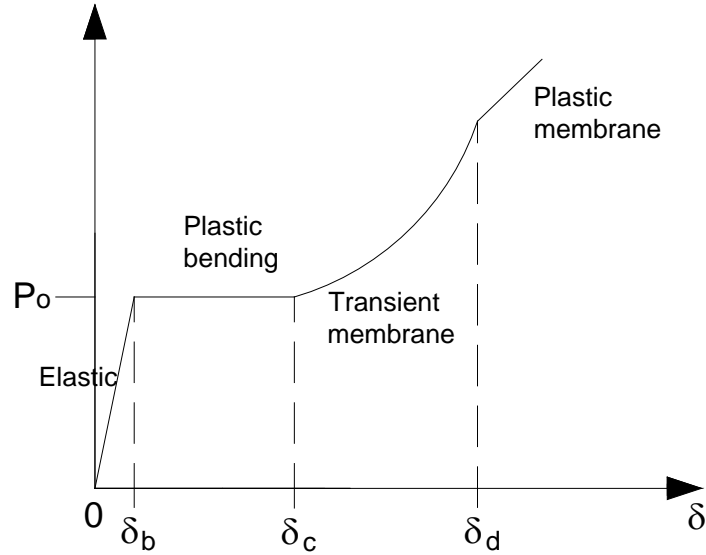


Figure 3.10: Elasto-plastic responses of the axially restrained steel beam.

During the elastic stage, the load is purely resisted by the flexural resistance and the membrane stress is ignored. The elastic load-displacement relationship for a simply supported beam under a mid-span point load or a uniformly distributed load is given as,

$$P_{tot} = \frac{\alpha_1 EI \delta}{L^3} \quad (3.49)$$

where P_{tot} is the total applied load, for beam subjected to a uniformly distributed load, $P_{tot} = qL$. For the beam subjected to a mid-span point load, $P_{tot} = P$. α_1 is the stiffness coefficient depends on the types of loading. For the point load at mid-span, α_1 is 48, while for the uniformly distributed load α_1 is 76.8. E is the Young's modulus of the steel, I is the second moment of area of the beam and L is the distance between supports.

The flexural load capacity of the beam can be determined from the plastic moment capacity,

$$P_o = \frac{\alpha_2 M_o}{L} \quad (3.50)$$

where $\alpha_2 = 4$ for the beam subjected to a point load at mid-span and $\alpha_2 = 8$ for the beam subjected to a uniformly distributed load. The mid-span displacement when the beam reached its flexural load capacity is given as:

$$\delta_b = \frac{\alpha_1 M_o L^2}{\alpha_2 EI} \quad (3.51)$$

After the beam reaches its flexural load capacity, the load remains constant for displacement up to δ_c (Figure 3.10). δ_c is the maximum displacement between δ_b or r_p .

$$\delta_c = \max(\delta_b, r_p) \quad (3.52)$$

During transient membrane resistance, the load increases as the displacement increases and the load-displacement relationship is influenced by the stiffness of the axial restraint. It is assumed that the overall stretching of the beam (Δ_{tot}), which includes elastic axial support extensions, is proportional to the square of the mid-span displacement.

$$\Delta_{tot} = \frac{2\delta^2}{L} \quad (3.53)$$

The effective axial stiffness of the beam is determined from the axial stiffness of the supports (K) and the elastic axial stiffness of the beam (L/EA),

$$K_e = \frac{1}{1/K + L/EA + 1/K} \quad (3.54)$$

The load-displacement relationship during the transient membrane resistance consists of cubic function of mid-span displacement:

$$P_{tot} = \frac{\alpha_2 [M_o + 2K_e(\delta - r_p)^3 / L]}{L} \quad (3.55)$$

The plastic membrane resistance is independent of the stiffness of the axial restraints and it is proportional to the mid-span displacement.

$$P_{tot} = \frac{\alpha_2 T_o \delta}{L} \quad (3.56)$$

3.5 Summary

From the literature review on membrane resistance, it has been demonstrated that axially restrained steel structural members possess significant reserve strength after the members yield in bending. At large deformation, axial tensile force develops in the cross section due to membrane mechanism that gives rise to load resistance. From the theoretical analysis, the membrane response can be divided into two stages, namely transient membrane resistance and plastic membrane resistance. During the transient membrane response, the axial tensile force is less than the axial yield force of the cross section, and an increase in axial tensile force and deflection contributes to the increase in the load resistance. The load increases non-linearly as the displacement increases. The member becomes a plastic membrane once the axial yield force of the cross section is reached, and the resistance increases linearly with the increase of deflection. The stiffness of axial restraint has significant effects on the transient membrane response. The member supported by semi-rigid axial restraint undergoes larger deflection before it turns into a plastic membrane compared to the fully fixed axial restrained member. The plastic membrane response is independent from the stiffness of the axial restraints.

CHAPTER 4

MEDIUM STRAIN RATE TESTING ON GRADE 304 STAINLESS STEEL

4.1 Introduction of strain rate effects

Structures under impact and blast loading deform rapidly, which induces strain rate effects in the material. The strain rate of structures under impact loading is in the range of 0.1s^{-1} to 200 s^{-1} , but is greater than 200 s^{-1} under blast loading. Instrumented falling weight impact (IFWI) testers are normally used to test material properties under medium strain rate ($0.1\text{-}200\text{ s}^{-1}$) while a split Hopkinson pressure bar can be used to obtain material properties under a high strain rate. The strain rate effects on the strength of steels are considered using the Cowper-Symonds coefficients.

Stainless steel is a type of high performance steel that has been used effectively in protective structures due to its high strength and ductility. Louca et al. (2004) and Schleyer et al. (2007) showed that profiled stainless steel blast panels can be used effectively to resist hydrocarbon explosions in offshore structures. Many studies investigated the dynamic behaviour of stainless steel under high strain rates, but only a few had tested it under medium strain rates. In addition, a literature search suggested that differences in the stress level, prior work hardening, heat treatment condition and microstructure could affect the mechanical properties under increasing strain rates. The existing Cowper-Symonds coefficients for stainless steel were derived in 1978 (Forrestal and Sagartz, 1978), where the yield stress was about 180 MPa. The main focus of this study is to investigate the validity of the Cowper-Symonds coefficients for Grade 304 stainless steel under medium strain rates since the yield strength of recent grades of stainless steel has improved significantly.

4.2 Literature review of strain rate effects on stainless steel

Steichen (1971) conducted experimental investigation on Grade 304 stainless steel at room temperature for strain rates between $3\times 10^{-5}\text{ s}^{-1}$ to $1\times 10^2\text{ s}^{-1}$. The Instron universal testing machine was used to test specimens at strain rates from $3\times 10^{-5}\text{ s}^{-1}$ to

$3 \times 10^{-4} \text{ s}^{-1}$, while the MTS high rate system was used for strain rates between $3 \times 10^{-3} \text{ s}^{-1}$ and $1 \times 10^2 \text{ s}^{-1}$. The specimens' strain rate was determined based on the velocity of the crosshead and initial specimen gauge length. The results showed that 0.2% proof stress from static test was about 180 MPa. When the strain rate increased, the yield stress increased significantly. However, the ultimate tensile strength only increased slightly. The total elongation and uniform elongation for stainless steel decreased as the strain rate increased. The lower ductility was attributed to adiabatic heating effects, which eliminated the austenite to martensite transformation process in the stainless steel. The transformation of austenite to martensite will increase the ductility of the stainless steel at room temperature.

Later, using similar experimental techniques, Steichen (1973) conducted an experiment on the strain rate effects on stainless steel Grade 304 at elevated temperatures between 315°C and 871°C . The strain rates covered was from $3 \times 10^{-5} \text{ s}^{-1}$ to $1 \times 10^2 \text{ s}^{-1}$. Generally, the 0.2% proof stress and the ultimate tensile strength of stainless steel decreased as the temperature increased under a constant strain rate. The results showed that for stainless steel specimens at temperatures below 538°C , the 0.2% proof stress increased when the strain rates exceeded $1 \times 10^1 \text{ s}^{-1}$, while the ultimate tensile strength was insensitive to the strain rate. The total elongation and uniform elongation slightly decreased as the strain rate increased. For specimens exposed to temperatures above 538°C , their responses were significantly different. The 0.2% proof stress slightly increased as the strain rate increased. For the ultimate stress, the strength increased when the strain rate increased up to $1 \times 10^1 \text{ s}^{-1}$, after that the ultimate stress was insensitive to the strain rate. The total elongation and uniform elongation showed an inconsistent trend with the increase in strain rate.

Forrestal and Sagartz (1978) derived the Cowper-Symonds coefficients for Grade 304 stainless steel based on the experimental results of Steichen (1971). The coefficients D and q proposed by Forrestal and Sagartz (1978) were 100 and 10, respectively. These Cowper-Symonds coefficients were derived based on the 0.2% proof stress of 180 MPa from the static test, and the strain rate was in the range of 3×10^{-5} to 1×10^2 . Jones (1989) presented the Cowper-Symonds coefficients derived by Forrestal and Sagartz (1978) for stainless steel Grade 304. These are the only

Cowper-Symonds coefficients available for stainless steel Grade 304 in literature and they are widely used in the dynamic design of stainless steel Grade 304.

Nicholas (1981) used a tensile split Hopkinson bar to investigate the strain rate effects on stainless steel Grade 304 at room temperature. MTS servo-controlled hydraulic testing machine was used to test specimens under strain rates of 1×10^{-4} – 20 s^{-1} . The strain on the specimens was determined from the specimen-grip-displacement of the MTS system. As a result, the elastic stress-strain relationship could not be obtained accurately. The tensile split Hopkinson bar used has the limitation of determining the elastic stress-strain relationship due to stress-wave reflections, stress nonuniformity and large variations in strain rate during initial portion of the test. The strain rate effects were evaluated at the strength of 10% of plastic strain, and it showed that the plastic strength increased as the strain rate increased. No Cowper-Symonds coefficients were derived from that study.

The strain rate effects on the mechanical properties of Grade 304L stainless steel was investigated by Lee and Lin (2001) for the strain rate ranged from $1 \times 10^2 \text{ s}^{-1}$ to $5 \times 10^3 \text{ s}^{-1}$ using a compression split Hopkinson bar and the microstructure evolution was studied. Based on the mechanical properties and microstructure evolution observed, they proposed a physically-based constitutive equation that incorporated the strain rate effects for the stress-strain relationship of Grade 304L stainless steel. It showed that the stress hardening decreases with increasing strain rate because of heat generated by plastic deformation. Andersson et al. (2005) investigated the dynamic response of three types of stainless steels, namely Hytens1000, SAF2304 and Nanoflex, at strain rates from $1 \times 10^{-2} \text{ s}^{-1}$ up to $1 \times 10^3 \text{ s}^{-1}$. This study was focused on fitting the experimental stress-strain relationship under various strain rates with mathematical functions which considered strain rate flow functions. The strain rate flow functions considered were the Cowper-Symonds equation, Johnson-Cook equation and Jones equation.

Peixinho (2006) studied the response of H400 stainless steel and dual-phase steel at strain rates between $1 \times 10^{-3} \text{ s}^{-1}$ to 1000 s^{-1} . The quasi-static test and intermediate loading rate test (2.25 s^{-1}) were performed using a servo hydraulic testing machine.

Different gauge lengths of specimens were used to obtain desired strain rates. In the quasi-static test, an extensometer was used while in the intermediate loading test, strain gauges were attached to the specimens to record the deformation. High strain rate tests were carried out by using a tensile split Hopkinson bar and a strain gauge was attached to the specimen. The maximum deformation of the specimen that could be obtained in this study was 14% due to the limitation of the striker bar length. The 0.2% proof stress of the specimens could be determined under various strain rates by using the extensometer and strain gauges. However, the ultimate tensile strength of the specimens at high strain rate could not be obtained due to the limitation of the test. The Cowper-Symonds coefficients derived for 0.2% proof stress and tensile strength at 10% plastic strain were different. Peixinho (2006) attributed this to the intrinsic disadvantage of the Cowper-Symonds equation. It is advised that these coefficients should be used carefully because using coefficients derived for 0.2% proof stress as the reference might yield an erroneous prediction for higher stress levels at large strains.

Cunat (2000) presented the Cowper-Symonds coefficients for various types of austenitic and duplex stainless steels manufactured according to the European standard. The most significant finding in this study is that the strain rate sensitivity for the stainless steel with the same chemical composition changed when the strength level and the thickness of the steel component changed. Therefore, the Cowper-Symonds coefficients were derived for the stainless steel with every strength and thickness category. Marais et al. (2004) investigated the strain rate effects on mild steel and copper using a split Hopkinson bar. The experimental results showed poor correlation between the previously published data for mild steel ($D = 40.4$ and $q = 5$), which they attributed to differences in the stress level, prior work hardening, heat treatment condition and microstructure.

Fernie and Warrior (2002) presented the design of impact test rigs for tensile and compressive testing of composite materials. Zabolkin et al. (2003) showed design concept of an instrumented falling weight impact (IFWI) tester for tensile testing. It showed that the IFWI test rig is a viable alternative technique for determination of material properties under medium strain rates and the strain rate that could be

achieved by this particular test rig is 200 s^{-1} . The mechanical properties for Grade 316L stainless steel, titanium alloy, and alloy C22 under medium strain rates were determined.

4.3 Cowper-Symonds equation

The Cowper-Symonds relationship is an empirical equation that describes material behaviour at different strain rates. The relationship between the dynamic stress of a material and the strain rate is given in Eq. 4.1.

$$\sigma_d = \sigma_s \left[1 + (\dot{\epsilon} / D)^{1/q} \right] \quad (4.1)$$

where σ_d is the dynamic stress or strength, σ_s is the static stress or strength, $\dot{\epsilon}$ is the strain rate, D and q are the Cowper-Symonds coefficients. Forrestal and Sagartz (1978) derived the Cowper-Symonds coefficients for 304 stainless steel as 100 (D) and 10 (q) respectively.

4.4 Design of IFWI test rig

Figure 4.1 shows the front view of the high capacity IFWI test rig developed at the University of Wollongong. It consists of: 1) an impact transmitter frame, 2) two guide rails, 3) a load cell, 4) a nut, 5) a steel base plate, 6) a load cell holder, 7) a cylindrical specimen, 8) four supporting columns, and 9) a layer of synthetic rubber. The 50 mm thick steel base plate is bolted to the strong floor using two M25 high tensile bolts. An Interface 1210 Precision model load cell is used for this test rig due to its accuracy up to 0.04% and it has a maximum capacity of 50 kN. It is connected to the load cell holder with eight M6 high tensile screws. Four supporting columns connect the load cell holder to the base plate and transfer the impact force to the ground. The specimen is screwed into the load cell and then attached to the impact transmitter frame with a nut. The nut is designed to allow for easy installation and removal of the specimen before and after the tests. The impact transmitter frame is made from 50 mm thick high strength steel to prevent any deformation under repeated impact.

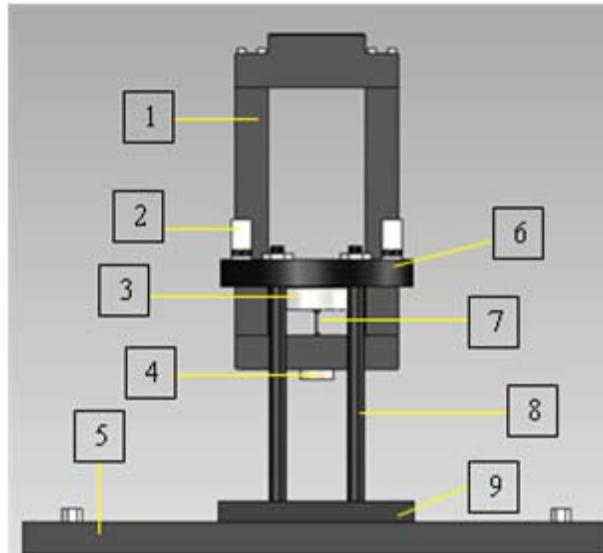


Figure 4.1: Front view of the instrumented falling weight impact (IFWI) test rig developed at the University of Wollongong.

The IFWI test rig is incorporated into the existing drop hammer facility at the University of Wollongong. The mass of the drop hammer is about 600 kg. The height of the drop hammer can be raised up to 5 m high to achieve the desired impact energy and velocity. During the test, the drop hammer is released from a predetermined height to impact on the top of the impact transmitter frame. The impact transmitter frame then accelerates downwards, pulling the specimen until it fractures. Obviously, varying the drop height means that the time needed to fracture the specimen varies, which means that different strain rates can be obtained.

Before the test rig was fabricated, preliminary FE analyses were carried out using the general purpose finite element program ABAQUS to evaluate the design concept. The actual geometry of the test rig with a cylindrical mild steel specimen were modelled. The mild steel was assumed to behave as an elasto-plastic material with a yield stress of 320 MPa. High strength steel with assumed elasto-plastic behaviour and yield stress of 700 MPa was applied to the impact transmitter frame. The guide rails, the load cell, and the nut were not modelled. The drop hammer was simplified into a cylinder striker with a mass of 600 kg in the FE model. The performance of the test rig was evaluated by subjecting it to different impact velocities. The FE results showed that the test rig could achieve various strain rates, depending on the impact velocity. The size of every component was adequate since no plastic deformation

was predicted for these components. Figure 4.2 shows the von Mises stress contour plot for the test rig subjected to an impact velocity of 5 m/s. It showed that the specimen reached a yield stress of 320 MPa and fractured whereas the stress distribution in the other components was low. A test rig was then fabricated and a full experimental set-up is shown in Figure 4.3.

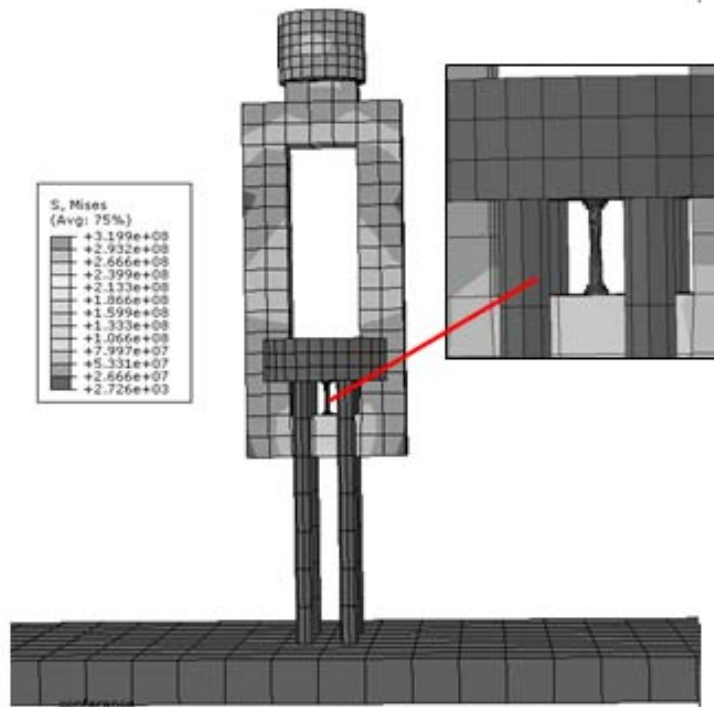


Figure 4.2: Von Mises stress contour plot for the test rig under impact.

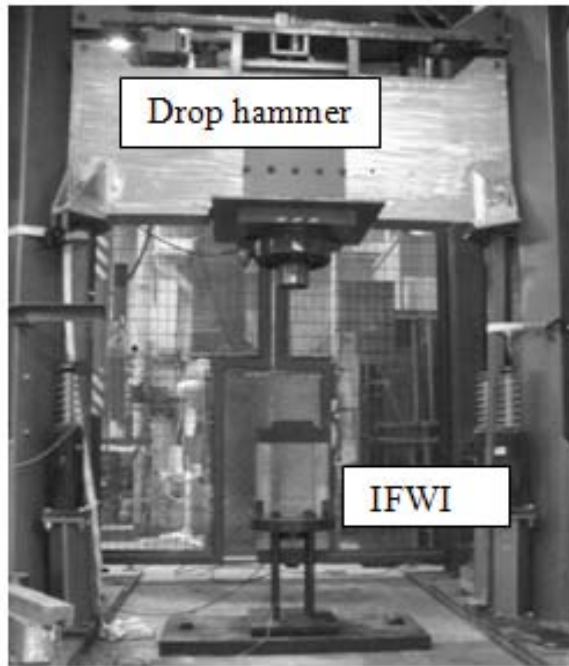


Figure 4.3: Full experimental set up for medium strain rate tests.

4.5 Experimental procedure

The chemical composition for Grade 304 stainless steel used in this study is presented in Table 4.1. The specimens were obtained from 16 mm diameter round bar solution annealed at 1040° for 1 to 2 hours and then water quenched. The grain size determined according to ASTM was fine (5-8). The round bar was machined into 6 mm diameter cylindrical specimens with a gauge length of 14 mm. The radius of transition was 6 mm, and the threads were prepared at both ends of the specimen, as shown in Figure 4.4. Threads were screwed into the testing equipment for the quasi-static and medium strain rate tests.

Table 4.1: Chemical composition of Grade 304 stainless steel used in this study.

Element	C	Si	Mn	P	S	Ni	Cr	Mo	N	Fe
% by mass	0.055	0.428	1.831	0.027	0.028	8.004	18.422	0.122	0.069	Balance



Figure 4.4: Geometry of a cylindrical specimen.

The specimens were tested under 5 different strain rates, where 3 specimens were tested under each strain rate condition. The experimental programme is listed Table 4.2.

Table 4.2: Experimental program of 304 stainless steel under quasi-static and medium strain rates.

	Test apparatus	Test condition	Number of specimens
1	Instron	Crosshead velocity = 2mm/min	3
2	Instron	Crosshead velocity = 1000mm/min	3
3	IFWI	Drop height = 100 mm	3
4	IFWI	Drop height = 500 mm	3
5	IFWI	Drop height = 2000 mm	3

For the Instron Universal machine testing using a crosshead velocity of 2 mm/min, an extensometer was used to record the elongation of specimens up to 4 mm displacement. After that, the extensometer was removed and the elongation of the specimens was recorded by the LVDT of the Instron. For the testing with a crosshead velocity of 1000 mm/min, a special strain gauge was attached to the specimen to record the initial elongation. The strain gauge was designed to measure a large strain up to 15-20%. The backing length and the width of the strain gauge were 12 mm and 4 mm, respectively.

The high capacity instrumented falling weight impact (IFWI) test rig developed at the University of Wollongong was used to perform tensile tests under medium strain rates. Three drop heights used were 100 mm, 500 mm, and 2000 mm. The force and the strain time histories in the specimen were measured by the load cell and the strain gauge, respectively. The strain gauges used in the dynamic tests were the same as

those used in the quasi-static tests. A high speed data acquisition system was used to record the load and strain time histories at a sampling frequency of 300 kHz.

4.6 Determination of strain rate

For the test carried out using the Instron Universal tester, the strain rates were determined based on the velocity of the crosshead and the initial gauge length of the specimen. Therefore, the strain rate achieved using the Instron machine in this study was 0.002 s^{-1} when the crosshead velocity was 2 mm/min, and it was 1.00 s^{-1} for the crosshead velocity of 1000 mm/min. The strain rate of the specimens tested using IFWI test rig was determined using Eq. 4.2 according to Andersson et al. (2005).

$$\dot{\varepsilon} = (\varepsilon_{UTS} - \varepsilon_{0.01}) / (t_{UTS} - t_{0.01}) \quad (4.2)$$

where ε_{UTS} is the strain at the ultimate tensile strength, $\varepsilon_{0.01}$ is the 1% strain, t_{UTS} is the time when the specimen reached the ultimate tensile strength, $t_{0.01}$ is the time when the specimen reached 1% strain. This equation gives the average strain rate over the plastic region before necking. Therefore, the effect of non-uniform elongation during elastic deformation can be eliminated.

4.7 Experimental results

4.7.1 Results from Instron universal testing machine

There were six specimens tested with the Instron Universal tester using two crosshead velocities, namely 2 mm/min and 1000 mm/min. For the tests carried out using the crosshead velocity of 2 mm/min, an extensometer was used to record the elongation of specimens up 4 mm, and then the elongation of the specimen was recorded by the LVDT of Instron. For the tests with the crosshead velocity of 1000 mm/min, a strain gauge was attached to the specimen to record the strain history and after the strain gauge failed, the elongation of the specimen was obtained from the record of LVDT of Instron. Therefore, the engineering strain of the specimens was constructed by combining records of the extensometer or strain gauge and the LVDT. The load was recorded by the load cell of the Instron universal tester.

The engineering stress-strain curves for the specimens under strain rates of 0.002 s^{-1} and 1 s^{-1} are shown in Figure 4.5 and Figure 4.6. The experimental data for one of the specimens tested under the strain rate of 1 s^{-1} could not be obtained due to experimental errors. By comparing engineering stress-strain curves in Figure 4.5 and Figure 4.6, it showed that the total strain and uniform strain reduced when the strain rate increased from 0.002 to 1 s^{-1} . The total strain was reduced from 0.64 to 0.46 , while the uniform strain reduced from 0.4 to 0.22 . The lower ductility was attributed to adiabatic heating effects, which eliminated austenite to martensite transformation process in the stainless steel. The transformation of austenite to martensite would increase the ductility of the stainless steel at room temperature (Steichen 1971).

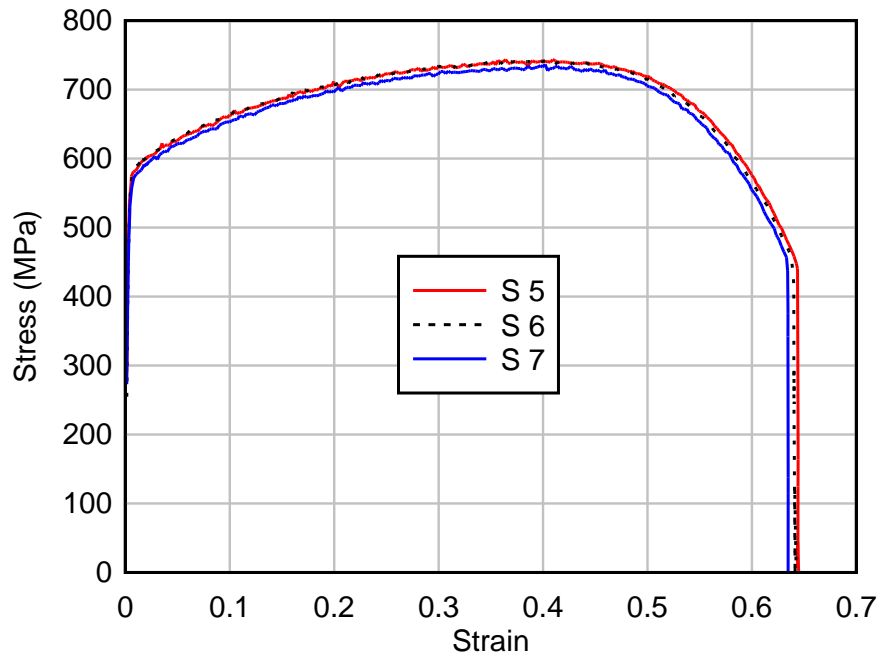


Figure 4.5: Engineering stress-strain curves for Grade 304 stainless steel at a strain rate of 0.002 s^{-1} .

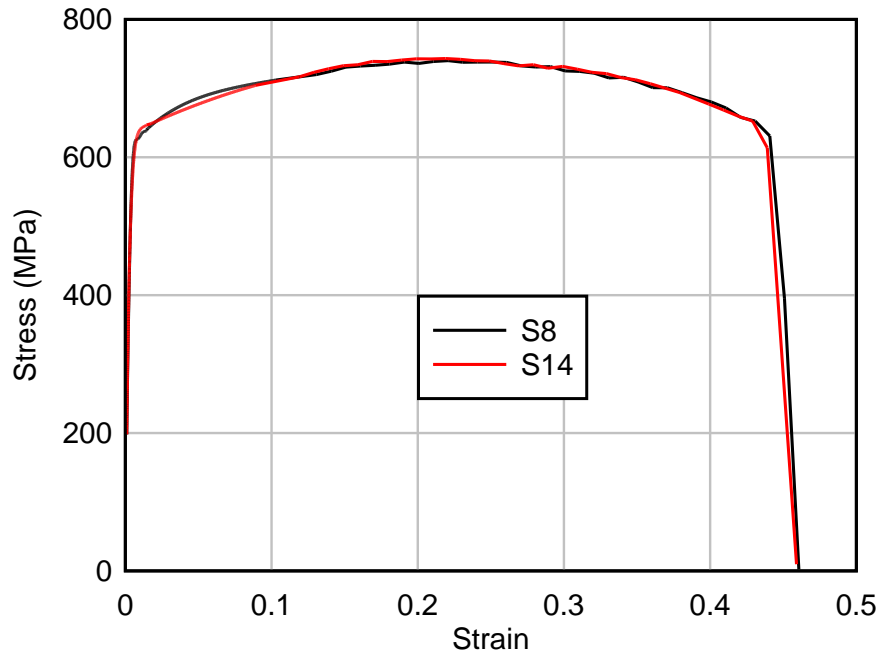


Figure 4.6: Engineering stress-strain curves for Grade 304 stainless steel at a strain rate of 1 s^{-1} .

The yield stress of the stainless steel was determined by using 0.2% proof stress. The 0.2 % proof stress and the ultimate tensile strength of specimens are summarized in Table 4.3. It was observed that the average 0.2% proof stress and average ultimate tensile strength under strain rate of 0.002 s^{-1} was 542 MPa and 741 MPa, respectively. When the strain rate increased to 1 s^{-1} , the average 0.2% proof stress slightly increased to 576 MPa, while the average ultimate tensile strength remained constant.

Table 4.3: Summary of the 0.2% proof stress and the ultimate tensile strength of 304 stainless steel specimens tested using Instron universal tester.

Strain rate (s^{-1})	Specimen	0.2% proof stress (MPa)	Ultimate tensile strength (MPa)
0.002	Specimen 5	548	744
	Specimen 6	543	743
	Specimen 7	534	737
	Average	542	741
1	Specimen 8	585	740
	Specimen 9	-	-
	Specimen 14	567	743
	Average	576	742

4.7.2 Results from IFWI test rig

There were nine stainless steel specimens tested under various drop heights (100 mm, 500 mm and 2000 mm) using the IFWI test rig. All the strain gauges attached to the specimens recorded strain up to 0.05 before the adhesive used to bond the strain gauges to the specimens failed for unknown reasons. The strain time histories recorded by the strain gauges showed that the strain increased non-linearly with time until it reached about 0.02, after which it increased almost linearly. This implied that the velocity of the impact transmitter frame increased non-linearly from zero to almost constant when the strain in the specimen reached 0.02.

To obtain a complete strain time history of the specimen, the gradient of the strain curve before the adhesive failed was first determined. Then, using this gradient, a straight line was extrapolated from the strain gauge records to the end of the impact duration. The fracture strain predicted by this straight line was compared to the fracture strain measured for each specimen after the tests. Generally, the fracture strain predicted by this method was close to the experimental fracture strain. In order to match the experimental fracture strain, the gradient of the straight line was slightly adjusted. The composite strain time history for the one of stainless steel specimens tested under a 500 mm drop height is shown in Figure 4.7.

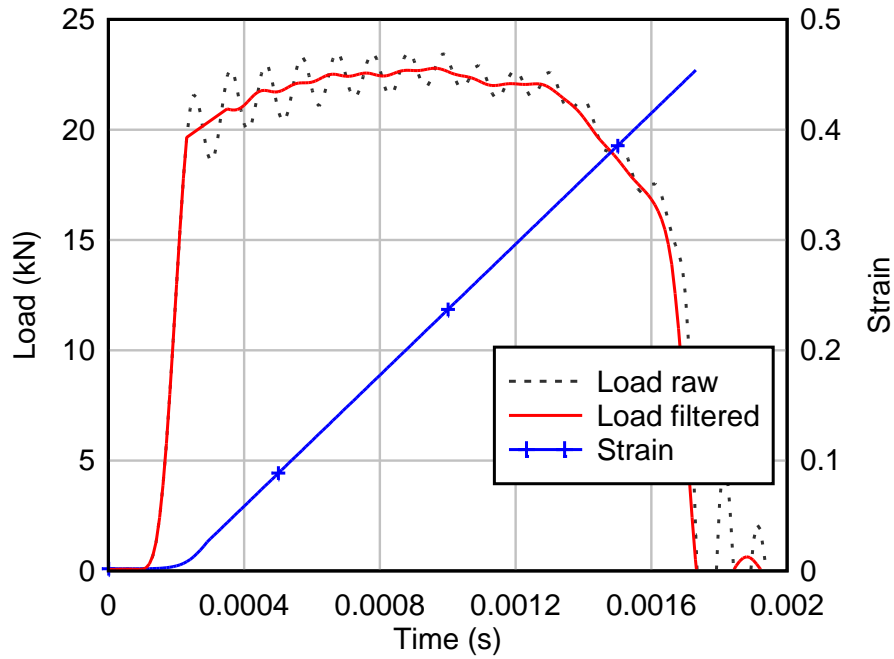


Figure 4.7: Processed load and strain time histories for the specimen 3 tested using the IFWI test rig under a drop height of 500 mm.

The raw load time histories contain high frequency oscillations due to a hard impact contact between the drop hammer and the impact transmitter frame, as shown in Figure 4.7. The stress time histories up to the initial peak were plotted against the experimental strain time histories, as exemplified by specimens subjected to 500 mm drop in Figure 4.8. The 0.2% proof stress for each specimen was determined from these initial elastic-plastic engineering stress-strain curves, and the results are presented in Table 4.4. To obtain actual load time histories, the load signal up to the yield strength was retained, and the high frequency oscillations were filtered using a fourth order low pass Butterworth digital filter with a cut-off frequency of 2.5 kHz. The processed load time history for the one of the stainless steel specimens tested under 500 mm drop height is illustrated in Figure 4.7. The processed load time histories are then plotted against their corresponding strain time histories in Figure 4.9 to Figure 4.11.

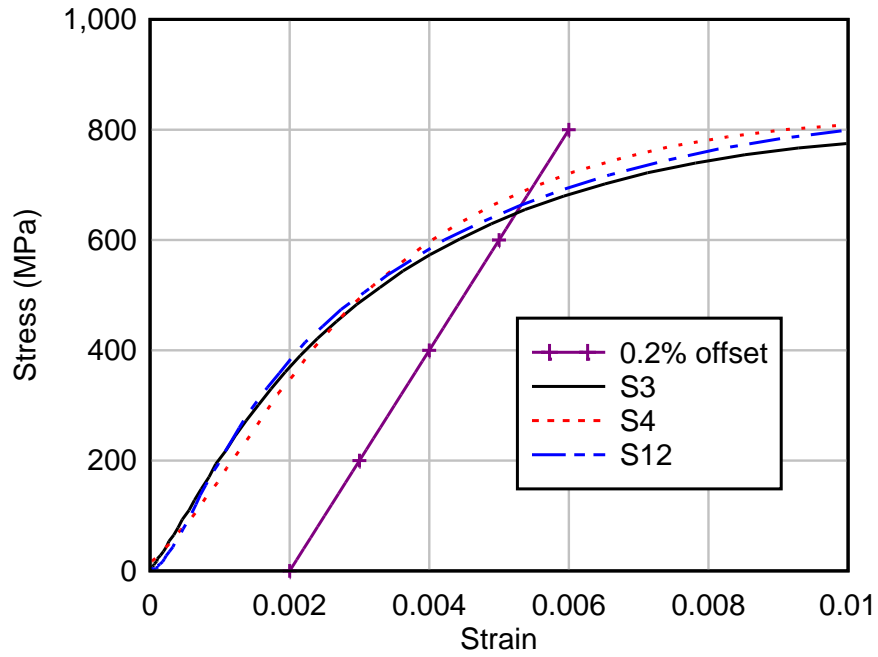


Figure 4.8: Initial elastic-plastic stress strain curves for stainless steel specimens under 500 mm drop height.

Table 4.4: Summary of experimental results obtained from the IFWI test rig.

Drop height (mm)	Specimen	Strain rate (s^{-1})	0.2% proof stress (MPa)	Ultimate tensile strength (MPa)
100	Specimen 1	88	641	810
	Specimen 2	89	657	811
	Specimen 11	87	640	809
	Average	88	646	810
500	Specimen 3	297	648	831
	Specimen 4	309	695	831
	Specimen 12	312	664	832
	Average	306	669	831
2000	Specimen 10	-	-	-
	Specimen 13	669	708	841
	Specimen 15	599	742	852
	Average	634	725	847

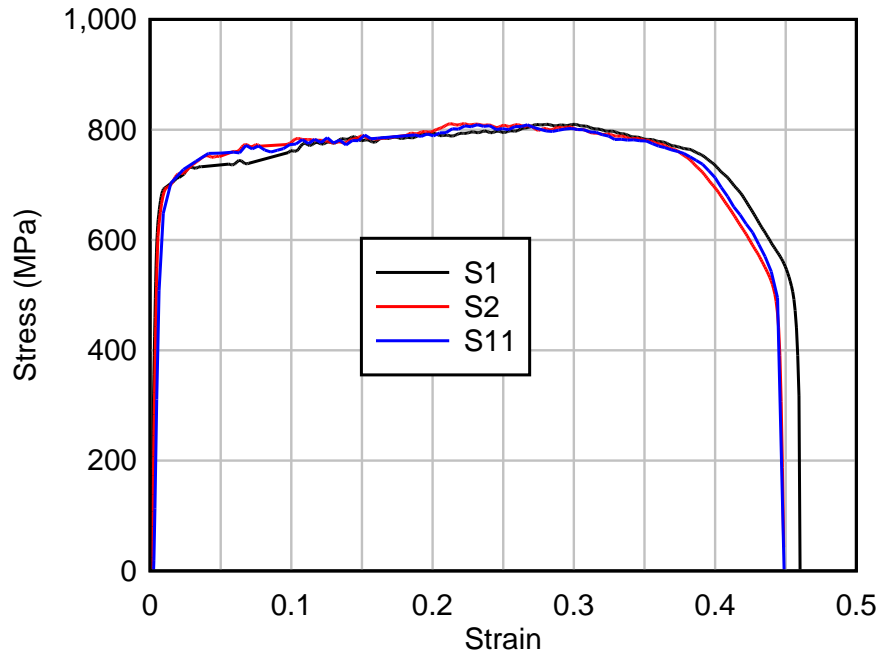


Figure 4.9: Engineering stress-strain curves for Grade 304 stainless steel at a strain rate of about 90 s^{-1} .

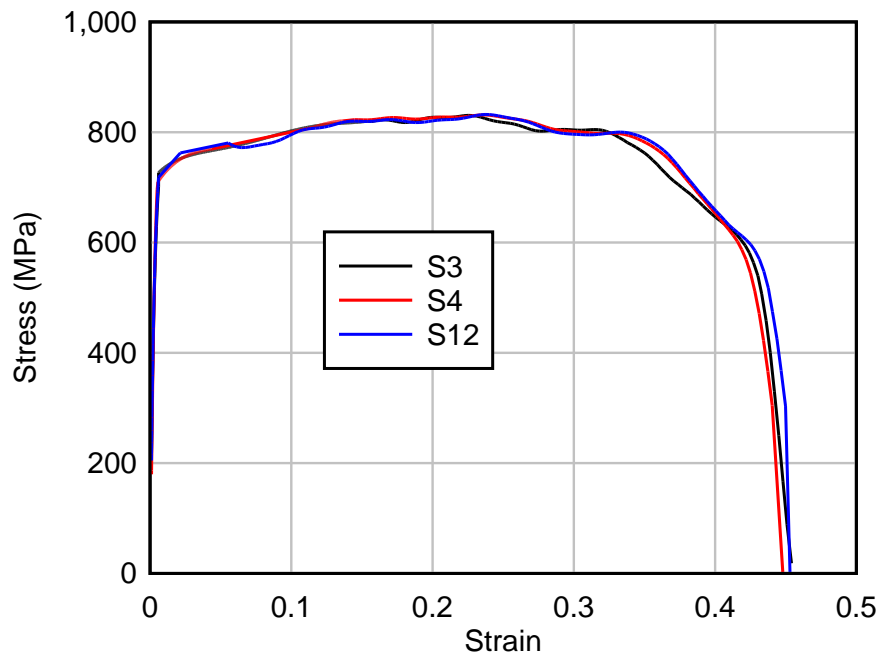


Figure 4.10: Engineering stress-strain curves for Grade 304 stainless steel at a strain rate of about 300 s^{-1} .

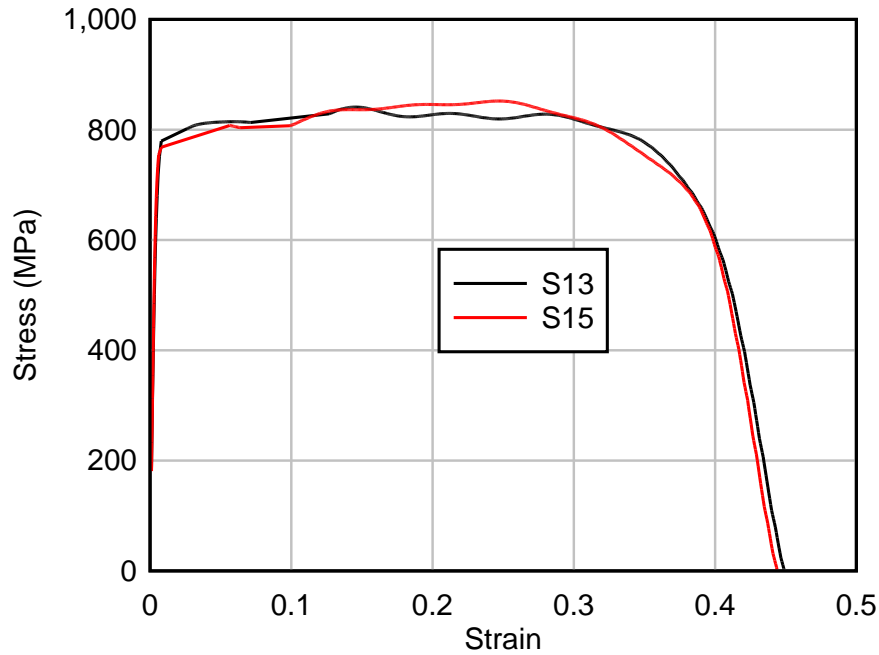


Figure 4.11: Engineering stress-strain curves for Grade 304 stainless steel at a strain rate of about 600 s^{-1} .

The yield stress and the ultimate tensile strength for stainless steel specimens tested using the IFWI test rig are summarised in Table 4.4. The strain rate for each specimen was determined according to Eq. 4.2, and the maximum strain achieved in this study was approximately 600 s^{-1} . Based on the experimental results, the yield stress and the ultimate tensile strength for stainless steel increased with an increasing strain rate. The average yield stress achieved under a strain rate about 600 s^{-1} was 725 MPa and the average ultimate tensile strength was 847 MPa . The yield stress increased about 34% when the strain rate increased from 0.002 s^{-1} to about 600 s^{-1} , while the ultimate tensile strength only increased 14%. This showed that the yield stress of stainless steel was more sensitive to strain rate effects than the ultimate tensile strength. The total strain of the stainless steel was reduced to about 0.45 when the strain rate exceeded 1 s^{-1} compared to about 0.6 for the stainless steel under static test. The uniform strain was in the range of 0.2 - 0.3 when the strain rate exceeded 1 s^{-1} , which was lower than static test of 0.4.

4.8 Comparison of experimental results with existing Cowper-Symonds coefficients

The experimental yield stress and the ultimate tensile strength under various strain rates are plotted in semi-log graphs as shown in Figure 4.12 and Figure 4.13. The experimental results were compared to the predicted dynamic yield stress and the ultimate tensile strength using the existing Cowper-Symonds coefficients of 100 and 10. It showed that the existing Cowper-Symonds coefficients significantly overestimated the experimental yield stress and the ultimate tensile strength of Grade 304 stainless steel used in this study. This could be attributed to differences in the stress level, prior work hardening, heat treatment condition and microstructure as discussed by Cunat (2000) and Marais et al. (2004).

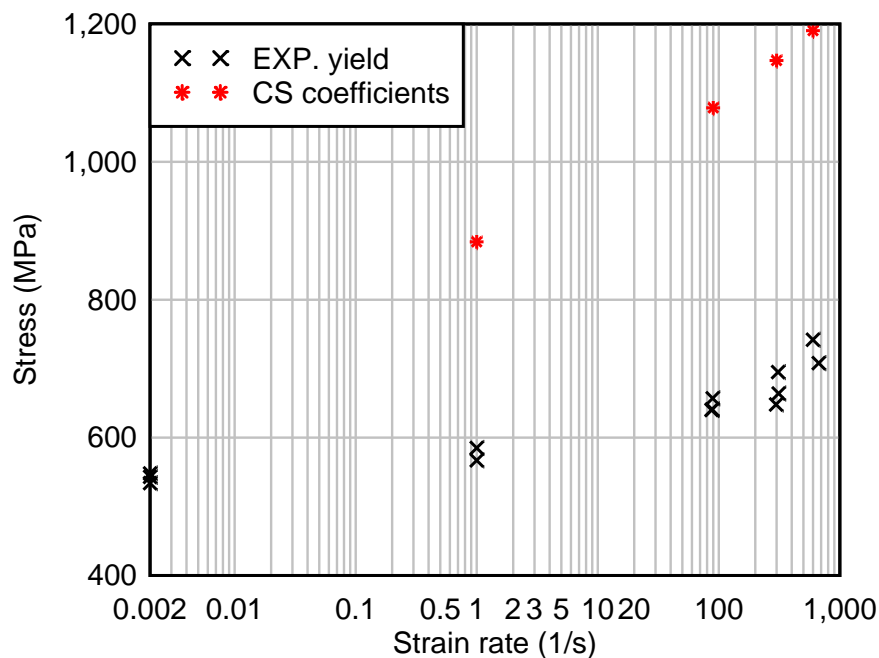


Figure 4.12: Comparison between the experimental yield stress and the theoretical dynamic yield stress predicted by the existing Cowper-Symonds coefficients.

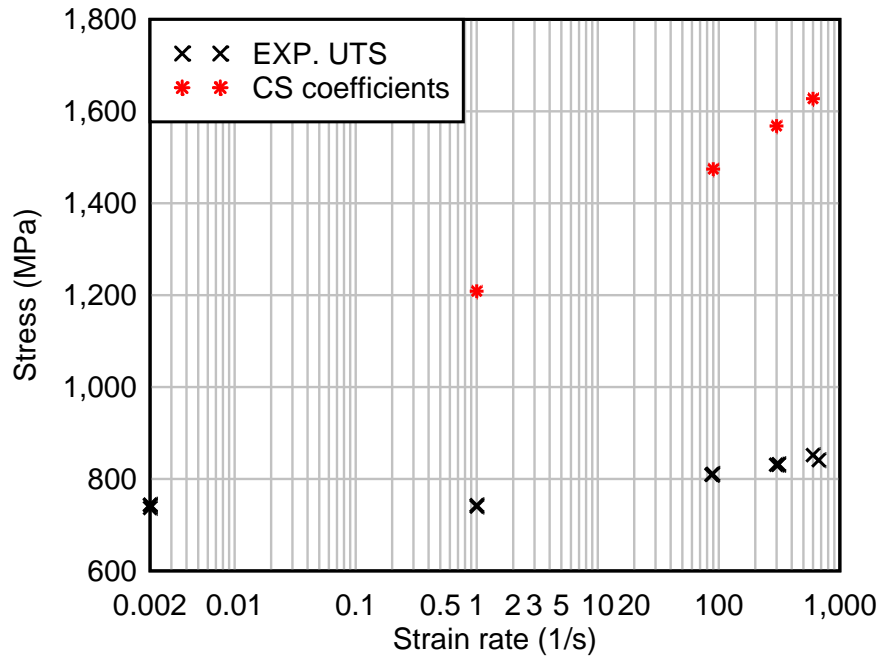


Figure 4.13: Comparison between the experimental ultimate tensile strength and the theoretical dynamic ultimate tensile strength predicted by the existing Cowper-Symonds coefficients.

4.9 Derivation of Cowper-Symonds coefficients

New proposed Cowper-Symonds coefficients for solution annealed stainless steel Grade 304 with fine grain size, and the static 0.2% proof stress of about 550 MPa were derived for strain rates in the range of 0.002 - 600 s⁻¹ at room temperature based on the experimental results. The coefficients were derived separately for the yield stress and the ultimate tensile strength since they showed different strain rate sensitivity under strain rates covered in this study. These coefficients were obtained by plotting $\ln(\sigma_d/\sigma_s - 1)$ against $\ln \dot{\epsilon}$, and then fitting the data with a straight line. The slope of the straight line represents the coefficient q and it will intercept the ordinate at $\ln D$. The curve fitting for the experimental data of the yield stress and the ultimate tensile strength are shown in Figure 4.14 and Figure 4.15. The proposed Cowper-Symonds coefficients for stainless steel 304 used in this study is presented in Table 4.5. The proposed coefficients for the yield stress are 14000 (D) and 3 (q), while they are 6000 (D) and 1.5 (q) for the ultimate tensile strength. The derived coefficients are significantly different from the existing coefficients, and they correlate better with the coefficients presented by Cunat (2000). It is also recognized

that by using Cowper-Symonds coefficients of the yield stress as the reference will yield an erroneous prediction for higher stress levels at large strains.

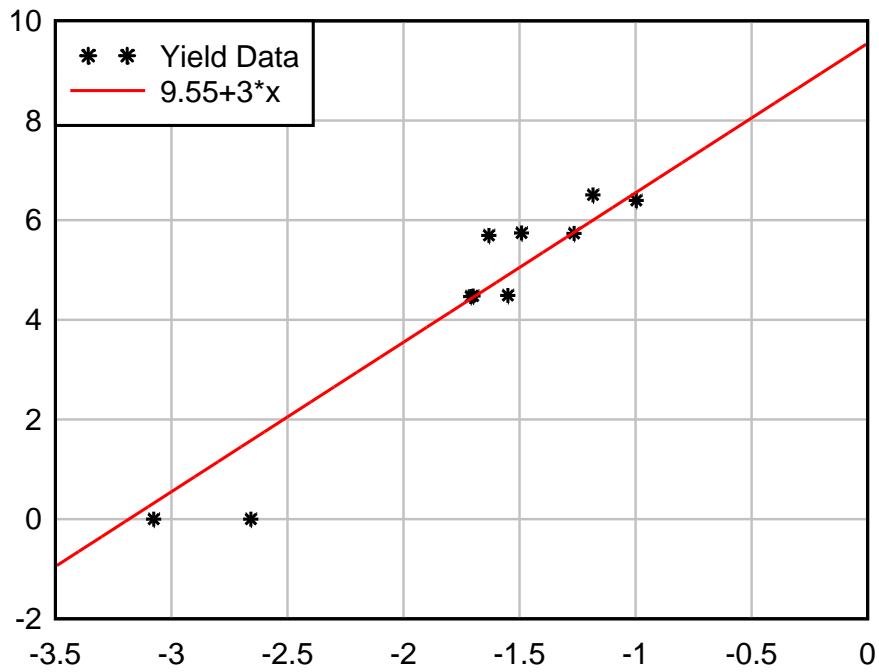


Figure 4.14: Curve fitting to obtain new Cowper-Symonds coefficients for the yield stress for Grade 304 stainless steel.

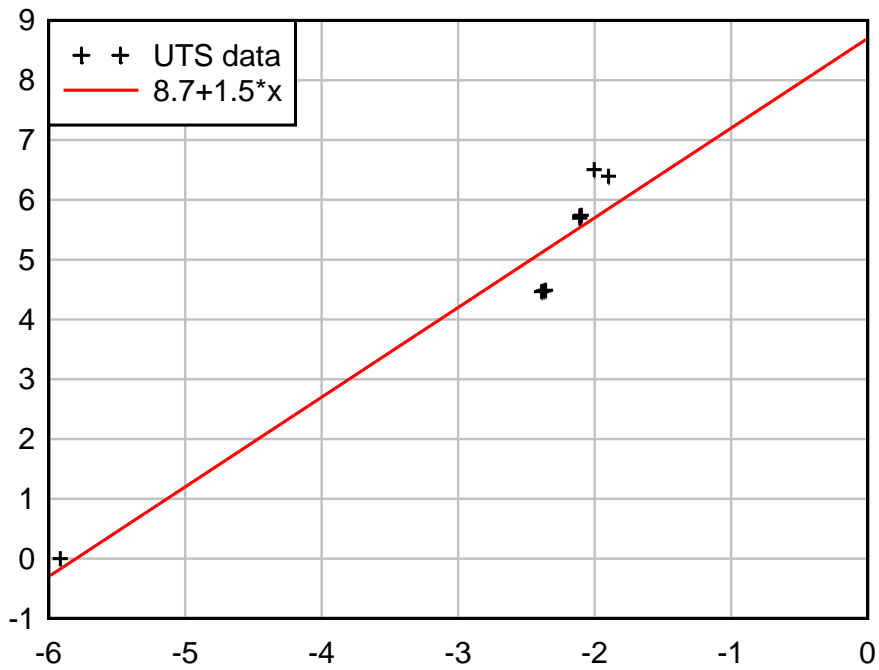


Figure 4.15: Curve fitting to obtain new Cowper-Symonds coefficients for the ultimate tensile strength for Grade 304 stainless steel.

Table 4.5: Proposed Cowper-Symonds coefficients for stainless steel Grade 304 used in this study.

	D	q
Yield stress	14000	3
Ultimate tensile strength	6000	1.5

4. 10 Conclusions

From the experimental results, several important observations are summarized below:

- (a) The yield stress of the 304 stainless steel increased as the strain rate increased. The ultimate tensile strength of the 304 stainless steel only slightly increased when the strain rate increased up to 600 s^{-1} .
- (b) The experimental results were compared to the theoretical prediction using the existing Cowper-Symonds coefficients. It showed that the experimental results were significantly lower than the existing theoretical prediction. This could be attributed to differences in the stress level, prior work hardening, heat treatment condition and microstructure of the stainless steel specimens used in this study. This implied that the Cowper Symonds' coefficients for Grade 304 stainless steel should be used with care to avoid overestimation of the yield stress and ultimate tensile strength in the design.
- (c) Using the experimental data, new Cowper-Symonds coefficients for solution annealed stainless steel 304 with fine grain size and 0.2% proof stress of about 550 MPa were derived for strain rates in the range of $0.002 - 600 \text{ s}^{-1}$ at room temperature. The coefficients were different for the yield stress and the ultimate tensile strength due to different strain rate sensitivity observed in the tests.
- (d) The total strain and uniform strain of stainless steel decreased as the strain rate increased. The lower ductility was attributed to adiabatic heating effects, which eliminated austenite to martensite transformation process in the stainless steel.
- (e) The maximum strain rate obtained in this study was about 600 s^{-1} . It is recommended to conduct further experimental investigation using the tensile split Hopkinson bar in order to study the strain rate effects at higher strain rates.

CHAPTER 5

STATIC TESTING OF AXIALLY RESTRAINED NON-COMPOSITE STEEL-CONCRETE-STEEL PANELS

The static behaviour of partially enclosed steel-concrete-steel (SCS) panels without shear connectors will be discussed in this chapter. Two flared ends were formed on each SCS panel to fit into specially design keyed connections, which could restrain the in-plane movement of the panel during testing. Firstly, a simply supported SCS panel was subjected to four-point bending to study the load-displacement response of the non-composite SCS panel. Then, static testing was carried out on axially restrained non-composite SCS panels to determine the flexural resistance and tensile membrane resistance. The effects of design parameters such as different types of infill material, degree of interaction between concrete and steel faceplates, and utilisation of stainless steel faceplates were studied as part of the experimental programme. The mechanical properties for steels and concrete used in the static tests were determined by conducting material properties tests in accordance with the relevant Australian Standards.

5.1 Concept of axially restrained non-composite SCS panels

Composite steel-concrete-steel (SCS) or double skin composite structures consist of a concrete core connected to two steel faceplates using mechanical shear connectors. Crawford and Lan (2006) presented the design concept of non-composite SCS panels without shear connectors in resisting blast loading and provided experimental verification for a full-scale blast wall. Remennikov et al. (2010 a,b) conducted an impact experimental study to evaluate the concept of axially restrained non-composite SCS sandwich panels and established that this form of construction has high energy absorption capability, and viable economic and technological characteristics. The non-composite SCS panels were restrained using specially

designed keyed connections to prevent in-plane movement of the panels when the loading was applied.

For non-composite SCS panels, the mass of the concrete core provides inertial resistance, which is important for resisting high-intensity impulsive loads. The imparted energy is dissipated by axial stretching of the steel faceplates and crushing of the concrete core. When the protective SCS panels are damaged, no hazardous projectiles are generated since the concrete core is confined by the steel faceplates. Additionally, the overall cost of construction is reduced by not providing shear connectors between the faceplates, thus simplifying their constructability and installation procedures.

5.2 Description of reduced scale SCS panels

Small-scale SCS panels were manufactured from 3 mm thick mild steel plates for static testing under increasing transverse loading. The top and bottom steel faceplates were bent into the required shape to produce flared ends and two end plates were then welded to the flared ends to produce a partially enclosed steel shell as shown in Figure 5.1. No shear connectors were provided in the panel, however two rows of small bracings (3 mm thick and 20 mm wide) were welded between the top and bottom faceplates to maintain the shape of the steel shell during concrete casting. The small bracings were positioned at mid-span, quarter-spans and near the flared ends. The thickness of the concrete core was 80 mm.

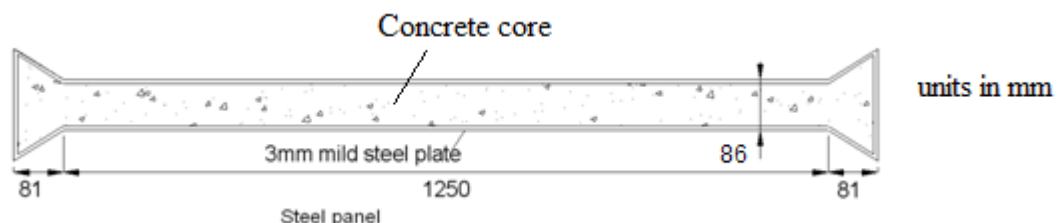


Figure 5.1: Geometry and dimension of the non-composite SCS panel used in this study.

Two mild steel shells were manufactured according to the geometry and dimension shown in Figure 5.1 and filled with normal weight concrete. Panel no. 1 was

subjected to static four-point bending under simple support condition. Panel no. 2 was subjected to static three-point bending under axial restraint support and was used as the control panel for the parametric study. To investigate effect of several design parameters, four mild steel and one stainless steel partially enclosed shells were prepared with their details summarised in Table 5.1. In panel no. 3, the mild steel shell was filled with lightweight concrete with a density of 1400 kg/m^3 . The mix design of the lightweight concrete will be described in the next section. Two layers of 4@ 50 mm wire mesh were inserted into the cavity of panel no. 4 before filling it with normal weight concrete. The distance from the steel shell to the wire meshes was 20 mm, as shown in Figure 5.2 (a). In panel no. 5, a layer of 3@25 mm wire mesh was tack-welded to the inner surface of the mild steel shell before casting of normal weight concrete, as shown in Figure 5.2 (b). For panel no. 6, two mild steel end caps of 3 mm thickness were welded to the mild steel shell to form a fully enclosed panel after concrete casting as shown in Figure 5.3. In the last panel, the stainless steel shell was filled with normal weight concrete.

The normal weight concrete used to prepare the SCS panels was ready-mix concrete ordered from the contractor (Western Suburbs Concrete) while the lightweight concrete was mixed in-situ. The concrete was poured into the steel shells and carefully vibrated to eliminate air voids in the concrete core. During concrete casting, standard concrete cylinders with a diameter of 100 mm and 200 mm height were prepared for the concrete compressive testing. Then, the panels and concrete cylinders were covered with wet gunny sacks to cure the concrete for 28 days.

Table 5.1: Details description for the SCS panels used in the static test.

No.	Panel	Parameters investigated	Description
1	Simply supported panel (SSP)	Simple support	<ul style="list-style-type: none"> • normal weight concrete core • mild steel faceplates
2	Control panel (CP)	Axial restraint	<ul style="list-style-type: none"> • normal weight concrete core • mild steel faceplates

3	Lightweight core panel (LP)	Infill material and axial restraint	<ul style="list-style-type: none"> • lightweight concrete core (1400 kg/m³) • mild steel faceplates
4	Reinforced core panel (RP)	Infill material and axial restraint	<ul style="list-style-type: none"> • normal weight concrete core reinforced with 2 layers of 4@50 mm wire mesh • mild steel faceplates
5	Improved bonding panel (IBP)	Interaction between steel and concrete, and axial restraint	<ul style="list-style-type: none"> • normal weight concrete core • a layer of 3@25 mm wire mesh tack welded to mild steel faceplates • mild steel faceplates
6	Fully enclosed panel (ECP)	Interaction between steel and concrete, and axial restraint	<ul style="list-style-type: none"> • normal weight concrete • two mild steel end caps of 3 mm thickness were welded to mild steel faceplates • mild steel faceplates
7	Stainless steel panel (SP)	Stainless steel and axial restraint	<ul style="list-style-type: none"> • normal weight concrete core • stainless steel faceplates

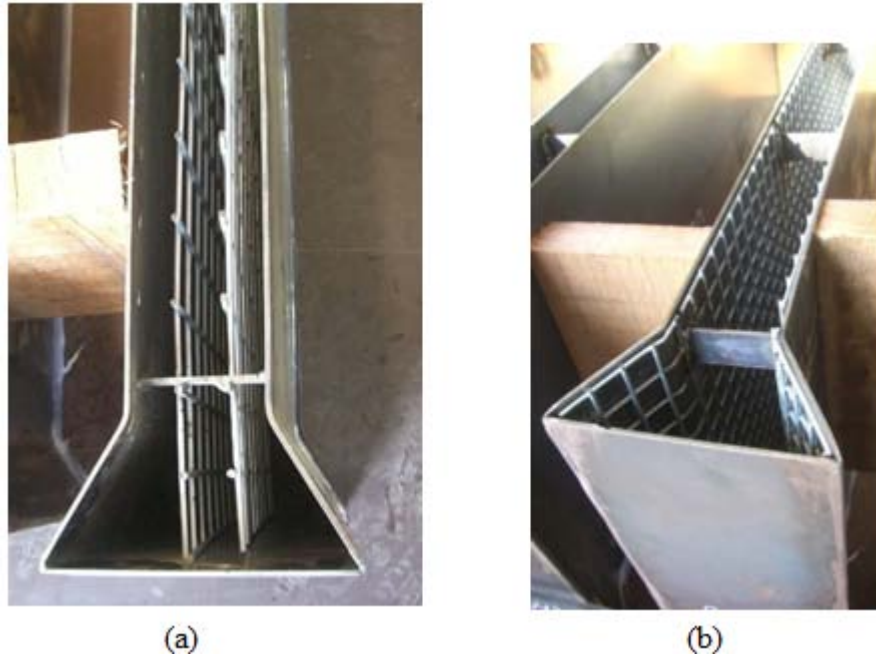


Figure 5.2: (a) two layers of 4@50 mm wire meshes inserted into the mild steel shell, (b) a layer of 3@25 mm wire mesh tack welded to the mild steel shell.



Figure 5.3: Welding of steel end cap to form a fully enclosed panel before testing.

5.2.1 Lightweight concrete preparation

Lightweight concrete with a density of 1400 kg/m^3 was produced based on the mix design specification for BST concrete. Polystyrene beads were used as aggregates and their coating generated about 12% of entrained air in the concrete to achieve

lightweight characteristic. The sample mix designs for BST concrete with various densities are shown in Table 5.2.

Table 5.2: Mix proportions for one cubic meter of BST concrete with various densities. (BST concrete information sheet number 3.2)

DENSITY (kg/m ³)	400	600	800	1,000	1,200	1,400	1,600	1,800	2,000
MIX PROPORTIONS									
Cement (kg) ⁽²⁾	250	350	350	350	450	450	450	450	500
10 mm Aggregate (kg) ⁽³⁾	-	-	-	-	-	-	550	700	800
Sand (kg) ⁽³⁾	40	120	320	540	640	850	520	580	620
BST Aggregate (litres) ⁽⁴⁾	1200	1100	975	900	800	700	600	450	300
Water (litres) ⁽⁵⁾	150	160	170	170	170	170	170	170	180
TYPICAL AVERAGE COMPRESSIVE STRENGTHS - MPa at 28 days									
Compressive strength (MPa)	0-0.5	1-2	3-4	6-8	8-10	12-14	14-18	22-25	25-30

A total of 0.12 m³ lightweight concrete was mixed in-situ with a targeted density of 1400 kg/m³. The average concrete compressive strength at 28 days according to BST specification is 12-14 MPa. The concrete was produced using General Portland (GP) cement, sand (50% fine and 50% coarse), BST#300 lightweight aggregate, BASF water reducing admixture and water. The quantity of materials used in the concrete mix is presented in Table 5.3. The proportion of the BASF 370C water reducing admixture is 300 millilitres to 100 kg of cementitious content. Therefore, 162 millilitres of BASF admixture was used for 54 kg of cement for this mix. The amount of water required according to BST mix design was 20.4 litres. During the mix, it was found that the concrete mix was too dry, so the total amount of water was increased to 28.7 litres to obtain a concrete slump of 80 mm. Figure 5.4 shows the BST aggregates (polystyrene beads) being poured into the concrete mixer to produce the lightweight concrete.

Table 5.3: Mix proportions for 0.12 m³ lightweight concrete.

Component	BST mix design specification
Cement (kg)	54
Sand (kg)	102
BST aggregate (litres)	84
Water (litres)	20.4 (28.72)*
BASF water reducing admixture (millilitres)	162

*the quantity of water was increased to achieve concrete slump of 80 mm



Figure 5.4: BST lightweight aggregates (polystyrene beads) being poured into concrete mix.

5.3 Experimental programme

5.3.1 Material testing

Material properties of different types of concrete infill were obtained from the unconfined concrete compressive test, while the material properties of steels were obtained through the tensile coupon test.

5.3.1.1 Unconfined concrete compressive tests

Three normal weight concrete cylinders and two lightweight concrete cylinders were tested on the days of panels testing to obtain the unconfined compressive strength of the concrete infill. A sulphur cap was casted on the top surface of each concrete cylinder to ensure the surface was flat prior to the testing. The compressive tests were carried out using the Instron Universal testing machine at a loading rate of 1 mm/min as shown in Figure 5.5.



Figure 5.5: Unconfined concrete compressive test using the Instron Universal testing machine for normal weight concrete at the University of Western Sydney.

5.3.1.2 Steel tensile coupon tests

Three mild steel and three stainless steel tensile coupons were prepared with the geometry and dimension illustrated in Figure 5.6, in accordance to AS 1391 (Standards Australia, 2007). The gauge length was 90 mm and the width was 20 mm. The tensile tests were carried out using Instron Universal testing machine at the University of Wollongong. The loading rate applied was 1 mm/min.

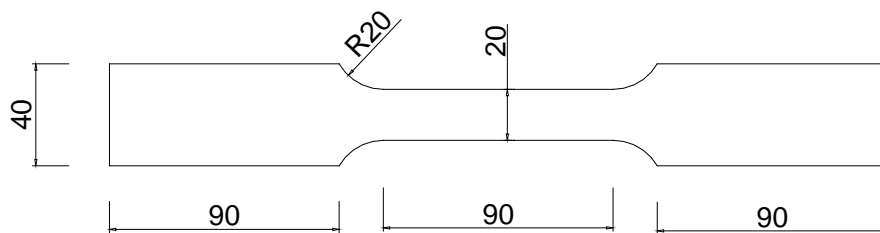


Figure 5.6: Geometry and dimension of a tensile coupon.

5.3.2 Push-out test

Two push out specimens were prepared to determine the bond strength between wire mesh and concrete core in the Improved bonding panel. A layer of 3@25 mm wire mesh was tack welded to a 10 mm thick steel plate at a spacing of 100 mm. The

width and the height of the steel plate were 200 mm and 300 mm, respectively. Concrete was filled into two steel plates to form a push out specimen as shown in Figure 5.7. The concrete compressive strength determined from the concrete cylinder testing was 31 MPa. The push-out tests were performed using the Instron Universal Testing Machine at the University of Wollongong. Two angle bracings were tied to the top and bottom of the specimens to avoid movement of the steel plates during testing, as shown in Figure 5.8. The nuts of the bracings were hand tied to avoid excessive pressure on the concrete infill. The load was applied through a 20 mm thick steel bar onto the concrete core and pushed it downward at a displacement rate of 1 mm/min. A layer of thin rubber was placed between the 20 mm bar and the concrete core so that the load was applied evenly on the concrete surface.

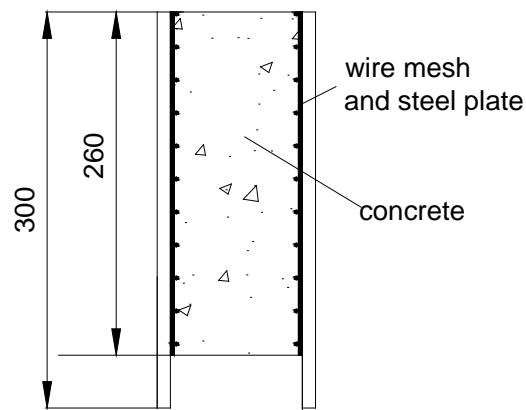


Figure 5.7: Geometry and dimension of a push out specimen.



Figure 5.8: Push out test set up.

5.3.3 Simply supported non-composite SCS panel under static four-point bending

A simply supported non-composite SCS panel was tested under four-point bending at the University of Wollongong to study the static behaviour of the panel without axial restraint. The panel was supported by a roller support and a knife-edge support placed on two concrete blocks as shown in Figure 5.9. The concrete blocks were tied to the strong floor using M25 high strength bolts. The load was applied by a 50 tonne hydraulic jack using the displacement control mode. Initial loading rate was set to 0.1mm/min until extensive cracks appeared in the concrete core. After that, the loading rate was increased to 0.5mm/min. The concrete surfaces of the panel were painted with lime water to increase the visibility of the cracks in the concrete core. The load from the hydraulic jack was applied onto a spreader beam, which distributed the load into two 100x100x5 mm stainless steel hollow sections. A roller support and a knife-edge support were used between the spreader beam and the stainless steel hollow sections. During the test, the applied load was recorded by a load cell attached to the hydraulic jack and the displacement was measured at bottom centre of the panel by a wire potential meter. A strain gauge was attached to the mid-span of the bottom steel plate to record the deformation of the bottom faceplate.



Figure 5.9: Experimental setup for a simply supported non-composite SCS panel under static four-point bending conducted at the University of Wollongong.

5.3.4 Static three-point bending test on axially restrained non-composite SCS panels

The non-composite SCS panels were connected to the axial restraint supports through the flared ends. The axial restraint supports consisted of key inserts, 310 UC sections, angle bracings and supporting I-beams, as shown in Figure 5.10. The key inserts used for creating a keyed connection were fabricated using the same mild steel plates as those used in the panels fabrication. The geometry and dimension of the key inserts are illustrated in Figure 5.11. Three clearance holes for the M16 high tensile bolts were prepared along the key inserts to fasten them to the UC sections. The cavity in the key insert was filled with 40 MPa concrete. The UC section used was 310UC96.8, and 16 mm thick steel gusset plates were welded to the UC sections to minimize their deformation during the test. The UC sections were bolted to supporting I-beams by using M25 high tensile bolts. Angle bracings were used to connect the web of UC sections to the supporting I-beams using M16 high tensile bolts.

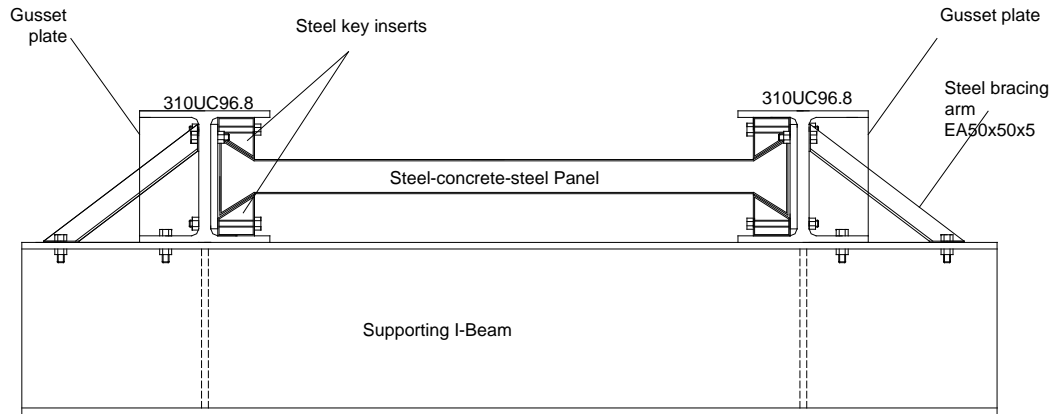


Figure 5.10: Axial restraint support components used in the experimental setup for static three-point bending test.

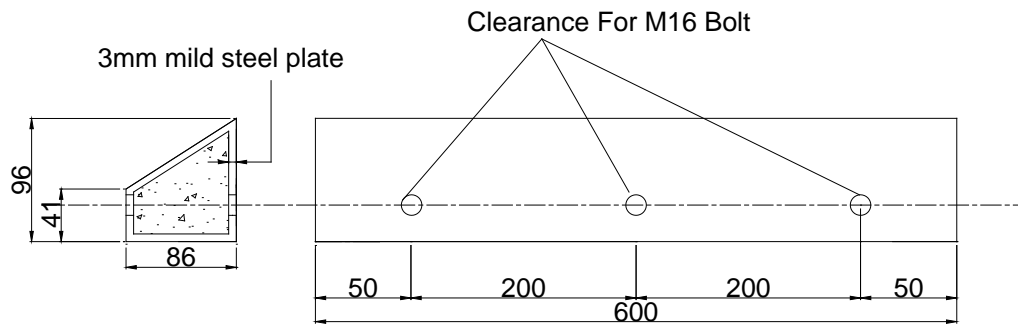


Figure 5.11: Geometry and dimension of a key insert.

Figure 5.12 shows the experimental set-up for axially restrained non-composite SCS panels under static three-point bending carried out at the University of Western Sydney. The load was applied by a 100 tonne hydraulic jack using displacement control mode. A spreader beam of 150 mm wide was positioned on the panels to spread the load across the width of the panels. A layer of thin rubber was placed between the spreader beam and the panels to eliminate movement of the beam during the test. The concrete surfaces of the panels were painted with lime water to increase the visibility of the cracks in the concrete core.

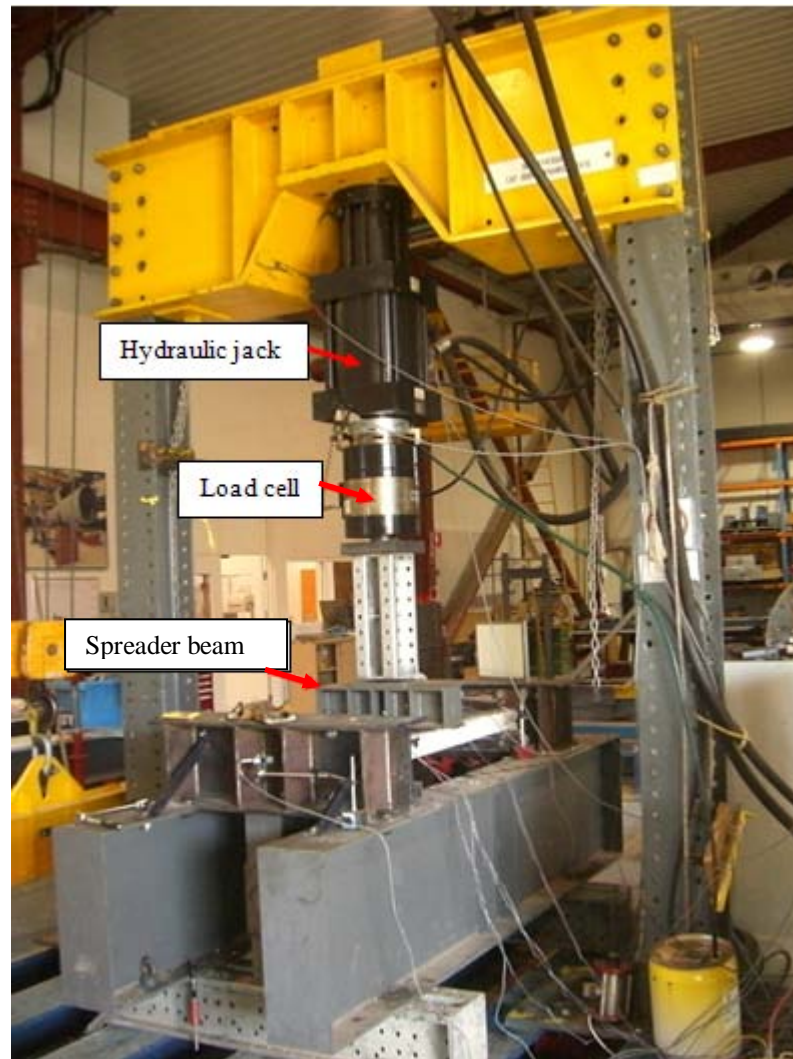


Figure 5.12: The experimental setup for static three-point bending test at the University of Western Sydney using the dynamic actuator test frame.

For each test, the applied load, panel displacements, deformation of steel faceplates and axial restraint support displacement were recorded. Mid-span displacement of the panel was measured using a laser displacement gauge. The displacement of the axial restraint supports, including the UC sections and the top key inserts, were measured using laser displacements gauges and their positions are shown in Figure 5.13. Figure 5.14 shows the laser displacement gauge used to measure the displacement. Deformations of the faceplates were measured using strain gauges. Two strain gauges were mounted on the top faceplate, which were located 150 mm from the mid-span on both sides. For the bottom faceplate, the strain gauges were attached at the centre and quarter-spans as shown in Figure 5.13. The initial loading

rate was 0.5 mm/min, up to the flexural capacity, and after that, the loading rate was increased to 1 mm/min.

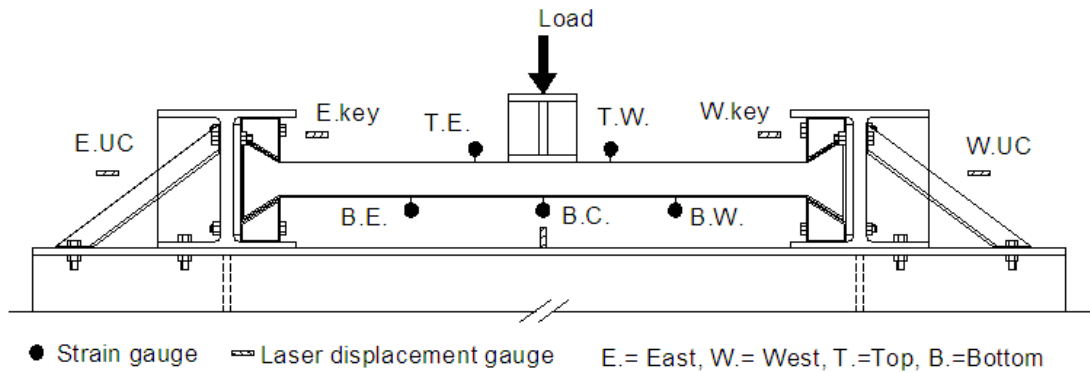


Figure 5.13: Instrumentation on axially restrained SCS panels under static three-point bending test.



Figure 5.14: The laser displacement gauge used to record the displacement.

5.4 Experimental results for material testing and push-out tests

The unconfined concrete compressive strength of concrete cylinders is presented in Table 5.4. It showed that the average unconfined compressive strength for normal weight concrete was 31 MPa and it was 13 MPa for the lightweight concrete. All the concrete cylinders showed shear failure as exemplified in Figure 5.15.

Table 5.4: Unconfined concrete compressive strength of normal weight concrete and lightweight concrete used in the static test.

Type of concrete	Specimen	Compressive strength (MPa)
Normal weight concrete	N1	32
	N2	29
	N3	31
	Average	31
Lightweight concrete	L1	14
	L2	12
	Average	13

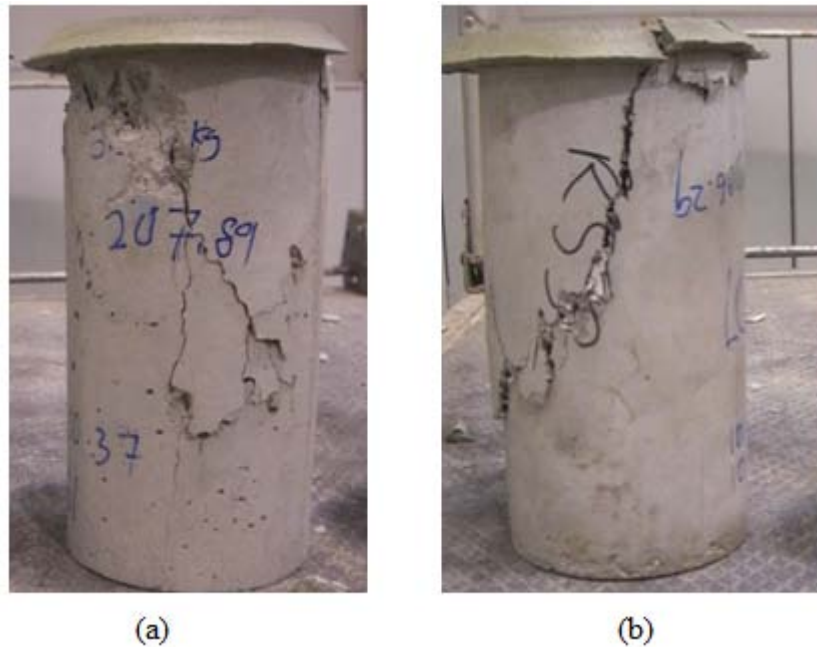


Figure 5.15: Shear failure of concrete cylinders under unconfined concrete compressive test (a) normal weight concrete, (b) lightweight concrete.

The engineering stress-strain curves for mild steel and stainless steel obtained from the tensile coupon tests are plotted in Figure 5.16 and Figure 5.17, respectively. The yield stress and the ultimate tensile strength for each specimen are presented in Table 5.5. The average yield stress and the average ultimate tensile strength for mild steel was 271 MPa and 332 MPa, respectively. The yield stress for the stainless steel was determined using 0.2% proof stress. The average yield stress for the stainless steel was 291 MPa. It showed significant strain hardening effect after yielding and the average ultimate tensile strength achieved was 579 MPa. For mild steel, the total

elongation was about 30% while the uniform elongation was about 20%. Stainless steel showed very high ductility, with the total elongation about 60% and the uniform elongation was about 50%. The tensile fracture of the mild steel and stainless steel coupons are illustrated in Figure 5.18.

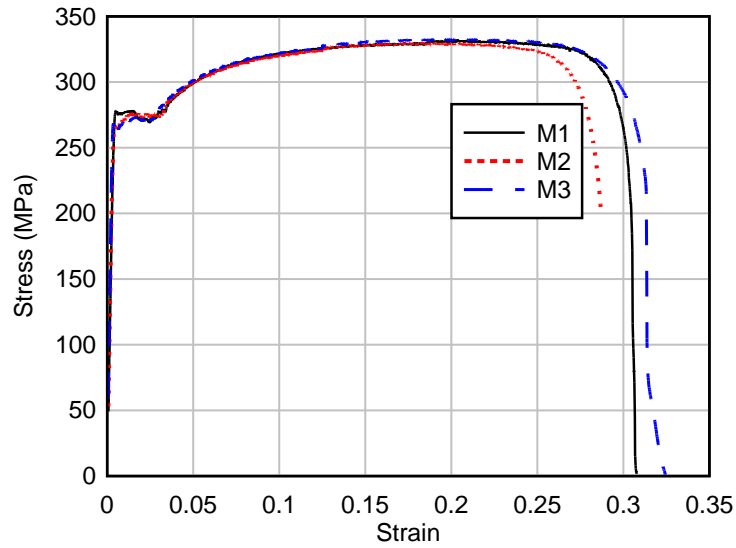


Figure 5.16: Engineering stress-strain curves for mild steel.

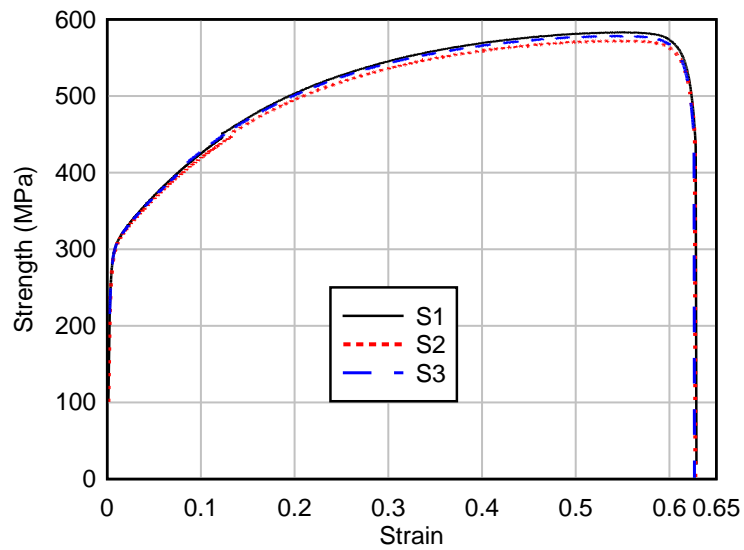


Figure 5.17: Engineering stress-strain curves for stainless steel.

Table 5.5: Yield stress and ultimate tensile strength for mild steel and stainless steel.

Type of steel	Specimen	Yield stress (MPa)	Ultimate tensile strength (MPa)
Mild steel	M1	277	333
	M2	267	330
	M3	268	333
	Average	271	332
Stainless steel	S1	293	584
	S2	287	573
	S3	292	579
	Average	291	579



Figure 5.18: Tensile fracture of mild steel and stainless steel coupons.

In this study, the shear resistance of the wire mesh tack welded to steel plates was obtained through the push-out tests. Figure 5.19 shows that the specimens reached an average maximum shear resistance of 93 kN at about 2.5 mm displacement. The resistance dropped significantly after the maximum shear resistance was reached, and the residual shear resistance was about 40 kN for displacements up to 20 mm. This showed that this type of shear connection was rather brittle where the shear resistance dropped and maintain at a constant residual level after reaching maximum shear resistance.

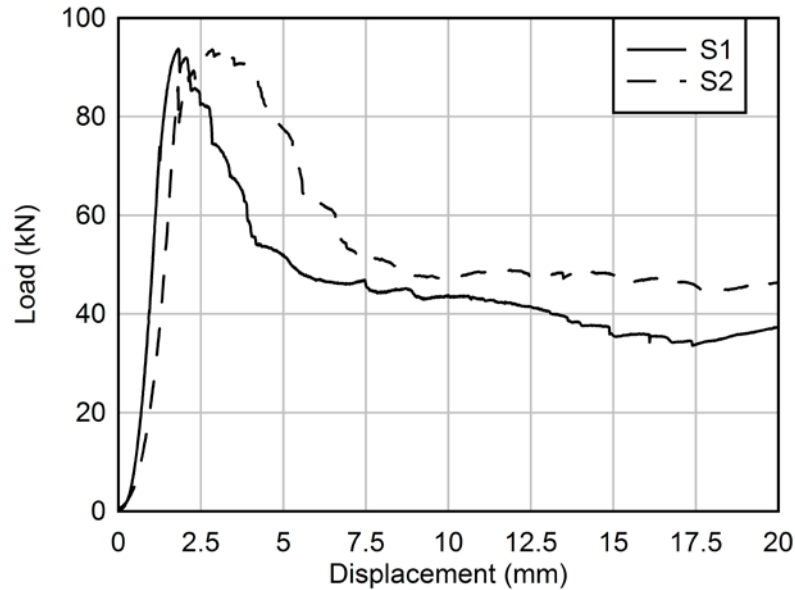


Figure 5.19: Load-displacement curves obtained from the push-out tests.

5.5 Test results of SCS panels

5.5.1 Simply supported non-composite SCS panel

Figure 5.20 shows the load-displacement relationship for a simply supported non-composite SCS panel subjected to static four-point bending. The end plates of the SCS panel provided lateral restraint for relative movement between the concrete core and steel faceplates. The chemical adhesion of concrete enabled shear transfer at the steel-concrete interfaces initially. After the chemical adhesion of concrete failed, the interface shear force was transferred by friction interaction between the elements and the lateral restraint provided by the end plates.

Flexural cracks appeared on the concrete core under the loading points when the total load reached about 50 kN. The flexural cracks formed at the supports when the load increased to about 60 kN, and the bottom steel faceplate at the flared ends was stretched and separated from the concrete core. This caused a slip between the concrete core and the bottom faceplate. The welded joints between the end plates and the bottom faceplate became highly stressed to resist the horizontal shear stress between the steel-concrete interface. When the shear stress exceeded the strength of the weld, the joint fractured. This welding fracture reduced lateral restraint on the relative movement of the concrete core and the steel faceplates. This failure was

classified as horizontal slip failure by Oduyemi and Wright (1989). The welding failure in one of the joints is shown in Figure 5.21 and it occurred at 86 kN with a corresponding deflection of 27 mm. After that, the total load resistance dropped significantly and the residual flexural resistance was about 40 kN. Figure 5.22 shows that the bottom faceplate was still elastic (maximum strain $820 \mu\epsilon$, $<$ yield strain of $1355 \mu\epsilon$) when the welding fractured.

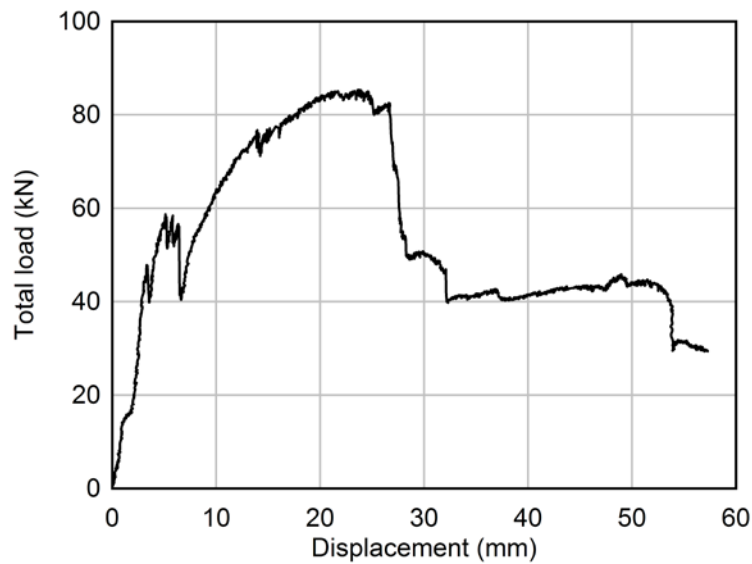


Figure 5.20: Load-displacement relationship for the simply supported non-composite SCS panel under static four-point bending test.



Figure 5.21: Welding fracture failure at the joint between the bottom faceplate and one of the end plates for the simply supported non-composite SCS panel under four-point bending test.

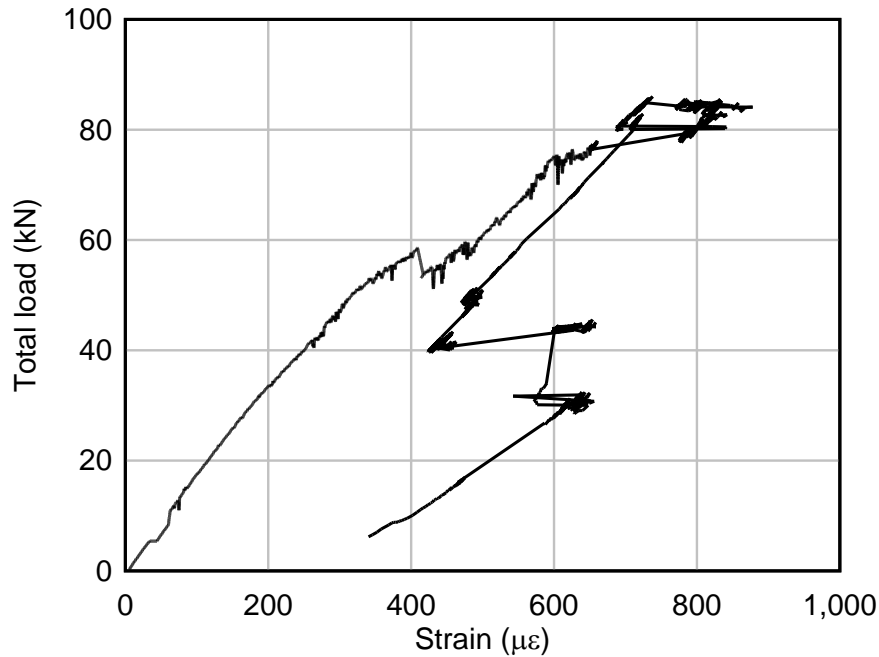


Figure 5.22: Total applied load versus centre deformation of the bottom faceplate of the simply supported non-composite SCS panel.

5.5.2 Control panel

The load-displacement relationship of the Control panel is shown in Figure 5.23. At the initial stage, the load was resisted by the flexural resistance of the panel, followed by the tensile membrane resistance of the steel faceplates at large displacement. It also showed that the tensile membrane resistance at large displacement (exceeded the thickness of the panel) was significantly higher than the flexural resistance. The test was terminated when the panel reached a mid-span displacement of about 170 mm, with the tensile membrane resistance of 380 kN. It should be noted that the steel faceplates did not fracture, and the load could still be increased as the displacement increased.

Flexural cracks started appearing on the concrete core at mid-span and the west support at 15 kN and these cracks significantly reduced the flexural stiffness of the panel. At 30 kN, the flexural crack at mid-span developed into a wide crack and a new crack was formed at the east support. The chemical adhesion of concrete failed, the top and bottom faceplates were stretched and separated from the concrete core adjacent to the keyed connections, as shown in Figure 5.24. The failure of chemical

bonding of concrete combined with the wide cracks at mid-span and supports caused excessive slip between the steel-concrete interface. The restraint provided by steel end plates inhibited horizontal slip failure and the friction resistance between the steel-concrete interface provided an interface shear transfer mechanism. The Control panel reached its maximum flexural load capacity at 58 kN and remained constant up to about 65 mm mid-span displacement.

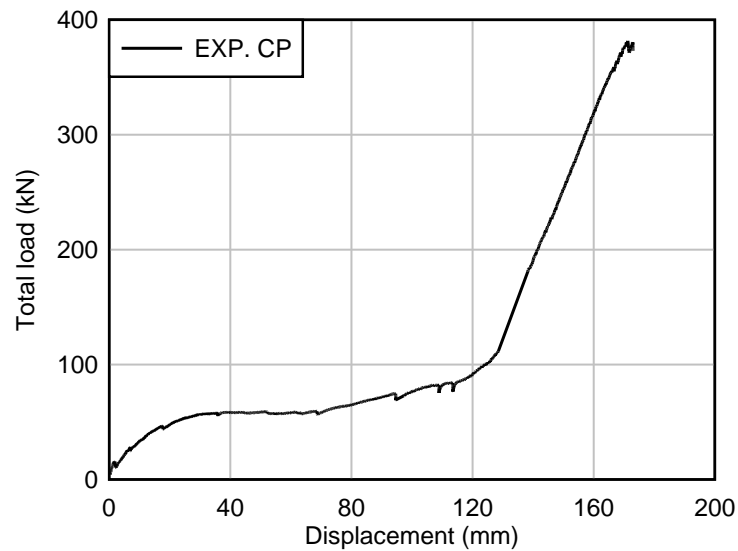


Figure 5.23: Load-displacement relationship for the Control panel (CP).



Figure 5.24: Separation of the bottom steel faceplate from the concrete core during the flexural response of the Control panel.

Figure 5.25 shows that the bottom faceplate had yielded (yield strain = $1355 \mu\epsilon$) at mid-span and the top faceplate was in compression when the Control panel reached

its maximum flexural load. This was classified as a flexural failure by Oduyemi and Wright (1989), where concrete crushing was preceded by steel yielding. As the applied load increased, it was observed that the compressive strain recorded by strain gauges on the top faceplate reduced and tensile strain began to develop. This strain transformation process showed that the tensile membrane force developed in the top faceplate at membrane resistance stage. Therefore, the load resisting mechanism had changed from flexural resistance of the SCS panel to membrane resistance of the steel faceplates. It showed that the strain on the bottom faceplate remained almost constant for loads between 50 kN to 270 kN. It also showed that the strain at 150 mm from the centre of the top plate and at the quarter-spans of the bottom faceplate were below the yield strain for the entire testing period.

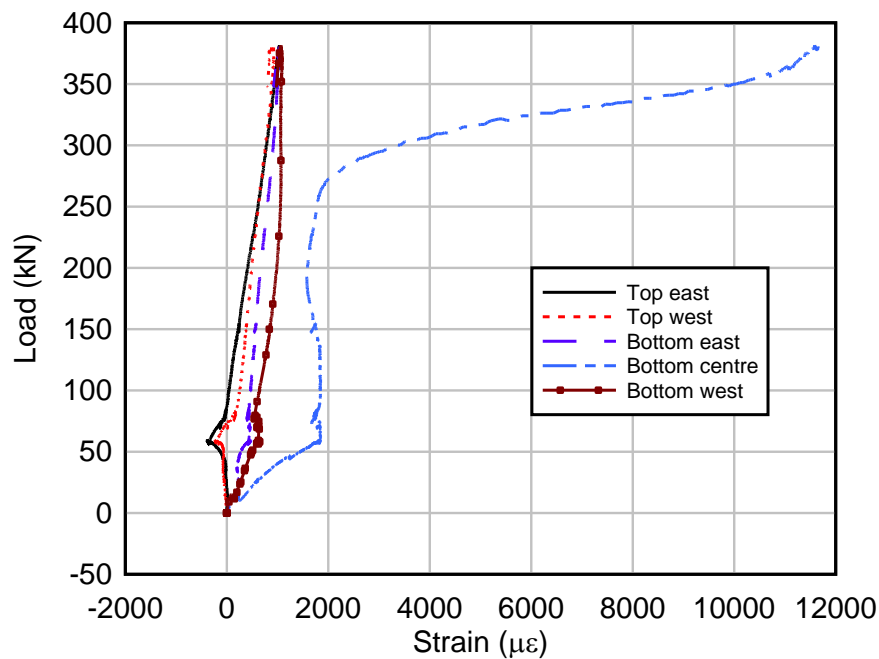


Figure 5.25: Applied load versus strain deformation of the steel faceplates at various locations of the Control panel.

The applied load versus in-plane displacement of the axial restraint supports are illustrated in Figure 5.26. The positive displacement of the east support and the negative displacement of the west support meant the supports were moving towards mid-span. It showed that the axial restraint supports started to move towards the mid-span after the panel reached its maximum flexural load of 58 kN, due to the development of in-plane membrane force in the steel faceplates. At initial stage of the support movement, the axial restraint supports (UC sections) moved with no

significant increased in the total applied load. This was due to the clearance holes in the bolt connections between the UC sections and the supporting I beams allowed the UC sections to slip. Once, the bolts started to bear against the UC sections and the supporting I beams, the movement of the UC sections were restrained and the applied load increased significantly. It was observed that the keyed inserts were pulled towards mid-span as the load increased. In addition, the top steel faceplate was pulled out from the keyed connections when the load increased as shown in Figure 5.27.

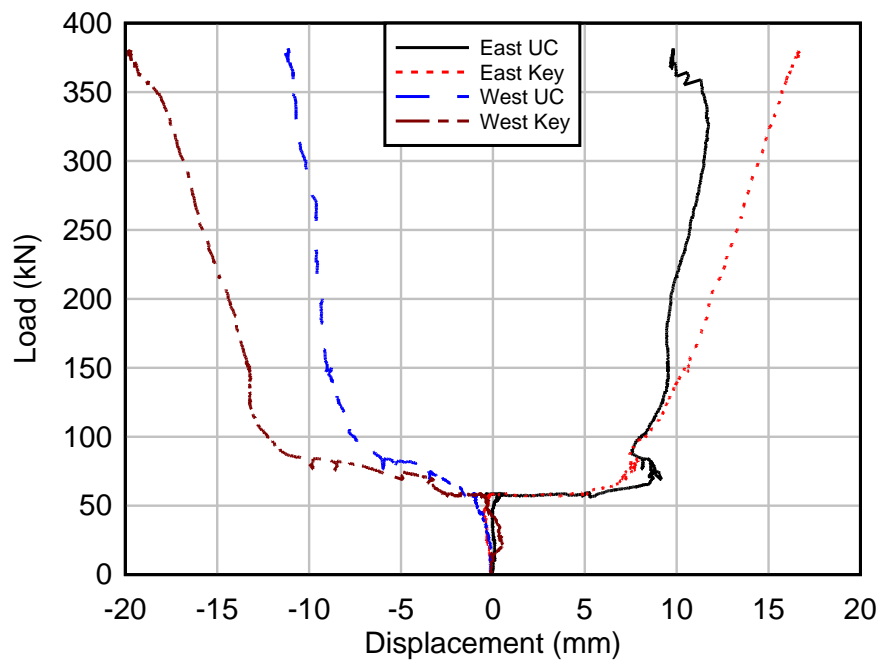


Figure 5.26: Applied load versus in-plane displacement of the axial restraint supports.



Figure 5.27: The flared end of the Control panel being pulled out from the keyed connection.

From the experimental results of the Control panel discussed above, it was confirmed that tensile membrane resistance had developed in the steel faceplates at large displacement. The load resistance provided by the tensile membrane action was significantly higher than the flexural resistance of the non-composite SCS panel. The stiffness of the axial restraint supports used in this test was very low due to clearance holes in the bolt connections and flexibility of the keyed connections such as movement of the key inserts and pulling out of panel from the keyed connections.

5.5.3 Lightweight core panel

The load-displacement curve for the Lightweight core panel which had a lightweight concrete core was compared to the response of the Control panel in Figure 5.28. The Lightweight core panel had a lower flexural load capacity and tensile membrane resistance at large displacement compared to the Control panel. Initial load-displacement response of the Lightweight core panel was similar to the Control panel such as, a wide crack at mid-span, separation of steel faceplates from the concrete core and excessive slip between these elements. At the maximum flexural load capacity of 32 kN, concrete core underneath the loading point started to crush due to low compressive strength of lightweight concrete. Figure 5.29 shows that the bottom steel faceplate was still elastic when the panel reached its maximum flexural load.

The top steel faceplate underwent a strain transformation process similar to the Control panel after the Lightweight core panel reached its maximum flexural load.

The axial supports were pulled towards the mid-span during the tensile membrane resistance stage similar to the Control panel. The stiffness of tensile membrane resistance of the Lightweight core panel was lower than the Control panel at large displacement. This was due to the crushing of concrete infill at the flared ends and buckling of the end plates (Figure 5.30), causing the panel to be pulled out more significant than the Control panel. At 170 mm mid-span displacement, the load resistance dropped slightly before it increased again with a lower stiffness of membrane resistance. At 265 kN with corresponding displacement of 193 mm, the test was terminated and the top faceplate was being pulled out about 30 mm from the keyed connections. The results from the Lightweight core panel showed that the infill material not only affected the flexural resistance of the non-composite SCS panel, it also influenced the development of the tensile membrane action in the steel faceplates by affecting the stiffness of flared ends of the panel under static loading condition.

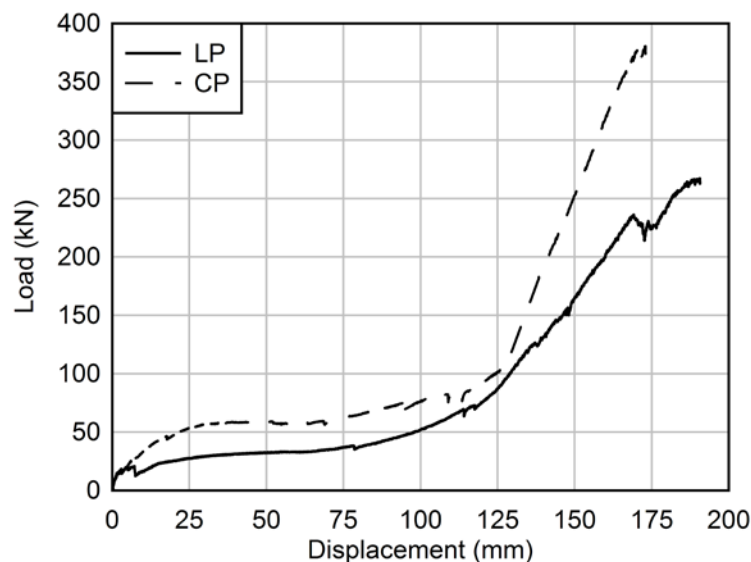


Figure 5.28: Load-displacement curve of the Lightweight core panel (LP) compared to the load-displacement relationship of the Control panel (CP).

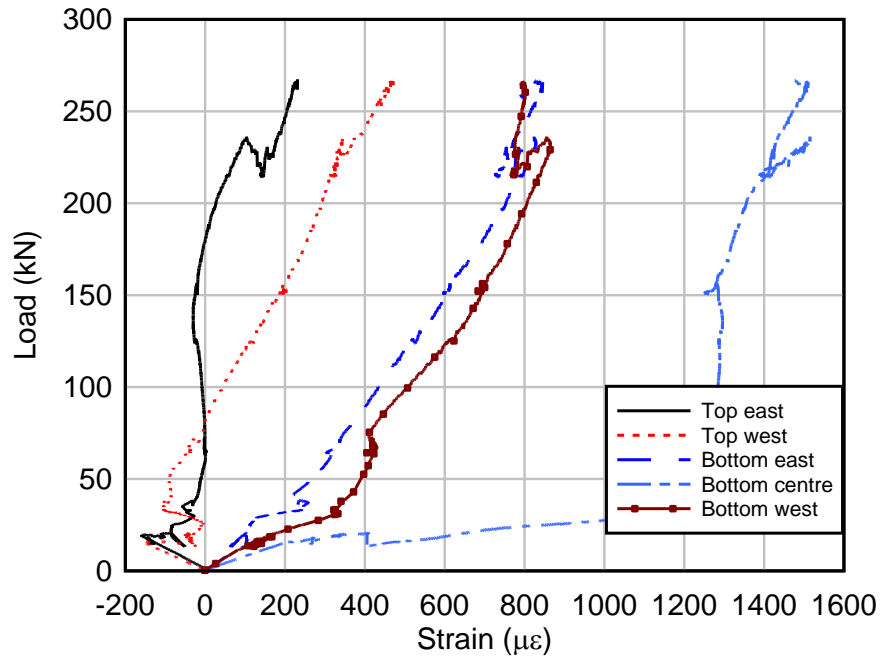


Figure 5.29: Applied load versus strain deformation curves of steel faceplates at various locations of the Lightweight core panel.



Figure 5.30: Crushing of lightweight concrete and buckling of steel end plate for the Lightweight core panel.

5.5.4 Reinforced core panel

The load-displacement curve of the Reinforced core panel was compared to the load-displacement curve of the Control panel in Figure 5.31. The normal weight concrete core was reinforced with two layers of 4@50 mm wire mesh. The Reinforced core panel showed a slightly higher flexural load capacity, but the tensile membrane resistance was significantly lower compared to the Control panel at the same displacement. With the reinforced concrete core, the cracking load was slightly increased to 20 kN and the flexural stiffness after cracking was slightly higher than the Control panel. The cracks in the concrete core were distributed along the span, and the width of the cracks was smaller compared to the Control panel due to the effects of reinforcements. The bottom faceplate was separated from concrete core and there was an excessive slip between the steel faceplates and the concrete.

The Reinforced core panel reached its maximum flexural load capacity at 65 kN, which was slightly higher than the Control panel of 58 kN. The bottom faceplate started to yield at the mid-span as shown in Figure 5.32. After that, the flexural resistance dropped gradually due to one of the welded joints between the end plates and the bottom faceplate started to fail. This was proven by the strain reading at the mid-span of the bottom faceplate, which started to drop after 65kN. Once the central displacement reached 70 mm, the welded joint fractured and the resistance dropped significantly. Figure 5.33 shows the welding fracture at the joint between the bottom faceplate and one of the end plates of the Reinforced core panel.

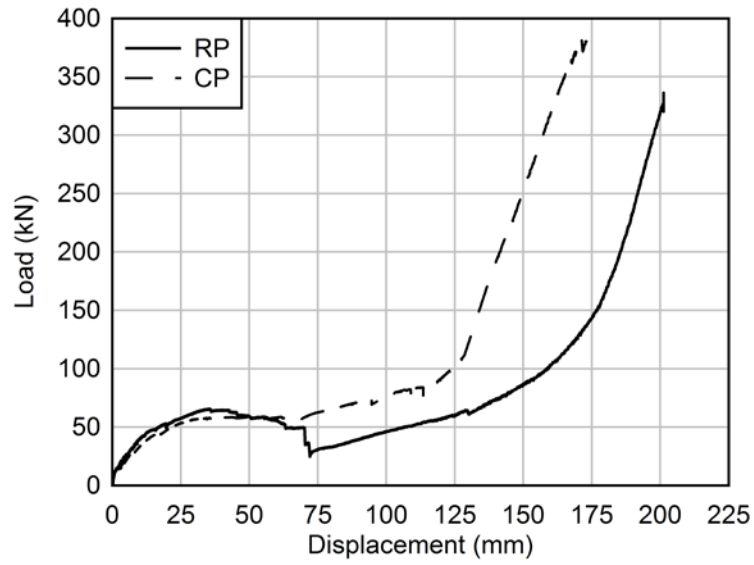


Figure 5.31: Load-displacement curve of the Reinforced core panel (RP) compared to the load-displacement relationship of the Control panel (CP).

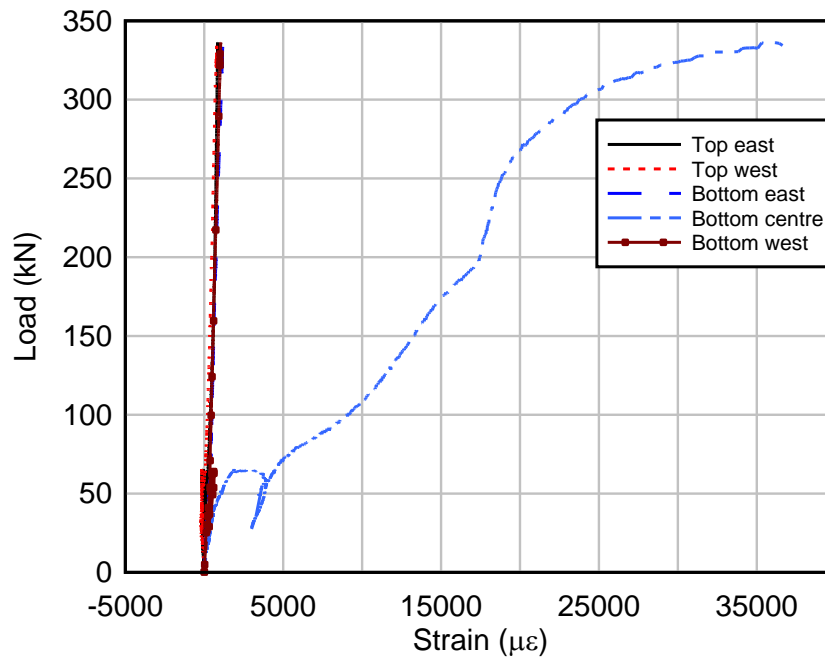


Figure 5.32: Applied load versus strain deformation curves of steel faceplates at various locations of the Reinforced core panel.



Figure 5.33: Welding fracture failure at the joint between the bottom faceplate and the end plate of the Reinforced core panel.

After the welded joint fractured, the load continued to rise as the displacement increased, implying that the tensile membrane resistance of the steel faceplates still existed. The axial restraint supports were pulled towards the mid-span of the panel similar to the results of the Control panel. Based on the strain records in Figure 5.32, the top faceplate of the Reinforced core panel underwent a strain transformation process similar to the Control panel. The strain at mid-span of the bottom faceplate increased with the increased applied load after the initial drop due to the fracture of welded joint. This showed that the bottom faceplate still contributed to the tensile membrane resistance of this panel. The friction between the bottom faceplate and the key inserts induced axial restraint to allow the development of tensile membrane force in the bottom faceplate, but at a lower axial restraint stiffness compared to the Control panel without weld fracture. This caused a lower tensile membrane resistance of the Reinforced core panel compared to the Control panel at the same displacement.

The test was terminated at the applied load of 321 kN corresponding to the mid-span displacement of 200 mm. The bottom faceplate was pulled out excessively from the keyed connection where the weld joint fractured. From the results of the Reinforced core panel, it showed that the flexural resistance of the non-composite SCS panel

increased slightly with the reinforced concrete core compared to the panel with the plain concrete core. However, the weld fracture failure at the joint between the bottom faceplate and the end plate caused the membrane resistance of the Reinforced core panel was significantly lower compared to the Control panel at the same displacement.

5.5.5 Improved bonding panel

The load-displacement curve of the Improved bonding panel was compared to the response of the Control panel in Figure 5.34. In the Improved bonding panel, a layer of 3@25 mm wire mesh was tack welded inside the steel shell at a spacing of 100 mm before casting it with concrete to improve interaction between the concrete and steel faceplates. The Improved bonding panel showed a higher flexural load capacity, but the tensile membrane resistance was significantly lower compared to the Control panel at the same displacement. The cracking load of the Improved bonding panel was increased to 25 kN compared to the Control panel of 15 kN. At 53 kN, the flexural resistance slightly dropped due to the failure of tack welding between the wire mesh and the bottom faceplate between the east support and the loading point. The bottom faceplate was separated from the concrete core with the wire mesh embedded in it near the east support.

The panel reached the flexural load capacity of 72 kN where the concrete started to crush under the loading point and the bottom faceplate started to yield at the mid-span as shown in Figure 5.35. At the tensile membrane resistance stage, the axial restraint supports were pulled towards the mid-span and the top faceplate of the Improved bonding panel underwent a strain transformation process, as discussed in the Control panel. At the mid-span displacement of 92 mm, it was observed that the load resistance started to drop due to the fracture of welded joint similar to the Reinforced core panel. After the welded joint fractured, the Improved bonding panel showed a lower tensile membrane resistance compared to the Control panel at the same displacement as discussed in the Reinforced core panel above. At the load of 330 kN with the corresponding displacement of 198 mm, the test was terminated due to excessive pull-out of the bottom faceplate from the keyed connection.

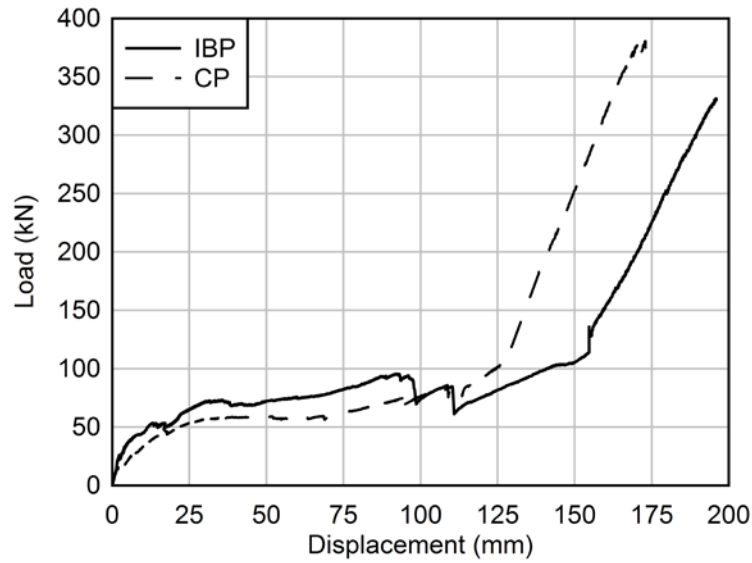


Figure 5.34: Load-displacement curve of the Improved bonding panel (IBP) compared to the load-displacement relationship of the Control panel (CP).

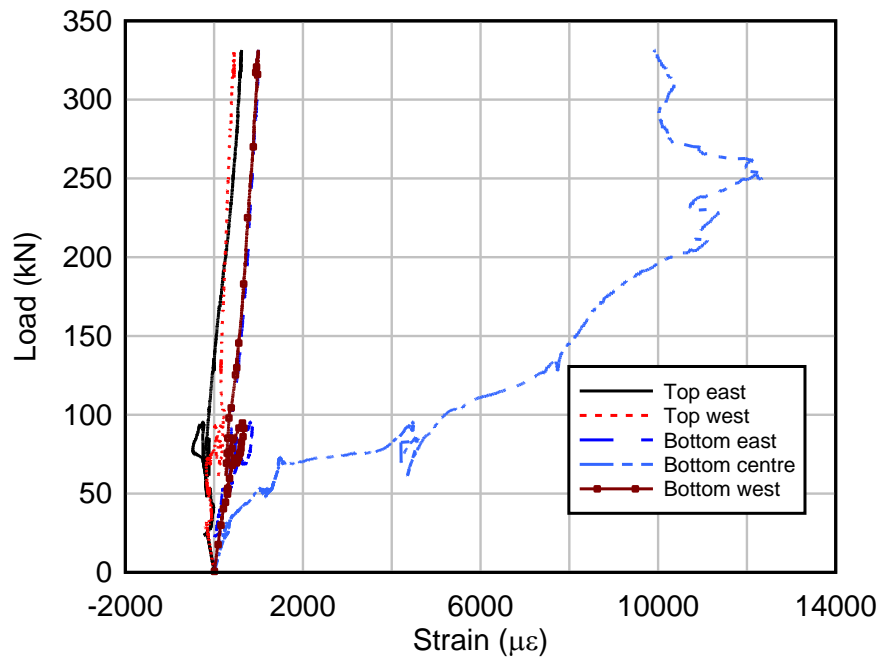


Figure 5.35: Applied load versus strain deformation curves of the steel faceplates at various locations of the Improved bonding panel.

5.5.6 Fully enclosed panel

Load-displacement curve of the Fully enclosed panel was compared to the response of the Control panel in Figure 5.36. The panel was fully enclosed by welding two

mild steel end plates of 3 mm thickness after concrete casting. It showed that the flexural load capacity was significantly increased compared to the Control panel. Initial tensile membrane resistance of the Fully enclosed panel was higher, but for displacements between 160 mm to 170 mm, the tensile membrane resistance was lower than the Control panel. The Fully enclosed panel showed a linear load-displacement relationship up to about 135 kN. Then, the bottom faceplate started to yield at mid-span as shown in Figure 5.37 and the flexural stiffness of the Fully enclosed panel reduced significantly. The strain gauges mounted on the top faceplate initially recorded compressive strain then tensile strain during the flexural response due to the buckling of top faceplate as shown in Figure 5.38 (a). The Fully enclosed panel reached its maximum flexural capacity at about 180 kN.

After that, the welding between one of the end caps and the steel faceplates started to fail. It started between the end cap and the top faceplate at the loading point, before moving towards the supports. The length of welding fracture increased with the increased loading. At about 290 kN, welding between the end cap and the bottom faceplate started to fracture. The end cap was fractured at mid-span as shown in Figure 5.38 (b). Figure 5.37 shows that the bottom faceplates yielded at mid-span and quarter-spans, while the strain gauge at the west quarter-span of the bottom faceplate failed at 294 kN. The strain gauges at the top faceplate showed that the top faceplate yielded near the loading point due to buckling. The test was terminated at 470 kN, corresponding to 209 mm displacement, and the panel was being pulled out about 25 mm from the keyed connection.

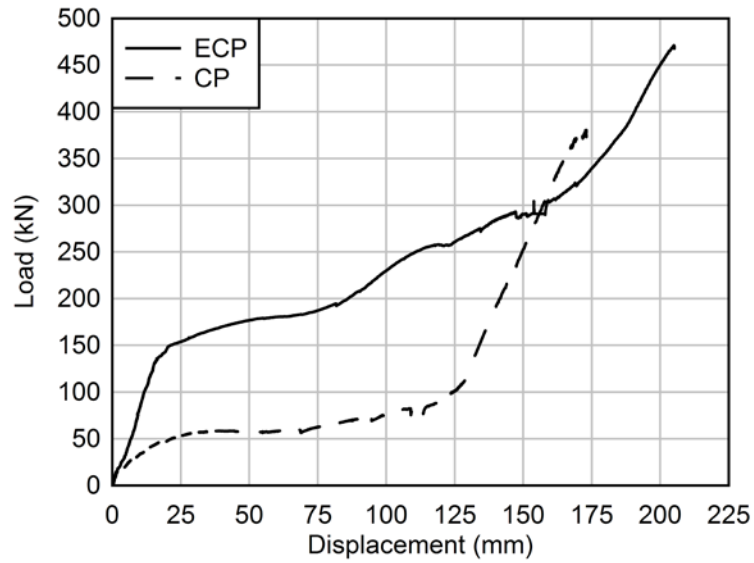


Figure 5.36: Load-displacement curve of the Fully enclosed panel (ECP) compared to the load-displacement relationship of the Control panel (CP).

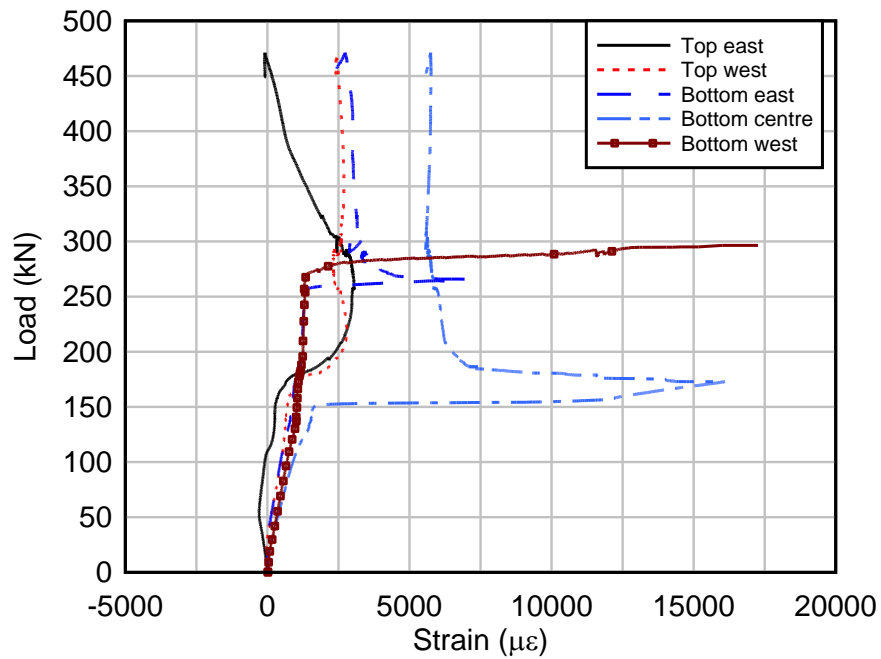


Figure 5.37: Applied load versus strain deformation curves of the steel faceplates at various positions of the Fully enclosed panel.

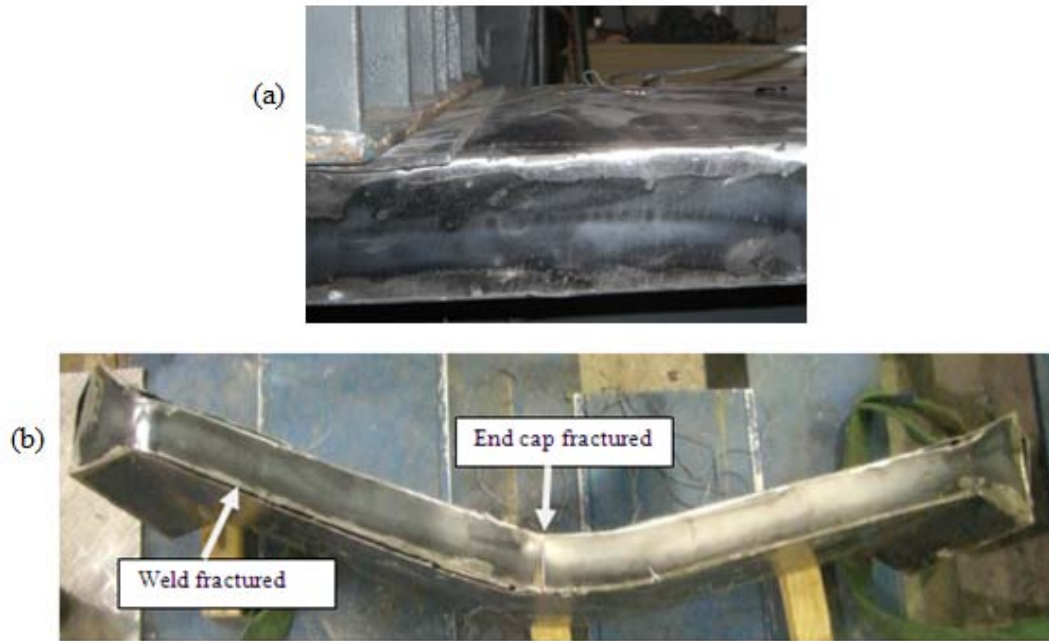


Figure 5.38: Deformation observed in the Fully enclosed panel, (a) buckling of top faceplate adjacent to the loading point, (b) fracture of the end cap and failure of weld between the end cap and steel faceplates.

5.5.7 Stainless steel panel

The load-displacement curve of the Stainless steel panel, which had 3 mm-thick stainless steel faceplates was compared to the response of the Control panel in Figure 5.39. The Stainless steel panel showed a higher flexural strength while the tensile membrane resistance at large displacement was similar to the Control panel. Initial load-displacement response of this panel was similar to the Control panel, such as the cracking load (15 kN), a wide crack at mid-span, separation of steel faceplates from concrete core and excessive slip between these elements. The maximum flexural capacity for this panel was 76 kN and the strain records in Figure 5.40 showed that the bottom faceplate had yielded at mid-span. The flexural strength of the Stainless steel panel was higher than the Control panel (58 kN) due to the effect of strain hardening of stainless steel after proof stress was reached as shown in Figure 5.17.

The test results showed that the initial tensile membrane resistance of the Stainless steel panel was higher than the Control panel, but due to unknown reasons, the resistance dropped slightly at 125 mm central displacement. After that, the tensile

membrane resistance of the Stainless steel panel was slightly lower than the Control panel at the same displacement. Figure 5.40 shows that the bottom faceplate had yielded at quarter-spans during the tensile membrane resistance. This was different from the Control panel where the bottom faceplate had yielded only at mid-span. The yielding of the quarter-spans of the bottom faceplate seemed to have no significant effects on the response of the tensile membrane resistance of the Stainless steel panel. The top faceplate underwent a strain transformation process and the axial restraint supports were pulled towards the mid-span as discussed in the Control panel. The test was terminated at 437 kN, corresponding to 185 mm mid-span displacement, and the top faceplate was being pulled out about 30 mm from the keyed connections.

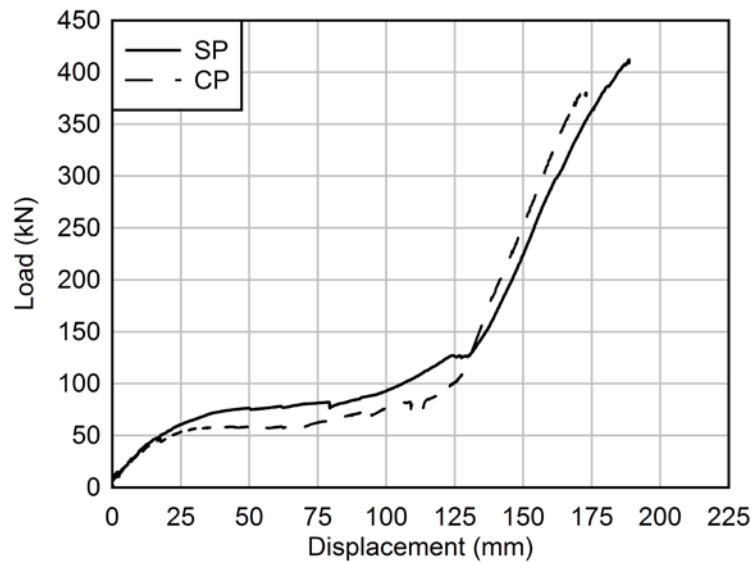


Figure 5.39: Load-displacement curve of the Stainless steel panel (SP) compared to the load-displacement relationship of the Control panel (CP).

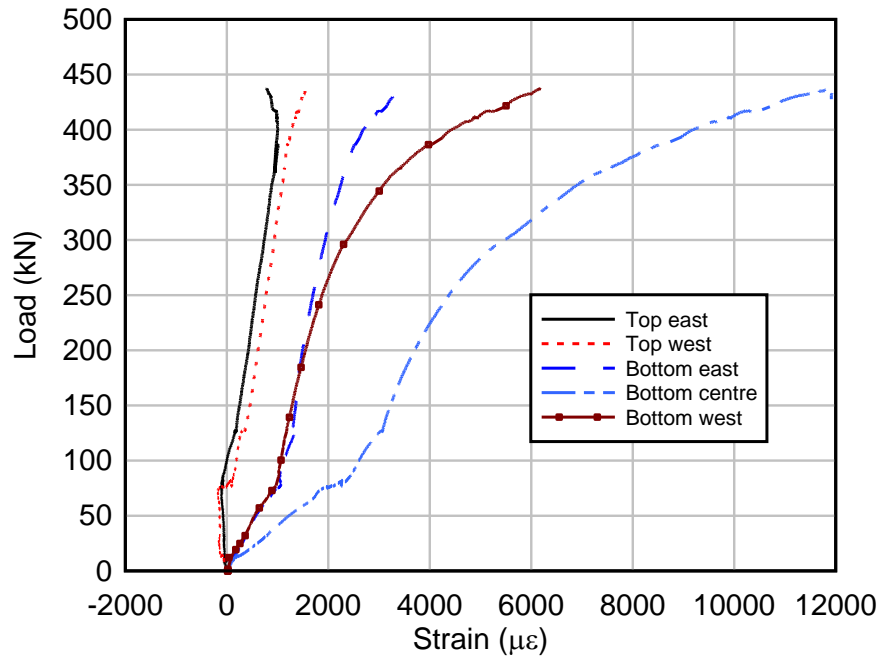


Figure 5.40: Applied load versus strain deformation curves of steel faceplates at various locations of the Stainless steel panel.

5.5.8 Summary and discussion on panel results

The experimental results for the simply supported non-composite SCS panel and axially restrained SCS panels under static loading conditions are summarized in Table 5.6. The flexural strength of the SCS panels tested under parameters study was compared to the flexural strength of the Control panel. The failure modes observed during the flexural response, the tensile membrane resistance and mid-span displacement when the tests terminated were recorded.

Table 5.6: Summary of experimental results of non-composite SCS panel under static loading conditions.

Panel	Flexural strength (kN)	Flexural load/Flexural load of Control panel	Membrane resistance (kN) /mid-span displacement (mm)	Support rotation (°)	Failure mode for flexural response
Simply supported panel (SSP)**	86	N.A.	-	2.4	Horizontal slip failure
Control panel (CP)	58	1	381/173	15.7	Flexural failure
Reinforced core panel (RP)	65	1.12	322/201	17.8	Flexural failure
Lightweight core panel (LP)	32	0.55	267/190	17.2	Concrete crushing
Improved bonding panel (IBP)	72	1.24	330/195	17.6	Horizontal slip failure
Fully enclosed panel (ECP)	180	3.10	469/205	18.5	Buckling of top steel faceplate
Stainless steel panel (SP)	76	1.31	410/188	18.0	Flexural failure

** Panel was tested under four-point bending.

Based on the comparison between the results of simply supported panel and the axially restrained panels, it was revealed that the simply supported non-composite

SCS panel could not develop tensile membrane resistance, and it resisted the load by flexural resistance. The simply supported non-composite SCS panel failed when the welded joint between the end plate and bottom faceplate fractured due to large shear demands, and the maximum support rotation was 2.4° . With the axial restraint, the SCS panels initially showed flexural resistance and tensile membrane resistance at large displacement. For axially restrained non-composite SCS panels, the tensile membrane resistance at large displacement was significantly higher than the flexural resistance. The axially restrained SCS panels were able to undergo more than 18° support rotation without fracture of steel faceplates.

The effect of lightweight concrete infill was evaluated by comparing experimental results of the Control panel and the Lightweight core panel (Table 5.6). It showed that the use of concrete core with a low compressive strength (lightweight concrete) had significant effect on the flexural resistance and tensile membrane resistance of the axially restrained non-composite SCS panel at large displacement under static loading condition. A non-composite SCS panel filled with concrete of low concrete compressive strength showed low flexural strength where the flexural load capacity was reached when the concrete started to crush before the bottom faceplate started to yield. Furthermore, the crushing of concrete at the flared ends caused the panel to be pulled out from the keyed connections. This phenomenon reduced the stiffness of the axial restraint on the panel, which caused a lower tensile membrane resistance compared to the non-composite SCS panel filled with normal weight concrete at the same displacement.

Comparison of experimental results between the Control panel and Reinforced core panel in Table 5.6 showed that a reinforced concrete core could increase slightly the flexural load capacity of the non-composite SCS panel due to additional flexural capacity from the reinforcement. It was expected that the tensile membrane resistance would be increased slightly due to the contribution of membrane force in reinforcement at large deflection compared to the panel with plain concrete core. However, this effect could not be observed in the test due to the failure of welded joint between the end plate and the bottom faceplate. The fracture of welded joint

caused a lower axial restraint on the steel faceplates. Therefore, the tensile membrane resistance was lower than the Control panel at the same displacement.

The effects of increased degree of interaction between steel faceplates and concrete core were studied from the experimental results of the Improved bonding panel and the Control panel. With the improved bonding between the steel faceplates and concrete core, the flexural strength was increased by 24% (Table 5.6). Full composite action between the steel faceplates and the concrete core could not be achieved in this case due to the fracture of tack welding between the steel faceplates and wire meshes. It was expected that the tensile membrane resistance of the Improved bonding panel would be increased slightly due to the contribution of membrane force in the wire mesh at large deflection compared to the Control panel. However, this effect could not be evaluated in the test due to the failure of welded joint between the end plate and the bottom faceplate.

Two end cover plates were welded between the top and bottom steel faceplates of the Fully enclosed panel to achieve composite action. The end caps provided a mechanism to transfer the horizontal shear stress between the top and bottom steel faceplates. In this case, concrete core prevented inward buckling of steel faceplates and the concrete strength was increased due to confinement effect of the steel shell. The test results showed that the flexural strength of the Fully enclosed panel was increased by almost 3 times compared to the Control panel (Table 5.6). The top faceplate buckled and the welding fracture between the end cap and faceplates caused the resistance to drop at large deflection. The tensile membrane resistance of the Fully enclosed panel was more complicated than the Control panel due to the buckling of the top faceplate, and fracture of the weld connection between the end cap and the steel faceplates.

Application of stainless steel faceplate to replace mild steel faceplate will increase the flexural strength of non-composite SCS panels due to the strain hardening effect of stainless steel, as shown in the experimental results of the Stainless steel panel (Table 5.6). Non-composite SCS panels with stainless steel faceplates should show a higher tensile membrane resistance at the same mid-span displacement compared to

the panel with mild steel faceplates as a result of the strain hardening effects. High ductility of stainless steel (up to 60% total elongation) will allow the SCS panels to undergo a larger deformation before the steel plate fractures compared to mild steel panel. In the test, the Stainless steel panel initially showed a higher tensile membrane resistance, but due to unknown reasons, the resistance dropped slightly and became slightly lower than the Control panel at the same displacement.

Table 5.6 summarised various flexural failure modes for the SCS panels under static loading conditions. Based on the experimental observations, failure modes during flexural resistance are classified into:

- (a) Flexural failure: concrete crushing is preceded by the yielding of the bottom steel faceplate,
- (b) Horizontal slip failure: the welded joint between the end plate and bottom faceplate fractured due to horizontal shear stress between steel-concrete interfaces,
- (c) Concrete crushing: due to the low concrete compressive strength, the concrete started to crush beneath the loading point before the yielding of the bottom steel faceplate,
- (d) Buckling: Top steel faceplate buckled adjacent to the loading point.

For the tensile membrane resistance of axially restrained SCS panels, tests were terminated before the steel faceplates fractured. A few possible failure modes during the tensile membrane resistance are pull-out of SCS panel from keyed connections, damage of keyed connections and fracture of the steel faceplate.

5.6 Conclusions

In this chapter, a comprehensive experimental programme was conducted on non-composite steel-concrete-steel (SCS) panels subjected to quasi-static loading under simply supported and axially restrained supports conditions, followed by a parametric study. The experimental results demonstrated that utilising the axial restraint supports would significantly enhance the load resistance and ductility of the non-composite SCS panels. Based on the observations made in this study, the following conclusions can be drawn:

- (a) The simply supported partially enclosed steel-concrete-steel (SCS) panel failed due to the horizontal slip failure when a welded joint between the end plate and the bottom faceplate fractured. The simply supported non-composite SCS panel resisted the applied load by flexural response. With the axial restraint, the SCS panels were able to develop tensile membrane resistance at large displacement, even though various failure modes had been observed during flexural response. The tensile membrane resistance was significantly higher than the flexural capacity of the non-composite SCS panels and the panels had very high ductility.
- (b) The most effective method to increase the flexural strength of a SCS panel was by increasing the degree of interaction between the steel faceplates and the concrete core, especially by welding two end caps to both steel faceplates to form a fully enclosed panel. The use of stainless steel faceplates in non-composite SCS panels would increase the flexural strength of the panels due to the strain hardening effect of stainless steel. The use of reinforcement in the concrete core increased flexural strength slightly, while a low compressive strength of the infill material would reduce the flexural strength significantly.
- (c) The stiffness of axial restraint had a significant effect on the development of tensile membrane resistance in the SCS panels. The stiffness of axial restraint was influenced by the stiffness of the axial restraint support and the stiffness of the panel at the flared ends. From the static test results, it was observed that the overall stiffness of axial restraint on the panels was low due to the clearance holes used in the bolt connection and pull-out of panels from the keyed connections. Lower axial restraint caused the tensile membrane resistance of the SCS panels to develop at larger mid-span displacement.

CHAPTER 6

DEVELOPMENT OF STATIC RESISTANCE FUNCTION FOR NON-COMPOSITE SCS PANELS

In this chapter, the static test results of axially restrained SCS panels were compared to the theoretical predictions. The flexural load capacity of the SCS panels was predicted using various analytical methods due to different types of interaction between the concrete and steel faceplates in the panels. The tensile membrane resistance of the axially restrained SCS panels was compared to the analytical solution derived by Hodge Jr. (1974) which considered the effect of the axial restraints stiffness. Based on the comparison between theoretical analyses and experimental results, the static resistance function for axially restrained non-composite SCS panels was proposed. The resistance function was required for the development of simplified modelling of SCS panels based on the single degree of freedom (SDOF) modelling methodology.

6.1 Flexural response of SCS panels

6.1.1 Flexural load capacity of SCS panels with natural interaction

Jeong (2008) investigated the behaviour of steel-concrete composite slab with natural interaction, where no shear connectors were used to connect the steel and concrete elements. The interface shear force was transferred by the chemical bonding of concrete and the friction resistance between these elements. The study was carried out using three dimensional finite element analyses. The slabs with various shear span ratios were analysed and the flexural load capacity of the slab with natural interaction was presented as a ratio of the ultimate flexural load of the cross section with full composite action. The results showed that the flexural load capacity of the slabs with natural interaction under a low shear span ratio was significantly lower than the flexural load capacity of the panel with full interaction. When the shear span ratio increased, the flexural load capacity of the slab with natural interaction

increased, and it approached to the flexural load capacity of the slab with full interaction as shown in Figure 6.1.

The non-composite SCS panels used in this study had several important characteristics similar to the steel-concrete composite slab with natural interaction investigated by Jeong (2008), including (i) no shear connectors were used to connect the steel and concrete elements, and (ii) the interface shear force was transferred by the chemical bonding of concrete and the friction resistance between the steel and concrete. Therefore, the strength ratio presented by Jeong (2009) was used to compare the flexural load capacity of the non-composite SCS panels obtained from the static test. The non-composite SCS panels tested in the static tests were the Control panel, Lightweight core panel, Reinforced core panel and Stainless steel panel.

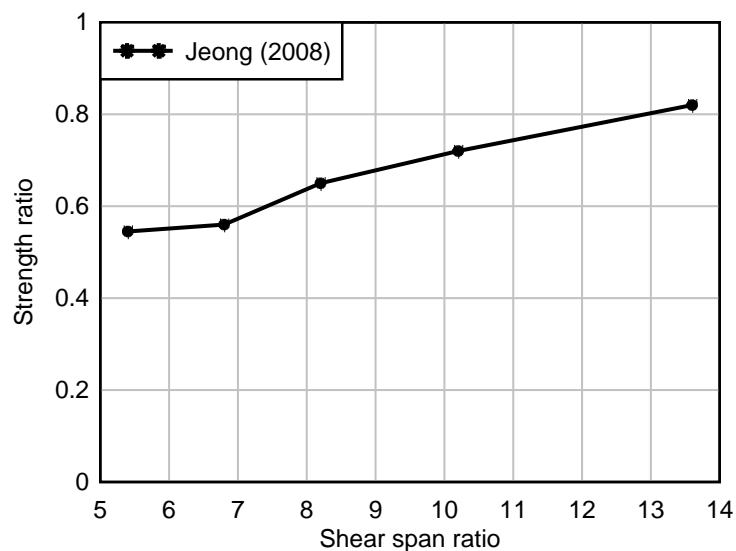


Figure 6.1: Strength ratio versus shear span ratio for the steel concrete composite slab under natural interaction. (Jeong, 2008)

The shear span ratio (ρ_s) is defined as the ratio of the shear span length to the effective depth of a cross section. The shear span is the distance from the support to the loading point, while the effective depth is the distance from the top of the panel to the centroid of the bottom faceplate as shown in Figure 6.2.

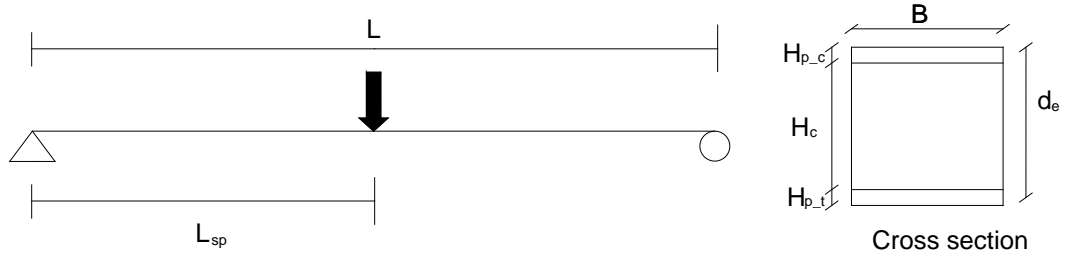


Figure 6.2: Definition of the shear span and effective depth of the panel cross section.

The shear span ratio for the SCS panels used in this study is,

$$\rho_s = L_{sp} / d_e = 625 / 84.5 = 7.4 \quad (6.1)$$

From Figure 6.1, the strength ratio, α_{nat} is 0.6. The flexural load capacity for non-composite SCS panels (with natural interaction) is,

$$P_{o_nat} = \alpha_{nat} P_o \quad (6.2)$$

where P_o is the ultimate flexural capacity of the cross section with full composite action.

6.1.1.1 Flexural load capacity of non-composite SCS panels (with natural interaction): non-reinforced concrete core

According to Liew and Soheli (2009), after the fully composite SCS panel with equal faceplates thickness reaches its flexural yield load, the tensile cracks in the concrete core causes the neutral axis to move towards the compression steel faceplate. The ultimate moment capacity of the cross section is reached when the neutral axis moves close to the bottom surface of the compression steel faceplate. Both steel faceplates will be fully yielded and the bottom steel faceplate will have a very large strain compared to the top steel faceplate. The ultimate moment capacity can be determined from the force couple of the steel faceplates and the contribution of the concrete can be ignored as shown in Figure 6.3.

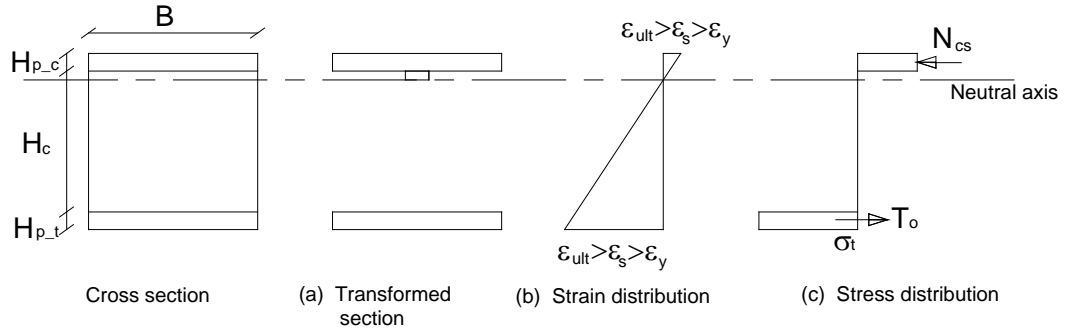


Figure 6.3: Cross section analysis for fully composite SCS panels with a non-reinforced concrete core at the ultimate moment capacity.

The theoretical ultimate moment capacity for the fully composite SCS panels:

$$M_o = \sigma_y B H_p (H_c + H_p) \quad (6.3)$$

where σ_y is the yield stress of the steel plate, B is the width of the plate, H_p is the thickness of the plate and H_c is the thickness of the concrete core. For the panels with mild steel faceplates, such as the Control panel and the Lightweight core panel, the ultimate moment capacity, assuming full composite action, is determined by using a yield stress of 271 MPa.

$$M_o = 271 \times 500 \times 3 \times (80+3)/10^6 = 33.7 \text{ kN.m} \quad (6.4)$$

These panels were analysed as simply supported since the concrete cracking and separation of the steel faceplates from the concrete core near the flared zones occurred before the flexural load capacity was reached in these panels. Therefore, low or no moment resistance developed at the supports when the panels reached their flexural load capacity. The theoretical ultimate flexural capacity for a simply supported SCS panel with full composite action under a mid-span point load is,

$$P_o = 4M_o/L = 4 \times 33.7/1.25 = 107.8 \text{ kN} \quad (6.5)$$

The theoretical flexural load capacity for the Control panel and Lightweight core panel (under natural interaction) is determined using Eq.(6.2):

$$P_{o_nat} = \alpha_{nat} P_o = 0.6 \times 107.8 = 64.7 \text{ kN} \quad (6.6)$$

For the panel with stainless steel faceplates, the theoretical ultimate flexural load capacity was determined using 0.2% proof stress of stainless steel (291 MPa) ignoring the strain hardening effect. Therefore, we get the following values of the

ultimate moment capacity and the ultimate flexural load capacity for the panel with full composite action:

$$M_o = 291 \times 500 \times 3 \times (80+3)/10^6 = 36.2 \text{ kN.m}$$

$$P_o = 4M_o/L = 4 \times 36.2/1.25 = 115.8 \text{ kN} \quad (6.7)$$

The theoretical flexural load capacity for the Stainless steel panel (under natural interaction) is,

$$P_{o_nat} = \alpha_{nat} P_o = 0.6 \times 115.8 = 69.5 \text{ kN} \quad (6.8)$$

6.1.1.2 Flexural load capacity of non-composite SCS panels (with natural interaction): reinforced concrete core

For the fully composite SCS panel with a reinforced concrete core, it is assumed that the neutral axis is located at the centre of the top layer of wire mesh when the panel reaches its ultimate moment capacity, as shown in Figure 6.4. The top steel faceplate, the bottom steel faceplate and the bottom layer of the wire mesh are yielded. Based the force equilibrium equation, the tensile force of the bottom steel faceplate (T_{o_plate}) is balanced by the compressive force of the top steel faceplate. The tensile force of the bottom layer of wire mesh (T_{o_wire}) is balanced by the concrete compressive force (N_{cc}). The concrete compressive force (N_{cc}) is assumed to be acting at the centre of the concrete depth ($d/2$). Therefore, the ultimate moment capacity for the fully composite SCS panel with a reinforced concrete core is given by:

$$M_{o_rein} = \sigma_y B H_p (H_c + H_p) + T_{o_wire} (H_c - 2d) + N_{cc} d/2 \quad (6.9)$$

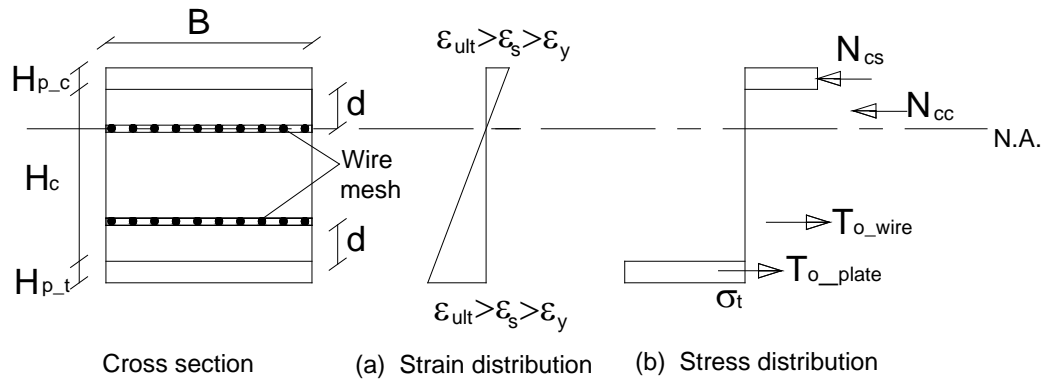


Figure 6.4: Cross section analysis for fully composite SCS panels with a reinforced concrete core at the ultimate moment capacity.

For the wire mesh, the yield stress was assumed as 500 MPa and the distance between the steel faceplate to the centre of the wire mesh was 20 mm. There were 10 strands of wire across the width of the panel. Therefore, the ultimate moment capacity and the ultimate flexural strength of the Reinforced core panel assuming full composite action are,

$$M_{o_rein} = 271 \times 500 \times 3 \times 83 + 10 \times 500 \times 2^2 \times 3 \times 3.142 \times (40+10) = 36.9 \text{ kNm}$$

$$P_o = 4M_o/L = 4 \times 36.9/1.25 = 118 \text{ kN} \quad (6.10)$$

The theoretical flexural load capacity for the Reinforced core panel (under natural interaction) is,

$$P_{o_nat} = \alpha_{nat} P_o = 0.6 \times 118 = 70.8 \text{ kN} \quad (6.11)$$

6.1.1.3 Flexural stiffness of non-composite SCS panels (with natural interaction)

The non-composite SCS panels used in this study showed three different stages of flexural stiffness during the flexural resistance, namely (1) flexural stiffness of the composite section, (2) flexural stiffness of the non-composite section, and (3) flexural stiffness of non-composite section with a cracked concrete core. Initially, the SCS panel acted as a composite section because of the chemical bonding of the concrete, and the neutral axis was located at the centre of the panel.

From the unconfined concrete compressive tests, the average compressive strength of concrete used in the static test was 31 MPa. The Young's modulus of concrete was determined in accordance to AS 3600 (Standards Australia, 2009), assuming the density of concrete as 2400 kg/m³.

$$E_c = \rho^{1.5} \times 0.043 \times f_{cm}^{0.5} = 2400^{1.5} \times 0.043 \times 31^{0.5} = 28 \text{ GPa} \quad (6.12)$$

The second moment of area for the SCS panel with composite action is,

$$\begin{aligned} I_{composite} &= \frac{2BH_p^3}{12} + 2BH_p d^2 + \frac{E_c}{E_s} \frac{BH_c^3}{12} \\ &= \frac{2 \times 500 \times 3^3}{12} + 2 \times 500 \times 3 \times 41.5^2 + \frac{28}{200} \frac{500 \times 80^3}{12} \\ &= 8.16 \times 10^6 \text{ mm}^4 \end{aligned} \quad (6.13)$$

After the chemical bonding of the concrete failed, the second moment of area of the SCS panel could be determined by the sum of the second moment of area of individual steel faceplate and concrete core. Assuming the chemical bonding of concrete failed before the flexural crack started to develop in the concrete core, the second moment of area for the non-composite SCS panel is,

$$\begin{aligned} I_{non\ composite} &= \frac{2BH_p^3}{12} + \frac{E_c}{E_s} \frac{BH_c^3}{12} \\ &= \frac{2 \times 500 \times 3^3}{12} + \frac{28}{200} \frac{500 \times 80^3}{12} \\ &= 2.99 \times 10^6 \text{ mm}^4 \end{aligned} \quad (6.14)$$

At the ultimate flexural capacity of the non-composite SCS panel, the flexural cracks propagated towards the top steel faceplate and the neutral axis was located near to the bottom surface of the top steel faceplate. The second moment of area of the panel could be determined by ignoring the concrete core,

$$\begin{aligned} I_{fully\ cracked} &= \frac{2BH_p^3}{12} \\ &= \frac{2 \times 500 \times 3^3}{12} \\ &= 2250 \text{ mm}^4 \end{aligned} \quad (6.15)$$

The flexural stiffness for a simply supported SCS panel subjected to a point load at the mid-span is given by:

$$K = \frac{48E_s I}{L^3} \quad (6.16)$$

The flexural stiffness of the panel under three different stages is given as:

$$\begin{aligned} K_{composite} &= \frac{48E_s I_{composite}}{L^3} = \frac{48 \times 200 \times 8.16 \times 10^9}{1250^3} = 40.1 \text{ kN/mm} \\ K_{non\ composite} &= \frac{48E_s I_{non\ composite}}{L^3} = \frac{48 \times 200 \times 2.99 \times 10^9}{1250^3} = 14.7 \text{ kN/mm} \\ K_{fully\ cracked} &= \frac{48E_s I_{fully\ cracked}}{L^3} = \frac{48 \times 200 \times 10^3 \times 2250}{1250^3} = 0.011 \text{ kN/mm} \end{aligned} \quad (6.17)$$

6.1.1.4 Comparison between experimental and theoretical flexural load capacity of non-composite SCS panels (with natural interaction)

The theoretical flexural stiffness based on the non-composite section corresponded well with the initial load-displacement relationship of the non-composite SCS panels before the flexural cracks developed in the concrete core, as shown in Figure 6.5 to Figure 6.8. The experimental results showed that the flexural stiffness of the non-composite SCS panels reduced significantly after cracking initiated in the concrete core. In this study, 25 % of the flexural stiffness of the non-composite section was used as the effective flexural stiffness for these panels, as shown in Figure 6.5 to Figure 6.8.

The theoretical flexural load capacity determined from the analysis of the cross section with full composite action and non-composite section (natural interaction) were compared to the experimental results of the Control panel, Lightweight core panel, Stainless steel panel and Reinforce core panel in Figure 6.5 to Figure 6.8. The experimental flexural load capacity of these panels was significantly lower than the theoretical ultimate flexural capacity of the SCS panel with a full composite action. The simplified approach by Jeong (2008) predicted the flexural load capacity of the Control panel, Reinforced core panel and Stainless steel panel with a reasonable accuracy, while it overestimated the flexural load capacity of the Lightweight core

panel. This was because the Lightweight core panel reached its flexural load capacity when the lightweight concrete core crushed in compression prior to the bottom steel faceplate yielding. For the other panels, the bottom steel faceplate yielded prior to the panels reaching their flexural load capacity, which conformed to the observation by Jeong (2008). Using the predictive relationships in Jeong (2008), the theoretical analysis overestimated the experimental flexural load capacity of the Control panel and the Reinforced core panel by 12.5% and 7.5%, respectively. The analytical analysis underestimated the flexural load capacity of the Stainless steel panel by 9.1%.

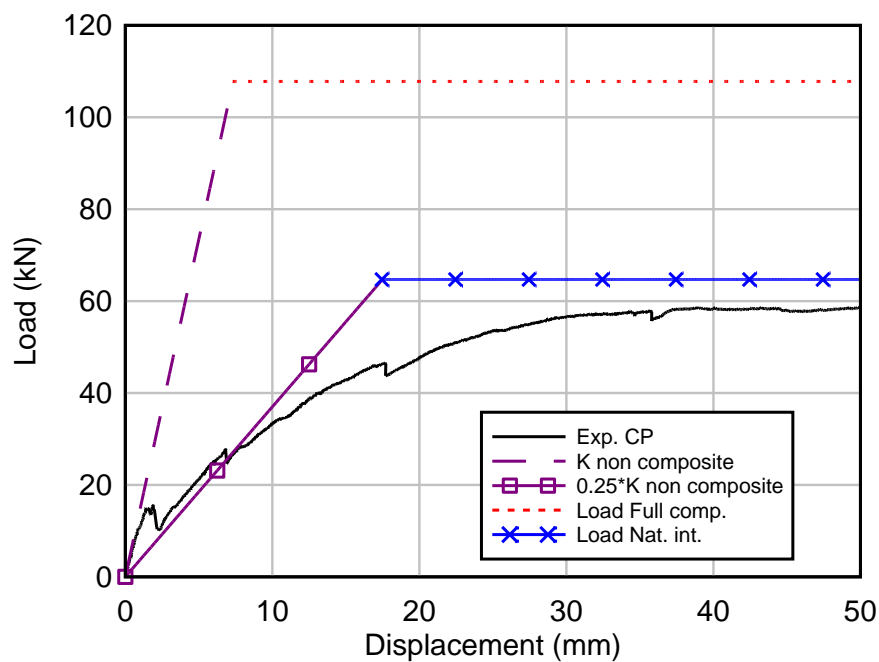


Figure 6.5: Comparison between predicted and experimental flexural response of the Control panel (CP).

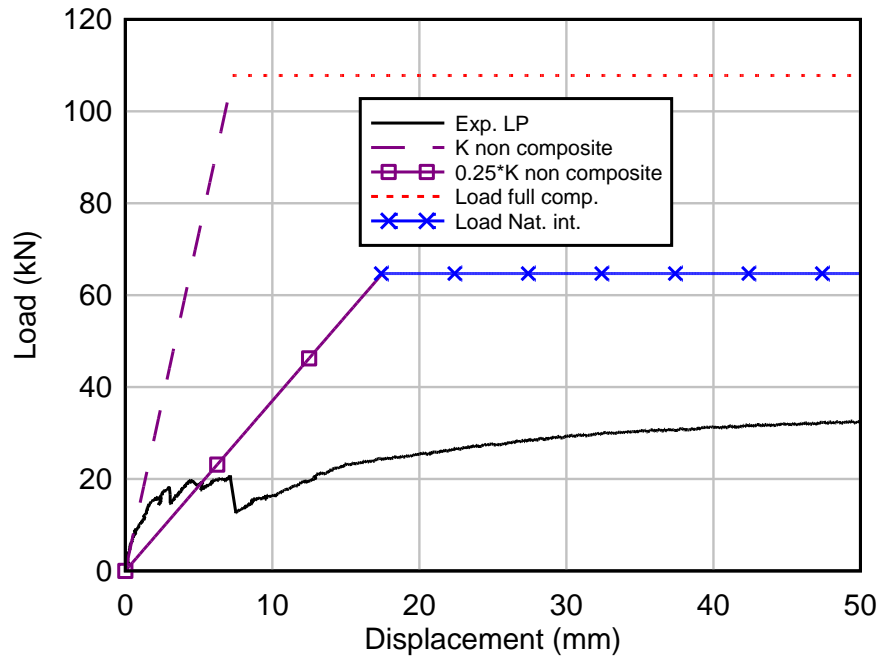


Figure 6.6: Comparison between predicted and experimental flexural response of the Lightweight core panel (LP).

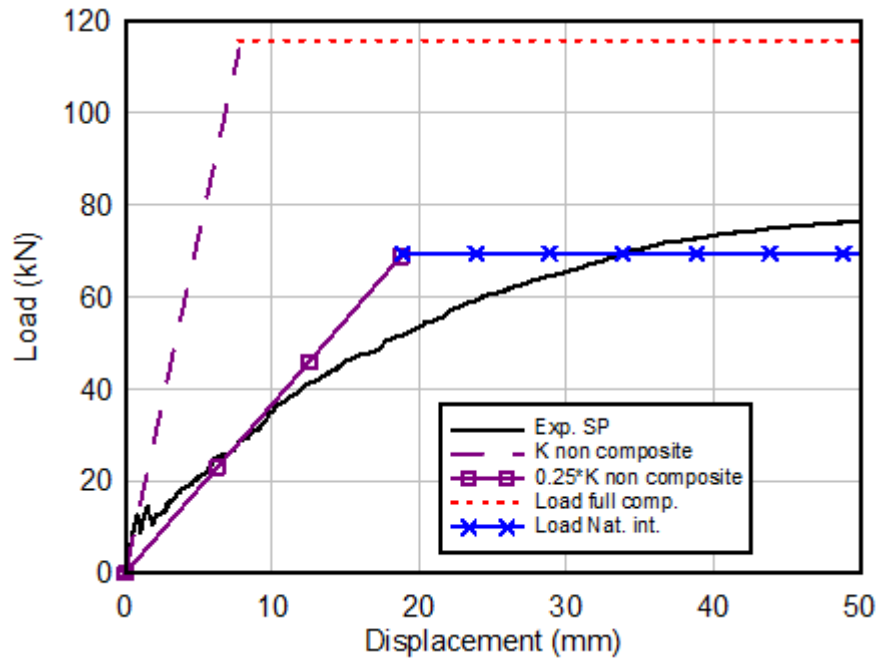


Figure 6.7: Comparison between predicted and experimental flexural response of the Stainless steel panel (SP).

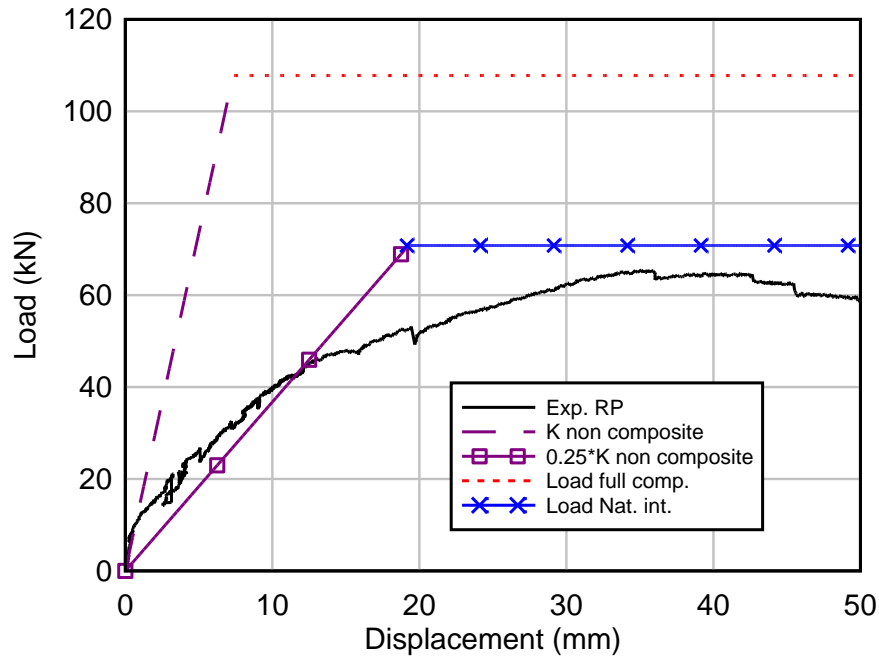


Figure 6.8: Comparison between predicted and experimental flexural response of the Reinforced core panel (RP).

6.1.2 Flexural load capacity of SCS panels with partial shear connection

The moment capacity of the Improved bonding panel was determined using cross section analysis for SCS panels with partial shear connection, according to Liew and Soheli (2009). The stress distribution in the cross section was assumed to be linear as shown in Figure 6.9. The concrete core below the neutral axis was cracked and ignored in the analysis.

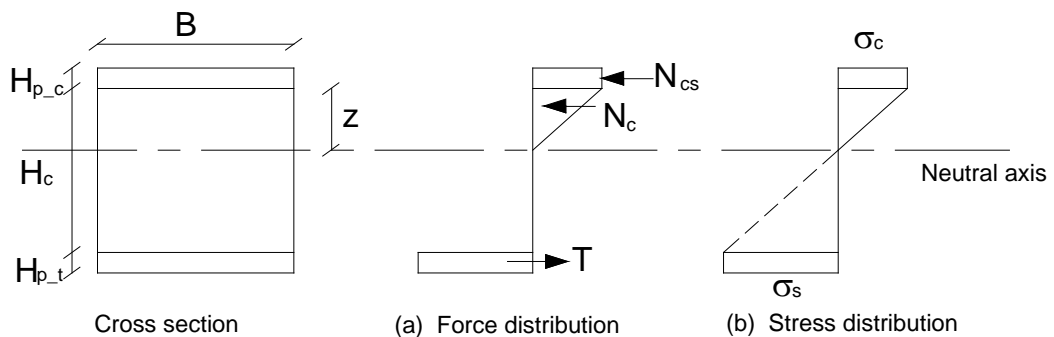


Figure 6.9: Cross section analysis for SCS panels with partial shear connection.

The position of the neutral axis, z , can be calculated as:

$$z = -n(H_{p-c} + H_{p-t}) + \sqrt{n^2(H_{p-c} + H_{p-t})^2 - n(H_{p-c}^2 - 2H_{p-t}H_c - H_{p-t}^2)} \quad (6.18)$$

where $n = E_s/E_c$, is the ratio of the modulus of elasticity between steel and concrete.

Using the assumption of linear stress distribution in the cross section as shown in Figure 6.9, the stress of the top faceplate can be determined from the stress of the bottom faceplate as:

$$\sigma_c = \frac{\sigma_s(z + H_{p-c}/2)}{(H_c - z + H_{p-t}/2)} \quad (6.19)$$

The moment capacity of SCS panels can be determined by taking moments about the line of action of the concrete compressive force:

$$M_{o_partial} = \sigma_c B H_c (z/3 + H_{p-c}/2) + \sigma_s B H_{p-t} (H_c - z/3 + H_{p-t}/2) \quad (6.20)$$

The modulus of elasticity of concrete determined in accordance to AS 3600 (2009) was 28 GPa (Eq. 6.12). Therefore, the modulus ratio is,

$$n = E_s/E_c = 200/28 = 7.14 \quad (6.21)$$

The position of the neutral axis of the SCS panel, z , is calculated as:

$$z = -7.14 \times 6 + [7.14^2 \times 6^2 - 7.14 \times (9 - 2 \times 3 \times 80 - 9)]^{1/2} = 29.7 \text{ mm} \quad (6.22)$$

The stress in the bottom steel faceplate of the Improved bonding panel when the bonding between the concrete and steel faceplate failed could be determined from the results of push-out tests. The results of push-out tests showed an average maximum load of 93 kN before the tack welding failed. The total contact area between the two steel plates and concrete infill of the push-out specimen was $2 \times 200 \times 260 \text{ mm}^2$. The shear resistance per unit area of the tack welded wire mesh is,

$$\tau = 93 \times 10^6 / (2 \times 200 \times 260) = 894 \text{ kPa} \quad (6.23)$$

The distance between the loading point and the support is 625 mm and the width of the panel is 500 mm. The maximum tensile force can be developed at the mid-span of the bottom faceplate due to the partial shear connection is,

$$T = \tau \times A_t \quad (A_t = \text{total area of contact from the support to the loading point})$$

$$\begin{aligned}
&= 894 \times 10^{-3} \times 500 \times 625 \\
&= 279 \text{ kN} < T_o = 271 \times 500 \times 3 = 407 \text{ kN}
\end{aligned} \tag{6.24}$$

The stress in the bottom faceplate when the shear connection failed is given by:

$$\sigma_t = T/A_p = 279 \times 10^3 / (3 \times 500) = 186 \text{ MPa} \tag{6.25}$$

The stress in the top faceplate is determined as:

$$\sigma_c = 186 \times (29.7 + 1.5) / (80 - 29.7 + 1.5) = 112 \text{ MPa} \tag{6.26}$$

The theoretical moment capacity of the Improved bonding panel is,

$$\begin{aligned}
M_{o_partial} &= 112 \times 500 \times 3 \times (29.7/3 + 1.5) + 186 \times 500 \times 3 \times (80 - 29.7/3 + 1.5) \\
&= 21.9 \text{ kN.m}
\end{aligned} \tag{6.27}$$

By assuming a simple supported condition, the theoretical flexural load capacity of the Improved bonding panel is:

$$P_{o_partial} = 4 \times 21.9 / 1.25 = 70.1 \text{ kN} \tag{6.28}$$

The theoretical flexural stiffness and flexural load capacity were compared to the experimental results of Improved bonding panel in Figure 6.10. The theoretical flexural stiffness based on the full composite section (Eq. 6.17) slightly overestimated the initial load-displacement relationship of the Improved bonding panel. After cracking appeared in the concrete core, the stiffness of the Improved bonding panel was reduced gradually. Therefore, 20 % of the theoretical flexural stiffness of full composite section was used as the effective flexural stiffness.

The theoretical ultimate flexural capacity determined assuming the full composite action (Eq.6.5) was significantly higher than the experimental flexural load capacity of the Improved bonding panel. It should be noted that the flexural load resistance of the Improved bonding panel dropped slightly when the load reached 53 kN at about 15 mm displacement, due to the failure of the tack welding between the wire mesh and bottom steel faceplate at one of the shear span. The panel reached the maximum flexural load capacity of 72 kN because the shear connection between the bottom steel faceplate and the concrete core still existed at another shear span, and at this

stage, the bottom faceplate had yielded at mid-span. So the theoretical flexural load capacity should be compared to the experimental flexural load when the tack welding failed at 53 kN. The predicted flexural load capacity of 70.1 kN was higher than the experimental result of 53 kN by about 30 %. The lower flexural load capacity of the experimental result could be attributed to imperfections in the tack welding in the panel.

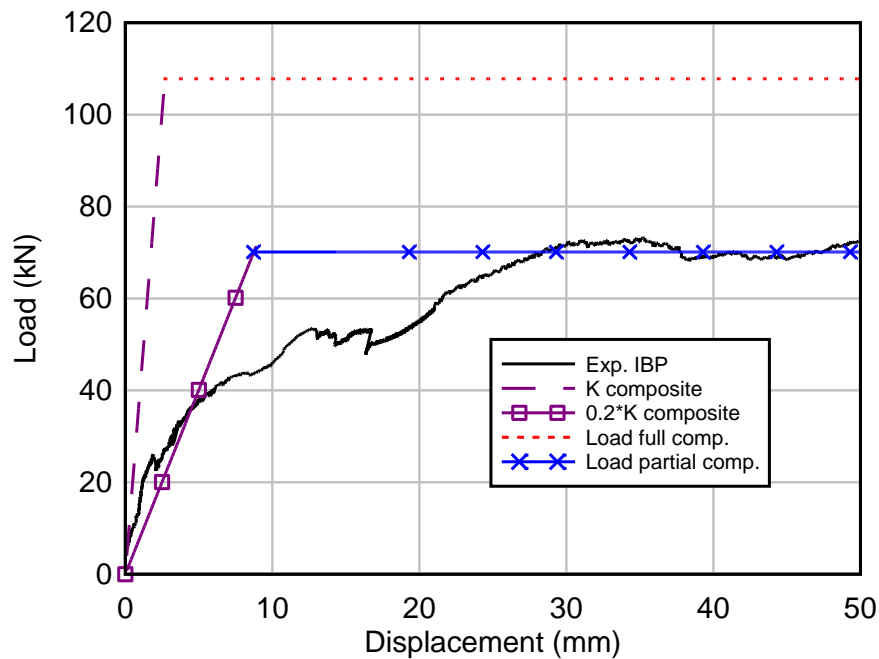


Figure 6.10: Comparison between predicted and experimental flexural response of the Improved bonding panel (IBP).

6.1.3 Flexural load capacity of fully enclosed SCS panels

For this panel, two end caps were welded to steel faceplates to form a rectangular steel section. The width of the steel section was 506 mm, the height was 86 mm, the thickness of the steel plates was 3 mm and the thickness of the concrete core was 80 mm. At the ultimate moment capacity, the steel section was assumed fully yielded and the concrete started to crush. The strain and stress distribution in the cross section is shown in Figure 6.11.

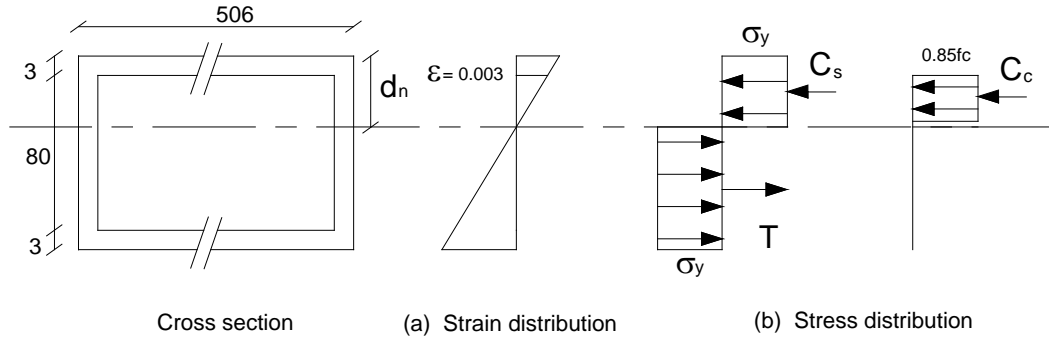


Figure 6.11: Strain and stress distribution in the Fully enclosed panel at the ultimate moment capacity.

The theoretical ultimate moment capacity of the Fully enclosed panel is determined using the equilibrium and compatibility method:

$$M_o = T_s d_{st} + C_s d_{sc} + C_c d_c \quad (6.29)$$

Steel compressive force is,

$$C_s = (500 \times 3 + 2 \times 3 \times d_n) \sigma_y \quad (6.30)$$

Concrete compressive force is,

$$C_c = 0.85 \times f_c \times 500 \times \gamma (d_n - 3) \quad (6.31)$$

According to Oehlers and Bradford (1995), the ratio γ could be determined as:

$$\gamma = 0.85 - 0.007(f_c - 28) = 0.85 - 0.007(31 - 28) = 0.83 \quad (6.32)$$

Steel tensile force is,

$$T_s = (500 \times 3 + 2 \times (86 - d_n) \times 3) \times \sigma_y \quad (6.33)$$

Solving $T_s = C_c + C_s$, we get $d_n = 12.2$ mm, the ultimate moment capacity of the cross section is,

$$\begin{aligned} M_o &= T_s d_{st} + C_s d_{sc} + C_c d_c \\ &= 500 \times 3 \times 271 \times (84.5 - 12.2) + 2 \times 3 \times (86 - 12.2)^2 / 2 + 500 \times 3 \times 271 \times (12.2 - 1.5) + 2 \times 3 \times 12.2^2 / 2 \\ &\quad + 0.85 \times 31 \times 500 \times 0.83 \times (12.2 - 3)^2 / 2 \\ &= 29.39 + 0.016 + 4.35 + 4.46 \times 10^{-4} + 0.46 \\ &= 34.2 \text{ kN.m} \end{aligned} \quad (6.34)$$

The theoretical flexural load capacity for the Fully enclosed panel subjected to a point load at mid-span under simply support condition is,

$$P_{o_simple} = 4 \times 34.2/1.25 = 109.4 \text{ kN} \quad (6.35)$$

The theoretical flexural load capacity for the Fully enclosed panel subjected to a point load at mid-span under fixed end support is,

$$P_{o_fix} = 2 \times 4 \times 34.2/1.25 = 218.8 \text{ kN} \quad (6.36)$$

The second moment of area of the Fully enclosed panel including the steel shell and the concrete core:

$$\begin{aligned} I_{composite} &= \frac{2BH_p^3}{12} + 2BH_p d^2 + \frac{E_c}{E_s} \frac{BH_c^3}{12} + \frac{2H_p (H_c + 2H_p)^3}{12} \\ &= \frac{2 \times 500 \times 3^3}{12} + 2 \times 500 \times 3 \times 41.5^2 + \frac{28}{200} \frac{500 \times 80^3}{12} + \frac{2 \times 3 \times 86^3}{12} \\ &= 8.47 \times 10^6 \text{ mm}^4 \end{aligned} \quad (6.37)$$

The flexural stiffness of the Fully enclosed panel including the steel shell and concrete core:

$$K_{composite} = \frac{48E_s I_{composite}}{L^3} = \frac{48 \times 200 \times 8.47 \times 10^9}{1250^3} = 41.6 \text{ kN/mm}$$

The second moment of area of the steel hollow section:

$$\begin{aligned} I_{hollow\ section} &= \frac{2BH_p^3}{12} + 2BH_p d^2 + \frac{2H_p (H_c + 2H_p)^3}{12} \\ &= \frac{2 \times 500 \times 3^3}{12} + 2 \times 500 \times 3 \times 41.5^2 + \frac{2 \times 3 \times 86^3}{12} \\ &= 5.49 \times 10^6 \text{ mm}^4 \end{aligned}$$

The flexural stiffness of the steel hollow section:

$$K_{hollow\ section} = \frac{48E_s I_{hollow\ section}}{L^3} = \frac{48 \times 200 \times 5.49 \times 10^9}{1250^3} = 27 \text{ kN/mm} \quad (6.38)$$

The theoretical flexural stiffness and ultimate flexural capacity were compared to the experimental results of the Fully enclosed panel in Figure 6.12. The experimental

flexural stiffness of this panel was significantly lower than the theoretical flexural stiffness of both composite section and hollow steel section. This could be attributed to the flexibility of the keyed connections. It was found that, the experimental flexural stiffness of the panel was approximately 40 % of the theoretical flexural stiffness of the steel hollow section under the simple support condition.

The experimental flexural load capacity of the Fully enclosed panel was higher than the theoretical ultimate flexural capacity for the simply supported panel but lower than the theoretical ultimate flexural capacity assuming the panel was fixed at the end. This showed that the axial restraint supports acted as semi-rigid connections for Fully enclosed panel and moment resistance was developed at the supports.

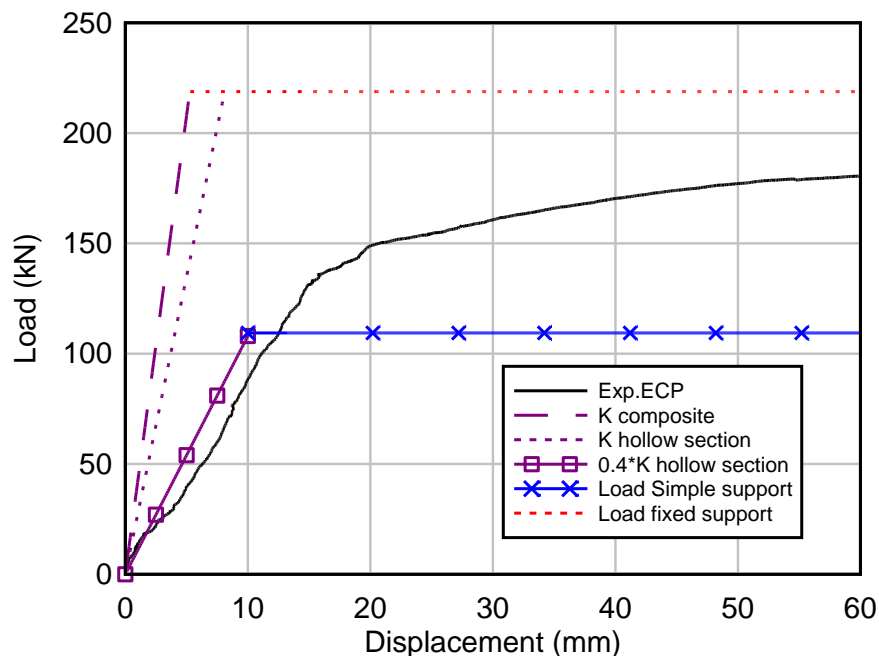


Figure 6.12: Comparison between theoretical and experimental flexural response of the Fully enclosed panel (ECP).

6.2 Tensile Membrane resistance of SCS panels

In this study, the tensile membrane resistance of SCS panels was predicted using the analytical solutions derived by Hodge Jr. (1974) for the steel beam with rectangular cross section supported by the semi-rigid axial restraints. The analysis was carried out on the assumption that steel had a rigid perfectly plastic response. The steel plate showed a transient membrane response after the ultimate moment capacity of the

plate was reached. The axial tensile force in the cross section increased with the increased displacement until the axial yield force of the section was reached, and then it became a plastic membrane. The load-displacement relationship for the membrane response according to Hodge Jr. (1974) is,

if $t < 1$

$$t = (e^{-2k\delta/H_p} + 2k\delta/H_p - 1) / k$$

$$p = 1 + 4\delta t/H_p - t^2 \quad (\text{transient membrane})$$

$$\text{else } p = 4\delta/H_p \quad (\text{plastic membrane}) \quad (6.39)$$

where t is the tensile force parameter, k is the stiffness parameter of the axial restraint supports, δ is the mid-span displacement, H_p is the thickness of the plate, and p is the applied force parameter.

In the experimental set-up for static tests, clearance holes were used in the bolted connections between the UC sections and supporting I-beams. The experimental results showed that these clearance holes allowed the UC sections to slip before the bolts started bearing against the UC sections and I-beams. After that, the in-plane displacement of the UC sections was restrained, but it was observed that the key inserts were pulled out from the UC sections when the load increased. In addition, the flared ends of the SCS panels were pulled out from the keyed connections. It should be noted that the top steel faceplate was in compression when the SCS panels resisted the applied load by the flexural mechanism and it underwent a strain transition process and developed tensile stress in the cross section during tensile membrane resistance.

There was no axial restraint on the panels initially due to the in-plane movement of the axial restraint supports. After that, the panels were supported by the semi-rigid axial restraints and the stiffness of the restraint was affected by the in-plane movement of the key inserts and pull-out of the panels from the keyed connections. The experimental results were used to calibrate the equivalent axial stiffness of the test rig and it was assumed that both steel faceplates contributed to the membrane resistance simultaneously at a large displacement.

6.2.1 Analysis of SCS panels with mild steel faceplates

The yield stress of the mild steel (σ_{y_m}) was 271 MPa and the distance between the supports (L) was 1250 mm. The thickness and width of the steel faceplate was 3 mm and 500 mm, respectively. The moment capacity of the mild steel plate is,

$$M_{o_m} = B H_p^2 \sigma_{y_m} / 4 = 500 \times 3^2 \times 271 / 4 = 304875 \text{ N.mm} \quad (6.40)$$

The plastic collapse load for a simply supported mild steel plate:

$$P_{o_m} = 4M_{o_m} / L = 4 \times 304875 / 1250 = 976 \text{ N} \quad (6.41)$$

The load-displacement relationship for one mild steel faceplate under tensile membrane resistance is,

if $t < 1$

$$t = (e^{-2k\delta H_p} + 2k\delta H_p - 1) / k = (e^{-k\delta/1.5} + k\delta/1.5 - 1) / k$$

$$p = 1 + 4\delta t / H_p - t^2 = 1 + 4\delta t / 3 - t^2$$

$$P = P_{o_m} (1 + 4\delta t / 3 - t^2) = 0.976 (1 + 4\delta t / 3 - t^2) \text{ kN } (\delta \text{ in mm})$$

else $p = 4\delta / H_p$

$$P = P_{o_m} (4\delta / 3) = 0.976 (4\delta / 3) \text{ kN } (\delta \text{ in mm}) \quad (6.42)$$

The total load-displacement relationship for two mild steel faceplates under tensile membrane resistance is,

if $t < 1$

$$P_{tot} = 2P_{o_m} (1 + 4\delta t / 3 - t^2) = 2 \times 0.976 (1 + 4\delta t / 3 - t^2) \text{ kN } (\delta \text{ in mm})$$

else

$$P_{tot} = 2P_{o_m} (4\delta / 3) = 2 \times 0.976 (4\delta / 3) \text{ kN } (\delta \text{ in mm}) \quad (6.43)$$

6.2.2 Analysis of SCS panel with stainless steel faceplates

The yield stress of the stainless steel was determined from 0.2% proof stress ($\sigma_{y_s} = 291 \text{ MPa}$) and the strain hardening effect was ignored in the analysis. The moment capacity of the stainless steel plate is,

$$M_{o_s} = B H_p^2 \sigma_{y_s} / 4 = 500 \times 3^2 \times 291 / 4 = 327375 \text{ N.mm} \quad (6.44)$$

The plastic collapse load for a simply supported stainless steel plate is,

$$P_{o_s} = 4M_{o_s}/L = 4 \times 327375/1250 = 1048 \text{ N} \quad (6.45)$$

The load-displacement relationship for one stainless steel faceplate under tensile membrane resistance is,

if $t < 1$

$$t = (e^{-k\delta/1.5} + k\delta/1.5 - 1) / k$$

$$P = P_{o_s} (1 + 4\delta/3 - t^2) = 1.05(1 + 4\delta/3 - t^2) \text{ kN } (\delta \text{ in mm})$$

else

$$P = P_{o_s} (4\delta/3) = 1.05(4\delta/3) \text{ kN } (\delta \text{ in mm}) \quad (6.46)$$

The total load-displacement relationship for two stainless steel faceplates is,

if $t < 1$

$$P_{tot} = 2P_{o_s} (1 + 4\delta/3 - t^2) = 2 \times 1.05(1 + 4\delta/3 - t^2) \text{ kN } (\delta \text{ in mm})$$

else

$$P_{tot} = 2P_{o_s} (4\delta/3) = 2 \times 1.05(4\delta/3) \text{ kN } (\delta \text{ in mm}) \quad (6.47)$$

6.2.3 Determination of stiffness of the axial restraint support

The stiffness of the axial restraint support was evaluated by first determining the horizontal force on the support from the load-displacement relationship of the panel. Figure 6.13 shows the free body diagram of the panel at a large displacement. The support rotation (θ) can be determined from the mid-span displacement:

$$\theta = \tan^{-1} \frac{\delta}{L/2} \quad (6.48)$$

where δ is the displacement of the panel at mid-span, and L is the span length of the panel. The horizontal force (F) can be determined using the force equilibrium equation at the support:

$$F = \frac{P}{2 \tan \theta} \quad (6.49)$$

where P is the total applied load. Then, the stiffness of the axial restraint support can be obtained by plotting the horizontal force versus the displacement of the axial support.

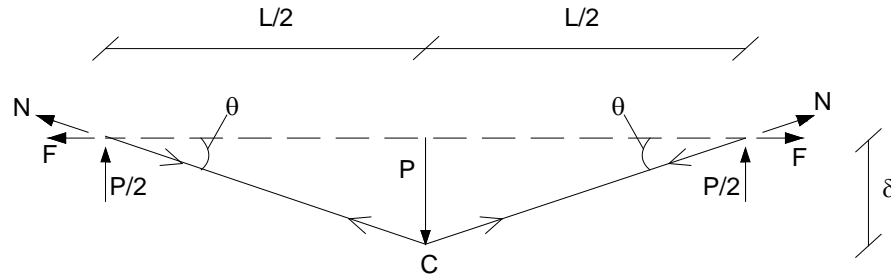


Figure 6.13: Free body diagram of the panel at a large displacement.

The stiffness of the axial restraint support used in this study was determined from the experimental results of the Control panel subjected to static three-point bending. The horizontal force on the support was determined after the Control panel reached its flexural load capacity, where the mid-span displacement exceeded 60 mm ($\theta > 5^\circ$). Then, the horizontal force was plotted against the corresponding displacement of the key inserts recorded during the test (Figure 5.26 in Chapter 5). Figure 6.14 shows the horizontal force versus displacement of the key inserts. Initially, the key inserts moved without restraint due to the clearance holes in the bolt connections between the UC sections and I-beams. The stiffness of the axial restraint support was zero at this stage. The horizontal force at the east keyed connection started to increase when the displacement exceeded 8 mm while the horizontal force at the west keyed connection increased as the displacement exceeded 12 mm. The stiffness of the east keyed connection and the west keyed connection at this stage was approximately 48.3 kN/mm and 47 kN/mm, respectively. The average stiffness of the keyed connections at the second stage was 47.7 kN/mm. The overall stiffness of the axial restraint supports considering the initial stage of slippage and the second stage of semi-rigid support was,

$$K = \frac{0 + 47.7}{2} = 23.9 \text{ kN/mm} \quad (6.50)$$

It should be noted that the SCS panels were pulled out from the keyed connections during the tests (Figure 5.27 in Chapter 5). This caused the actual stiffness of the axial restraint on the panels to be lower than the theoretical stiffness of the axial restraint support determined above, which ignored the pull-out of the panels.

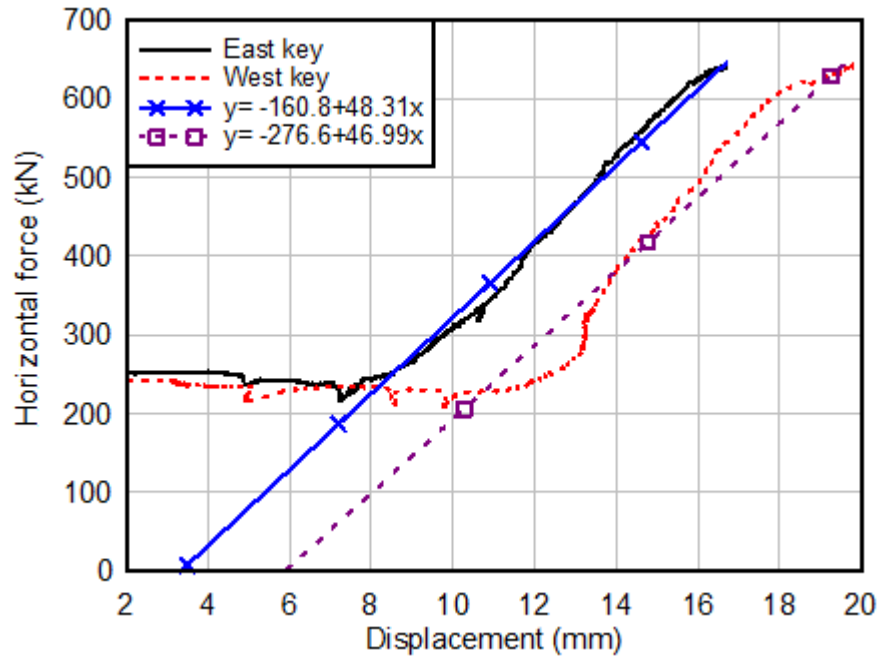


Figure 6.14: Load-displacement relationship for the axial restraint supports.

According to Hodge Jr. (1974), the axial stiffness parameter (k) is given as:

$$k = \frac{hK}{2\sigma_y B} \quad (6.51)$$

where h is equals H/L , H is the thickness of the plate, L is the span length of the plate, and K is the axial support stiffness, σ_y is the yield stress and B is the width of the section. Therefore, the axial stiffness parameter is,

$$k = \frac{3 \times 23900}{1250 \times 2 \times 271 \times 500} = 0.0002 \quad (6.52)$$

6.2.4 Comparison between theoretical and experimental results

The predicted tensile membrane response was compared to the experimental results in Figure 6.15 to Figure 6.20. The experimental tensile membrane resistance at large displacement was lower than the resistance of two plastic membranes but higher than one plastic membrane. This showed that the effects of axial restraint stiffness should be taken into consideration to improve the prediction of tensile membrane resistance. It was found that using an axial stiffness parameter, $k = 0.00012$, the theoretical analysis by Hodge Jr. (1974) predicted the tensile membrane resistance of the Control panel (Figure 6.15) and Stainless steel panel (Figure 6.16) at large

displacement reasonably well. The axial stiffness parameter (k) was lower than the theoretical axial stiffness parameter (0.0002) which could be attributed to the pull-out of the SCS panels from the keyed connections during the test.

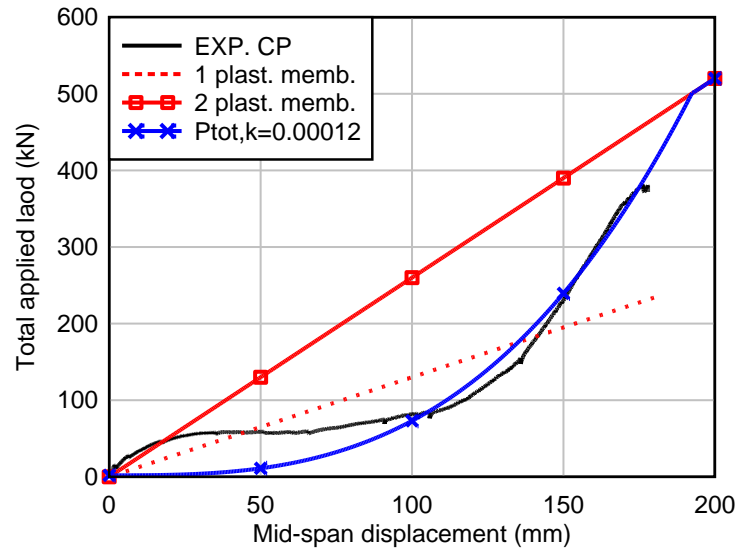


Figure 6.15: Comparison between theoretical and experimental membrane resistance of the Control panel (CP).

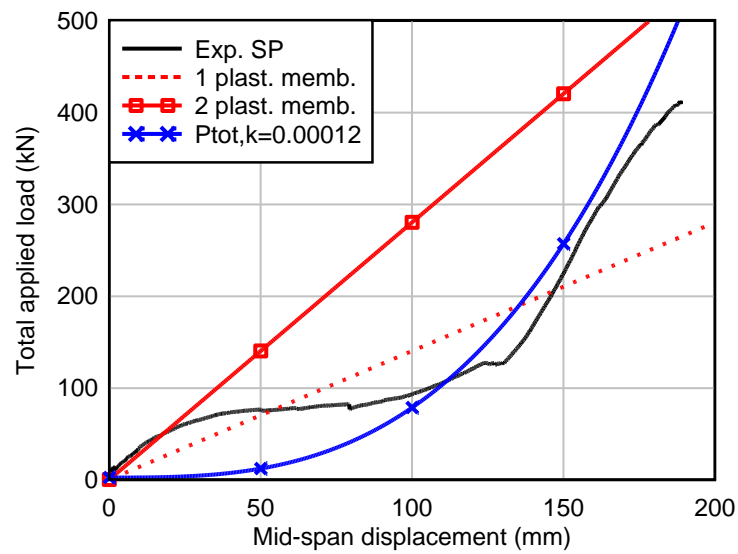


Figure 6.16: Comparison between theoretical and experimental membrane resistance of the Stainless steel panel (SP).

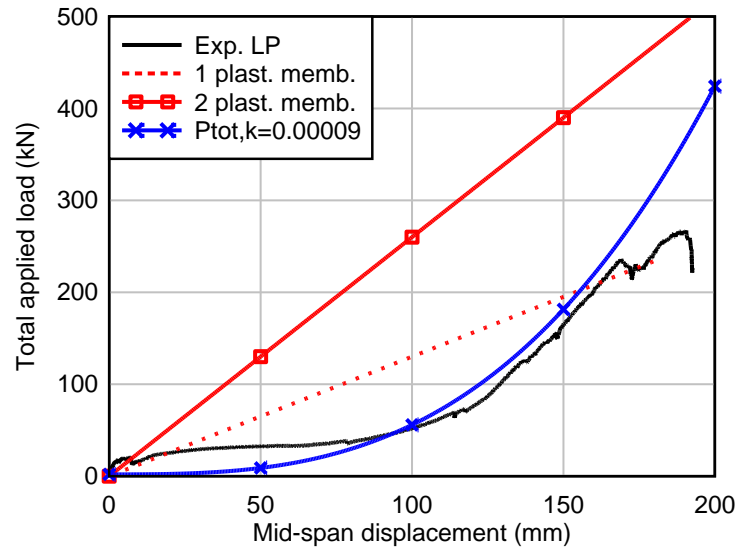


Figure 6.17: Comparison between theoretical and experimental membrane resistance of the Lightweight core panel (LP).

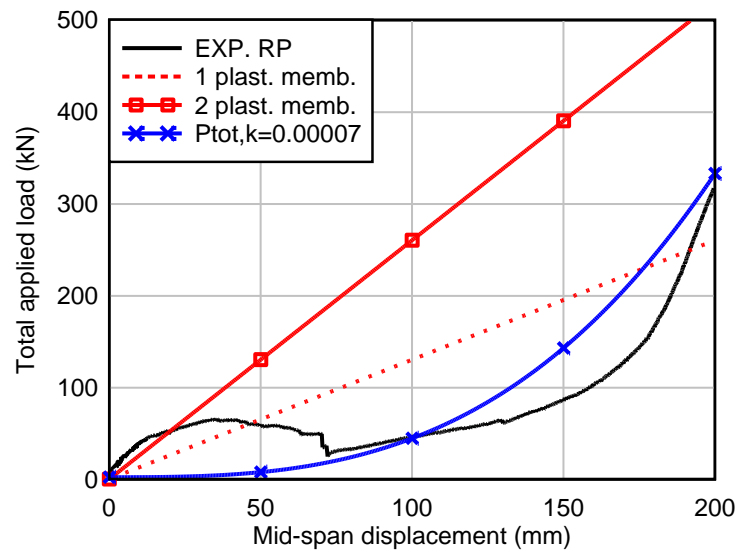


Figure 6.18: Comparison between theoretical and experimental membrane resistance of the Reinforced core panel (RP).

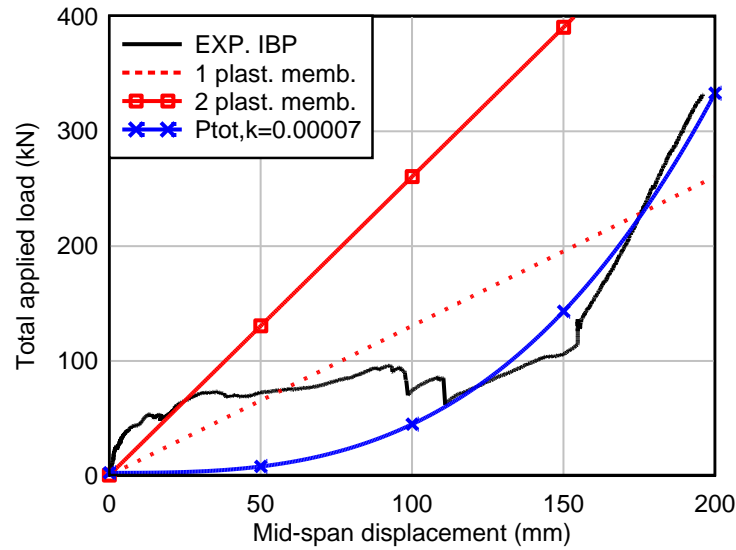


Figure 6.19: Comparison between theoretical and experimental membrane resistance of the Improved bonding panel (IBP).

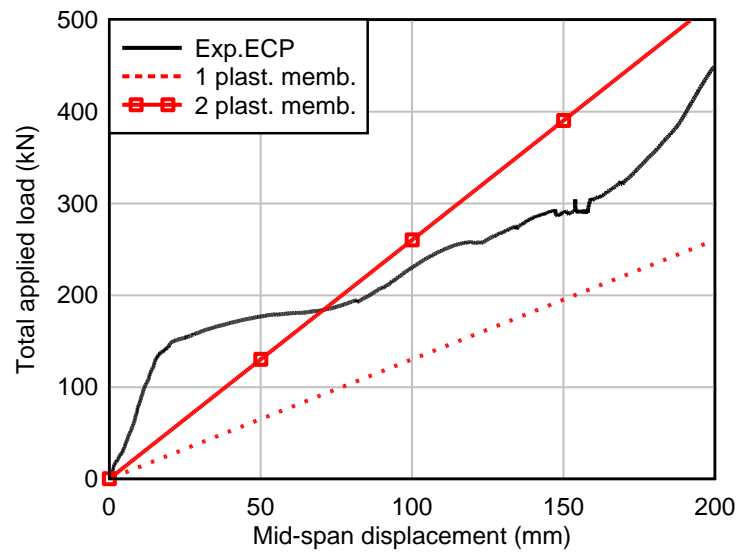


Figure 6.20: Comparison between theoretical and experimental membrane resistance of the Fully enclosed panel (ECP).

For the Lightweight core panel, Reinforced core panel and Improved bonding panel, a slightly lower axial stiffness parameter (k) was used in the analyses compared to the Control panel. For the Lightweight core panel, the axial stiffness parameter was 0.00009 (Figure 6.17) while for the Reinforced core panel (Figure 6.18) and Improved bonding panel (Figure 6.19), it was 0.00007. The axial restraint stiffness on the Lightweight core panel was lower than the Control panel due to crushing of

the lightweight concrete at the flared ends. This caused the Lightweight core panel to be pulled out from the keyed connections more than the Control panel. For the Reinforced core panel and Improved bonding panel, the axial restraint stiffness was reduced compared to the Control panel because of the failure of the welded joint between the bottom faceplate and end plate.

For the Fully enclosed panel, the experimental tensile membrane resistance was in between the resistance of one plastic membrane and two plastic membranes, as shown in Figure 6.20. It seemed the tensile membrane resistance of this panel at large displacement was close to the total resistance of two plastic membranes. The simplified analysis method used in this study could not predict accurately the tensile membrane resistance of this panel at large mid-span displacement.

6.3 Static resistance function for axially restrained SCS panels

6.3.1 Axially restrained non-composite SCS panels

From the analyses of static test results of axially restrained non-composite SCS panels (with natural interaction), it was found that the flexural load capacity and tensile membrane response at a large displacement could be predicted using the analytical methods presented by Jeong (2008) and Hodge Jr. (1974), respectively. The static resistance function of the Control panel is shown in Figure 6.21. The following procedure was proposed to develop the static resistance function of the axially restrained non-composite SCS panel filled with normal strength concrete:

- (a) The flexural load capacity and tensile membrane resistance are predicted separately, and then combine together to form the static resistance function.
- (b) The equivalent flexural stiffness is determined using 25 % of the flexural stiffness of the non-composite SCS section assuming there is no crack in the concrete core. The panel is assumed as simply supported.
- (c) The flexural load capacity of the non-composite SCS panel is determined as follow:

- i. Calculate the shear span ratio for the panel:

$$\rho_s = L_{sp} / d_e \quad (6.53)$$

- ii. Determine the strength ratio (α_{nat}) from Figure 6.1,

- iii. The ultimate moment capacity of the SCS panel with an unreinforced concrete core assuming full composite action:

$$M_o = \sigma_y B H_p (H_c + H_p) \quad (6.54)$$

- iv. Calculate the ultimate flexural capacity of the SCS panel assuming the panel is as simply supported:

$$P_o = 4M_o/L \quad (6.55)$$

- v. Determine the flexural load capacity of the non-composite SCS panel (with natural interaction):

$$P_{o_nat} = \alpha_{nat} P_o \quad (6.56)$$

- (d) For the tensile membrane resistance, it is assumed that both steel faceplates contribute to the membrane resistance simultaneously:

- i. The load-displacement relationship for two steel faceplates subjected to a point load at mid-span under tensile membrane response is,

if $t < 1$

$$t = (e^{-2k\delta/H_p} + 2k\delta/H_p - 1)/k$$

$$P = 2(1 + 4\delta t/H_p - t^2) P_{o_plate}$$

$$\text{else } P = 2 \times 4\delta P_{o_plate}/H_p \quad (6.57)$$

- ii. The axial stiffness parameter, k can be determined from experiment or based on theoretical analysis:

$$k = hK/2\sigma_y B \quad (6.58)$$

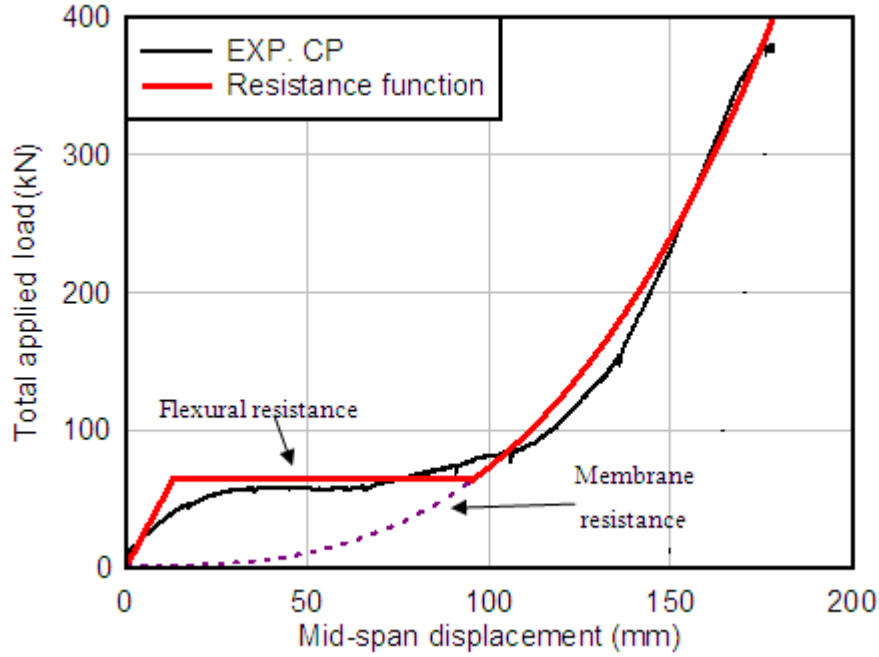


Figure 6.21: Static resistance function of the Control panel (CP).

6.3.2 Axially restrained SCS panels with partial shear connection

The procedure to develop the static resistance function for axially restrained SCS panels with partial shear connection was similar to the non-composite SCS panels, except for the method used to determine the flexural load capacity. Figure 6.22 shows the static resistance function of the Improved bonding panel.

- (a) The flexural load capacity and tensile membrane resistance are predicted separately, and then combine together to form the static resistance function.
- (b) The equivalent flexural stiffness is determined using 20 % of the flexural stiffness of SCS panels with full composite action where the neutral axis is located at centre of the concrete core. The panel is assumed as simply supported.
- (c) The flexural load capacity is predicted as follow:

- i) The position of the neutral axis, z , can be calculated as:

$$z = -n(H_{p_c} + H_{p_t}) + [n^2(H_{p_c} + H_{p_t})^2 - n(H_{p_c}^2 - 2H_{p_t}H_c - H_{p_t}^2)]^{1/2} \quad (6.59)$$

- ii) The stress in the bottom faceplate is determined using the shear connection capacity obtained from the push-out test:

$$\sigma_t = \tau \times A_t / A_p \quad (6.60)$$

- iii) The stress in the top faceplate can be determined as:

$$\sigma_c = \sigma_s (z + H_{p_c}/2)/(H_c - z + H_{p_t}/2) \quad (6.61)$$

- iv) The moment capacity of the panel with partial shear connection is calculated as:

$$M_{o_partial} = \sigma_c B H_c (z/3 + H_{p_c}/2) + \sigma_s B H_{p_t} (H_c - z/3 + H_{p_t}/2) \quad (6.62)$$

- v) The flexural load capacity of the panel is determined assuming the panel is simply supported,

$$P_o = 4M_o/L \quad (6.63)$$

- (d) For tensile membrane resistance, it is assumed that both steel faceplates contribute to the membrane resistance simultaneously:

- i) The load-displacement relationship for two steel faceplates subjected to a point load at mid-span under membrane response is,

if $t < 1$

$$t = (e^{-2k\delta/H_p} + 2k\delta/H_p - 1)/k$$

$$P = 2(1 + 4\delta t/H_p - t^2)P_{o_plate}$$

$$\text{else } P = 2 \times 4\delta P_{o_plate}/H_p \quad (6.64)$$

- ii) The axial stiffness parameter, k can be determined from experiment or based on theoretical analysis:

$$k = hK/2\sigma_y B \quad (6.65)$$

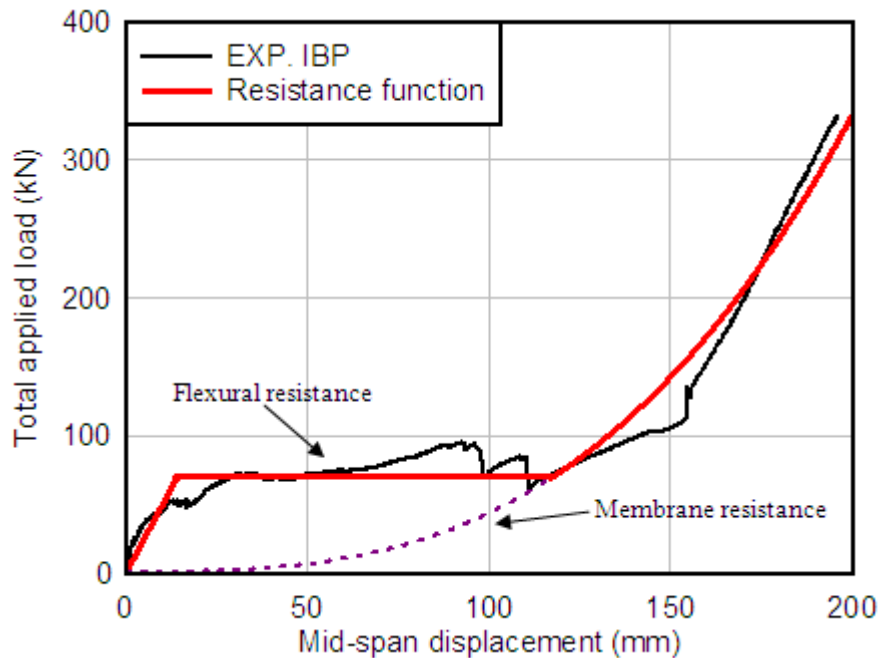


Figure 6.22: Static resistance function of the Improved bonding panel (IBP).

6.4 Conclusions

The static experimental results of axially restrained SCS panels were compared to the analytical predictions in this chapter. Generally, the theoretical analysis could predict the flexural response and the membrane resistance at large deformation with reasonable accuracy. The static resistance function of axially restrained SCS panels had been developed. The flexural load capacity and tensile membrane resistance were predicted separately, and then combined together to form the static resistance function. Based on the analyses of the experimental results, several key findings are summarised below:

- (a) The flexural load capacity of non-composite SCS panels (with natural interaction) was significantly lower than the theoretical ultimate flexural capacity for the equivalent full composite panel. For the non-composite SCS panels filled with normal strength concrete, the simplified approach by Jeong (2008) was used to predict the flexural load capacity. This approach overestimated the flexural load capacity of the SCS panels with mild steel faceplates by less than 15%. For the SCS panel with stainless steel faceplates, this method underestimated the flexural load capacity by about 10%. The SCS panels were analysed as simply supported since concrete cracking and separation of the steel faceplates from the concrete core occurred at the connections before the flexural load capacity was reached. Therefore, low or no moment resistance could develop at the supports when the panel reached its flexural load capacity. For the non-composite SCS panel filled with lightweight concrete core, the flexural load capacity was significantly lower than the predicted flexural load capacity due to crushing of the concrete core before the bottom steel faceplate yielded.
- (b) For the SCS panel with partial shear connection, the flexural load capacity depended on the strength of the shear connection. The flexural load capacity was predicted using the analysis method presented by Liew and Soheli (2009) and the strength of shear connector required in the analysis was determined from the push-out test. In this study, the theoretical flexural load capacity was approximately 30% higher than the experimental results due to the imperfections in the shear connection in the panel.
- (c) For the Fully enclosed panel, the axial restraint supports acted as semi-rigid connections causing moment resistance developed at the supports. Therefore, the

experimental flexural load capacity was in between the flexural load capacity of a simply supported panel and a fixed end panel.

- (d) Analysis of the tensile membrane resistance was carried out using analysis solutions of Hodge Jr. (1974). The experimental tensile membrane resistance of SCS panels at large displacement was lower than the resistance of two plastic membranes but higher than the resistance of one plastic membrane. The experimental results of the Control panel were used to calibrate the axial stiffness parameter, k . It was assumed that both steel faceplates contributed to the membrane resistance simultaneously. By using axial stiffness parameter, ranging from 0.00007 to 0.00012, the simplified analysis method was able to predict the membrane resistance at large displacement for all the panels with reasonable accuracy except for the Fully enclosed panel.

CHAPTER 7

IMPACT TESTING OF AXIALLY RESTRAINED NON-COMPOSITE SCS PANELS

The impact testing on axially restrained non-composite SCS panels were conducted to study the behaviour of these panels under large impact energy. The experimental programme included a comprehensive parametric study to observe the effects of lightweight concrete core, increased degree of interaction between the concrete and steel faceplates, reinforced concrete core and application of stainless steel faceplates on the impact response of steel SCS panels. Similar studies had been carried out under static load condition, and the impact test results were compared to static test results to investigate the effects of impact loading on the response of axially restrained SCS panels. Then, based on the static resistance function for the axially restrained panels proposed in previous chapter, theoretical analyses were performed to predict the impact response of axially restrained SCS panels.

7.1 Experimental program

7.1.1 Unconfined concrete compressive test

The unconfined compressive tests were conducted on concrete cylinders on the days of the impact testing to obtain the concrete compressive strength of the SCS panels. The top of the concrete cylinders were capped with high strength plaster before testing, as shown in Figure 7.1. The test was carried out using the Avery compression testing machine at the University of Wollongong.



Figure 7.1: The concrete cylinders have been capped with high strength plaster before the unconfined concrete compressive test is conducted.

7.1.2 Impact testing of axially restrained SCS panels

Impact tests were carried out on the axially restrained SCS panels using an instrumented large-capacity drop hammer apparatus at the University of Wollongong. Figure 7.2 shows the high capacity drop weight impact machine. The experimental set up for the impact tests is similar to the static ones, as illustrated schematically in Figure 7.3. The UC sections were bolted to I-beams using high tensile M25 bolts, and angle bracings were used to tie the webs of the UC sections to the I-beams in order to prevent lateral movement and overturning of the supports. The panels were connected to the UC sections through keyed connections. The dimension of the UC sections, bracing and keyed connections was described in Chapter 5.

In the impact tests, a 600 kg drop hammer was released from the height of 3 m to produce an impact load at the mid-span of the SCS panels. The data collected during the experiments included time histories of impact force, mid-span deflection and bottom faceplate strain at a sampling rate of 50 kHz by a high-speed data acquisition system. The impact load was measured by a dynamic load cell (Interface model 1200) mounted on the drop hammer as shown in Figure 7.3. The maximum capacity of the dynamic load cell is 1200 kN. The dynamic load cell will measure the contact force between the drop hammer and the specimen when they are in contact.

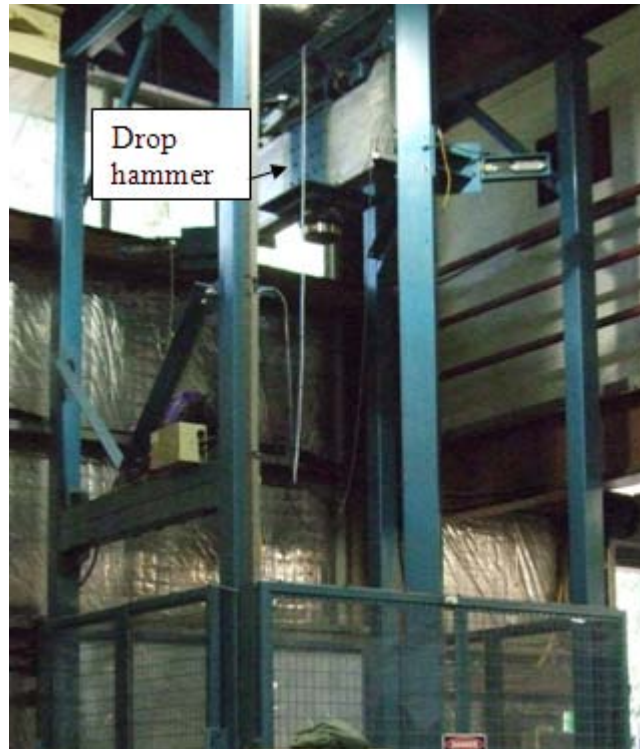


Figure 7.2: The high capacity drop hammer impact apparatus at the University of Wollongong.

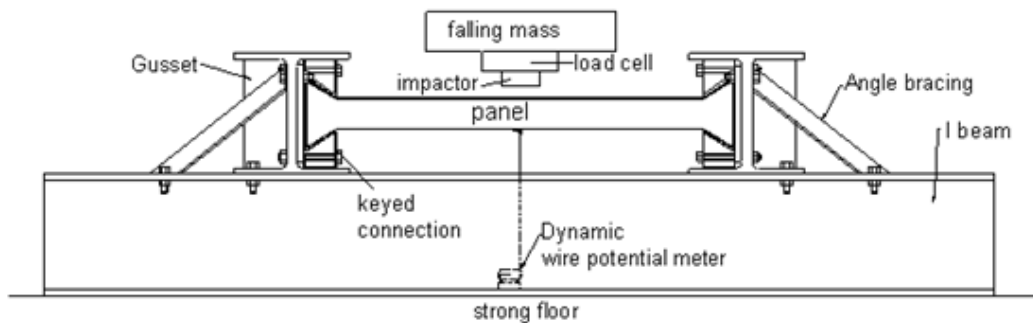


Figure 7.3: The experimental setup for axially restrained SCS panels subjected to a drop mass impact.

The strain history at the centre of the bottom steel faceplate was recorded by a foil strain gauge. The mid-span displacement of the bottom steel faceplate was measured using a high-speed draw wire potential meter, Micro-epsilon WDS-MPM model. The experimental data was acquired by a National Instrument DAQ system and the maximum sampling frequency for this system is 300 kHz. A laser was used to trigger the data acquisition system. The laser was positioned above the specimens so that the drop hammer passed through the laser and triggered the data acquisition system

before it struck the specimens. A LabView program was used to obtain, process, analyse and record the experimental data from the data acquisition.

High-velocity impact tests were performed on nine axially restrained SCS panels. The configurations of the SCS panels are described in Table 5.1. The geometry and dimension of the SCS panels used in the impact tests are the same with the panels used in the static tests, except that no small bracing was used to connect the steel faceplates. The impact experimental programme was similar to the static experimental programme, where the effects of reinforced concrete core, lightweight concrete core, degree of interaction between steel and concrete, and application of stainless steel were investigated. The Control panel in the impact test had a normal weight concrete core and mild steel faceplates, and it was subjected to impact energy of the drop hammer released from a height of 3 m. For other panels, one design parameter was varied to obtain a more detailed picture of the response of the SCS panels under impact loading condition.

Three additional panels prepared were the Increased impact energy panel, Panel with bracing elements and Double reinforced core panel compared to the static experimental programme. These panels were used to evaluate the effects of increased impact energy, the small bracings connecting steel faceplates and reinforcement amount on the impact response of SCS panels. In the Panel with bracing elements, 30 mm wide steel plates of 3 mm thickness were used to connect the steel faceplates at mid-span, quarter-spans and at the flared, similar to the SCS panels in the static test. The SCS panel preparation process and the mix design of lightweight concrete was presented in Chapter 5.

Table 7.1: Detailed description of the SCS panels used in the impact test.

	Panel	Parameters investigated	Description
1	Control panel (CP)	Axial restraint	<ul style="list-style-type: none"> • normal weight concrete core and mild steel faceplates • 3 m drop height
2	Increased impact	Increased impact energy	<ul style="list-style-type: none"> • normal weight concrete core and mild steel faceplates

	energy panel (4mP)		<ul style="list-style-type: none"> • 4 m drop height
3	Panel with bracing elements (BP)	Small bracings connecting steel faceplates	<ul style="list-style-type: none"> • normal weight concrete core and mild steel faceplates • 30 mm wide steel plates of 3 mm thickness used to connect the steel faceplates at mid-span, quarter-spans and at the flared • 3 m drop height
4	Lightweight core panel (LP)	Lightweight concrete core	<ul style="list-style-type: none"> • lightweight concrete core (1400 kg/m³) and mild steel faceplates • 3 m drop height
5	Reinforced core panel (RP)	Reinforced concrete core	<ul style="list-style-type: none"> • normal weight concrete core reinforced with 2 layers of 4@50 mm wire mesh (reinforcement ratio = 0.6%), mild steel faceplates • 3 m drop height
6	Double reinforced core panel (DRP)	Reinforcement amount	<ul style="list-style-type: none"> • normal weight concrete core reinforced with 2 layers of 4@25 mm wire mesh (reinforcement ratio = 1.2%), mild steel faceplates • 3 m drop height
7	Improved bonding panel (IBP)	Degree of interaction between steel and concrete	<ul style="list-style-type: none"> • normal weight concrete core and mild steel faceplates • a layer of 3@25 mm wire mesh tack welded to mild steel faceplates before concrete casting • 3 m drop height
8	Fully enclosed panel (ECP)	Degree of interaction between steel and concrete	<ul style="list-style-type: none"> • normal weight concrete and mild steel faceplates • two mild steel end caps of 3 mm thickness were welded to mild steel faceplates • 3 m drop height
9	Stainless steel panel (SP)	Stainless steel	<ul style="list-style-type: none"> • normal weight concrete core and stainless steel faceplates • 3 m drop height

It is important to note that the steel faceplates were separated from the concrete core due to the failure of concrete chemical bonding during experiment set up for some panels. This phenomenon occurred to all the SCS panels except the Panel with bracing elements and the Improved bonding panel, where small steel plate bracings and improved bonding between the steel and concrete core, preserved the bonding between the concrete core and steel faceplates. Figure 7.4 shows the separation of steel faceplates from the concrete core prior to the impact test.



Figure 7.4: Separation of the steel faceplates from the concrete core for the Control panel prior to the impact test.

7.2 Experimental results

7.2.1 Concrete compressive strength

The normal weight concrete used to fill the SCS panels was ready-mix concrete obtained from a contractor with a targeted compressive strength of 40 MPa. Different batches of concrete were used to fill the SCS panels. It was discovered that the compressive strength of the concrete used to fill the Control panel, Reinforced core panel, Double reinforced core panel and Increased impact energy panel was 23 MPa on the days of panel testing. The concrete compressive strength was significantly lower than the targeted compressive strength (40 MPa) due to the poor concrete mix design. For the Stainless steel panel, Improved bonding panel and Fully enclosed panel, the concrete compressive strength was 37 MPa. The concrete compressive strength for the Panel with bracing elements and the Lightweight core panel was 40 MPa and 11 MPa, respectively.

Table 7.2: Concrete compressive strength for the concrete infill in the SCS panels.

Panels	Concrete compressive strength (MPa)
Control panel, Reinforced core panel, Double reinforced core panel and Increased impact energy panel	23
Stainless steel panel, Improved bonding panel and Fully enclosed panel	37
Lightweight core panel	11
Panel with bracing elements	40

7.2.2 Response of axially restrained SCS panels under impact loading condition

7.2.2.1 Control panel

The Control panel had mild steel faceplates and a normal weight concrete core. The drop hammer was released from a height of 3m to produce an impact load at mid-span. The impact load and displacement time histories of the Control panel are shown in Figure 7.5. Due to the hard impact contact between the high strength steel impactor and top steel faceplate of the panel, the dynamic load cell mounted on the drop hammer recorded high frequency noises during the test. The raw load time histories of all the panels were digitally filtered using a low-pass fourth-order Butterworth filter in accordance with CFC1000 (ISO 6487, 2002). The cut-off frequency for the CFC1000 Butterworth filter was 1650 Hz. From the load time history of the Control panel, it could be observed that there were three distinct load resisting mechanisms, namely inertial effect at the initial stage (0-0.005 s), flexural resistance of the panel (0.004-0.014 s), followed by the tensile membrane resistance of the steel faceplates (>0.014 s).

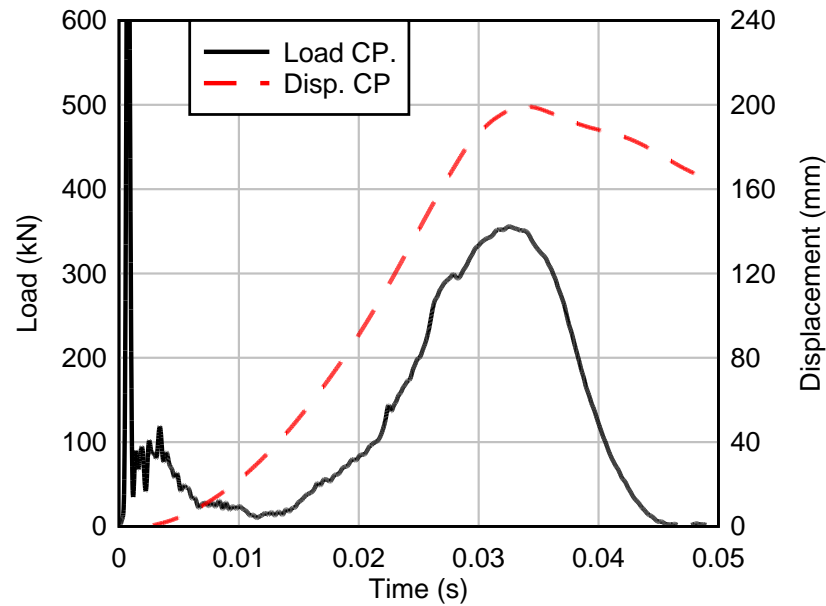


Figure 7.5: Impact load and displacement time histories of the Control panel (CP).

When the drop hammer and panel first came into contact, the load increased instantaneously to more than 600 kN. It was discovered that when the hammer first hit the specimen, a significant force was observed due to the acceleration of the mass of the specimen in accordance to the speed of the hammer. This inertial force peak set the specimen and load cell to a very rapid vibration and, therefore, the impact load measured from the load cell bore no actual resemblance to the real load which was acting on the specimen during the first 1 or 2 milliseconds.

After the initial peak force, the load time history of the Control panel showed high frequency oscillations at around 100 kN up to 5 milliseconds. Due to the impact momentum from the drop hammer, the specimen tried to fly off from the drop hammer. As the drop hammer lost contact with the panel, the recorded impact force diminished. At the same time, the panel started to bend and the reaction forces started to appear at the supports. The deformation of the panel dissipated the impact energy, and the drop hammer came into contact with the panel again causing the impact force to increase. This process of repeat impact phenomenon caused the dynamic load cell to record high frequency oscillations at this stage. Therefore, the impact force recorded in the load cell during this period represented a combination of inertial force and the flexural resistance of the Control panel. The magnitude of this

impact force depended on the stiffness and the mass of the panel (Liew et al. 2009). The impact force increased with the increased stiffness of the panel. From the displacement time history in Figure 7.5, the displacement of the Control panel at mid-span was small during this stage. From the strain time history in Figure 7.6, it showed that the centre of bottom faceplate had yielded during this stage, where the strain recorded was about 0.002 and exceeded the yield strain of 0.00135 for mild steel faceplates.

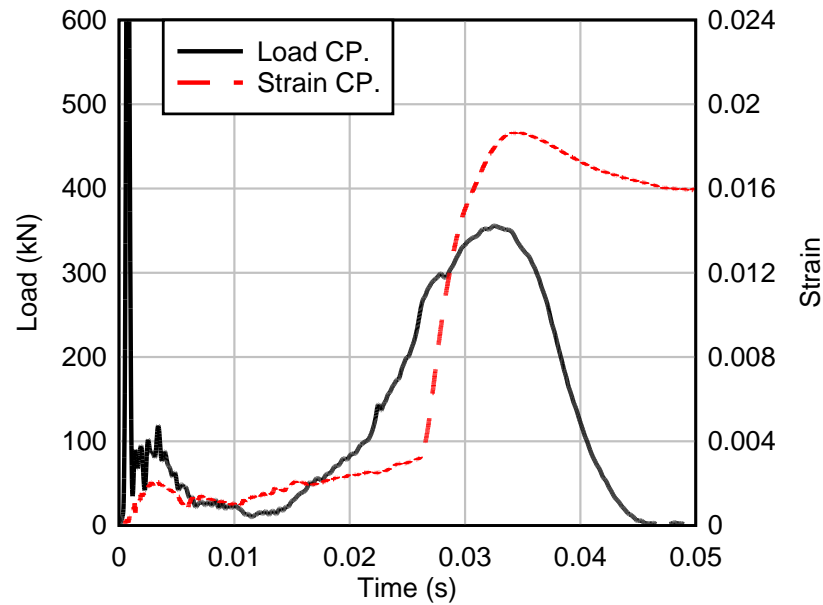


Figure 7.6: Impact load and strain time histories of the Control panel (CP).

The flexural resistance occurred after the inertial resistance stage. The actual flexural load capacity of the Control panel was difficult to determine from the experimental results as the flexural resistance dropped significantly after the inertial effects due to the damage of concrete core sustained during the inertial stage. Therefore, the resistance measured by the dynamic load cell during 0.007 s to 0.012 s was the residual flexural resistance of the Control panel. The residual flexural resistance of the Control panel was about 20 kN.

When the mid-span displacement of the Control panel reached about 40 mm (Figure 7.5), the resistance increased due to development of tensile membrane resistance in the steel faceplates. The tensile membrane resistance became dominant and exceeded the impact force of 100 kN (due to combination of inertial effect and flexural

resistance), as the mid-span displacement exceeded 80 mm. The strain at the centre of the bottom faceplate increased during tensile membrane resistance stage, and when the membrane resistance exceeded 300 kN, the strain increased significantly (Figure 7.6). The Control panel reached the peak tensile membrane resistance of 354 kN at a maximum displacement of 199 mm. The panel then bounced back to a residual mid-span displacement of about 160 mm. The drop hammer rebounded from the panel, and the impact force diminished to zero. The impact load-displacement relationship of the Control panel is illustrated in Figure 7.7. It should be noted that the peak tensile membrane resistance obtained in this test does not represent the ultimate tensile membrane capacity of the Control panel, as there was not failure mode observed in the membrane resistance stage. The tensile membrane resistance could increase if higher energy demands were imposed, e.g. due to close-range blast loadings. The maximum displacement of the SCS panels in this study was limited by the impact energy delivered from the drop hammer.

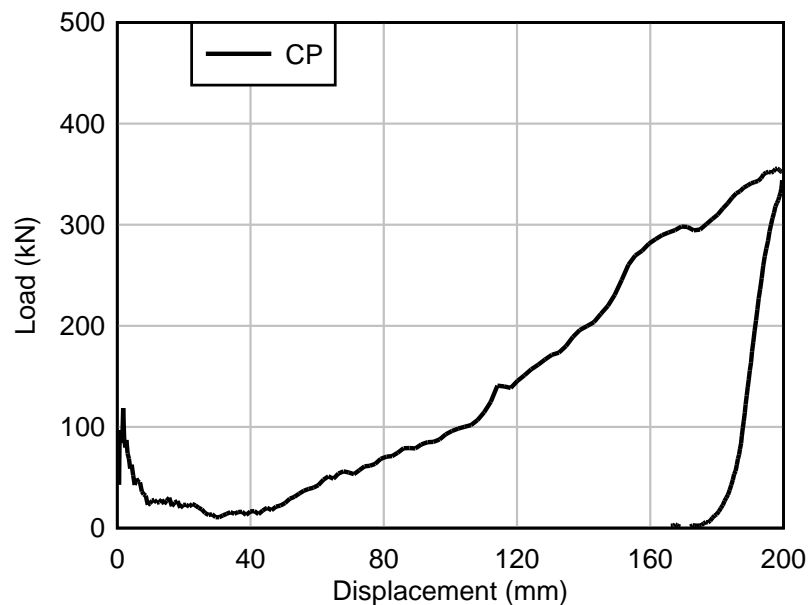


Figure 7.7: Impact load-displacement relationship of the Control panel (CP) subjected to mid-span impact.

The damage on the Control panel observed after the impact test is illustrated in Figure 7.8. The top steel faceplate was indented by the impactor. The concrete core at the mid-span experienced severe damage, where the concrete fractured and fell out from the panel. A wide crack was observed in the concrete core at the support and the end plate buckled.



Figure 7.8: Damage on the Control panel observed after the impact test, (a) indentation on the top steel faceplate, (b) extensive damage of concrete core at mid-span, (c) wide crack at the support and buckling of steel end plate.

7.2.2.2 Increased impact energy panel

In this test, the height of the drop hammer was increased to 4 m to evaluate the effects of increased impact energy to the response of the SCS panel. The Increased impact energy panel had mild steel faceplates, and it was filled with normal weight concrete. The impact load-displacement relationship of the Increased impact energy panel was compared to the Control panel in Figure 7.9. The impact force after initial peak force was about 130 kN, slightly higher than the Control panel of 100 kN. The residual flexural resistance of the Increased impact energy panel was similar with the Control panel, about 20 kN. The strain time history in Figure 7.10 shows that the bottom faceplate of the Increased impact energy panel had yielded at mid-span during the inertia stage and fluctuated during the flexural resistance stage. The tensile membrane response of the Increased impact energy panel was similar to the Control panel for displacements up to 130 mm. After that, the Increased impact energy panel showed higher tensile membrane resistance than the Control panel at the same displacement. After the impact load exceeded 360 kN, the strain at the centre of the

bottom faceplate increased significantly. From both load-displacement relationship and strain time history of the Increased impact energy panel, it showed that the tensile membrane resistance started to drop before the maximum displacement and maximum strain were reached. The peak tensile membrane resistance of 430 kN was reached at 193 mm mid-span displacement. The maximum mid-span displacement was 205 mm and the maximum strain at the bottom faceplate was 0.021. After that, the panel bounced back and the impact force decreased to zero.

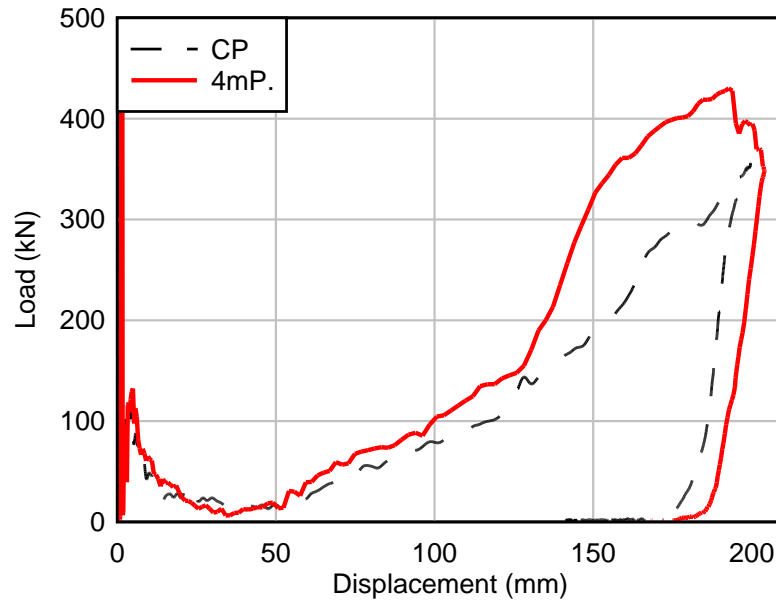


Figure 7.9: A comparison of impact load-displacement relationship between the Increased impact energy panel (4mP) and Control panel (CP).

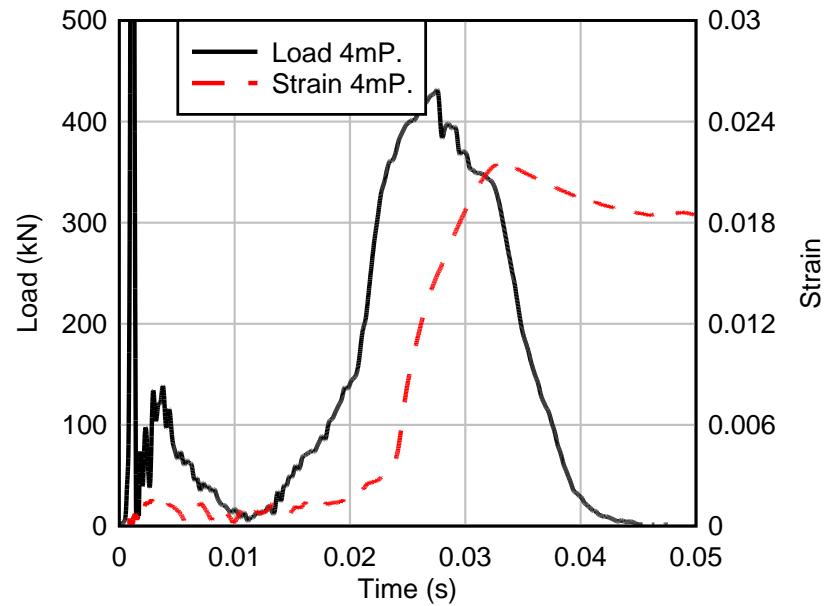


Figure 7.10: Impact load and strain time histories of the Increased impact energy panel (4mP).

The decrease in tensile membrane resistance before the panel reached its maximum displacement implied that the panel was beginning to fail. The failure of the tensile membrane resistance in the Increased impact energy panel could be attributed to the partial fracture of the top steel faceplate and the buckling end plate, as shown in Figure 7.11. These results showed that when SCS panels subjected to very high impact energy from a hard projectile, the localized damage, such as penetration and buckling of end plate could cause the failure of the panel.



Figure 7.11: Damage on the Increased impact energy panel, (a) a partial fracture of the top faceplate, (b) buckling of the end plate.

7.2.2.3 Lightweight core panel

The Lightweight core panel had mild steel faceplates and it was filled with lightweight concrete. The density and compressive strength of the lightweight concrete were 1400 kg/m^3 and 11 MPa , respectively. Figure 7.12 shows the comparison between the impact load-displacement relationship of the Lightweight core panel and Control panel. The impact force after the initial peak force of the Lightweight core panel was about 80 kN , which was slightly lower than the Control panel of 100 kN . The Lightweight core panel displayed very low residual flexural strength similar to the Control panel. Figure 7.13 shows that the centre of the bottom faceplate remained elastic at the beginning of the tensile membrane resistance stage, until the resistance exceeded 200 kN . At about 120 mm displacement, the resistance of the Lightweight core panel slightly dropped due to unknown reasons and increased again at 160 mm displacement. The Lightweight core panel reached the maximum displacement of 195 mm and the peak tensile membrane resistance of 333 kN . The maximum displacement of the Lightweight core panel was slightly lower than that of the Control panel. The maximum strain at the centre of the bottom faceplate was significantly lower than that of the Control panel.

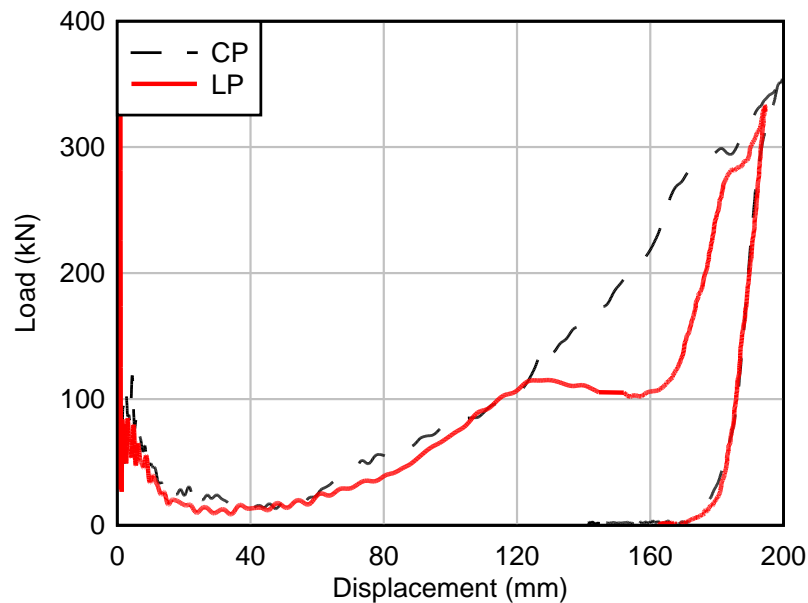


Figure 7.12: A comparison of impact load-displacement relationship between the Lightweight core panel (LP) and Control panel (CP).

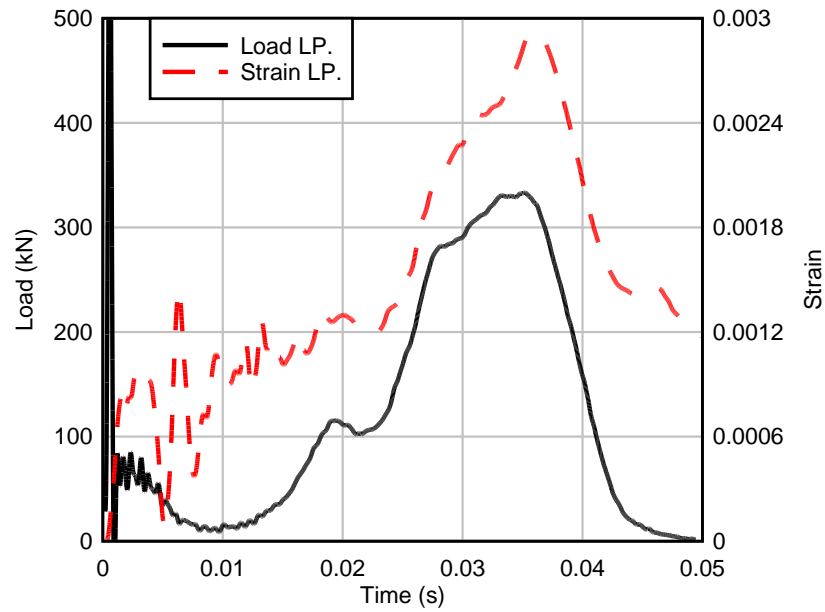


Figure 7.13: Impact load and strain time histories of the Lightweight core panel (LP).

Due to lower concrete compressive strength, the end plate of the Lightweight core panel buckled as shown in Figure 7.14 (a). Figure 7.14 (b) shows that the lightweight concrete core was extensively cracked along the span. The results of this test showed that the lightweight concrete core only had minor effects on the load-displacement relationship of SCS panel under this impact condition.

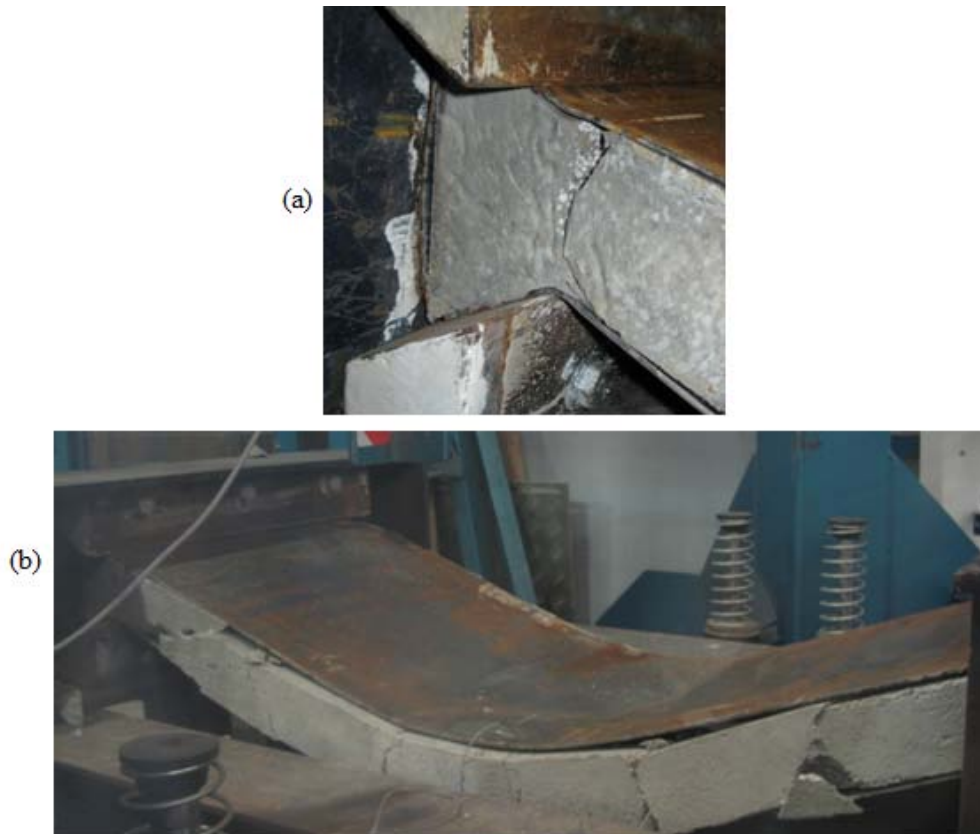


Figure 7.14: Damage of the Lightweight core panel: (a) buckling of the end plate, (b) extensive cracking on the concrete along the span.

7.2.2.4 Panel with bracing elements

Small steel plate bracings were used to connect the steel faceplates before concrete casting for the Panel with bracing elements. Figure 7.15 shows that the impact force after the initial peak force was similar to the Control panel of 100 kN. The Panel with bracing elements showed a flexural load capacity of about 75 kN, before it dropped to a residual flexural resistance of 30 kN, which was higher than the Control panel's of 20 kN. Figure 7.16 shows the centre of the bottom faceplate had yielded during the flexural response. The peak tensile membrane resistance was 242 kN at the maximum displacement of 181 mm. The maximum strain at the bottom faceplate was about 0.0055. The tensile membrane resistance of the Panel with bracing elements was lower than the Control panel at the 181 mm displacement, which was about 300 kN. Figure 7.17 shows the damage of the concrete core was concentrated at the position of bracings and no damage could be observed at the flared ends. The results of this panel showed that the flexural resistance of SCS panel was significantly

increased compared to the Control panel, due to the bracings maintaining integrity of its concrete core under impact loading conditions. The tensile membrane resistance of the Panel with bracing elements was slightly lower than the Control panel, due to unknown reasons.

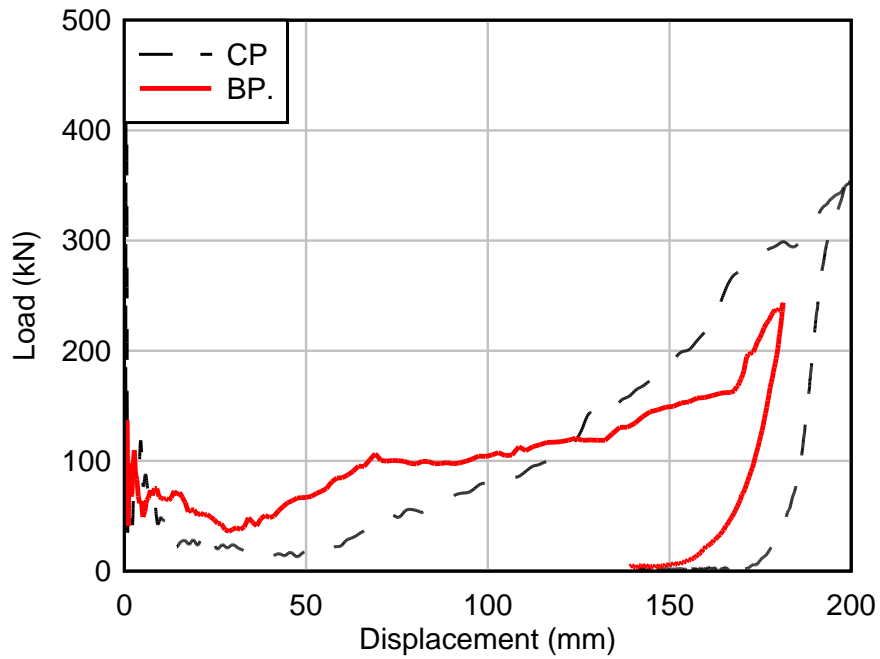


Figure 7.15: A comparison of impact load-displacement relationship between the Panel with bracing elements (BP) and Control panel (CP).

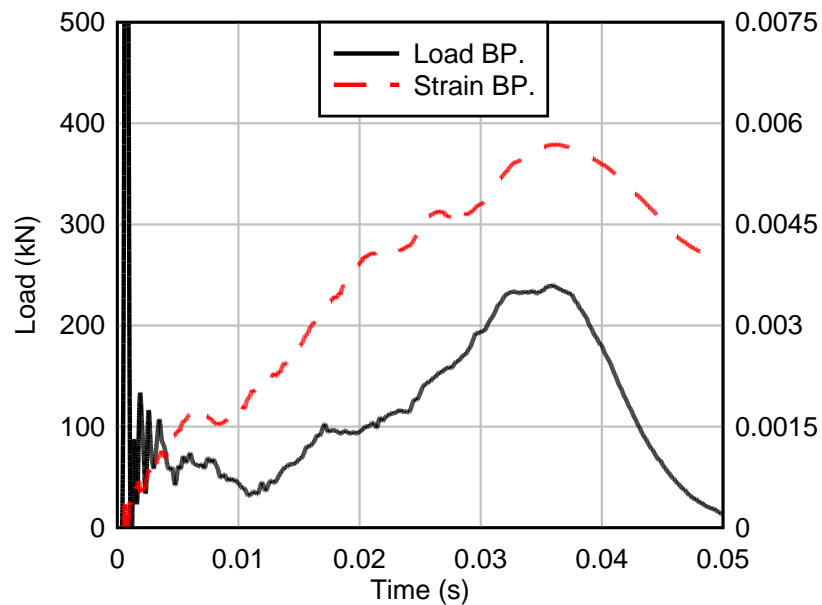


Figure 7.16: Impact load and strain time histories of the Panel with bracing elements (BP).

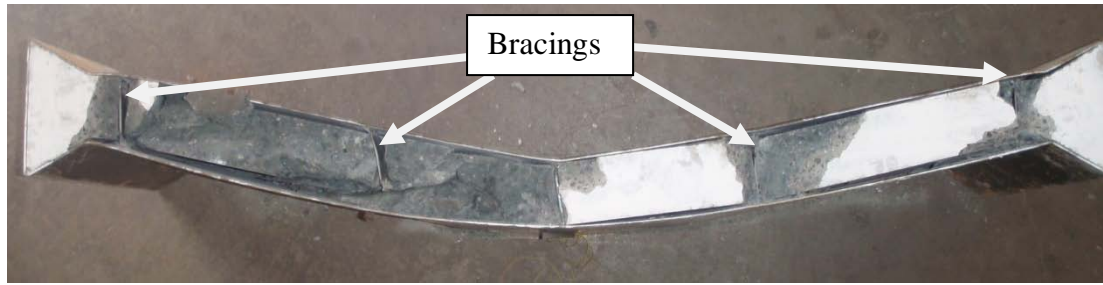


Figure 7.17: Damage of concrete for the Panel with bracing elements.

7.2.2.5 Reinforced core panel and Double reinforced core panel

Two SCS panels with reinforced concrete core tested were the Reinforced core panel and the Double reinforced core panel. The reinforcement ratio for the Reinforced core panel was 0.6% and the Double reinforced core panel was 1.2%. The impact load-displacement relationships for these panels were compared to the Control panel in Figure 7.18. The impact force after the initial peak load for both panels was about 200 kN, which was significantly higher than the Control panel's of 100 kN. This was due to the increased stiffness of the SCS panels when the reinforcement was provided in the concrete core. After that, the impact load decreased to almost 10 kN due to the drop hammer losing contact with the panels. The impact force increased again when the drop hammer came into contact with the panels. The flexural load capacity of the Reinforced core panel and the Double reinforced core panel was about 86 kN and 102 kN, respectively. The flexural load capacity of these panels was significantly increased compared to the Control panel because the reinforcement maintained the integrity of the concrete core, and the reinforced concrete core provided additional moment resistance. Figure 7.19 and Figure 7.20 show that the bottom steel faceplates had yielded at mid-span during the flexural resistance stage where the yield strain of mild steel was at 0.00135.

The peak tensile membrane resistance of the Reinforced core panel was 285 kN at a maximum displacement of 183 mm. As for the Double reinforced core panel, it reached a peak tensile membrane resistance of 211 kN at the maximum mid-span displacement of 177 mm. The maximum displacements for both panels were lower than the maximum displacement of the Control panel (199 mm). The tensile membrane resistance for both panels at the maximum displacement were compared

to the Control panel. For the Reinforced core panel, the tensile membrane resistance was 285 kN compared to the Control panel's 300 kN, at a displacement of 183 mm. The Double reinforced core panel showed 211 kN at a displacement of 177 mm compared to 300 kN for the Control panel. Both panels showed a lower tensile membrane resistance compared to the Control panel at the same displacement due to the damage of concrete infill at the flared ends, as shown in Figure 7.21 (a).

Figure 7.19 shows that the strain at the centre of the bottom faceplate of the Reinforced core panel remained almost constant during the tensile membrane resistance stage due to unknown reasons. For the Double reinforced core panel, the strain at the centre of the bottom faceplate increased until the peak of the membrane resistance was reached as shown in Figure 7.20. The maximum strain of these panels was lower than the maximum strain of the Control panel as the peak tensile membrane resistance for these panels was lower than the Control panel. The crushing and cracking of the concrete core at the mid-span for the Reinforced core panel is illustrated in Figure 7.21 (b). Figure 7.21 (c) shows the buckling of the top layer of wire mesh at mid-span. The damage of the Double reinforced core panel was similar to the Reinforced core panel. The results of these panels showed that the flexural load capacity could be increased significantly by adding reinforcement to the concrete core of the SCS panels. However, due to the damage of the concrete infill at the flared ends, the stiffness of axial restraint was reduced and the tensile membrane resistance was lower than the Control panel at large displacement.

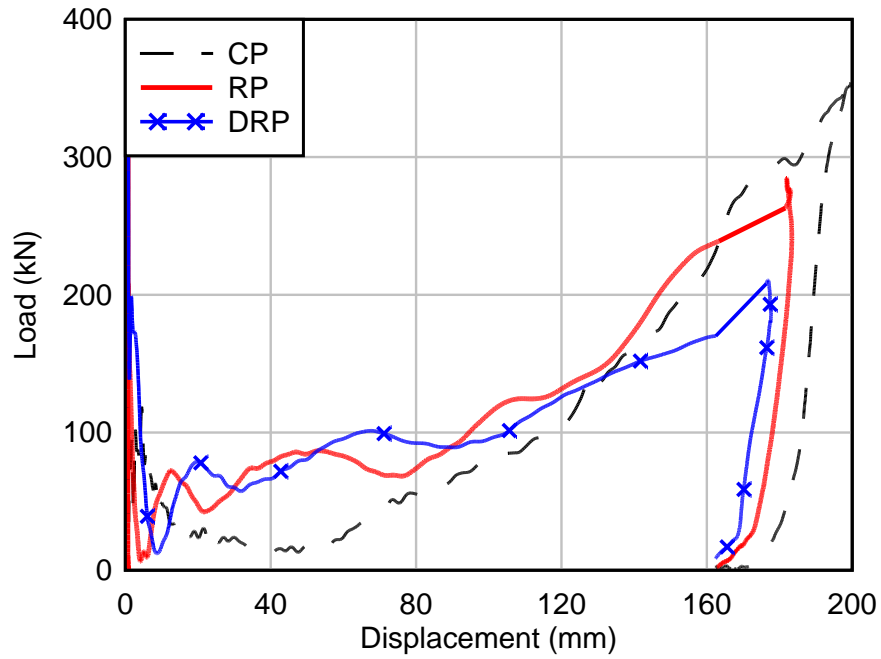


Figure 7.18: A comparison of impact load-displacement relationship between the Reinforced core panel (RP), Double reinforced core panel (DRP) and Control panel (CP).

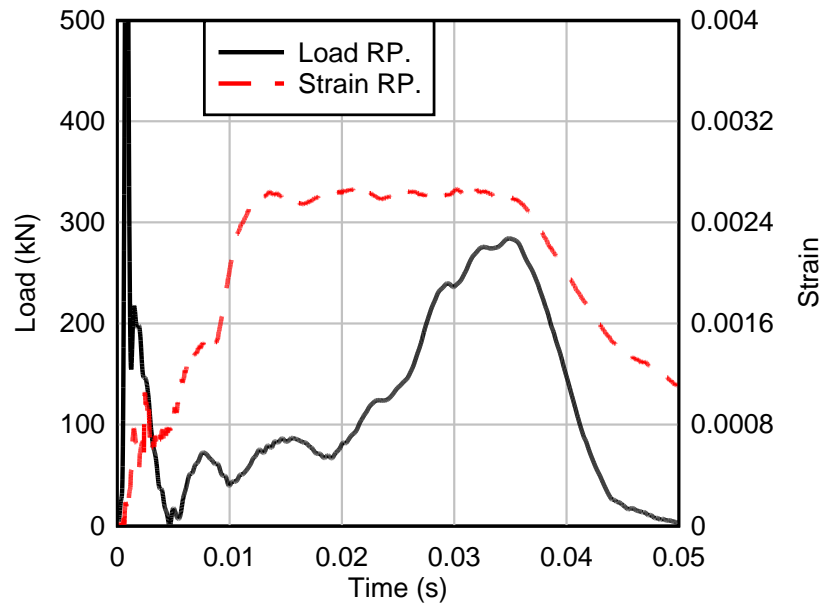


Figure 7.19: Impact load and strain time histories of the Reinforced core panel (RP).

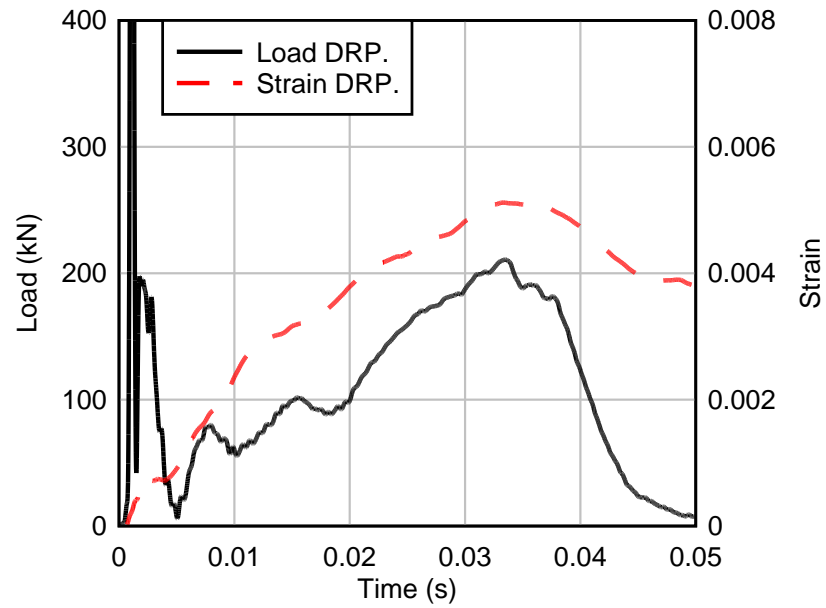


Figure 7.20: Impact load and strain time histories of the Double reinforced core panel (DRP).



Figure 7.21: Damage on the Reinforced core panel: (a) cracking of concrete at flared zone, (b) crushing and cracking of concrete at mid-span, (c) buckling of top layer of wire mesh at mid-span.

7.2.2.6 Stainless steel panel

The impact load-displacement relationship of the Stainless steel panel was compared to the Control panel in Figure 7.22. The inertial response of the Stainless steel panel was similar to the Control panel, where the impact force after the first peak load was about 100 kN. The Stainless steel panel showed a flexural load capacity of 66 kN before the resistance dropped gradually to the residual flexural strength of 20 kN. The centre of bottom steel faceplate had yielded during the inertial stage with a strain of 0.0021 as shown in Figure 7.23. The strain increased slightly during the flexural resistance stage.

The tensile membrane resistance only started to develop in the Stainless steel panel after the displacement exceeded 120 mm. The tensile membrane resistance increased significantly after the displacement of the panel exceeded 150 mm due to significant increment of strain at the centre of the bottom faceplate, as shown in Figure 7.23. The Stainless steel panel reached a maximum displacement of 181 mm with the peak tensile membrane resistance of 378 kN. The maximum strain of the bottom faceplate at mid-span was 0.0245. When the tensile membrane resistance was compared at 181 mm displacement, the Stainless steel panel (378 kN) showed a higher resistance than the Control panel of 300 kN. The tensile membrane resistance is proportional to the displacement and the yield stress of the steel plate as shown in Chapter 3. The Stainless steel panel showed a higher tensile membrane resistance at the same displacement because its yield stress was higher than the mild steel plate used in this study. In addition, the strain hardening effects of the stainless steel also contributed to the higher tensile membrane resistance compared to mild steel panels at the same displacement. The indentation of the top steel faceplate and fracture of the concrete core on the Stainless steel panel were similar to the Control panel.

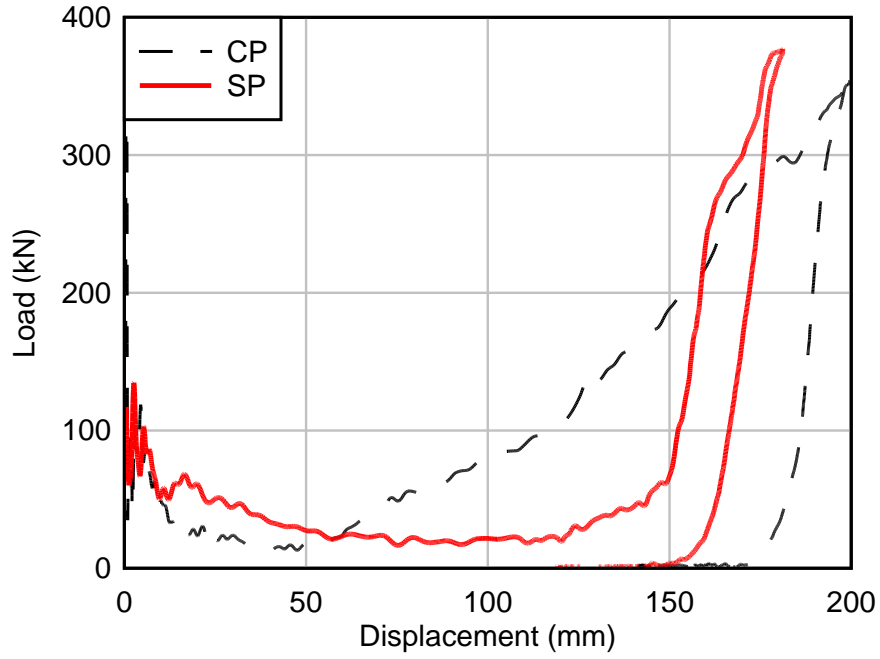


Figure 7.22: A comparison of impact load-displacement relationship between the Stainless steel panel (SP) and Control panel (CP).

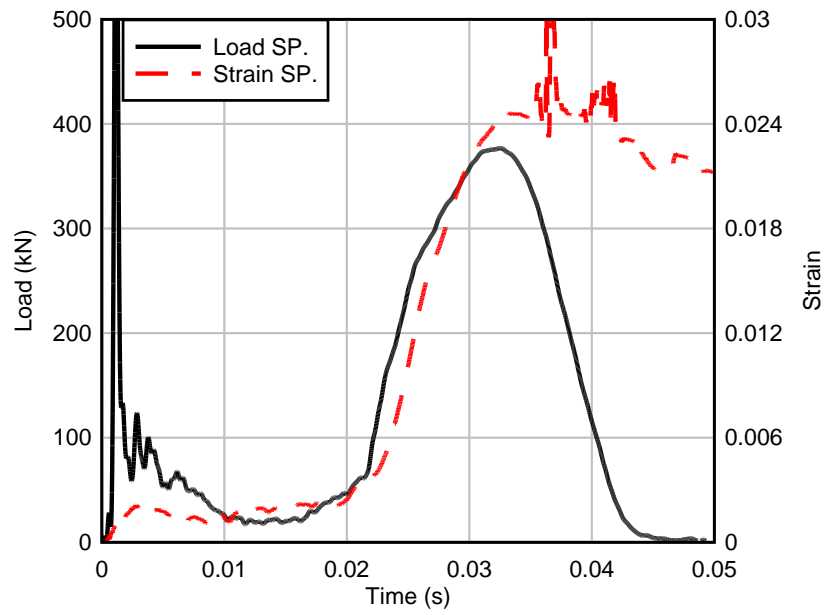


Figure 7.23: Impact load and strain time histories of the Stainless steel panel (SP).

7.2.2.7 Improved bonding panel

A layer of 3@25 mm wire mesh was tack welded to the inner surface of the top and bottom faceplates before concrete casting to increase the bond strength between the steel and concrete core. Figure 7.24 shows that the impact force after the initial peak force of the Improved bonding panel was about 240 kN, which was significantly higher than that for the Control panel of 100 kN, due to the increased stiffness when the wire mesh was added. The flexural load capacity for this panel was about 125 kN, and the centre of the bottom faceplate had yielded as shown in Figure 7.25. After the panel reached its flexural load capacity, the load resistance dropped and remained at around 90 kN until the mid-span displacement reached 150 mm. Then, the tensile membrane resistance started developing in the steel faceplates, and the load resistance started increasing.

The panel reached the maximum displacement of 169 mm at the peak tensile membrane resistance of 210 kN. The tensile membrane resistance of this panel was lower than that for the Control panel (300 kN) at the same displacement. Figure 7.26 shows that the wire meshes were embedded in the concrete core and separated from the steel faceplates due to failure of the tack welding between the wire mesh and steel faceplates. The damage of the concrete core at the mid-span was similar to the Reinforced core panel. The results of this panel showed that the flexural load capacity increased significantly with increased degree of interaction between the steel and concrete core. The panel underwent large displacement of about 150 mm before the tensile membrane resistance started to develop.

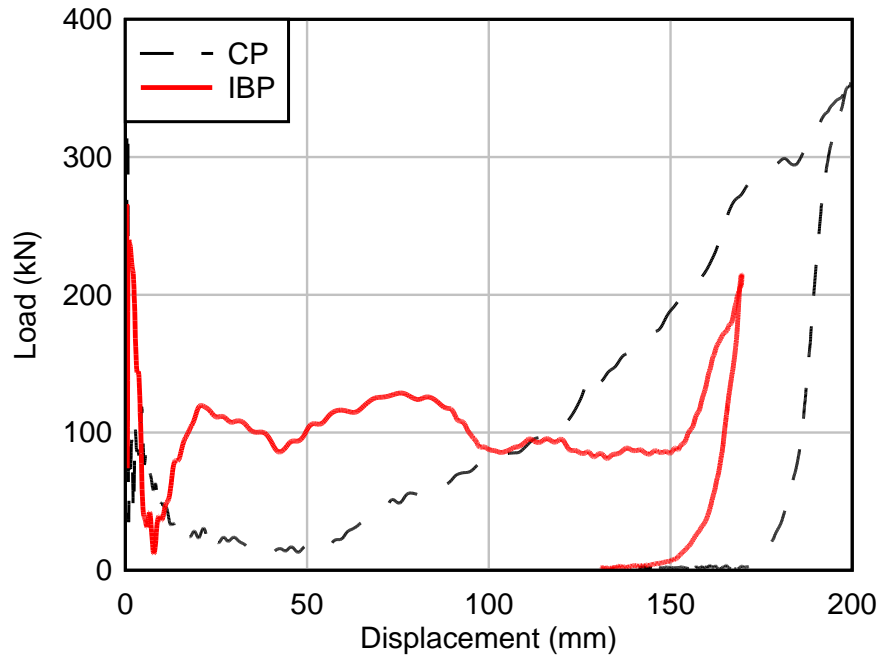


Figure 7.24: A comparison of impact load-displacement relationship between the Improved bonding panel (IBP) and Control panel (CP).

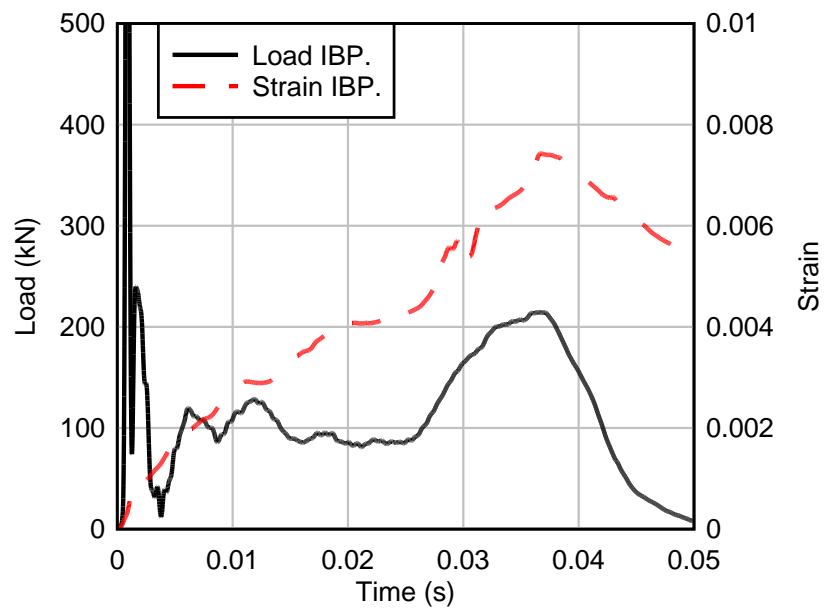


Figure 7.25: Impact load and strain time histories of the Improved bonding panel (IBP).



Figure 7.26: Separation of wire meshes from the steel faceplates on the Improved bonding panel.

7.2.2.8 Fully enclosed panel

Two end caps were welded to the steel faceplates after concrete casting to form a fully enclosed panel. Figure 7.27 shows that the impact force after the initial peak force was about 280 kN for the Fully enclosed panel. It was significantly higher than that for the Control panel of 100 kN because the stiffness of panel was increased by adding the end caps to the panel. After that, the panel showed a flexural load capacity of about 130 kN and the resistance dropped gradually to about 80 kN before tensile membrane resistance started developing. Figure 7.28 shows that the centre of the bottom faceplate yielded when the panel reached its flexural load capacity. The tensile membrane resistance of the Fully enclosed panel started at about 120 mm displacement, and the stiffness of the tensile membrane resistance was similar to the Control panel. The peak tensile membrane resistance for this panel was about 150 kN at the maximum displacement of 138 mm. After the test, it was observed that the welding between one of the end caps and the steel faceplates had failed, and the panel showed non-symmetrical damage. Figure 7.29 shows one of the end caps had buckled and a welding failure between another end cap and the steel faceplates.

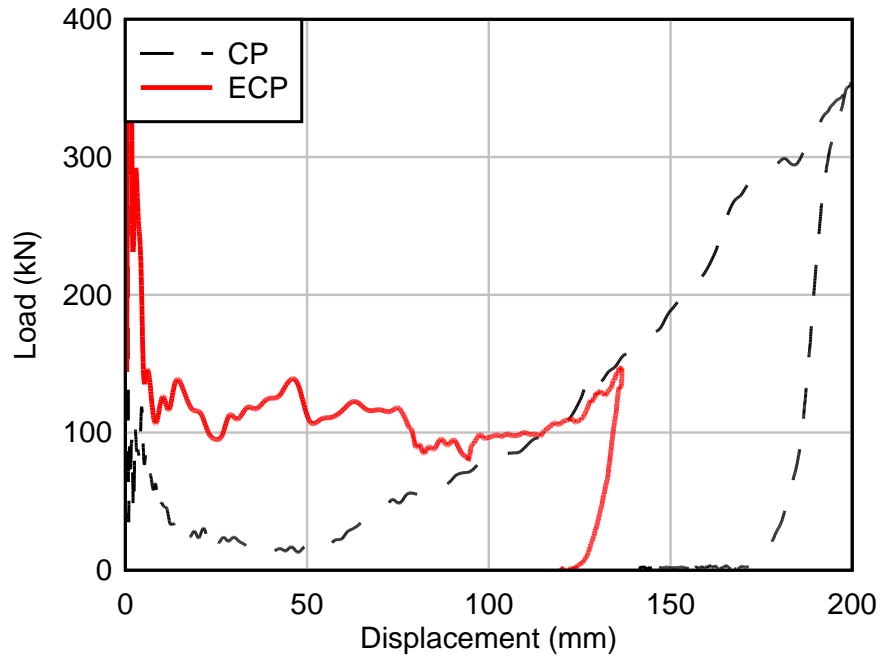


Figure 7.27: A comparison of impact load-displacement relationships between the Fully enclosed panel (ECP) and Control panel (CP).

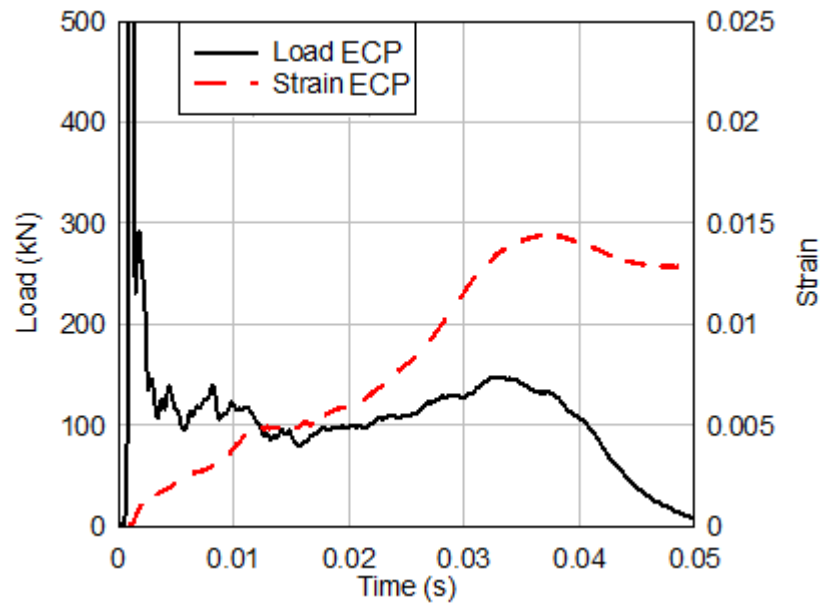


Figure 7.28: Impact load and strain time histories of the Fully enclosed panel (ECP).

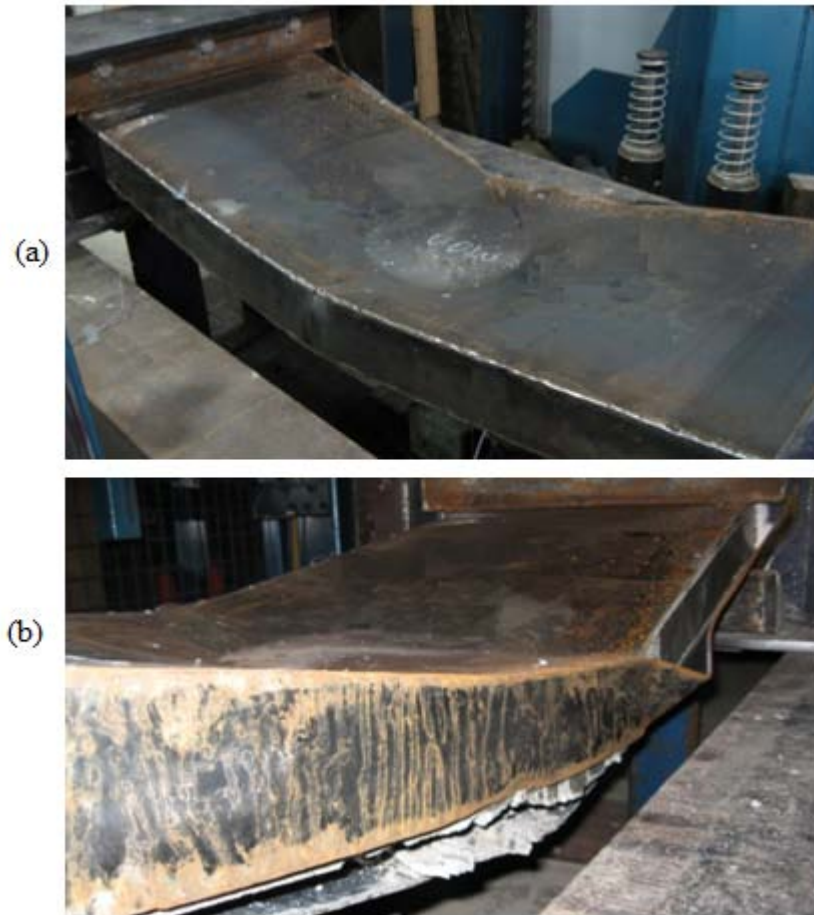


Figure 7.29: Damage on the Fully enclosed panel: (a) buckling of the end cap and indentation of the top faceplate, (b) failure of the welding between the steel faceplates and end cap.

7.3 Analysis of impact test results of axially restrained SCS panels

7.3.1 Control panel versus Increased impact energy panel

The impact load-displacement relationship of the Control panel was compared to the load-displacement relationship of the Control panel obtained from the static three-point bending test as shown in Figure 7.30. It should be noted that small steel plate bracings were provided to connect the top and bottom steel faceplates for the Control panel used in the static test, while in the impact test, no bracing was provided. It was observed that the Control panel subjected to impact loading resisted the impact force of 100 kN at the initial stage, which was higher than the static flexural load capacity of 58 kN. The residual flexural strength of the Control panel in the impact test was very low due to the fracture of the non-reinforced concrete core when no small bracing was used to connect the steel faceplates.

The tensile membrane resistance from the static and impact tests was similar for the displacements in the range of 100 mm to 160 mm. After that, the stiffness of the Control panel under impact loading was reduced compared to the static response, which could be attributed to the buckling of the steel plate (Figure 7.8). The theoretical tensile membrane resistance was predicted using the analytical solution by Hodge Jr. (1974). It was found that the impact load-displacement relationship of the Control panel correlated well with the theoretical tensile membrane resistance of two steel plates with an axial stiffness parameter, $k = 0.00012$ for the displacements between 30 mm to 160 mm. The axial stiffness parameter (k) was the stiffness of axial restraint on the SCS panel determined from the static test in Chapter 6. The strain rate effects of mild steel were ignored in the theoretical analysis.

This showed that the tensile membrane resistance of the two steel faceplates could be used as the static resistance function for the Control panel under impact loading. The inertial effect and the flexural resistance of the Control panel under impact loading condition was negligible as the impact energy dissipated by these mechanisms was insignificant compared to the energy dissipated by the tensile membrane resistance. It should be noted that the experimental impact membrane resistance was lower than the theoretical prediction at large displacement (>160 mm) due to the buckling of the end plate at the flared end.

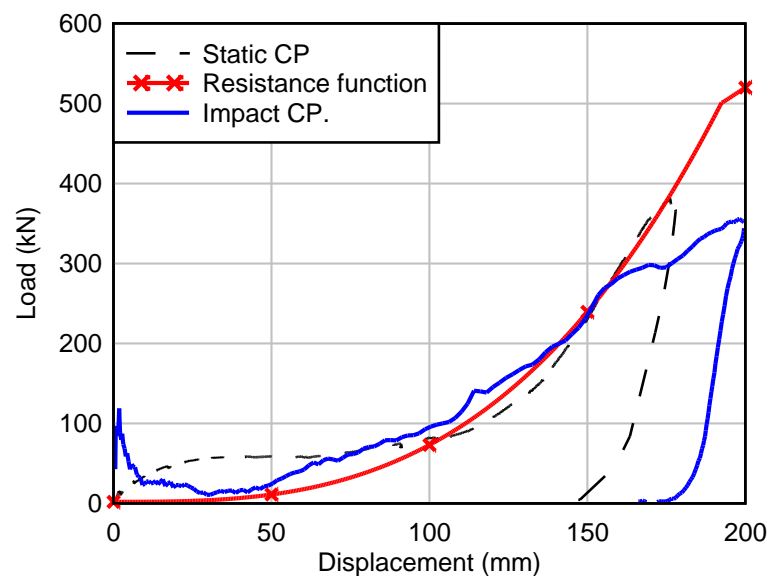


Figure 7.30: A comparison between the quasi-static and impact load-displacement relationships of the Control panel (CP), and the theoretical static resistance function.

The impact load-displacement relationship of the Increased impact energy panel was compared to the quasi-static load-displacement relationship of the Control panel in Figure 7.31. The configuration of the Increased impact energy panel was similar to the Control panel used in the static test except no small steel plate bracing was used to connect the steel faceplates in the Increased impact energy panel. During the initial stage of response, the impact force of 130 kN was recorded in the panel and it was significantly higher than the static flexural load capacity of 58 kN. The residual flexural strength of the Increased impact energy panel was very low due to fracture of the concrete core.

It showed that the tensile membrane response of the panels from both static and impact tests was similar for the displacements in the range of 100 mm to 170 mm, with the tensile membrane resistance of the Increased impact energy panel higher than the static membrane resistance of the Control panel. After the displacement of the Increased impact energy panel exceeded 160 mm, the stiffness of the tensile membrane resistance reduced and the membrane resistance started to drop before the panel reached its maximum displacement. This was due to the partial fracture failure of the top steel faceplate and the damage at the flared zone, as shown in Figure 7.11.

The theoretical membrane analysis of two steel faceplates (Hodge Jr., 1974) using an axial stiffness parameter of $k = 0.00012$ (Chapter 6), could predict the tensile membrane resistance of the Increased impact energy panel with reasonable accuracy for displacements in the range of 30 mm to 170 mm. It should be noted that the strain rate effects of mild steel were ignored in the theoretical analysis and the analysis could not predict the partial fracture failure of the top steel faceplates. By ignoring the strain rate effects of mild steel, the static resistance function was slightly more conservative than the experimental tensile membrane resistance under impact loading condition.

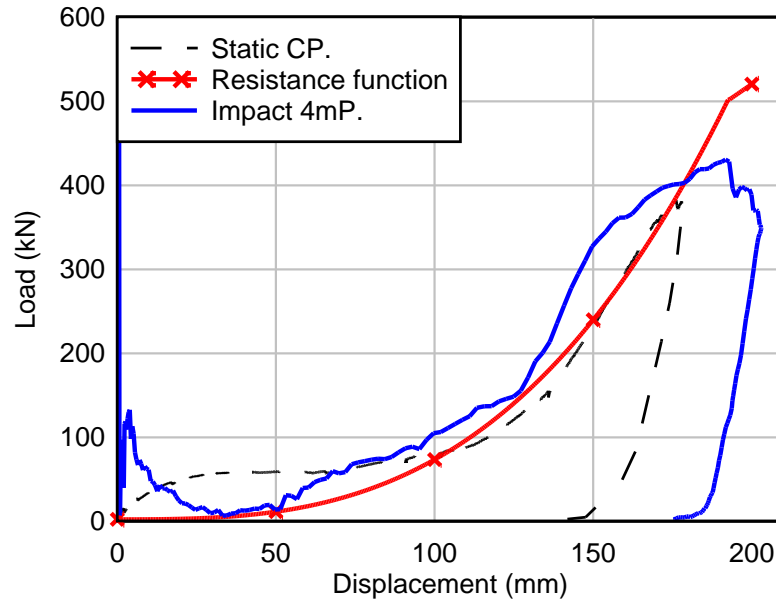


Figure 7.31: A comparison between the impact load-displacement relationship of the Increased impact energy panel (4mP), the static load-displacement relationship for the Control panel (CP), and the theoretical static resistance function.

7.3.2 Lightweight core panel

Figure 7.32 shows the comparison between the impact and quasi-static load-displacement relationships for the Lightweight core panel. In the quasi-static test, small steel plate bracings were used to connect the steel faceplates of the Lightweight core panel, while no bracings were used in the impact test. It showed that the impact force of about 80 kN at the initial stage was higher than the static flexural load capacity of 30 kN. The residual flexural strength of the Lightweight core panel under impact loading was lower than the static flexural strength due to fracture of the concrete core.

Generally, the tensile membrane resistance under impact loading was similar to the static tensile membrane resistance if the sudden drop in the tensile membrane resistance under impact load was not taken into account. For the mid-span displacements in the range of 170 mm to 190 mm, the static tensile membrane resistance of the Lightweight core panel was lower than the tensile membrane resistance under impact loading. The lightweight concrete infill at the flared ends was crushed and the end plate had buckled under static loading, while under impact

loading, only the end plate had buckled as shown in Figure 7.14. The severe damage at the flared end of the Lightweight core panel under static loading condition showed a lower tensile membrane resistance compared to the tensile membrane resistance of the panel under impact loading condition. The static resistance function of the Lightweight core panel was predicted using the theoretical membrane resistance of the two steel faceplates (Hodge Jr. 1974) with a stiffness parameter (k) of 0.00009 (Chapter 6). The inertial effect and strain rate effects of mild steel were ignored in the theoretical analysis and the analysis could not predict the sudden drop in tensile membrane resistance at displacements of 120 mm and below under impact loading condition.

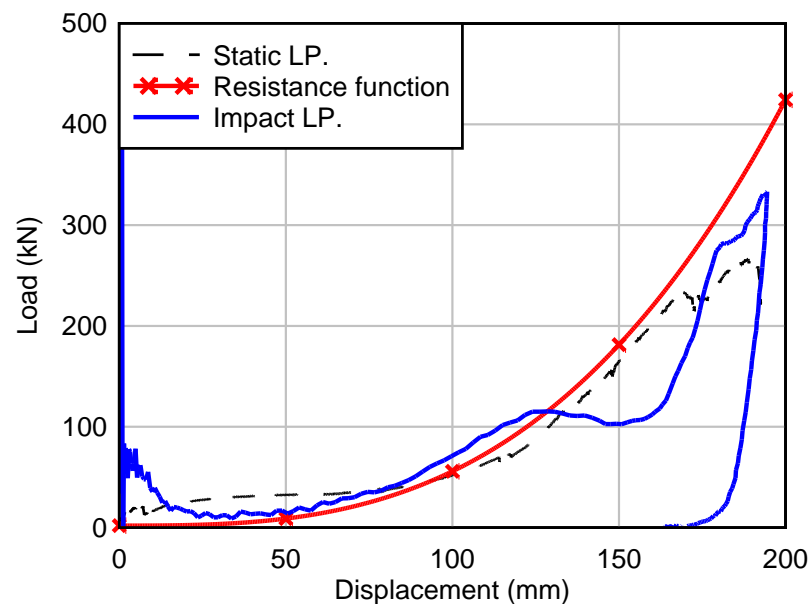


Figure 7.32: A comparison of the quasi-static and impact load-displacement relationship of the Lightweight core panel (LP), and the theoretical static resistance function.

7.3.3 Stainless steel panel

Figure 7.33 shows the impact and quasi-static load-displacement relationships for the Stainless steel panel. The impact force of about 100 kN at the initial stage was higher than the static flexural load capacity of 75 kN. After that, the Stainless steel panel under impact loading showed a flexural resistance of 66 kN, which was slightly lower than the static flexural load capacity, which could be attributed to damage of concrete core sustained during the inertial stage. The flexural resistance of the

Stainless steel panel under impact loading dropped gradually to the residual flexural load of about 20 kN due to the fracture of the concrete core.

The tensile membrane resistance of the Stainless steel panel under impact loading was different from the static tensile membrane response because the tensile membrane resistance in the impact test only started to develop at a displacement of 120 mm compared to 80 mm in the static test. The tensile membrane resistance of the panel under impact loading increased significantly after the panel reached 150 mm mid-span displacement. The tensile membrane resistance under impact loading approached to the static tensile membrane resistance after the displacement exceeded 160 mm. The theoretical membrane resistance of two stainless steel faceplates (Hodge Jr. 1974) using an axial stiffness parameter (k) of 0.00012 (Chapter 6) was compared to the tensile membrane resistance of the Stainless steel panel under impact loading. It showed that the static resistance function corresponded poorly with the impact experimental result for the displacement up to 160 mm. For the displacements greater than 160 mm, the experimental result was slightly lower than the theoretical prediction.

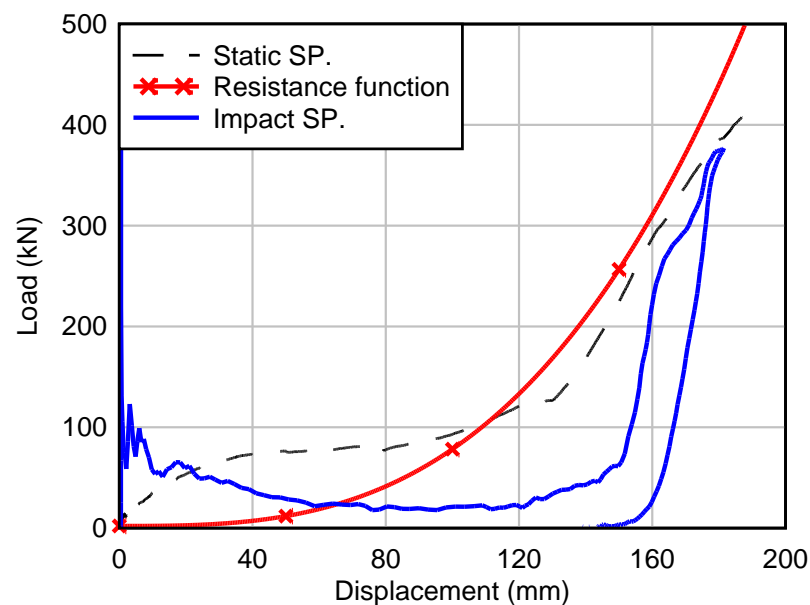


Figure 7.33: A comparison of the quasi-static and impact load-displacement relationships of the Stainless steel panel (SP), and the theoretical static resistance function.

7.3.4 Panel with bracing elements

The Panel with bracing elements in the impact test programme had the same configuration with the Control panel in the static test programme where small steel plate bracings were used to connect the steel faceplates together before they were filled with normal weight concrete. Figure 7.34 shows the impact load-displacement relationship of the Panel with bracing elements and the quasi-static load-displacement relationship of the Control panel. The impact force of 100 kN at the initial stage and the impact flexural resistance of 70 kN were higher than the static flexural load capacity of 58 kN. The flexural resistance of the Panel with bracing elements dropped to 35 kN before tensile membrane resistance started to develop at about 40 mm. The membrane resistance stiffness of the Panel with bracing elements was lower than the stiffness of the Control panel under static test.

The static resistance function of the Panel with bracing elements was constructed from a combination of flexural resistance and tensile membrane resistance at large displacement. The flexural load capacity was conservatively predicted based on the static flexural load capacity of the SCS panels with natural interaction presented in Chapter 6. The strain rate effects of the mild steel were not considered in the theoretical analysis. It showed that the predicted flexural load capacity (64.7 kN) was slightly lower than the impact flexural load capacity. The membrane resistance of two steel faceplates was predicted according to Hodge Jr. (1974) and compared to the impact test tensile membrane resistance. It was found that using an axial stiffness parameter (k) of 0.00007, the theoretical analysis could predict the tensile membrane resistance reasonably well when the mid-span displacement exceeded 125 mm.

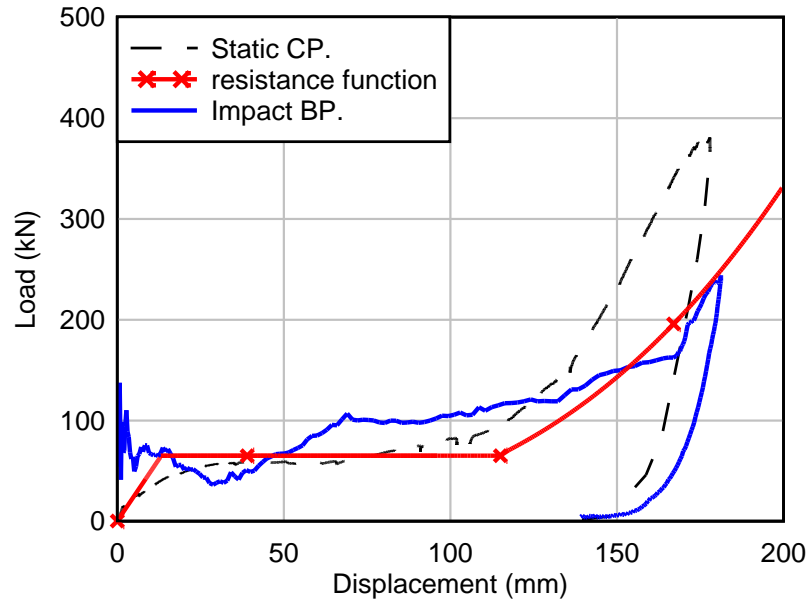


Figure 7.34: The impact load-displacement relationship of the Panel with bracing elements (BP), the quasi-static load-displacement relationship of the Control panel (CP), and the theoretical static resistance function.

7.3.5 Reinforced core panel and Double reinforced core panel

The reinforcement ratio in the longitudinal direction of the Reinforced core panel and the Double reinforced core panel was 0.6% and 1.2%, respectively. The impact load-displacement relationships of the Reinforced core panel and the Double reinforced core panel were compared to the quasi-static load-displacement relationship of the Reinforced core panel. The Reinforced core panel used in the quasi-static test had small steel plate bracings connecting the steel faceplates while there were no bracings in the Reinforced core panel and Double reinforced core panel used in the impact tests. The impact force after the initial peak force of both panels at the initial stage was about 200 kN. Under impact loading, the Reinforced core panel and the Double reinforced core panel showed a flexural load capacity of 86 kN and 101 kN, respectively. The impact force and the impact flexural load capacity of these panels were significantly higher than the static flexural load capacity of the Reinforced core panel (64 kN).

The static tensile membrane resistance of the Reinforced core panel was lower than the tensile membrane resistance of both panels under impact loading due to welding

fracture at the welded joint in the static test. In the impact test, the damage of concrete at the flared ends reduced the stiffness of axial restraint on the panels. This caused the tensile membrane resistance of both panels to approach the static tensile membrane resistance of the Reinforced core panel when the displacement exceeded 160 mm. The static resistance function of the Reinforced core panel determined in Chapter 6 (ignoring the strain rate effects of mild steel) was compared to the experimental impact load-displacement relationships of both panels in Figure 7.35. The theoretical flexural load capacity was conservative compared to the impact flexural load capacity for both panels. The theoretical tensile membrane resistance was lower than the impact experimental tensile membrane resistance for both panels for displacements up to about 160 mm.

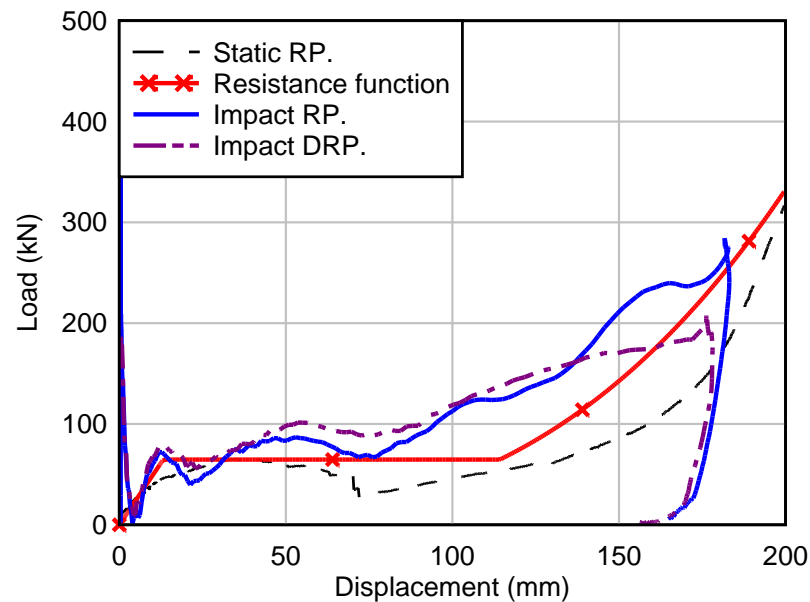


Figure 7.35: A comparison between the impact load-displacement relationships of the Reinforced core panel (RP) and Double reinforced core panel (DRP) with the static load-displacement relationship for the Reinforced core panel (RP), and the theoretical static resistance function.

7.3.6 Improved bonding panel

The impact and quasi-static load-displacement relationships of the Improved bonding panel are illustrated in Figure 7.36. The Improved bonding panel used in the impact test was slightly different from the panel used in the static test, where no small steel plate bracings were used to connect the steel faceplates. The impact force of 240 kN

at the initial stage was significantly higher than the static flexural load capacity of 72 kN. Under impact loading condition, the Improved bonding panel showed a flexural load capacity of 127 kN, which was slightly higher than the theoretical ultimate flexural load capacity of 108 kN calculated for a full composite section (Chapter 6). This meant that the Improved bonding panel probably achieved full composite action under impact loading condition. After that, the flexural load capacity dropped to 85 kN, and tensile membrane resistance started to develop when the mid-span displacement exceeded 150 mm.

The tensile membrane resistance of the Improved bonding panel under impact and quasi-static loading conditions were similar. The static resistance function of the Improved bonding panel developed by ignoring the strain rate effects of mild steel (Chapter 6) was compared to the impact results in Figure 7.36. The static flexural load capacity was very conservative compared to the impact flexural load capacity, which could be attributed to the panel achieving full composite action under impact loading compared to the SCS panel with partial shear connection in the static test. The experimental tensile membrane resistance corresponded well with the theoretical membrane resistance of two steel faceplates produced by Hodge Jr. (1974) using an axial parameter (k) of 0.007 (Chapter 6).

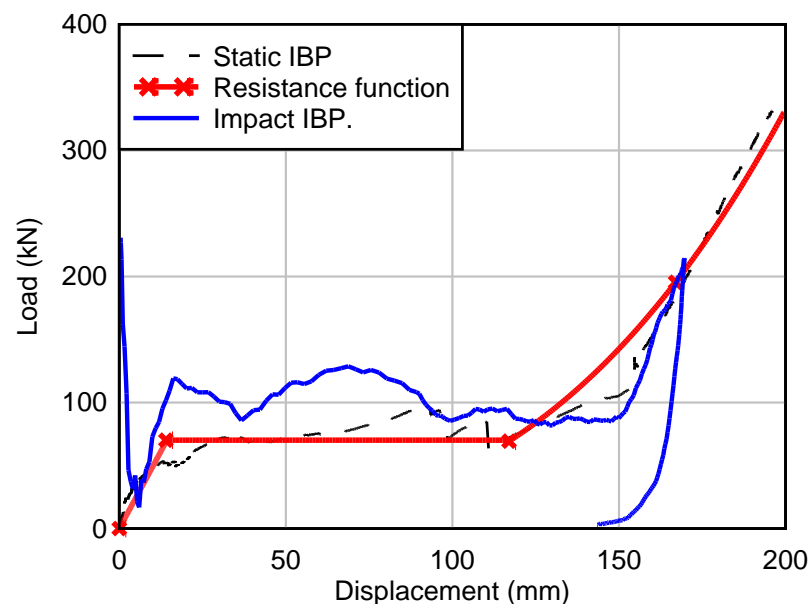


Figure 7.36: A comparison of the quasi-static and impact load-displacement relationships of the Improved bonding panel (IBP), and the theoretical static resistance function.

7.3.7 Fully enclosed panel

The impact and quasi-static load-displacement relationships of the Fully enclosed panel are illustrated in Figure 7.37. The Fully enclosed panel used in the quasi-static test had small steel plate bracings connected to the steel faceplates, while no bracings were provided in the impact test. The impact force of the Fully enclosed panel at the initial stage was about 280 kN, which was higher than the static flexural load capacity of 180 kN. After that, the flexural resistance for the panel under impact load dropped to about 140 kN and fluctuating around 120 kN. The flexural resistance from the impact test was lower than the static flexural load capacity. This meant that the welding fracture of the end cap (Figure 7.29) could have occurred during this stage. The impact flexural load capacity of 140 kN was higher than the theoretical ultimate flexural load capacity of a full composite section at 109 kN under simple support conditions. The tensile membrane resistance of the panel under impact loading was significantly lower than the static tensile membrane resistance. No static resistance function was proposed for this panel due to the welding fracture in both static and impact testing which caused inconsistencies in the response of the Fully enclosed panel.

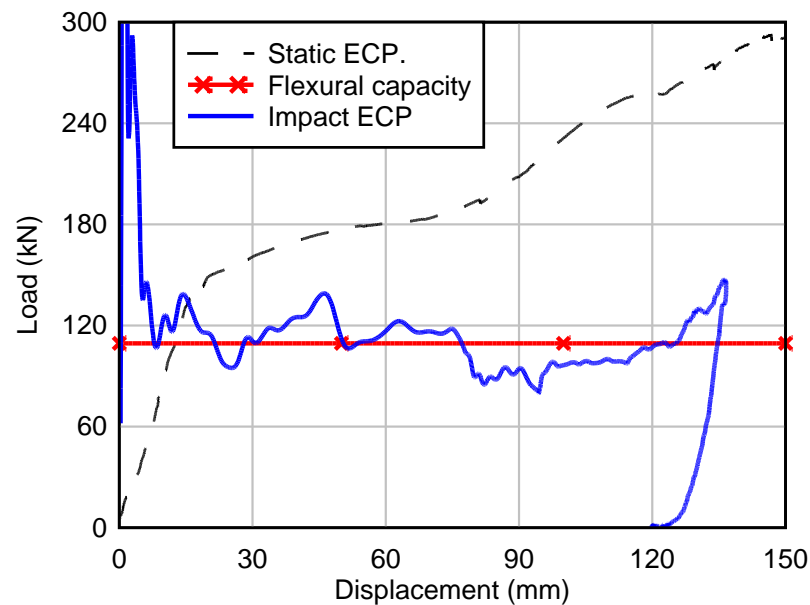


Figure 7.37: A comparison of the quasi-static and impact load-displacement relationships of the Fully enclosed panel (ECP), and the theoretical static resistance function.

7.4 Theoretical prediction of maximum displacement of axially restrained SCS panels subjected to impact loading

From the static resistance function, the maximum displacement of axially restrained SCS panels subjected to impact loading condition can be determined by using the energy balance method. In this method, the kinetic energy of the drop hammer was dissipated through the strain energy in the panels, assuming no energy loss in the system. In the impact tests, the weight of the drop hammer was 600 kg, and two drop heights used in the tests were 3 m and 4 m. The kinetic energy could be determined from the potential energy of the drop hammer, using the theory of conservation of energy. The kinetic energy for the drop hammer released from the height of 3 m and 4 m was determined to be 17.6 kJ and 23.5 kJ, respectively. The strain energy in the panel was the area under the static resistance function, which could be divided into three components, namely the elastic flexural energy, the plastic flexural energy and the membrane energy. The energy balance equation is given by:

Kinetic energy of drop hammer = strain energy of panel

= elastic flexural energy + plastic flexural energy + membrane energy

$$= \frac{1}{2}P_o \delta_e + P_o (\delta_m - \delta_e) + \int_{\delta_m}^{\delta_f} P_m d\delta$$

(7.1)

where P_o is the flexural load capacity, δ_e is the displacement when the panel reached the flexural load capacity, δ_m is the displacement when the tensile membrane resistance exceeded the flexural load capacity, δ_f is the final displacement, and P_m is the tensile membrane resistance. For the SCS panels such as the Control panel, Increased impact energy panel, Lightweight core panel and Stainless steel panel, the static resistance function was simplified into tensile membrane resistance only, as shown in Figure 7.30 to Figure 7.33. Therefore, only the membrane energy needed to be considered in these panels.

For the Reinforced core panel, Double reinforced core panel, Improved bonding panel, and Panel with bracing elements, the static resistance functions determined from the static tests were used in the energy balance analysis. The impact energy on

the panels was converted to strain energy, namely flexural energy and membrane energy. No static resistance function was proposed for the Fully enclosed panel. Therefore, it was not considered for the energy balance analysis. The predicted maximum displacement and tensile membrane resistance were compared to the experimental results in Table 7.3.

Generally, the predicted results corresponded well with the experimental results, with the maximum discrepancy for the displacement and tensile membrane resistance being 11% and 26%, respectively. The theoretical analysis underestimated the maximum displacement of the Control panel, Increased impact energy panel, Lightweight core panel and Stainless steel panel because the theoretical membrane resistance of these panels were higher than the experimental tensile membrane resistance at large displacement. For the Panel with bracing elements, Reinforced core panel, Double reinforced core panel and Improved bonding panel, the predicted maximum displacement was higher than the experimental maximum displacement. This was due to the theoretical flexural load capacity and tensile membrane resistance used in the analyses were more conservative than the experimental results.

Table 7.3: Comparison between experimental and theoretical maximum displacement and tensile membrane resistance.

Panel	Exp. max. displ. (mm)	Predicted max. displ.(mm)	Predicted /Exp. displ.	Exp. peak membran -e force (kN)	Predicted peak membran -e force (kN)	Predicted/ Exp. membrane force
Control panel	199	177	0.89	357	388	1.09
Increased impact energy panel	204	190	0.93	430	480	1.12
Stainless steel panel	181	173	0.96	375	395	1.05
Lightweigh	194	189	0.97	331	363	1.10

-t core panel						
Panel with bracing elements	181	183	1.01	243	256	1.05
Reinforced core panel	183	185	1.01	274	265	0.97
Double reinforced core panel	178	185	1.04	211	265	1.26
Improved bonding panel	169	183	1.08	214	256	1.20

7.5 Conclusions

In this chapter, the impact test results of axially restrained non-composite SCS panels were discussed and the effects of different parameters such as reinforced concrete core, lightweight concrete core, stainless steel faceplates, and the degree of interaction between steel and concrete had been identified. The impact test results were compared to the static test results of axially restrained SCS panels and the proposed static resistance function. Then, the impact response of axially restrained SCS panels was predicted using the energy balance method based on static resistance function. Based on predicted and experimental results, the energy balance method had been shown to be a simple and effective approach for the impact analysis. The conclusions are as below:

- (a) Axially restrained non-composite SCS panels could withstand very large impact loading conditions through development of tensile membrane resistance in the steel faceplates. The possible failure modes identified in this study were the penetration of steel faceplate under very large impact load, and the failure of the axial restraint on the panel. The failure of the axial restraint could be due to the damage of concrete infill at the flared end or buckling of end plate.
- (b) From the impact test results, the lightweight concrete infill does not have significant effect on the impact response of the axially restrained non-composite

SCS panel. The use of reinforced concrete core, stainless steel faceplates and increased degree of interaction between the steel faceplates and the concrete core will reduce the maximum displacement up to 15%. It is noted that severe damage to the concrete infill tends to occur at the flared ends of the reinforced concrete core SCS panels. This will reduce the axial restraint stiffness of the panel. The Fully enclosed SCS panel showed a significant reduction (30%) of the maximum displacement. However, due to the premature failure of the welding between the end cap and the steel faceplates, the actual reduction could be quantified.

- (c) Generally, the response of axially restrained SCS panels under impact loading condition was similar to the static load-displacement relationship of the panels. Initially, the panels showed inertial effect, followed by flexural resistance and tensile membrane resistance at large displacement. For the Reinforced core panel, Double reinforced core panel and Improved bonding panel, the flexural load capacity under impact test was significantly higher than the static flexural load capacity. For the Control panel, Lightweight core panel, Increased impact energy panel and Stainless steel panel, the residual flexural strength under impact loading condition was very low due to the fracture of their concrete core.
- (d) The maximum displacement of axially restrained SCS panels subjected to impact energy can be predicted with reasonable accuracy by using the energy balance equation. The accuracy of the static resistance function is essential in the energy balance equation, and a conservative static resistance function will give a higher estimate for the SCS panels' maximum displacement and ensure a safe design.

CHAPTER 8

FINITE ELEMENT MODELLING OF AXIALLY RESTRAINED SCS PANELS UNDER IMPACT LOADING

8.1 Introduction to LS-Dyna

Finite element analysis of axially restrained steel-concrete-steel sandwich panels was carried out using three-dimensional non-linear transient dynamic finite element code LS-DYNA (Hallquist, 2010). This program uses explicit time integration for transient dynamic analysis which is suitable for the application of short duration events such as vehicle crash and explosion. The explicit analysis considers dynamic equilibrium of each node at every time step as follows:

$$M a_n = (F_{ex})_n - (F_{int})_n \quad (8.1)$$

where the M is the mass on the node, a is the acceleration, F_{ex} is the external force, F_{int} is the internal force and n is the time step.

The accuracy of the simulation is determined by monitoring the total energy in the structures during the analysis. The total energy in the structures consists of kinetic energy (E_{kin}), internal energy (E_{int}), friction energy (E_{fr}), damping energy (E_{damp}) and hourglass energy (E_{hg}). The internal energy includes elastic strain energy and work done in plastic deformation. The hourglass energy is attributed to non-physical modes of deformation occurred in under-integrated element formulation. It should be less than 10% of the peak internal energy of each part.

$$E_{kin} + E_{int} + E_{fr} + E_{damp} + E_{hg} = E_{total} = \text{constant} \quad (8.2)$$

Many material models are developed in the LS-DYNA to include the strain rate effects of materials under impact and blast loading conditions. For instance, the material model Piecewise Linear Plasticity, takes into account the strain rate effects

of steel by specifying the Cowper-Symonds coefficients. Furthermore, FE model (in the LS-DYNA input format) for various types of vehicle are developed by the National Crash Analysis Centre (NCAC) at the George Washington University. These vehicle models enabled a high-fidelity vehicle crash analysis being carried out through computer simulation.

8.2 Numerical model description

In the finite element (FE) models developed for this study, only a quarter of the experimental setup was considered due to the symmetry of the specimen, loading and support conditions, to save the computational time. The axial restraint, including the keyed inserts, bolted connections, steel UC section and steel I-beam were modelled in detail, as shown in Figure 8.1. From the convergence study, a mesh size of 10 mm was found to be appropriate for the concrete core and the steel faceplates. Details of the mesh convergence study will be discussed later in this chapter. Fully integrated selectively reduced (S/R) solid element formulation was applied to the steel UC section, I-beam, and the bolts, to avoid hourglass effects in these elements. Under large deformation, the fully integrated S/R solid elements become unstable and may cause error termination (negative volume) in the simulation. To avoid the negative volume effect, the concrete core of the SCS panels was modelled using constant stress solid elements. The steel faceplates were modelled using Belytschko-Tsay shell elements. The Hughes-Liu with cross section integration beam elements was used to model the reinforcing steel elements. The bolts of the keyed inserts were simplified as square bars with the cross sectional area equivalent to M16 bolts. This simplification has no significant effect on the accuracy of the model as shown by Lee et al. (2008).

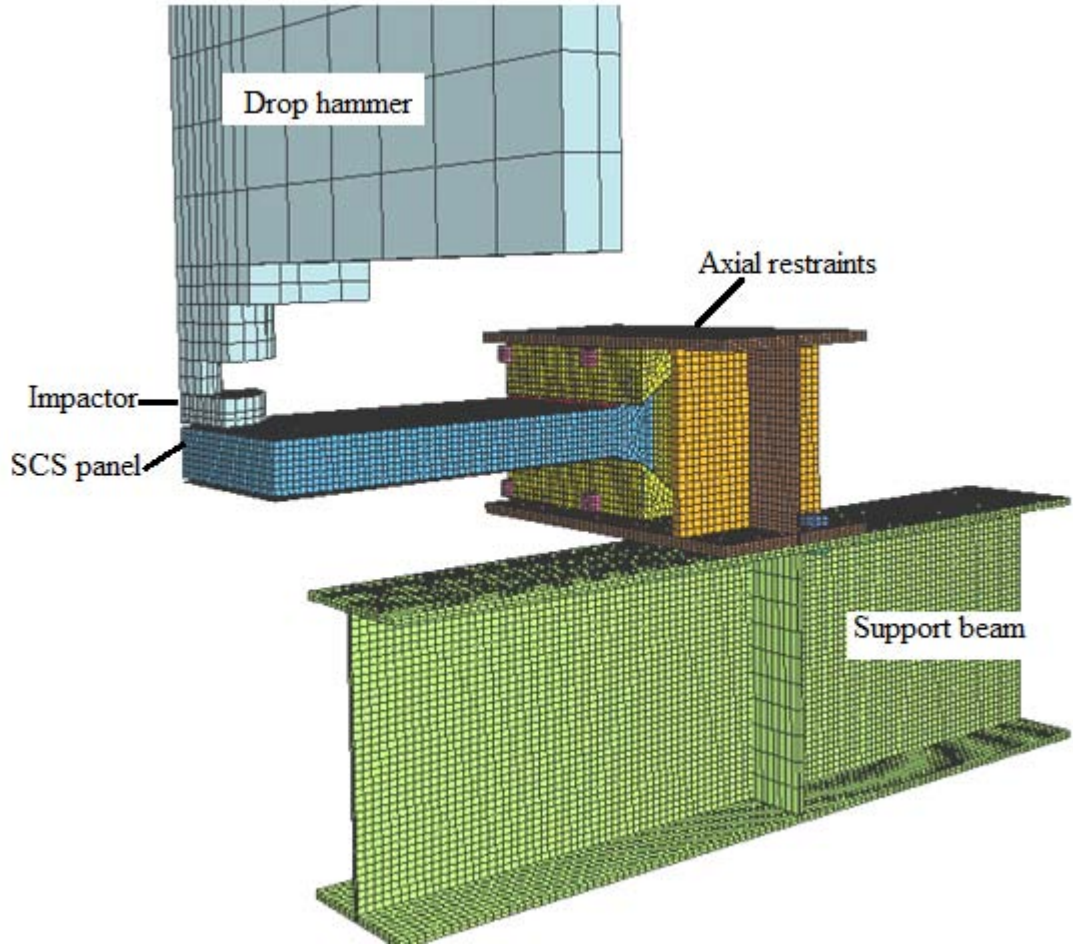


Figure 8.1: FE model for axially restrained SCS panels subjected to a drop mass impact at mid-span (quarter model).

8.2.1 Boundary conditions

The FE models were defined so that they were symmetrical in the x- and y-directions. For symmetry in the x-direction, the x translational degree of freedom of the solid elements was restrained. For the symmetry in the y-direction, the y translational degree of freedom of solid elements was restrained. For the shell elements, there are six degrees of freedom at each node, namely translational and rotational at the x-, y- and z-directions. For the x symmetry of the shell elements, the x translational, and y and z rotational degrees of freedom were fixed. While the y translational degree of freedom, and x and z rotational degrees of freedom of shell elements were restrained for the y symmetry.

The I-beam was bolted down to the strong floor in the experimental setup. In the FE model, all the nodes at the bottom surface of the I-beam were restrained in the three translational degrees freedom, x, y and z, so no movement was allowed at these nodes. The drop hammer was positioned 2 mm from the top faceplate, and it was assigned with an initial velocity in the z direction that corresponded to the drop height used in the tests. Two drop heights used in the test were 3 metres and 4 metres. By using the energy conservation approach, an initial velocity of the drop hammer immediately before it struck the panel could be calculated. The initial velocity was determined as 7.67 m/s and 8.86 m/s for the 3 m and 4m drop height, respectively.

8.2.2 Contact surfaces

The interaction between different parts in the FE model was important in order to predict the behaviour of the SCS panels correctly. In this study, the Automatic-Surface-to-Surface contact algorithm in LS-DYNA was used to model the interaction between the following parts in the model:

- 1) Impactor and steel faceplates
- 2) Steel faceplates and the concrete core
- 3) Steel faceplates with the UC section and keyed inserts
- 4) Steel UC section and I-beam
- 5) Bolts and the UC section and I-beam

In this penalty-based contact algorithm, when a penetration is found for the parts in contact, a force proportional to the penetration depth is applied to these interfaces to eliminate the penetration (Hallquist, 2006). Thus, the impact load time histories for the FE models can be obtained by using this contact algorithm between the impactor and the steel faceplates. The definition of the master surface and slave surface is arbitrary, but normally the surface with a finer mesh will be defined as the slave surface.

This sliding contact algorithm only considers the friction interaction between the contact interfaces. The dynamic coefficient of friction of 0.2 was applied to the mild

steel and concrete core interfaces. For the contact interfaces between the stainless steel and the concrete core, the dynamic coefficient of friction of 0.1 was used considering the surface of the stainless steel was smoother than the mild steel. In these FE models, the chemical bonding of the concrete was ignored. This was a realistic assumption because the chemical bonding failed during the panel handling and experimental set up before the tests commenced. For panels with wire meshes in the concrete core such as the Reinforced core panel, Double reinforced core panel and Improved bonding panel, the nodes of the beam elements were merged with the nodes of the concrete elements and the slippage between these interfaces in reality was ignored.

8.2.3 Material models

8.2.3.1 Steel material model

The complete stress-strain relationships for both mild steel and stainless steel faceplates were modelled using the LS-DYNA Piecewise Linear Plasticity material model. For the mild steel, the yield stress was 271 MPa from the tensile coupon tests, while for the stainless steel, the yield stress was 291 MPa. The non-linear behaviour after yielding was considered by defining plastic stress-strain relationships for both steels according to the tensile coupon tests, as shown in Chapter 5. The strain rate effects of the mild steel and the stainless steel was considered in the FE models by specifying the Cowper-Symonds coefficients. The Cowper-Symonds coefficients for mild steel are 40.4 (D) and 5 (q), while for the stainless steel, they are 100 (D) and 10 (q) (Jones, 1989). The drop hammer was assumed to be absolutely rigid since there was no deformation observed on the drop hammer during the tests. The steel UC section, I-beam, bolts and wire meshes were assumed to behave as elastic perfectly plastic material and modelled using the LS-DYNA Plastic Kinematic material model. The yield stress for the UC section and I-beam was assumed as 300 MPa, while the yield stress for the bolts was assumed as 600 MPa. The yield stress of the wire mesh was assumed as 500 MPa.

8.2.3.2 Concrete material model

The material model CSCM (Continuous Surface Cap Model) was developed for the US Federal Highway Administration (FHWA) to simulate the reinforced concrete structures subjected to impact loading conditions (FHWA, 2007a). This material model is simple to use as it can generate default parameters for the concrete by only requiring some basic inputs. The details of theoretical description and validation of this material model are provided in the Federal Highway Administration reports (2007a, 2007b). For this material model, the three inputs required to generate the default parameters are the unconfined compressive strength, aggregate size and the units used in the finite element model (Hallquist, 2010).

According to the FHWA report (2007b), this material model is applicable for concrete grade between 20 MPa to 58 MPa with the aggregate size between 8 mm to 32 mm. The unconfined compressive strength will affect all the generated parameters such as stiffness, three dimensional yield strength, hardening and softening, while the aggregate size only affect the softening behaviour. The parameters are generated based on the Comité Euro-International Du Béton-Fédération Internationale de la Précontrainte Model (CEB-FIP) Code.

The yield surface of this concrete material model is defined by three invariants and the cap hardening parameter κ , as follows:

$$f(J_1, J_2, J_3, \kappa) = J_2 - K^2 F_f^2 F_c \quad (8.3)$$

where J_1 is the stress invariant of stress tensor, J_2 is the second invariant of the deviatoric stress tensor, and J_3 is the third invariant of the stress tensor. F_f is the shear failure surface and F_c is the hardening cap. K is the Rubin three invariants reduction factor to account for lower concrete strength under triaxial extension and torsion compared to triaxial compression when concrete subjected to the same pressure. It has a smooth intersection between the shear yield surface and the hardening cap as shown in Figure 8.2. The strength of the concrete is modelled by the shear surface when the concrete is subjected to tensile and low confining pressure regimes. In the low to high confining pressure regimes, the strength of the concrete is modelled by a combination of shear and the cap surface. The cap surface expands to

simulate the plastic volume compaction while it contracts to simulate the plastic volume expansion.

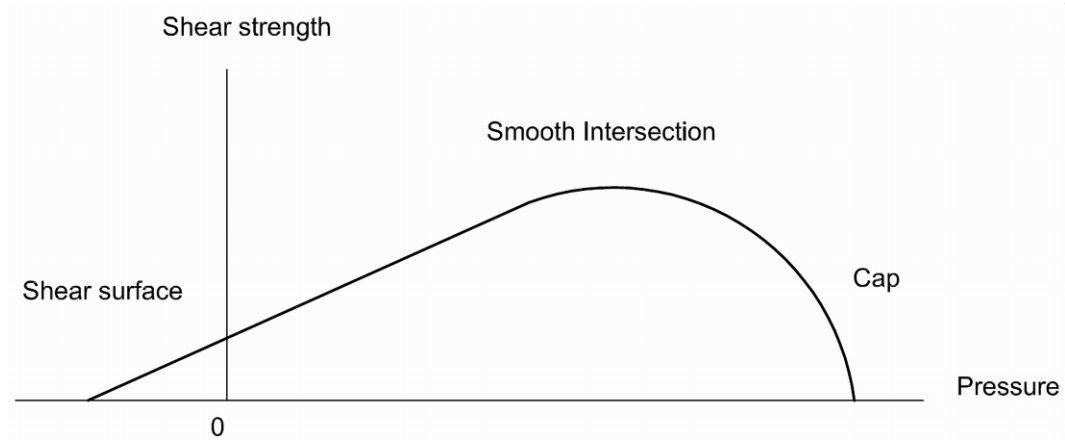


Figure 8.2: Schematic of the shear failure surface and the cap surface in the material model CSCM. (reproduced from FHWA, 2007a)

Concrete shows strain softening behaviours where the strength decreases as the strain increases after it reaches the peak tensile or compressive strength. The softening is modelled by a scalar damage parameter (d):

$$\sigma^d = (1-d) \sigma^{vp} \quad (8.4)$$

where σ^d is the stress tensor with damage, σ^{vp} is the stress tensor without damage and d is the scalar damage parameter. The damage of the concrete whether cracking or crushing is represented by the damage parameter that ranges from 0 to 1. The concrete elements lose all strength and stiffness when the damage parameter approaches to one.

The damage parameter in tension (brittle damage) or compression (ductile damage) is determined from the following formulations:

$$d(\tau_t) = \frac{0.999}{D} \left[\frac{1+D}{1+D \exp^{-C(\tau_t - \tau_{ot})}} - 1 \right] \quad \text{Brittle damage}$$

$$d(\tau_c) = \frac{d \max}{B} \left[\frac{1+B}{1+B \exp^{-A(\tau_c - \tau_{0c})}} - 1 \right] \quad \text{Ductile damage} \quad (8.5)$$

where the parameters A , B , C and D are shape softening parameters. τ_t is the tensile energy term, τ_{ot} is the tensile damage threshold, τ_c is the compressive energy term,

and τ_{oc} is the compressive damage threshold. The parameter d_{max} is the maximum damage level that can be attained, depending on the confining pressure.

In this concrete material model, the strain rate effect is applied to the plasticity surface, the damage surface, and the fracture energy. The strain rate effect on the plasticity surface is applied through viscoplastic formulation. For concrete under uniaxial tensile or unconfined compression, the strength increases depending on the strain rate as,

$$\begin{aligned} f_T'^{dyn} &= f_T' + E \dot{\varepsilon} \eta \\ f_C'^{dyn} &= f_C' + E \dot{\varepsilon} \eta \end{aligned} \quad (8.6)$$

where $f_T'^{dyn}$ is the dynamic tensile strength, f_T' is the static tensile strength, $f_C'^{dyn}$ is the dynamic compressive strength, f_C' is the static compressive strength, E is the Young modulus of concrete, $\dot{\varepsilon}$ is the effective strain rate and η is the fluidity coefficient. The dynamic increase factor (DIF) for the concrete in this material model is based on the developer's experiences and is different from DIF given in the CEB-FIP. This concrete model has a built in feature that allows a user to include data for the strain rate effect by selecting the strain rate option.

In this study, it was found that the hourglass energy in the concrete core exceeded 50% of its peak internal energy when the strain rate effect was considered. The hourglass control formulations, Flanagan-Belytschko viscous form with exact volume integration for solid elements (HG type 3) and Flanagan-Belytschko stiffness form with exact volume integration for solid elements (HG type 5) were not effective to control the hourglass energy. This was due to localized impact condition and the panel underwent very large deformation. The hourglass energy in the concrete core could be reduced to about 15% of the peak internal energy when the strain rate effect was ignored. The detail investigation of the hourglass energy in the concrete core will be presented later in this chapter. Therefore, the strain rate effect of the concrete was ignored in this study to minimise the hourglass energy in the concrete core.

The concrete compressive strength for SCS panels was different because the panels were casted using different batches of concrete. For the Control panel, Reinforced core panel and Double reinforced core panel, the concrete compressive strength was 23 MPa. For the Stainless steel panel, Improved bonding panel and Fully enclosed panel, the concrete compressive strength was 37 MPa. For the Panel with bracing elements, the concrete compressive strength was 40 MPa while the concrete compressive strength for the Lightweight core panel was 11 MPa.

The density of lightweight concrete was 1400 kg/m^3 and no aggregates were used in the mix. Single element simulation (FHWA, 2007a) was carried out to evaluate the ability of the concrete model CSCM (Mat. 159) to generate parameters for the lightweight concrete. It was found that using the density of 1400 kg/m^3 , concrete compressive strength of 16 MPa and ignoring the aggregate size, this concrete material model could generate a stress-strain curve with the compressive strength of 10.8 MPa and tensile strength of 0.9 MPa, as shown in Figure 8.3. It was assumed that this stress-strain relationship was appropriate for the lightweight concrete in this study. The stress-strain relationships for different grades of concrete used in this study were generated by the single element simulation and the results are shown in Figure 8.3. The stress-strain relationships included the compressive strength, tensile strength, softening curves after the concrete reached its maximum strengths.

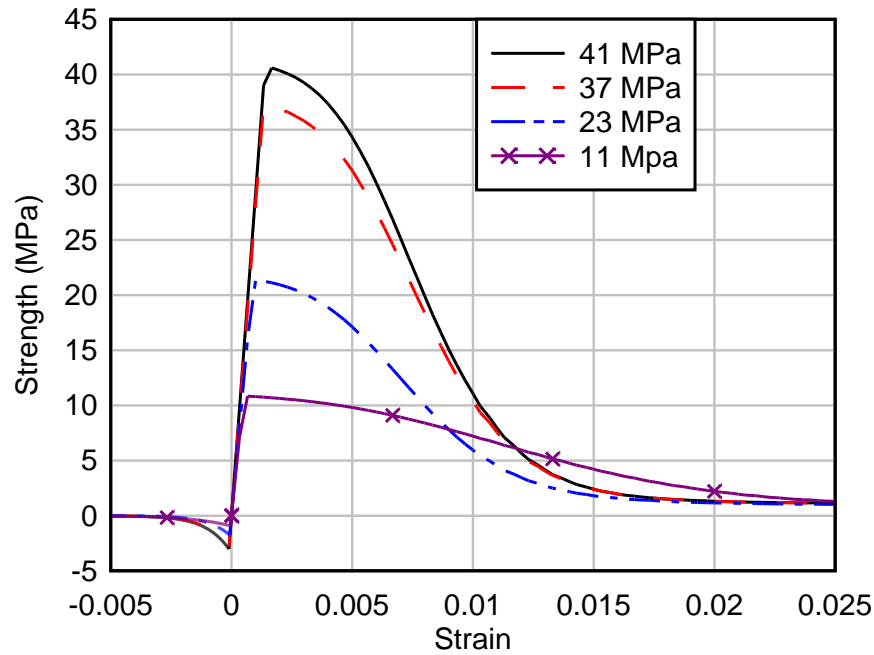


Figure 8.3: Numerically generated stress-strain relationships for concrete infill using a single element simulation.

8.2.4 Element erosion

An erosion algorithm is available in the LS-DYNA code which allows computation to be carried out without the need for re-zoning distorted regions of the mesh during a large deformation loading. The erosion algorithm is based on the concept that the highly strained elements of the deformed mesh have failed completely and may no longer contribute to the physics of structural response. Upon erosion, the sliding interface between the steel faceplates and the concrete core needs to be re-defined dynamically due to the total element failure.

The erosion of the elements is based on somewhat ad-hoc criteria related to a deformation or stress measure in the element. In the LS-DYNA concrete material model CSCM (Mat. 159), the element removal can be activated by specifying an erosion coefficient ≥ 1 . When the erosion coefficient is < 1 , no erosion occurs, while erosion coefficient of 1 means the erosion is independent of the strain. For erosion depending on the maximum principal strain, erosion coefficient is set to values greater than 1. For example, when the erosion coefficient is set to 1.05, the element is deleted once it reaches maximum principal strain of 5%. Federal Highway

Administration (2007b) recommends the use of erosion coefficient within 10% of the maximum principal strain for reinforced concrete structures. It should also be realised that the erosion strain has no correlation with the fracture strain and is solely a measure of how much plastic deformation an element can undergo before it is removed from the numerical computation. In this study, based on *a priori* knowledge of the experimental outcomes, it was found that it would not be beneficial to include the eroding-element technique for the concrete core of the SCS panels. It was demonstrated through running a number of trial models that the inclusion of erosion algorithm may result in significant underestimation of the overall ultimate load-carrying capacity of the non-composite SCS sandwich panels under impact loading.

8.3 Calibration of FE model

In this section, a mesh convergence study was first carried out using a FE model of a simply supported non-composite SCS panel subjected to impact loading. After that, the Control panel and the axial restraints were modelled. Various parameters evaluated in the FE model calibration were the support conditions, shell element formulations, dynamic coefficients of friction, concrete material models, hourglass energy in the concrete core, and strain rate effects of concrete and steel. The experimental load time history of the Control panel was used to validate the FE models.

8.3.1 Mesh convergence study

Four mesh sizes considered were 40 mm, 20 mm, 10 mm and 5 mm. In the mesh convergence study, a quarter of a SCS panel and an impactor were modelled due to symmetry. The axial restraint supports used in the tests were simplified into two roller supports at the top and bottom of the panel, to reduce the computational time. The top roller support was modelled to prevent excessive rebound of the panel under impact loading condition. The FE model using a mesh size of 10 mm is illustrated in Figure 8.4. The impactor and the roller supports were assumed to be rigid, while the mild steel faceplates were assigned with elastic-plastic material properties, with a yield stress of 271 MPa. The concrete core was modelled using the concrete material model CSCM (Mat. 159) with a compressive strength of 23 MPa. An initial velocity

of 7.67 m/s was assigned to the impactor. The mass scaling technique was applied to the FE models in the convergence study, where the density of all the materials was increased by a factor of 10, to reduce the simulation time. The minimum time step for the FE model using 5 mm mesh size was increased from 1.12×10^{-6} s to 3.53×10^{-6} s when the mass scaling technique was used. Therefore, increasing the density by a factor of 10 could reduce the simulation duration by almost 3 times (square root of 10).

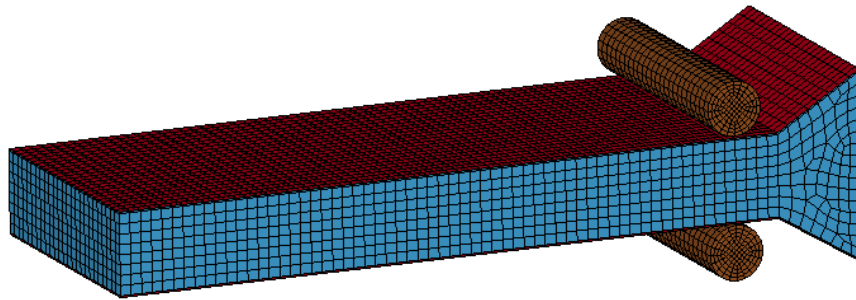


Figure 8.4: The FE model of a simply support non-composite SCS panel with a mesh size of 10 mm used in the mesh convergence study.

The number of elements and the simulation duration for each FE model are presented in Table 8.1. Four processors of a work station, Dell Precision model T7400, were used to run the simulations. The simulation duration increased significantly for the FE model using 5 mm mesh size, compared to other models. The maximum displacement for every model was measured and used as a convergence criterion. The maximum displacement of the FE model using 5 mm mesh size was set as the reference. The FE model using a mesh size of 10 mm predicted a slightly higher maximum displacement (6.6%) compared to the FE model using 5 mm mesh size, but the simulation duration could be reduced significantly. Therefore the mesh size of 10 mm was chosen for the FE models in this study.

Table 8.1: Summary of the mesh convergence study.

Mesh size of FE model (mm)	Number of elements	Simulation duration	Maximum central displacement (mm)	Percentage difference of displacement (%)
5	1582361	1 hour 1 min.	15.2	-
10	276335	11 mins.	16.2	6.6
20	100610	4 mins.	20.8	26.9
40	74132	2 mins.	33.3	54.5

8.3.2 Support conditions

8.3.2.1 Spacing between keyed inserts and UC sections

In the experimental setup, the panels were connected to the UC sections through the keyed connections. The stiffness of the axial restraint supports had significant effects on the tensile membrane resistance of the SCS panels as discussed in Chapter 3, therefore it is important that these supports were modelled correctly. In the experimental setup, the keyed inserts were attached to the UC sections using 16 mm diameter high tensile bolts. It was observed that there was approximately 3 mm spacing between the keyed inserts and the flanges of the UC sections. In this section, the effects of this spacing were investigated. Two FE models were generated for the Control Panel, where the first FE model considered the spacing between the keyed inserts and the UC section, while the second model ignored this spacing. The modelling techniques were described in the Section 8. 2. It was assumed that the bolt connection between the UC section and the I-beam has 10 mm clearance in both FE models.

The load time histories predicted by the FE models were compared to the experimental result of the Control panel in Figure 8.5. The load time history from the FE model with the spacing corresponded better to the experimental result. The FE model ignoring the spacing predicted a significantly higher flexural resistance and a lower peak tensile membrane resistance compared to the experimental result. These results showed that the spacing between the keyed inserts and the UC section had

significant effects on the flexural resistance and tensile membrane resistance of axially restrained SCS panels, thus this spacing was included in the FE models.

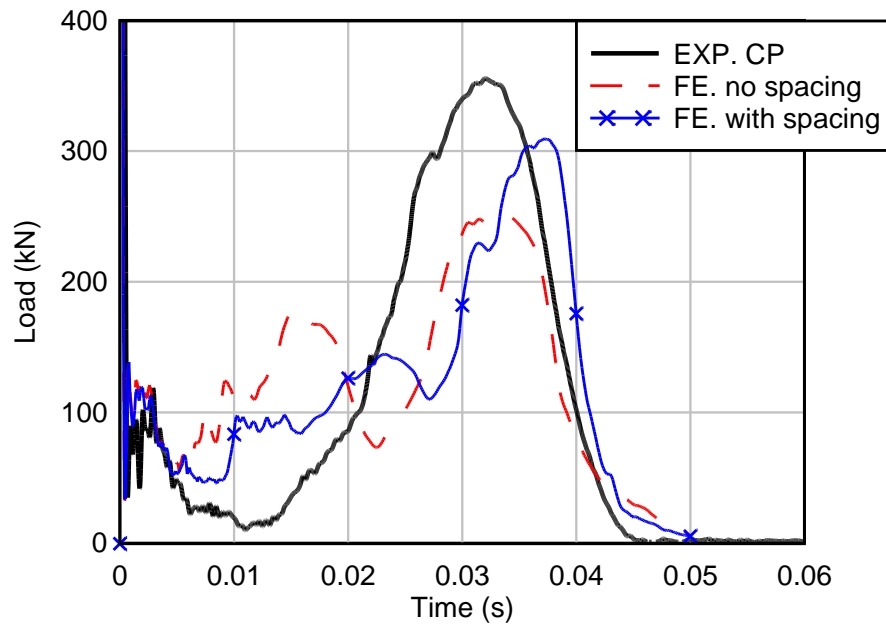


Figure 8.5: Load time histories of FE models with different spacing between the keyed inserts and the UC sections compared to the experimental result of the Control panel (CP).

8.3.2.2 Bolt connection between UC section and I-beam

The UC sections were attached to the I-beams using 25 mm diameter high strength bolts. The clearance spacing in the bolt holes will affect the development of tensile membrane resistance in the steel faceplates. In order to study the effects of this spacing, three FE models were generated with the spacing of 1 mm, 4 mm and 10 mm, respectively. The spacing between the keyed inserts and the UC section was included in these FE models. The predicted load time histories were compared to the experimental result of the Control Panel in Figure 8.6. It was found that the clearance spacing affected the time when the panel reached its peak tensile membrane resistance, where the FE model with smaller clearance spacing reached the peak tensile membrane resistance earlier. The magnitude of the peak tensile membrane resistance was slightly affected by this spacing, while it seemed to have no effect on the flexural resistance. The result of the FE model with a spacing of 4 mm corresponded better with the experimental load time history of the Control panel, thus this FE model will be used in the next section of model calibration.

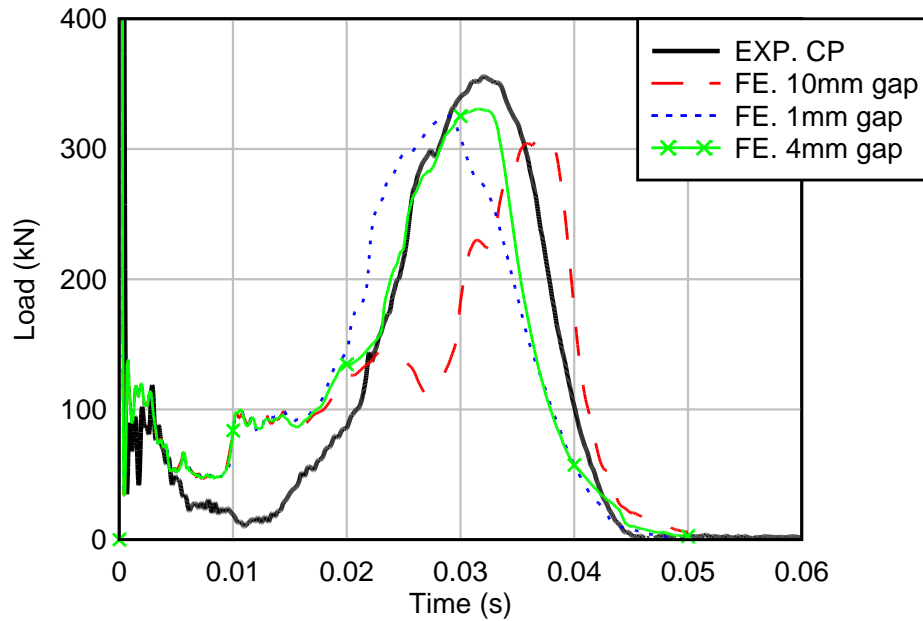


Figure 8.6: Load time histories of FE models with different clearance spacing in the bolt connection compared to the experimental result of the Control panel (CP).

8.3.3 Separation of steel faceplates from concrete core

The chemical bonding of concrete had failed in the Control panel and the steel faceplates were separated from the concrete core prior to the impact testing. No separation was observed between the steel faceplates and the concrete core at the flared ends due to the restraining effects from the keyed connection. The spacing between the steel faceplates and the concrete core increased as the distance from the keyed connection increased, and reached maximum at mid-span. The spacing at mid-span was about 5 mm. The effects of this separation were investigated in this section. Two FE models generated in this section had 3 mm spacing between the keyed inserts and the UC section, and 4 mm clearance for the bolt connection between the UC section and I-beam. In the first FE model, the concrete core was in contact with the steel faceplates along the span, while the separation between the concrete core and the steel faceplates was considered in the second FE model. The gap was 5 mm at mid-span and it reduced linearly to zero at the flared end, as shown in Figure 8.7. The load time histories predicted by the FE models were compared to the experimental result of the Control panel in Figure 8.8. Both FE models predicted similar load time histories, with the FE model considered the separation showed a

slightly lower peak tensile membrane resistance. This showed that the small gap between the steel faceplates and the concrete core only had minor effects on the response of axially restrained non-composite SCS panels subjected to impact loading. The FE model with separation of the steel faceplates from the concrete core will be used to evaluate shell element formulations in the next section.

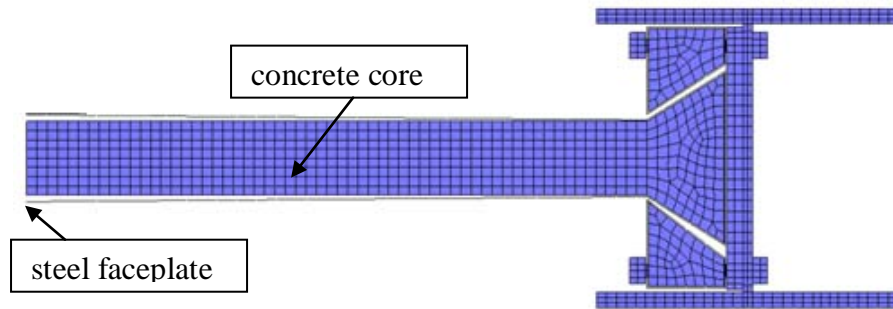


Figure 8.7: Separation of the steel faceplates from the concrete core in the FE model.

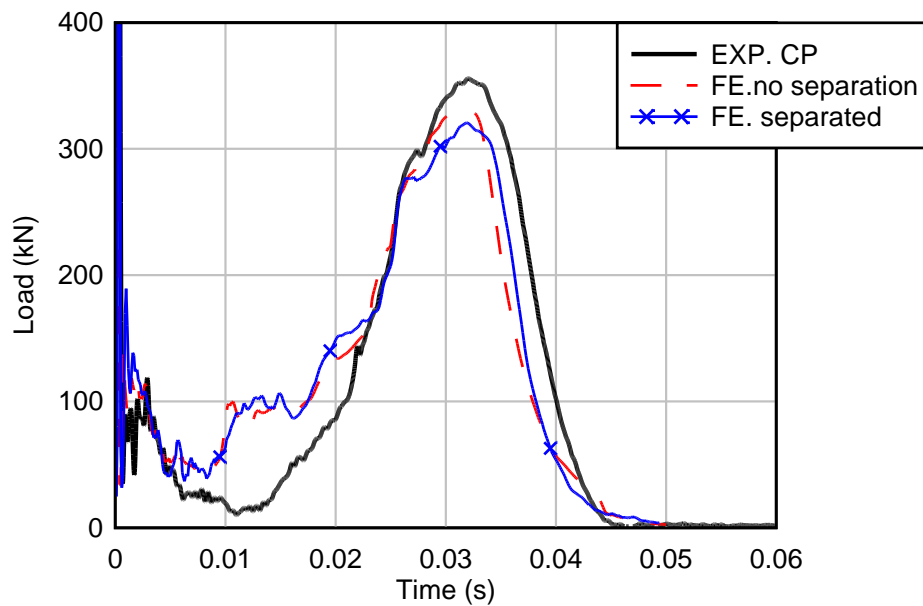


Figure 8.8: Load time histories of FE models with and without separation between the steel faceplates and the concrete core compared to the experimental result of the Control panel (CP).

8.3.4 Shell element formulations

Shell elements were used to model the steel faceplates in FE models. Two types of shell element formulations evaluated were Hughes-Liu shell elements and Belytschko-Tsay shell elements. According to the LS-DYNA theory manual (2006), a Hughes-Liu shell element has nodal translational and rotational degrees of freedom degenerated based on a 8-node brick element, and it includes finite transverse shear strains. While the Belytschko-Tsay shell elements formulation is the default choice of shell element formulation for the explicit analysis in LS-DYNA due to its computational efficiency. For a shell element with 5 through thickness integration points, the Belytschko-Tsay shell element only requires 725 mathematical operations while the under integrated Hughes-Liu shell element needs 4050 operations (LS-DYNA theory manual, 2006). Both FE models predicted similar load time histories as shown in Figure 8.9. Since both shell element formulations showed similar results, the Belytschko-Tsay shell element formulation was chosen due to its computational efficiency.

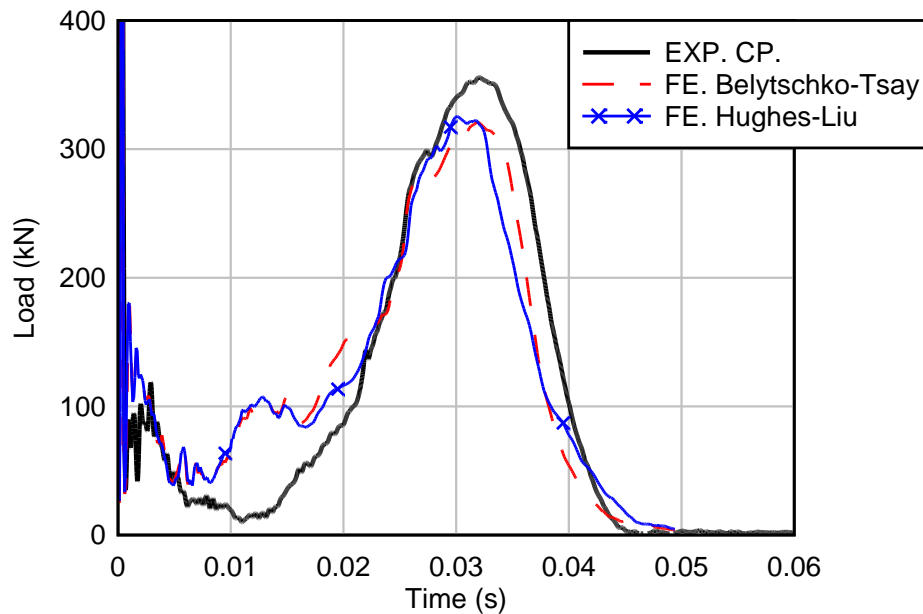


Figure 8.9: Load time histories of FE models with different types of shell element formulations compared to the experimental result of the Control panel (CP).

8.3.5 Dynamic coefficient of friction between the steel faceplates and the concrete core

In this section, effects of the dynamic coefficient of friction between the steel faceplates and the concrete core were investigated. Three FE models with the dynamic coefficient of friction of 0.1, 0.2 and 0.3 were generated. All the FE models used the concrete material model CSCM (Mat. 159), the Belytschko-Tsay shell elements, and strain rate effects of materials were ignored. The simulation results showed that the models with the dynamic coefficients of friction in the range of 0.1 to 0.3 predicted similar load time histories (Figure 8.10). The dynamic coefficient of friction of 0.2 was chosen for the contact interaction between the mild steel faceplates and the concrete core in this study.

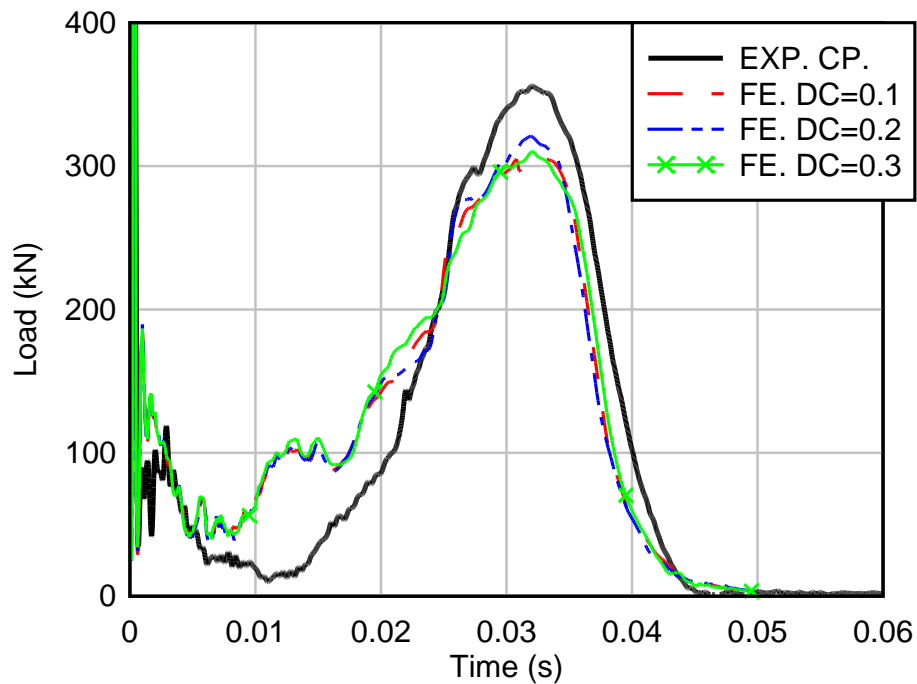


Figure 8.10: Load time histories of FE models with different values of dynamic coefficient of friction between the steel faceplates and the concrete core compared to the experimental result of the Control panel (CP).

8.3.6 Concrete material models

In LS-DYNA, there are two concrete material models can generate default parameters for concrete by specifying basic input data. They are the material model CSCM (Mat. 159) and the concrete model Damage Release III (Mat. 72 R3). In this

section, the capability of these concrete material models to predict the impact response of axially restrained SCS panels was investigated. The FE models generated in this section used the Belytschko-Tsay shell elements for steel faceplates, the separation of the steel faceplates from the concrete core was modelled, and the dynamic coefficient of friction was 0.2.

8.3.6.1 Concrete material model CSCM (Mat. 159)

For this material model, three inputs needed to generate default parameters of concrete are the unconfined compressive strength, aggregate size and the units used in the FE model. According to Federal Highway Administration (2007b), this material model is applicable for concrete grade between 20 MPa to 58 MPa with the aggregate size between 8 mm to 32 mm. In this material model, the damage of concrete whether cracking or crushing is represented by a scalar damage parameter ranges that from 0 to 1. The concrete elements lose all strength and stiffness when the damage parameter approaches to one. An element erosion option is provided in this material model, where concrete elements reached the specified maximum principal strain can be eliminated to prevent computational difficulties.

Three FE models were generated using erosion coefficients of 0.9, 1.0 and 1.2. When the coefficient is less than 1, no erosion occurs, while erosion coefficient of 1 means the erosion is independent of the strain. For the erosion coefficient of 1.2, erosion occurs on the concrete elements when they reached maximum principal strain of 20%. The predicted load time histories were compared to the experimental load time history of the Control panel in Figure 8.11. It was observed that both FE models with the erosion coefficients of 0.9 and 1.2 predicted similar load time histories. Both FE models showed a higher flexural load capacity and residual flexural resistance compared to the experimental result. The peak tensile membrane resistance predicted by both FE models was slightly lower than the experimental result. The FE model with the erosion coefficient of 1 predicted a lower residual flexural resistance compared to the other two FE models, but it corresponded better with the experimental residual flexural resistance. However, the load resistance for the FE model using the erosion coefficient of 1 dropped significantly at 0.028 s, therefore

the predicted peak tensile membrane resistance was significantly lower than the experimental result.

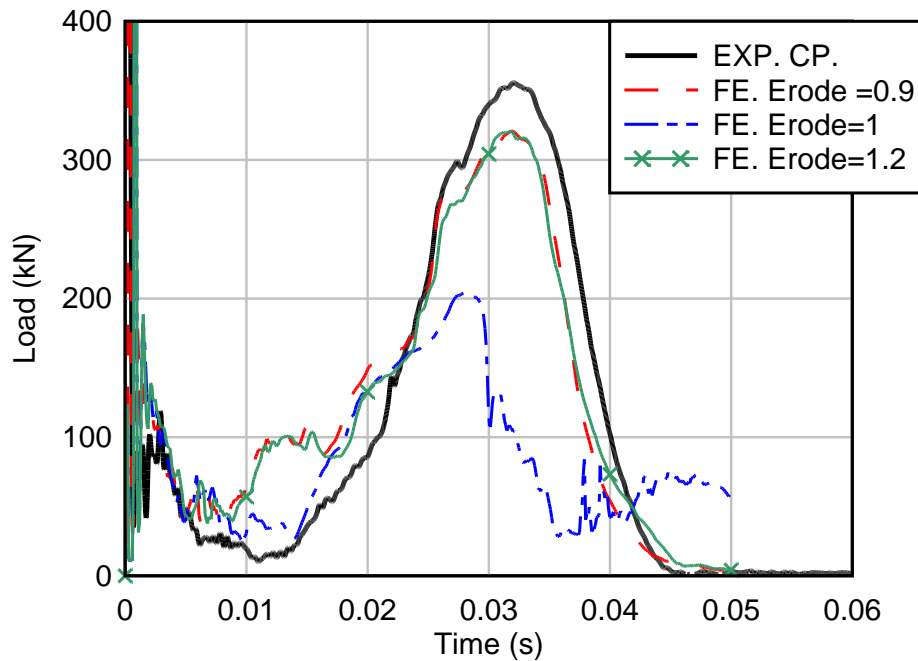


Figure 8.11: Load time histories of FE models using the material model CSCM with different values of erosion coefficients compared to the experimental result of the Control panel (CP).

Damage contour plot of the concrete core for these FE models are shown in Figure 8.12 to Figure 8.14. Figure 8.12 shows the FE model using the material model CSCM (Mat. 159) without erosion predicted damage of concrete core at the impact zone and the flared end similar to the experimental observation of the Control panel. For the FE model using the erosion coefficient of 1, a large number of concrete elements were eliminated, causing a shattering effect on the concrete core, as shown in Figure 8.13. There was virtually no concrete infill to separate the two steel faceplates and this caused the load resistance to drop significantly at about 0.03 s. For the FE model using the erosion coefficient of 1.2, only a small number of concrete elements were deleted, as shown in Figure 8.14. This erosion had little effect on the impact response of SCS panels since the steel faceplates were still effectively separated by the concrete core.

From these simulation results, it could be concluded that the FE model using an erosion coefficient of 1.0 could better predict the residual flexural resistance of SCS panels. However, shattering of concrete elements caused no concrete infill to separate the steel faceplates and affected development of the tensile membrane resistance. In addition, when the erosion coefficient was equal to or greater than 1.2, it had little effects on the impact response of SCS panels.

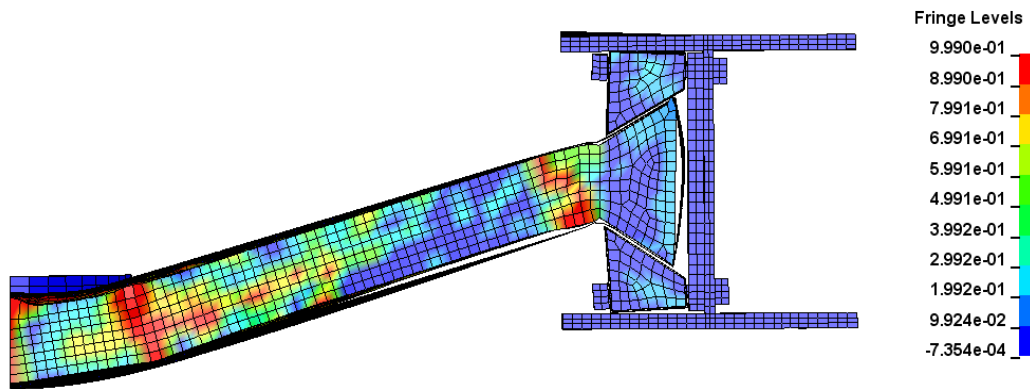


Figure 8.12: Damage contour plot of the concrete core using the material model CSCM (Mat. 159) with an erosion coefficient of 0.9 (no erosion).

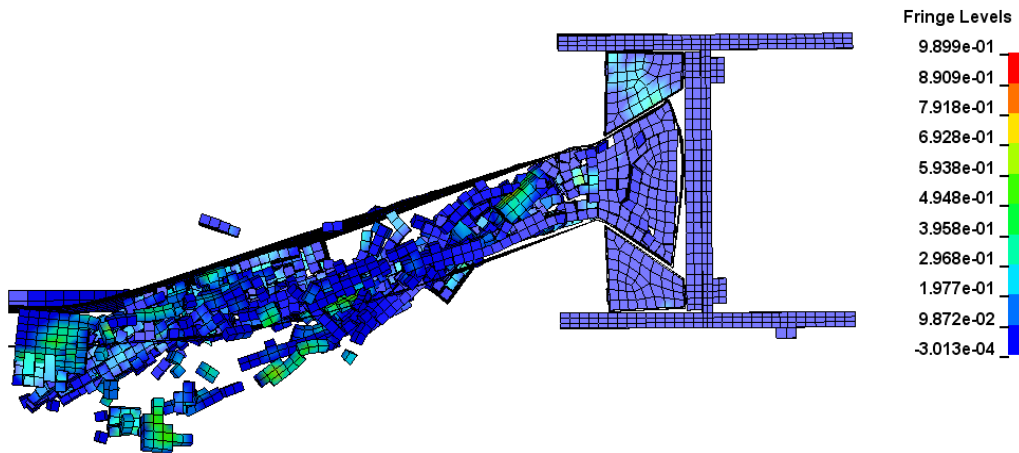


Figure 8.13: Damage contour plot of the concrete core using the material model CSCM (Mat. 159) with an erosion coefficient of 1.

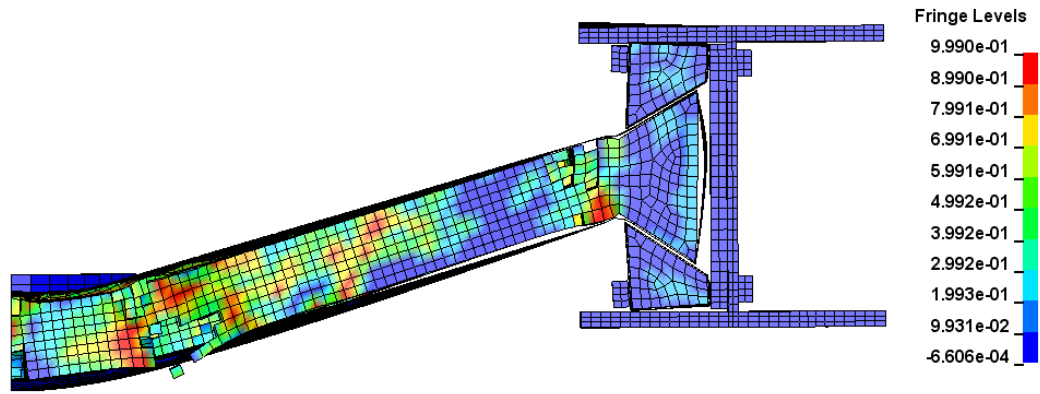


Figure 8.14: Damage contour plot of the concrete core using the material model CSCM (Mat. 159) with an erosion coefficient of 1.2.

8.3.6.2 Concrete material model 72R3

The concrete material model Damage Release III (Mat. 72 R3) can be used either with a complete user specified inputs or internal parameters generation. For the parameters generation, it only requires the unconfined compressive strength of concrete. The parameters are generated based on the English units, thus for the user using the SI units, two conversion factors need to be specified in the input file. In Card 3 of the input, the RSIZE is the conversion factor for length, and it is 3.972×10^{-2} to convert inches to millimetres. While the UCF is the conversion factor for pressure, it is 145 to convert the pressure from unit psi to MPa. This material model allows the user to define a complete set of model parameters and the Equation-of-State for the pressure volume-strain response. Malvar et al. (1997) provided detail description about the improvements of this material model compared to the Pseudo-TENSOR model (Mat. 16). The improvements are: (i) implementation of a third, independent yield failure surface, (ii) removal of the tensile cutoff and extension of the plasticity model in tension and (iii) shear modulus correction.

In the FE model, the concrete core was assigned with the concrete material model Damage Release III (Mat. 72 R3) using the internal parameter generation option. The predicted load time history was compared to the experimental result of the Control panel in Figure 8.15. It showed that the model predicted a slightly lower impact force during the inertia stage and a higher residual flexural resistance compared to the experimental result. It predicted the tensile membrane resistance well up to 0.022 s.

After that, the predicted tensile membrane resistance dropped to about 120 kN before the simulation was terminated at 0.035 s. The damage contour plot of the concrete core is illustrated in Figure 8.16. The concrete infill at the flared end was extensively damaged causing the panel being pulled out of the keyed connection. This caused the load resistance dropped significantly during the tensile membrane resistance stage.

Further investigation was carried out by using the material model CSCM (Mat. 159) to model the concrete elements at the flared end, and the material model Damage Release III for the concrete elements along the span. The predicted load time history is shown in Figure 8.15 and the damage contour plot for the concrete core is illustrated in Figure 8.17. It showed that by using the combination of both concrete material models, the predicted flexural response was similar to the flexural response of the FE model using the material model Damage Release III. However, the FE model using combined concrete material models could prevent extensive damage of concrete infill at flared end. The predicted peak tensile membrane resistance was slightly lower than the experimental result.

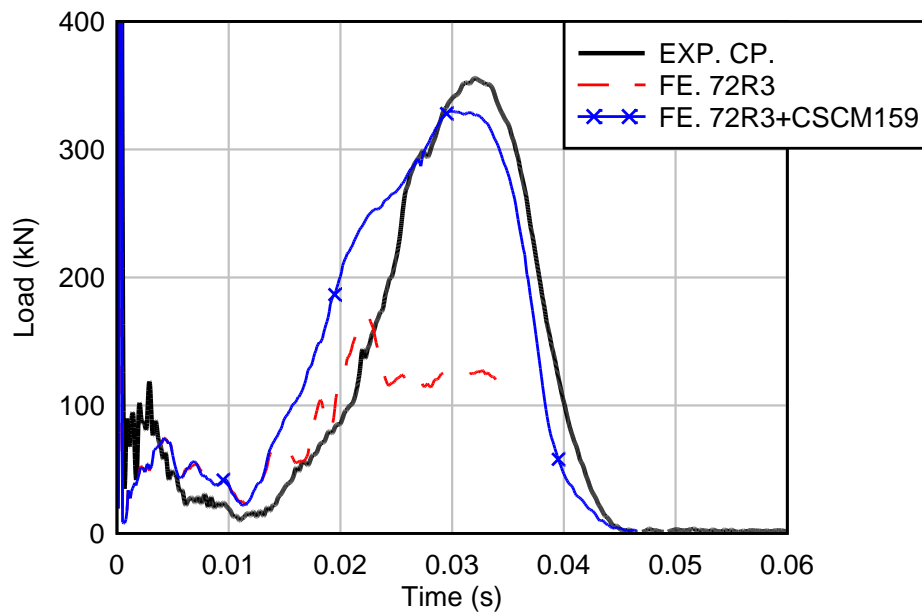


Figure 8.15: Load time histories of the FE models using the concrete material model Damage Release III compared to the experimental result of the Control panel (CP).

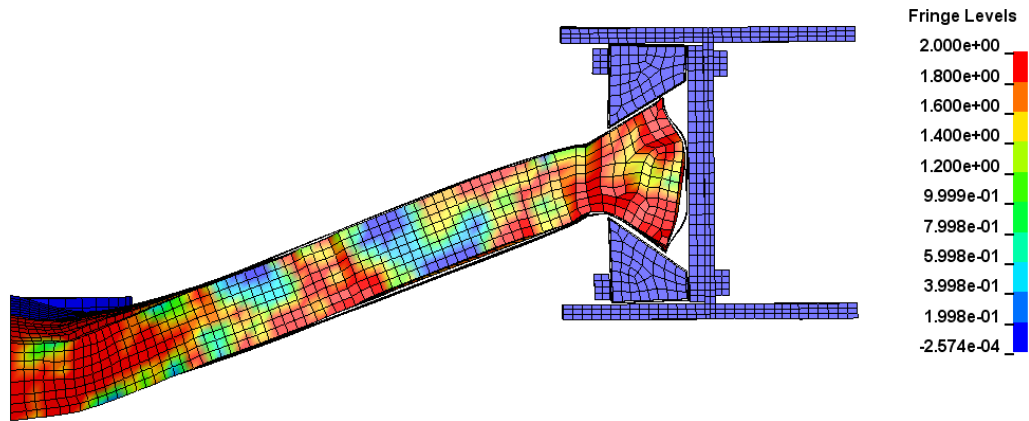


Figure 8.16: Damage contour plot of the concrete core for the FE model using the concrete material model Damage Release III.

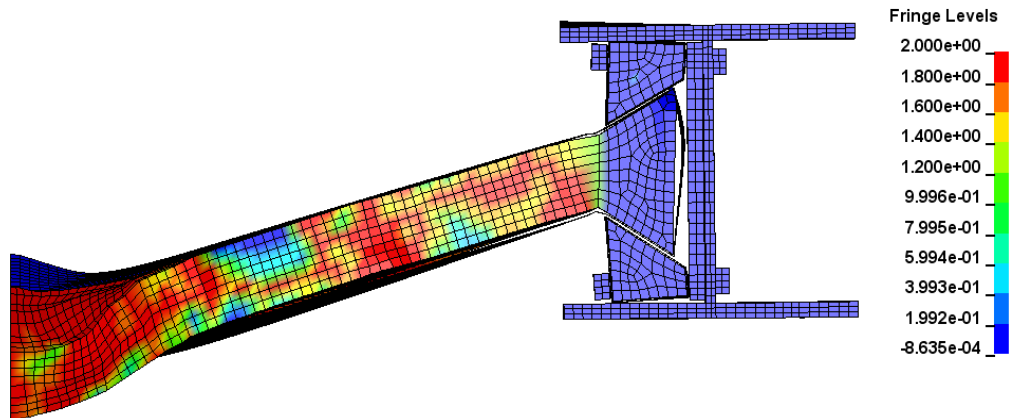


Figure 8.17: Damage contour plot of the concrete core for the FE model using combined material models of CSCM 159 and Damage Release III.

In this section, two types of concrete material models have been used to calibrate the FE model of the Control panel. It showed that the concrete material model had significant effects on the predicted flexural response and the tensile membrane resistance of axially restrained SCS panels under impact loading condition. It was found that the material model CSCM without erosion could better predict the impact response of the Control panel than the material model Damage Release III, and therefore the material model CSCM was chosen for further model calibration.

8.3.7 Hourglass energy of the concrete core

The concrete core was modelled using constant stress solid elements because the fully integrated S/R solid elements become unstable under large deformation and

may cause error termination (negative volume) in the simulation. The constant stress solid elements show nonphysical modes of deformation (hourglass energy) which should be limited in order to obtain accurate simulation results. In this section, the hourglass energy of the concrete core was first evaluated when the default hourglass control formulation (HG type 1) in the LS-DYNA was used. Then the effectiveness of two advanced hourglass control formulations was investigated. The hourglass control formulations were Flanagan-Belytschko viscous form with exact volume integration for solid elements (HG type 3) and Flanagan-Belytschko stiffness form with exact volume integration for solid elements (HG type 5). It is recommended in the LS-DYNA support website to reduce the hourglass coefficient in the range of 0.03 to 0.05 to minimize stiffening of the response when the HG type 5 was used. In this study, the hourglass coefficient was reduced to 0.05.

Figure 8.18 shows the damage contour plot of the concrete core when the default hourglass control formulation (HG type 1) was used. The concrete core was severely damaged at mid-span and the solid elements were slightly distorted. The ratio of peak hourglass energy to the peak internal energy of the concrete core was 17% as presented in Table 8.2. When the HG type 3 was used, damage of the concrete core was similar to the FE model using the HG type 1, except more damage could be observed at the flared end. The ratio of peak hourglass energy to the peak internal energy of the concrete core was 18%. When the HG type 5 was used, the FE model predicted very severe damage of the entire concrete core as shown in Figure 8.19. The predicted damage of the concrete core was more severe than the experimental observations of the Control panel. It was found that the HG type 5 could cause the hourglass energy ratio increased to 33% under this impact condition.

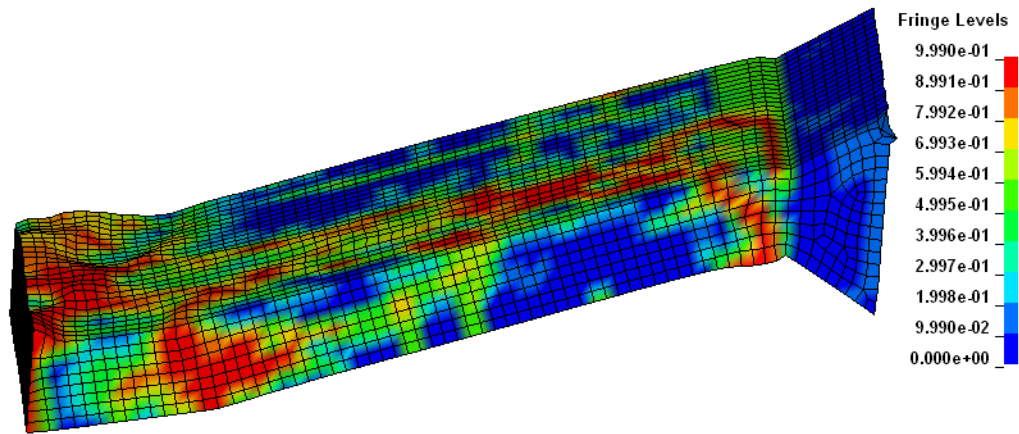


Figure 8.18: Damage contour plot and mesh distortion of the concrete core for the FE model using the default hourglass control formulation (HG type 1).

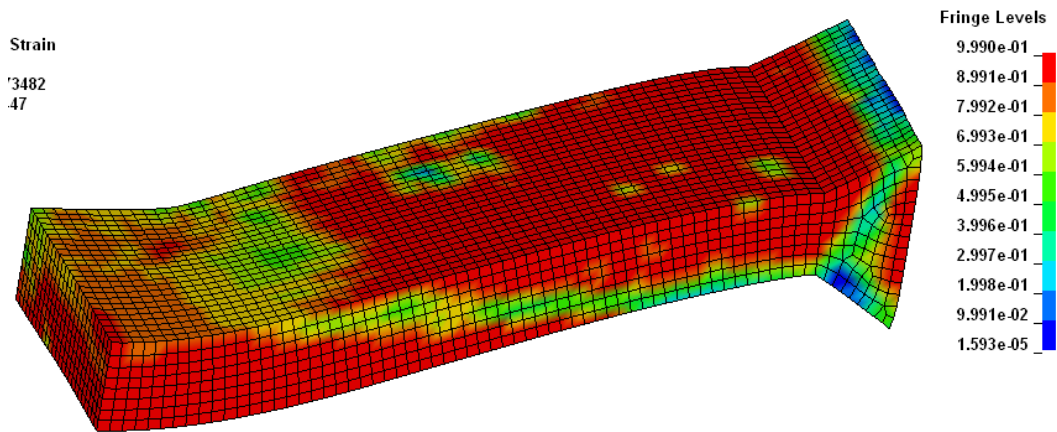


Figure 8.19: Damage contour plot of the concrete core for the FE model using the hourglass control formulation type 5.

Table 8.2: Hourglass energy in the concrete core.

Hourglass control formulations	Peak hourglass energy/peak internal energy
Default HG type 1	17%
HG type 3	18%
HG type 5	33%

The load-time histories predicted by the FE models using different types of hourglass control formulations were compared to the experimental result of the Control panel in Figure 8.20. The simulation result of the FE model using the default hourglass control formulation (HG type 1) corresponded better with the experimental load time

history. Based on the ratio of peak hourglass energy to the peak internal energy of the concrete core and the load-time history, it could be concluded that the default hourglass control formulation, HG type 1, was more effective in this impact loading condition and should be used in the FE model.

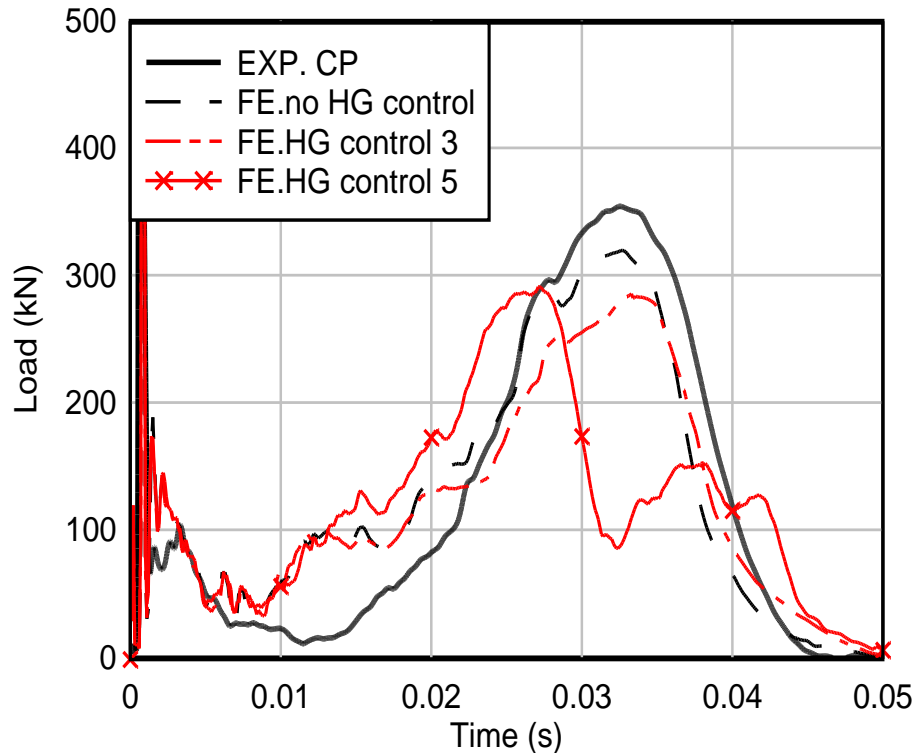


Figure 8.20: Load time histories of FE models using different types of hourglass control formulations for the concrete core compared to the experimental result of the Control panel (CP).

8.3.8 Strain rate effects of materials

8.3.8.1 Strain rate effects of concrete

Concrete is a strain rate sensitive material, the strength of concrete increases when it is subjected to high strain rate loading conditions such as impact or blast loading. In this section, the strain rate effects of concrete were evaluated by using the concrete material model CSCM (Mat. 159). In this material model, the strain rate is considered by using the viscoplastic formulation, and the strain rate effects are applied to the plasticity surface, the damage surface and the fracture energy (Federal Highway Administration, 2007a). Two FE models were generated, where the first model ignored the strain rate effects and the second model considered the strain rate

effects of concrete. Both FE models used the concrete material model CSCM (Mat. 159) without the erosion formulation, the Belytschko-Tsay shell elements, and the dynamic coefficient of friction of 0.2.

The predicted load-time histories were compared to the experimental result of the Control panel in Figure 8.21. By comparing the load time histories, both FE models predicted similar flexural response and tensile membrane resistance. Both FE models predicted a higher residual flexural resistance and a lower peak tensile membrane resistance compared to the experimental result. The damage contour plot of the concrete core for the FE model considering the strain rate effects of concrete is illustrated in Figure 8.22. It was observed that the concrete core exhibited local mesh distortion at the impact zone, and the ratio of peak hourglass energy to the peak internal energy of the concrete core was about 56%. When the hourglass control formulation HG type 5, was applied to the concrete core, it could prevent the mesh distortion, but the FE model predicted an extensive damage of concrete core similar to the damage observed in Figure 8.19. In addition, the ratio of peak hourglass energy to the peak internal energy of the concrete core remained at about 56%. The higher hourglass energy in the concrete core caused the maximum displacement was reduced by 10 mm compared to the maximum displacement of the FE model ignored the strain rate effects of the concrete.

From the simulation results, it could be concluded that the FE model considering the strain rate effects of the concrete showed severe mesh distortion close to the impact zone and a higher amount of hourglass energy. The hourglass control formulation, HG type 5, was not effective in reducing the hourglass energy of concrete core in this impact loading condition. The strain rate effects of concrete were ignored in this study to minimize the hourglass energy of the concrete core in the simulation.

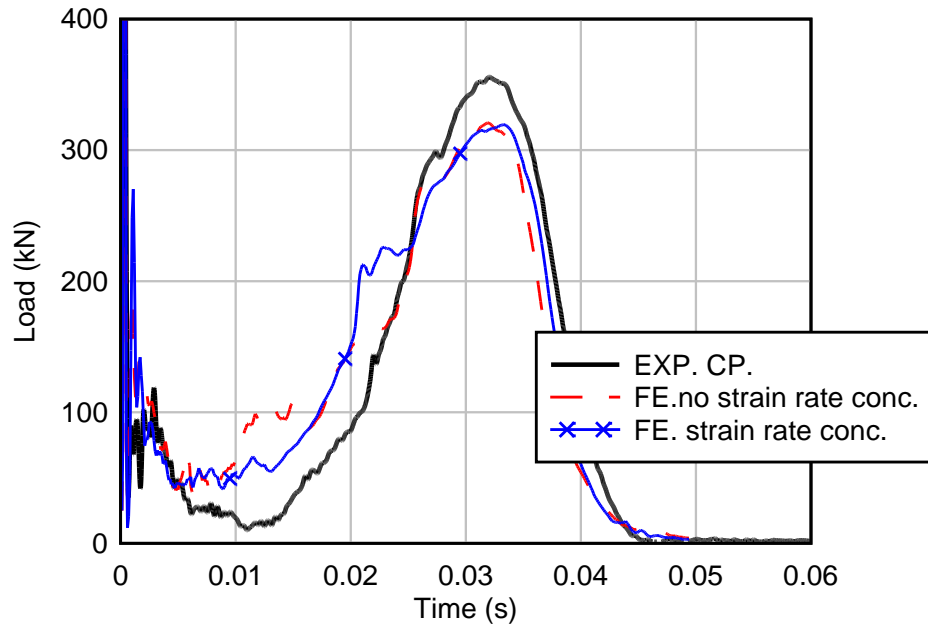


Figure 8.21: Load time histories of FE models with and without the strain rate effects of the concrete compared to the experimental result of the Control panel (CP).

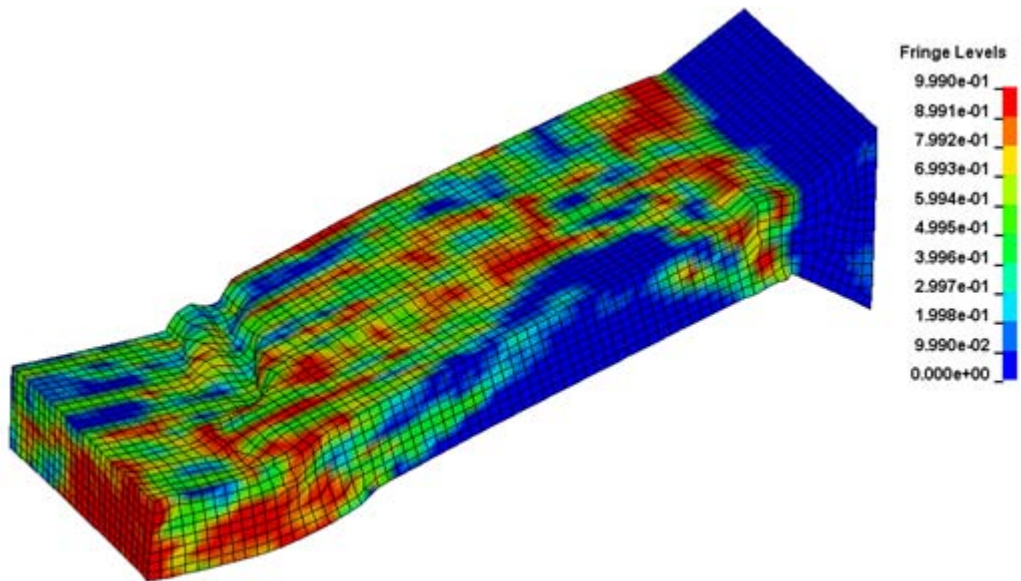


Figure 8.22: Damage contour plot of the concrete core at 0.012 s for the FE model using the material model CSCM considering the strain rate effect of the concrete.

8.3.8.2 Strain rate effects of mild steel

The yield stress of mild steel increases significantly when the strain rate increases. The strain rate effects of mild steel on the impact response of the Control panel were evaluated in this section. The complete stress-strain relationship for the mild steel

was modelled using the Piecewise Linear Plasticity material model. Two FE models were generated, the first model ignored the strain rate effects and the second model considered the strain rate effects of mild steel. The Cowper-Symonds coefficients, 40.4 (D) and 5 (q) were defined and the default rate effects formulation was used to scale the yield stress. Both FE models used the concrete model CSCM ignoring the strain rate effects of the concrete, the Belytschko-Tsay shell elements, and the dynamic coefficient of friction of 0.2.

The predicted load time histories were compared to the experimental result of the Control panel in Figure 8.23. Both FE models predicted similar flexural response, which was higher than the experimental flexural resistance. The FE model considering the strain rate effects of the mild steel predicted a slightly higher peak tensile membrane resistance than the experimental result. While the FE model ignoring the strain rate effects of the mild steel predicted a lower peak tensile membrane resistance compared to the experimental result. The von Mises stress contour plots of the steel faceplates for the FE model ignoring the rate effects of the mild steel are shown in Figure 8.24. Figure 8.25 shows the von Mises stress contour plots of the steel faceplates for the FE model considering the strain rate effects. Without the strain rate effects of mild steel, the maximum stress on the faceplates was about 350 MPa, and it increased to about 590 MPa when the strain rate effects were considered. The maximum displacement of the bottom faceplate was reduced by 6 mm for the FE model considering the strain rate effects compared to the FE model without the strain rate effects.

From these simulation results, it was found that the FE model with the strain rate effects of the mild steel predicted a higher peak tensile membrane resistance at a lower displacement than the FE model ignoring the strain rate effects, due to the higher stress in the steel faceplates when the strain rate effects were considered. Furthermore, the strain rate effects of mild steel had little influence on the flexural response of the Control panel.

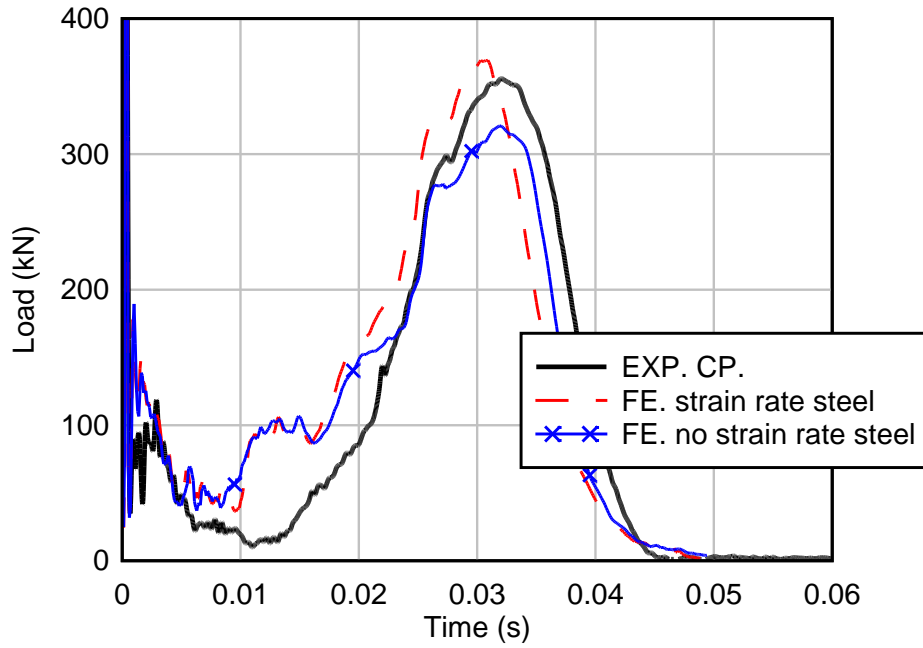


Figure 8.23: Load time histories of FE models with and without the strain rate effects of the mild steel compared to the experimental result of the Control panel (CP).

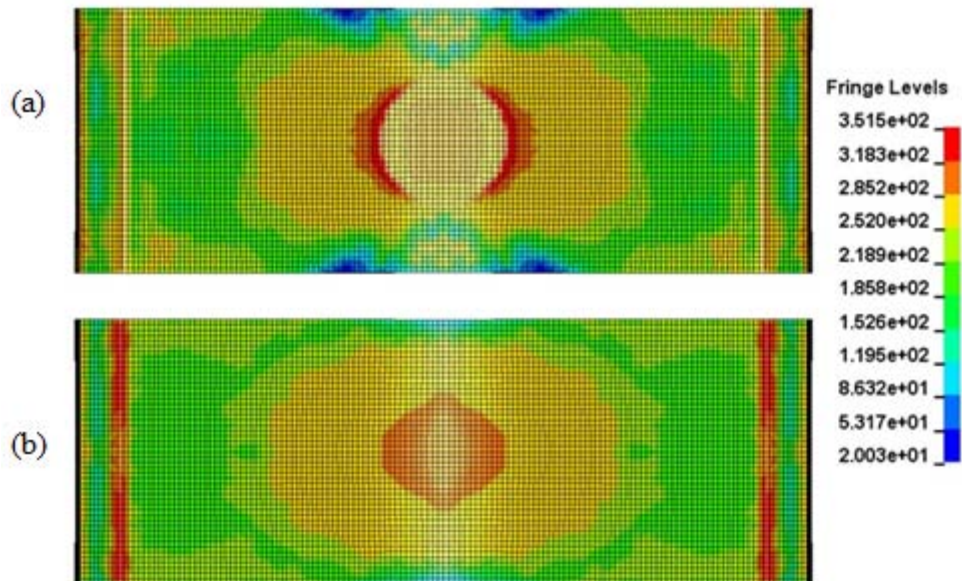


Figure 8.24: Von Mises stress contour plot on the faceplates for the FE model ignoring the strain rate effects of mild steel at the peak tensile membrane resistance (a) top faceplates and (b) bottom faceplates.

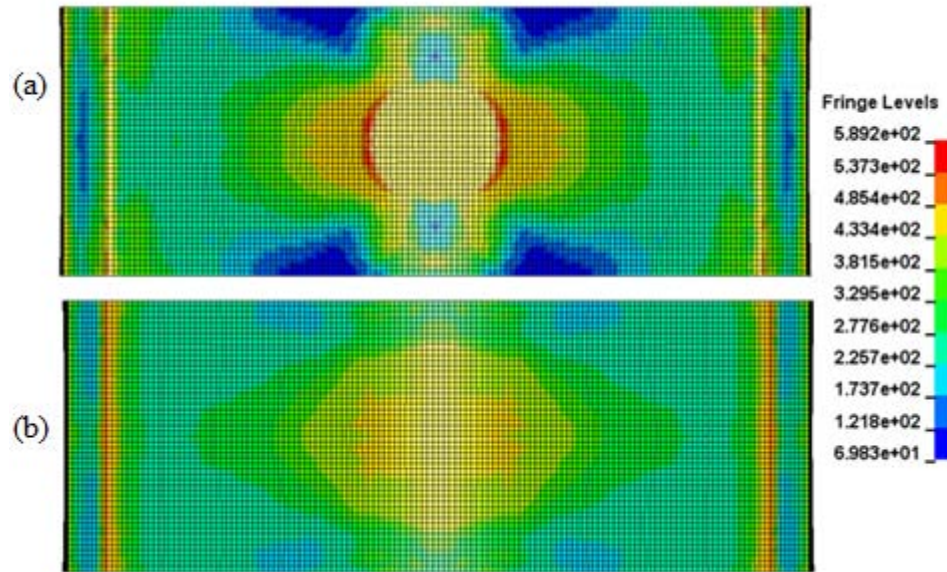


Figure 8.25: Von Mises stress contour plot of the faceplates for the FE model considering the strain rate effects of the mild steel at the peak tensile membrane resistance (a) top faceplate and (b) bottom faceplate.

8.4 Simulation results and discussion

8.4.1 Control panel

The predicted load and displacement time histories of the Control panel were compared to the experimental results in Figure 8.26. It showed that the FE model had the capacity to predict initial inertial effects during the instrumented impact testing and flexural response of the Control panel quite closely. After the initial flexural capacity was reached, the experimental flexural resistance of the Control panel reduced significantly to about 20 kN due to fracture of the concrete core. Then, the tensile membrane resistance started to develop in the steel faceplates resulting in the significantly increased load-carrying capacity, with the peak tensile membrane resistance of 356 kN. The FE model predicted the residual flexural strength of 48 kN, which was higher than the experimental residual flexural strength of 20 kN. The FE model was able to predict the development of the tensile membrane resistance and it showed the peak tensile membrane resistance of 384 kN. The maximum experimental displacement of the Control panel was 200 mm, compared to the maximum predicted displacement of 182 mm. The FE model underestimated the maximum displacement by 9% compared to the experimental result.

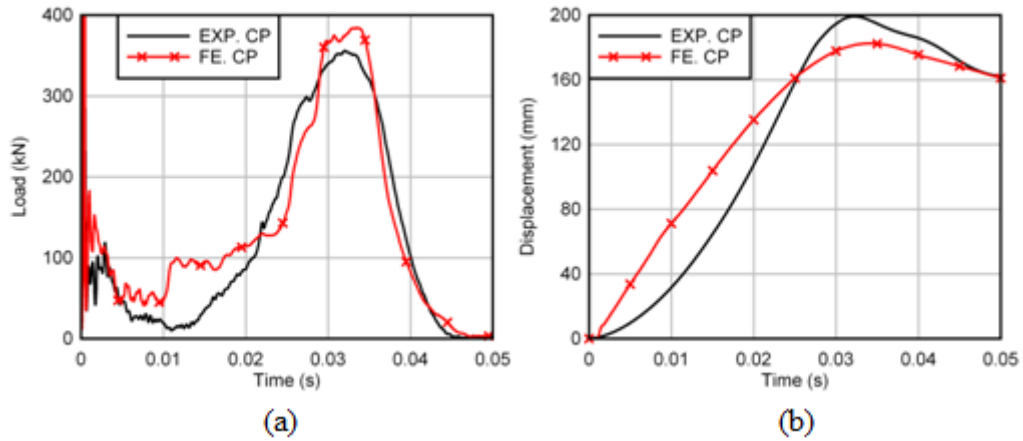


Figure 8.26: A comparison between experimental and predicted results for the Control panel (CP) (a) load time histories, (b) displacement time histories.

The FE model predicted extensive damage of the concrete core at the impact zone and near the support similar to the experimental observation, as shown in Figure 8.27. Contour plot of the von Mises stress on the top steel faceplate is shown in Figure 8.28. The indentation of the top steel faceplate was visualised by the shell elements with very a high stress concentration forming a circular shape at the mid-span. The maximum stress on the top steel faceplate was 623 MPa, exceeding the static yield stress of the mild steel (271 MPa) due to the strain rate effects included in the FE model. From the comparison of the numerical and test data for the impact load, maximum displacement, physical damage of the concrete and steel plates, it can be concluded that the finite element model is capable of capturing the most important structural response characteristics of the Control panel.

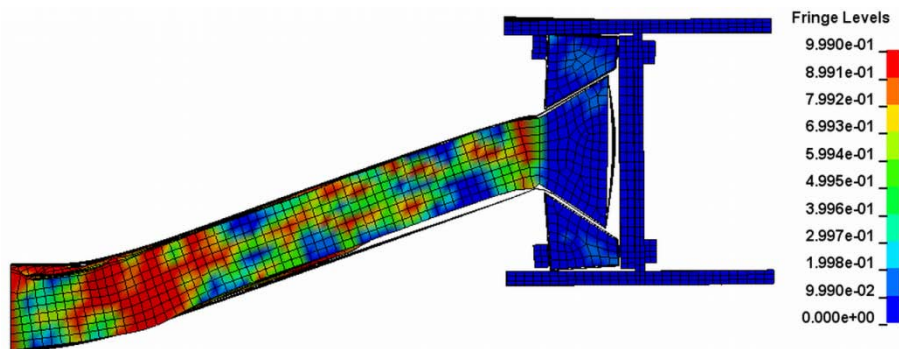


Figure 8.27: Damage contour plot for the concrete core of the FE model for the Control panel.

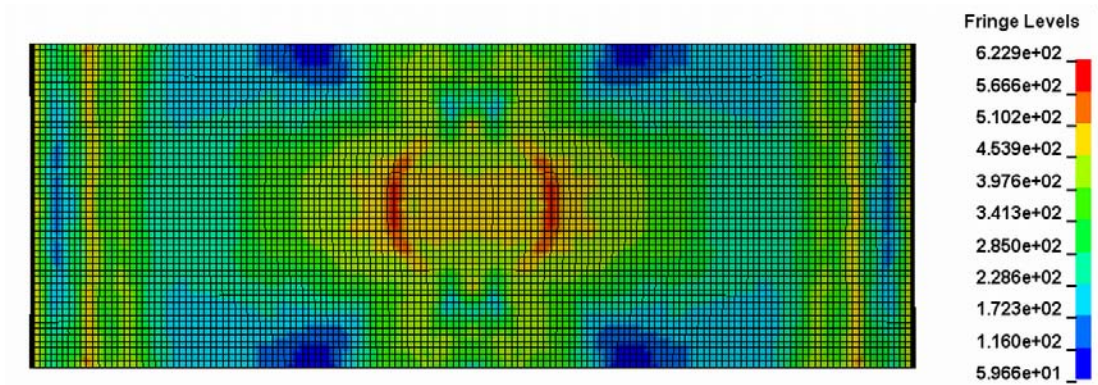


Figure 8.28: Von Mises stress contour plot on the top faceplate of the FE model of the Control panel.

8.4.2 Increased impact energy panel

The experimental set up of the Increased impact energy panel was similar to the Control panel, except the drop height of the impactor was increased from 3 m to 4 m. They both had the same mild steel faceplates and concrete compressive strength. Thus the FE model of the Control panel was modified, by changing the initial velocity of the impactor from 7.67 m/s to 8.86 m/s for the FE model of Increased impact energy panel. The predicted load and displacement time histories were compared to the experimental results in Figure 8.29. The FE model predicted the flexural strength reasonably well but it overestimated the residual flexural strength. The predicted peak tensile membrane resistance of 401 kN was lower than the peak experimental tensile membrane resistance of 431 kN. The maximum displacement predicted by the FE model was 188 mm, and it was 8% lower than the maximum experimental displacement of 204 mm. It should be noted that the FE model predicted severe damage of concrete core at the flared end similar to the experimental observation. However, it could not predict the partial fracture failure of the top steel faceplate.

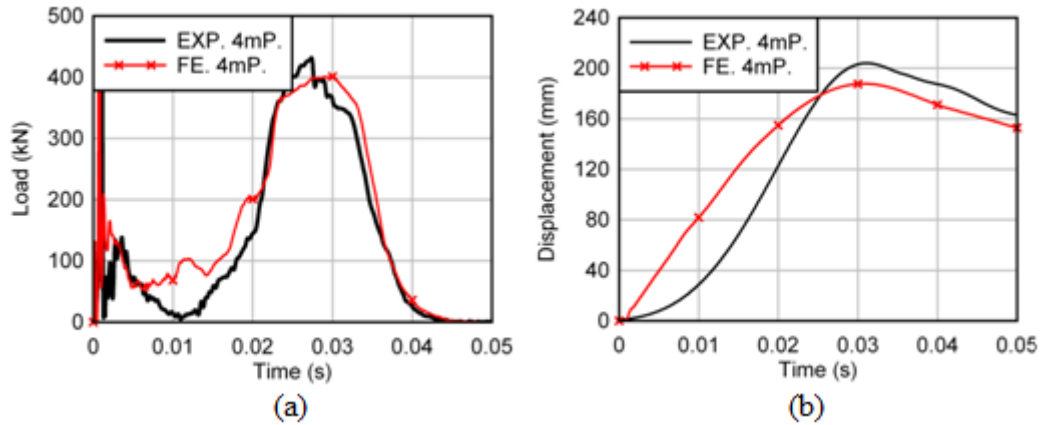


Figure 8.29: A comparison between experimental and predicted results for the Increased impact energy panel (4mP) (a) load time histories, (b) displacement time histories.

8.4.3 Stainless steel panel

This panel used stainless steel faceplates and the stress-strain relationship of the stainless steel shown in Chapter 5 was defined in the FE model. The Cowper-Symonds coefficients of 100 and 10 were defined to include the strain rate effects in the material model of the stainless steel. As shown in Figure 8.30, the FE model produced reasonable prediction of the inertial effects and flexural capacity of the Stainless steel panel. Between 0.01s to 0.02 s of the response, the FE model predicted significantly higher flexural resistance than the experimental residual flexural strength of the Stainless steel panel. The predicted flexural resistance could be reduced by using the erosion option in the concrete material model CSCM (Mat. 159) as discussed in Section 8.3.6.1. However, the erosion of concrete elements affected the development of tensile membrane resistance at large displacement, therefore it was ignored.

The peak tensile membrane resistance predicted by this FE model was 380 kN, and it was only slightly higher than the experimental peak resistance of 377 kN. The maximum displacement of the bottom faceplate for this FE model was 162 mm, which was 10 % lower than the experimental displacement of 181 mm. In the test, the concrete core of the Stainless steel panel was extensively damaged at the mid-span and near the support, while the top faceplate was indented by the impactor.

These failure modes were similar to the experimental observations of the Control panel shown in Figure 8.27. The contour plot of von Mises stresses for the FE model of the Stainless steel panel was similar to the Control panel as shown in Figure 8.28.

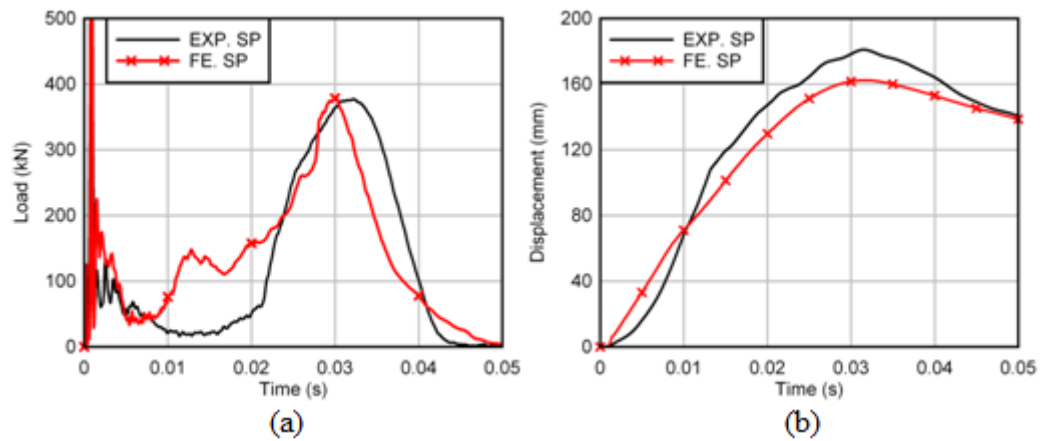


Figure 8.30: A comparison between the experimental and predicted results for the Stainless steel panel (SP) (a) load time histories, (b) displacement time histories.

8.4.4 Lightweight core panel

Lightweight concrete with a density of 1400 kg/m^3 and the concrete compressive strength of 11 MPa was used as the infill for this panel. The load and displacement time histories predicted by the numerical model were compared to the experimental results in Figure 8.31. The FE model predicted higher values for the flexural capacity and the residual flexural strength than the experimental results. As previously discussed, the erosion of the concrete elements can reduce the predicted residual flexural strength, but it will also affect the tensile membrane resistance of the steel faceplate due to the shattering of the concrete elements. Therefore, the erosion formulation was not considered in the FE model of the lightweight concrete panel. The peak tensile membrane resistance predicted by the FE model was 358 kN compared to the experimental value of 333 kN. The maximum predicted displacement of the bottom faceplate was 174 mm. The model underestimated the experimental maximum displacement of 196mm by 11 %. In the test, the physical damage of the Lightweight core panel was similar to the Control panel, except the concrete core of the Lightweight core panel experienced more severe damage. The

numerical model was capable to represent the main stages of the response of the panel with lightweight concrete infill with reasonable accuracy.

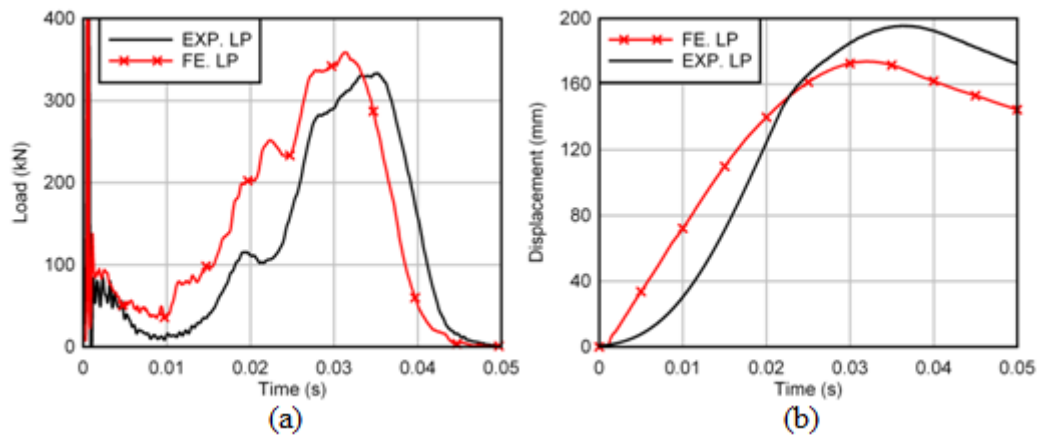


Figure 8.31: A comparison between the experimental and predicted results for the Lightweight core panel (LP) (a) load time histories, (b) displacement time histories.

8.4.5 Reinforced core panel and Double reinforced core panel

In these panels, two layers of 4@50 mm and 4@25 mm wire mesh were used to reinforce the concrete core. The wire meshes were modelled using the Hughes-Liu beam elements and their nodes were merged with the concrete elements. Figure 8.32 and Figure 8.33 show the comparison between the experimental results and simulation results for the Reinforced core panel and the Double reinforced core panel, respectively.

From Figure 8.32(a) and Figure 8.33(a), it was found that the numerical models predicted the initial response of the panels quite accurately. The flexural strength predicted by both FE models was significantly higher than that in the tests. This could be attributed to the modelling of the bond between the wire meshes and the concrete core by merging the nodes of the beam elements to the nodes of the concrete elements. This full interaction between the concrete and the wire meshes ignored the slippage at the steel wire-concrete interface thus causing a higher flexural capacity.

For the Reinforced core panel, the peak tensile membrane resistance predicted by the FE model was 294 kN, which was slightly higher than the experimental result of 284 kN. The maximum displacement of the bottom faceplate predicted by the FE model was 168 mm. It was 8 % lower than the experimental displacement of 183 mm. For the Double reinforced core panel, the FE model predicted the peak tensile membrane resistance of 242 kN, which was higher than experimental result of 211 kN. The maximum displacement predicted by the FE model was 158 mm compared to the experimental displacement of 178 mm. The predicted maximum displacement was 11% lower than the experimental result.

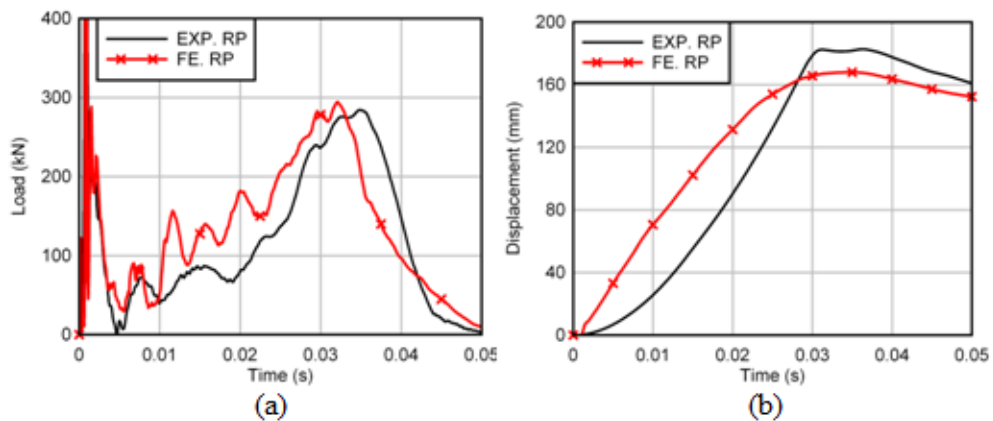


Figure 8.32: A comparison between experimental and predicted results for the Reinforced core panel (RP) (a) load time histories, (b) displacement time histories.

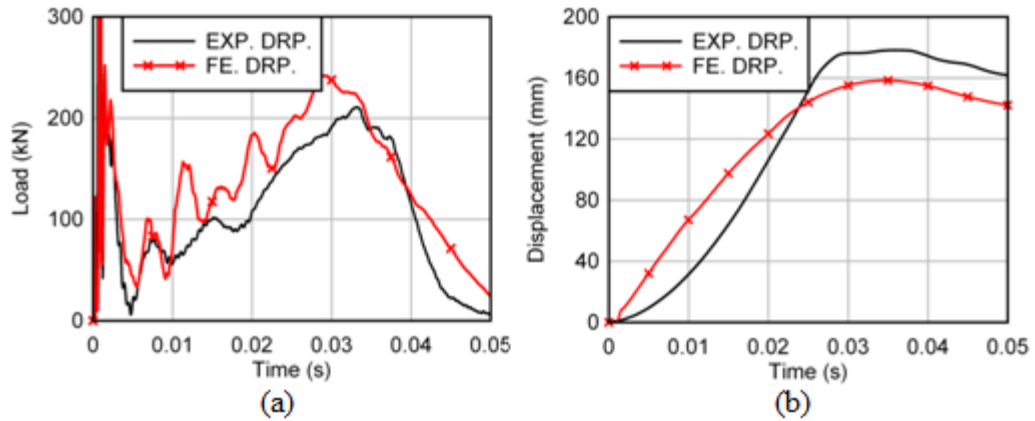


Figure 8.33: A comparison between experimental and predicted results for the Double reinforced core panel (DRP) (a) load time histories, (b) displacement time histories.

In the impact test, it was observed that the concrete core at the impact zone was crushed at the top and cracked at the bottom for both panels, as exemplified in Figure 7.21 in Chapter 7. The top layer of the wire mesh at the mid-span buckled and the top steel faceplate was indented. There was some cracking of concrete at the flared zone, as shown in Figure 7.21 in Chapter 7. The damage contour plot of the concrete core of the Reinforced core panel is illustrated in Figure 8.34. It showed that the FE model predicted similar damage of concrete core at the mid-span and flared end with the experimental observations. The axial force contour plot of the wire meshes is illustrated in Figure 8.35. It showed that the top layer of wire mesh suffered local buckling at the impact zone and fractured near the support.

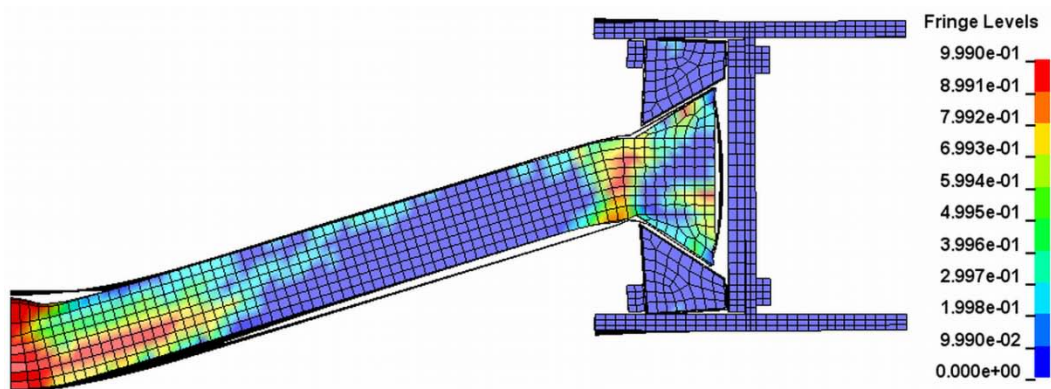


Figure 8.34: Damage contour plot for the concrete core of the FE model for the Reinforced core panel.

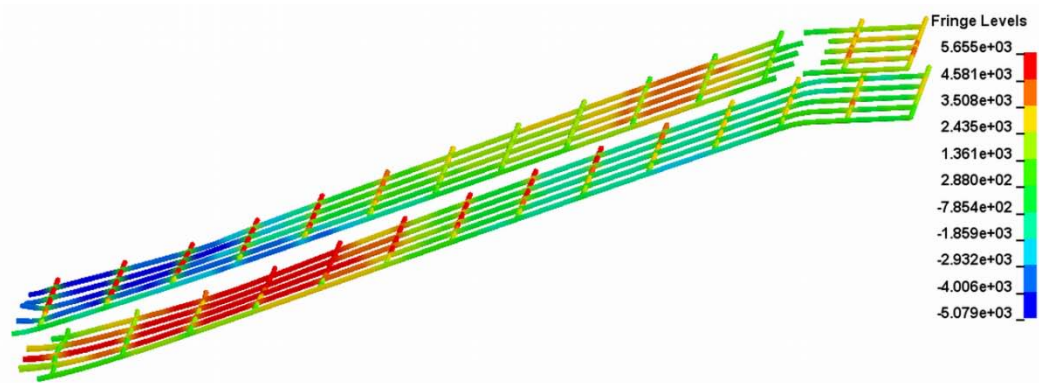


Figure 8.35: Deformation and axial force distribution in the wire meshes of the FE model for the Reinforced core panel.

8.4.6 Panel with bracing elements

In this panel, small steel plates with a thickness of 3 mm and 20 mm wide were used to connect the top and bottom faceplates. They were welded at mid-span, quarter-spans and adjacent to the flared ends, at a distance of 50 mm from the edges of the steel faceplates before concrete casting. In the FE model, the steel faceplates were in contact with the concrete core, since in reality the concrete core was bonded to the steel faceplates before the impact test commenced. The FE model ignored the chemical bonding of concrete and it only considered the friction interaction between the steel faceplates and the concrete core. The small steel plate bracings were modelled with the Belytschko-Tsay shell elements, and the contact between these bracings and the concrete core elements was defined using the constraint algorithm Lagrange in Solid. The nodes of the small bracings were merged with the nodes of the steel faceplates.

The predicted load and displacement time histories were compared to the experimental results of the Panel with bracing elements in Figure 8.36. The FE model predicted a higher flexural strength compared to the experimental result. The FE model could not predict the drop in the flexural capacity at about 0.01 s, and it showed a higher tensile membrane resistance during 0.012 s to 0.025 s. After that, the predicted tensile membrane resistance corresponded well with the experimental result. The predicted and experimental peak tensile membrane resistance was about

244 kN. The predicted displacement of 165 mm was 9% lower than the experimental result of 181 mm.

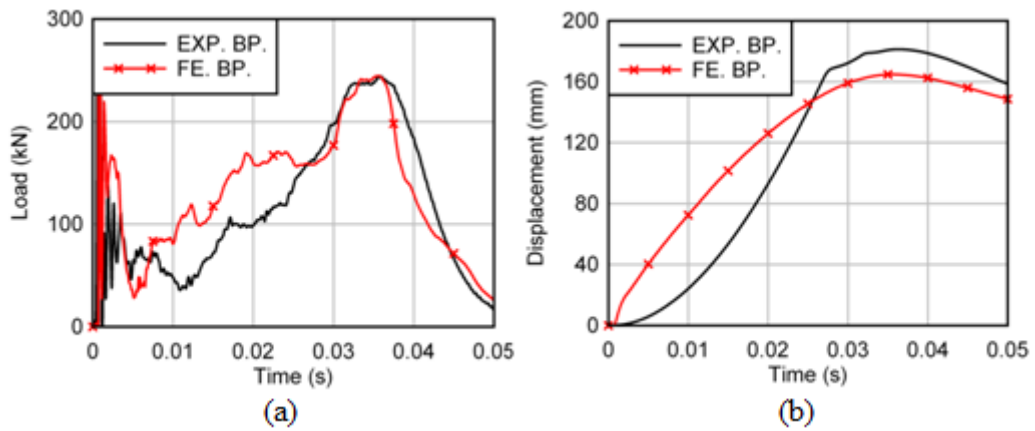


Figure 8.36: A comparison between experimental and predicted results for the Panel with bracing elements (BP) (a) load time histories, (b) displacement time histories.

The von Mises stress contour plot of the top faceplate is shown in Figure 8.37. The high stress concentration at mid-span represented the indentation of the top steel faceplate by the impactor. It also showed a high stress concentration at the locations where the bracings were merged to the steel faceplates. However, the FE model could not predict the welding fracture failure of these small bracings as observed in the test.

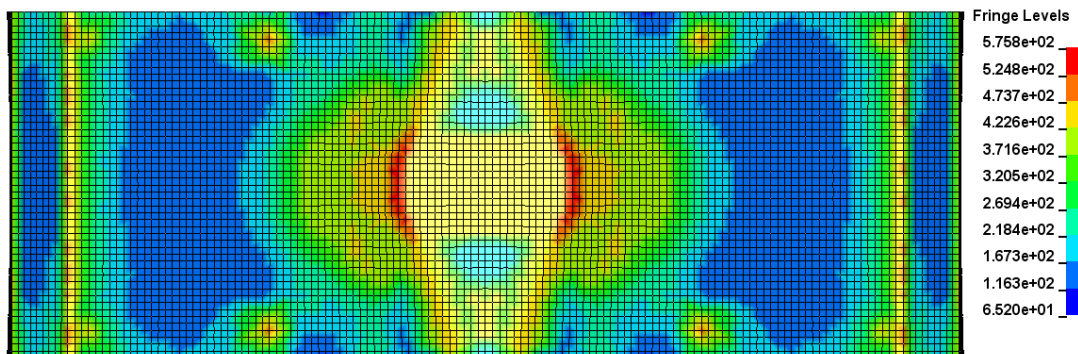


Figure 8.37: Von Mises stress contour plot on the top faceplate for the FE model of the Panel with bracing elements.

8.4.7 Improved bonding panel

In this panel, a layer of 3@25 mm wire mesh was tack welded to the inner surface of the mild steel faceplates before concrete casting. After the test, it was found that the wire meshes were embedded in the concrete core and separated from the steel faceplates, which implied that the tack welding had failed during the test. Thus, the tack welding between the wire meshes and the steel faceplates was ignored in the FE model to simplify the modelling. The wire meshes were modelled using the Hughes-Liu beam elements and their nodes were merged with the nodes of concrete elements. In the FE model, the steel faceplates were in contact with the concrete core but the chemical bonding of concrete was ignored.

The impact force during the inertial stage predicted by the FE model was about 160 kN and it was lower than the experimental result of 240 kN. This could be attributed to the lower panel's stiffness when the tack welding was ignored in the model. The predicted flexural strength of 130 kN was similar to the experimental result. However, the FE model could not predict the drop in the flexural resistance during 0.015 s to 0.025 s. The FE model predicted the peak tensile membrane resistance of 218 kN, which was similar to the experimental peak tensile membrane resistance. The FE model predicted a maximum displacement of 167 mm, which was 1% lower than the experimental displacement of 169 mm. The FE model predicted severe concrete cracking and crushing at mid-span, and cracking near the support as shown in Figure 8.39. The predicted damage of concrete was similar to the experimental observations.

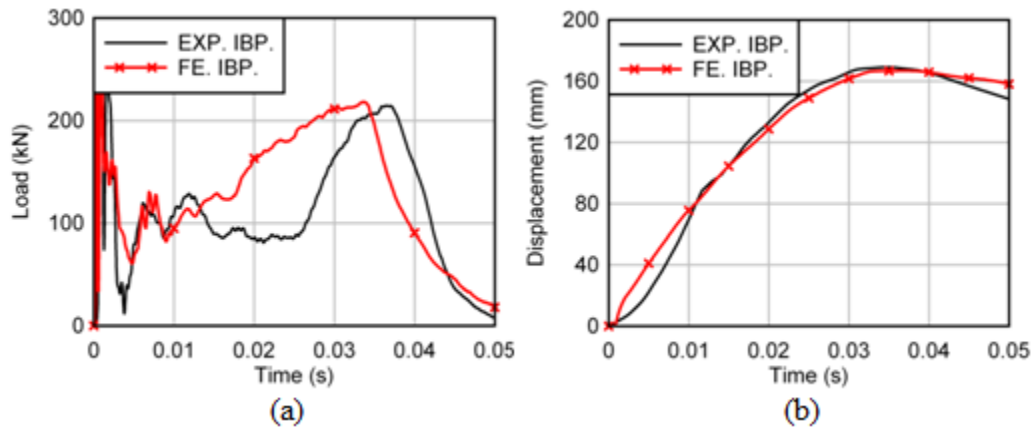


Figure 8.38: A comparison between experimental and predicted results for the Improved bonding panel (IBP) (a) load time histories, (b) displacement time histories.

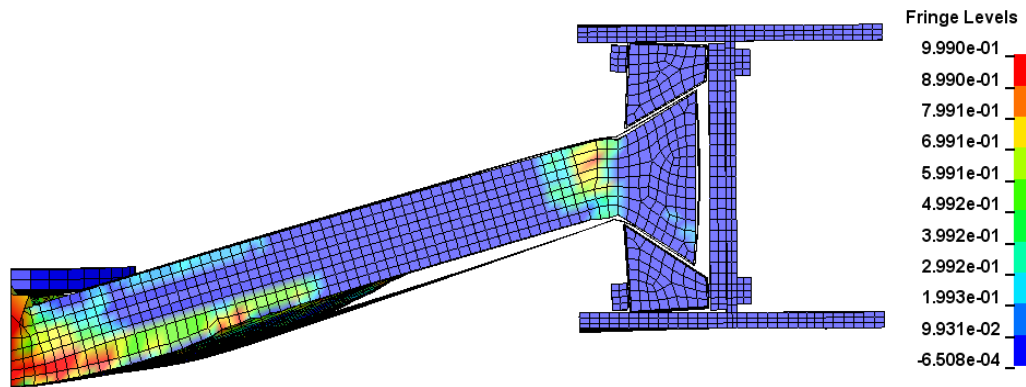


Figure 8.39: Damage contour plot of the concrete core for the FE model of the Improved bonding panel.

8.4.8 Fully enclosed panel

In this panel, two mild steel end caps of 3 mm thickness were welded to the top and bottom faceplates to form a fully enclosed panel. After the impact test, one of the end caps was found partially detached from the faceplates due to poor quality of welding. So, the failure mode of this panel was non-symmetry in the longitudinal direction. For the side where the end cap still fully attached to the steel faceplates, the failure mode was the outward buckling of the top faceplate and end cap at the mid-span. While at the other side, the end cap was partially detached from the faceplates and no buckling could be observed.

Two FE models were generated, where the first model considered the strain rate effects of mild steel while the second model ignored the strain rate effect. A quarter model of the experimental set up was modelled, and the end cap was modelled using the Belytschko-Tsay shell elements. The nodes of the end cap were merged with the nodes of the faceplates. By using the quarter model of the experimental setup and merging nodes of the end cap to the nodes of the steel faceplates, the FE model would predict a symmetrical failure mode without the weld failure of the end cap. The FE models predicted a slightly higher impact force at the inertial stage, about 330 kN compared to the experimental impact force of 290 kN. Then the experimental flexural resistance was significantly lower than the predicted flexural resistance due to the welding fracture failure of the end cap.

The predicted flexural resistance fluctuating due to the contact conditions between the drop hammer and the panel as discussed in Chapter 7. The maximum flexural resistance increased significantly when the strain rate effects of mild steel were considered. The maximum flexural load for the FE model with the strain rate effects was about 450 kN compared to 310 kN for the model ignored the strain rate effects. The maximum displacement predicted by the FE models was significantly lower than the experimental result. The maximum displacement for the FE model considered the strain rate effects was 65 mm. The FE model ignored the strain rate effects predicted a maximum displacement of 85 mm compared to the experimental displacement of 138 mm. The simulation results showed that the top steel faceplate was buckled outward at the impact zone, but no buckling could be observed at the end cap. From the simulation results, it showed that the Fully enclosed panel could increase the flexural resistance significantly, and reduce the maximum displacement of the panel if the welding fracture failure of the end cap could be avoided.

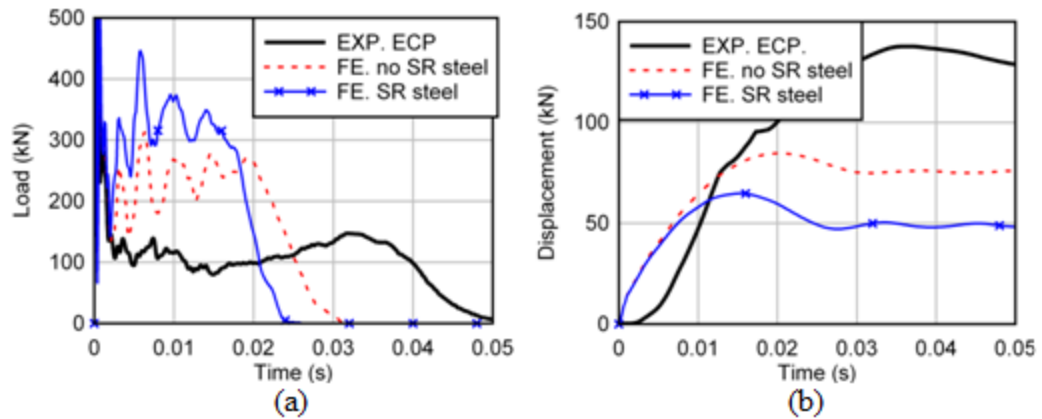


Figure 8.40: A comparison between experimental and predicted results for the Fully enclosed panel (ECP) (a) load time histories, (b) displacement time histories.

8.5 Conclusions

The numerical simulations presented a three-dimensional modelling of the axially restrained steel-concrete-steel (SCS) panel subjected to the impact of a falling mass. The numerical results demonstrated reasonable correlation with the impact test results. They also revealed some differences in modelling the failure mechanisms between the steel plates and the concrete infill under impact conditions. Several important modelling observations are summarised below:

- (a) Support conditions: The axial restraint supports used in the impact tests consisted of the UC sections, keyed inserts, I-beam and bolt connections. These components affected the flexural response and tensile membrane resistance of the SCS panels. In this study, the axial restraint supports were modelled in detail and calibrated against the experimental result of the Control panel.
- (b) The contact surface algorithm: The LS-DYNA Automatic-Surface-to-Surface contact algorithm which only considered the friction resistance between interfaces was appropriate for the non-composite SCS panels since the chemical bonding of the concrete had failed before the testing. However, the assumption of a full bond between the wire meshes and the concrete core in the FE model with reinforced concrete infill may overestimate the flexural capacity of the panel.
- (c) Concrete material model: Two concrete material models used to calibrate the FE models were the concrete model CSCM and the concrete model Damage Release III. It was found that the material model CSCM could predict the response of

axially restrained SCS panels better than the concrete model Damage Release III under this impact circumstance.

- (d) The strain rate effects: The strain rate effects of the steel were considered by defining the Cowper-Symonds coefficients. These coefficients increased the static yield stress of the steels. The maximum stress achieved by the mild steel faceplates in the simulation was more than 600 MPa compared to the static yield stress of 271 MPa. It was found that the hourglass energy exceeded 50% of the internal energy of the concrete core when the strain rate effects of the concrete were considered. Therefore the strain rate effects of concrete were ignored to minimise the hourglass energy of the concrete core in this study.
- (e) Erosion formulation of concrete elements: The concrete elements can be eliminated once they reached the strain threshold defined in the LS-DYNA concrete material model CSCM (Mat. 159). The erosion of the concrete elements could improve the prediction of the residual flexural strength of the SCS panel. On the other hand, the erosion formulation was not recommended in this study because it may result in significant underestimation of the tensile membrane resistance of the non-composite axially-restrained sandwich panels under large deformation.
- (f) The FE model used in this study could not predict the partial fracture failure of top steel faceplate observed in the Increased impact energy panel.

CHAPTER 9

RESPONSE OF AXIALLY RESTRAINED NON-COMPOSITE SCS PANELS SUBJECTED TO BLAST LOADING

In this chapter, the structural behaviour of axially restrained non-composite SCS panel under blast loading was investigated using a non-linear transient dynamic finite element software LS-DYNA. Firstly, the response of non-composite SCS panels under fully fixed support condition was investigated, followed by a study on the performance of the barrier consisted of the posts and the non-composite SCS panels. It was found that the overall response of the axially restrained non-composite SCS panel was similar to the protective catcher system, where the rear steel faceplate dissipated most of the impulsive energy. The existing analytical model for the thin sheet catcher system was improved to account for the effects of the rear faceplate thickness. For non-composite SCS panels supported by posts, the flexural yield load of the post had significant effect in the development of strain energy in the rear faceplate. It will be demonstrated that a certain percentage of the kinetic energy of the SCS panel was dissipated by the strain energy in the post due to the panel-post interaction. The post underwent excessive deformation under blast loading conditions, and the failure of the posts was one of the limiting factors in the design of the barrier supported by the posts. The application of two degrees of freedom system to predict the response of the barrier under blast loading was investigated. The results of two degrees of freedom system showed that the rear faceplate could not achieve full capacity of the plastic membrane due to deformation of the post, and it was vital to consider the transient membrane response in the static resistance function of the rear faceplate. In the end, the performance of the prototype barrier with non-composite SCS panels was compared to the performance of the concrete blast wall. This comparison showed that the barrier with non-composite SCS panels is a viable alternative to the concrete blast wall in term of economy and safety considerations.

9.1 Introduction to the catcher system

The catcher systems have been developed to improve the blast resistance of concrete masonry wall and glazing façades. The glazing façade and concrete masonry wall are brittle, and have low energy absorption capacity. They always fail catastrophically under blast loading condition and generate hazardous debris. The thin sheet catcher system can be used for concrete masonry wall, and the cable catcher system can be utilized for the glazing façade to protect personnel from hazardous debris generated by external concrete masonry wall or glazing. The thin sheet catcher is normally composed of ductile materials such as sheet metal, polymer, woven fabric and wire mesh. The catcher system is placed behind the wall, anchored to the supporting structures and it is designed to dissipate energy through the membrane stretching. The thickness of the sheet material is normally less than 5 mm.



Figure 9.1: Masonry wall retrofitted by the thin steel sheet catcher system. (Crawford et al. 2009)

Davidson et al. (2004) showed that the spray-on polymer was effective in strengthening the blast resistance of the concrete masonry wall. Salim et al. (2008) carried out experimental study to develop the static resistance function of the thin steel sheet under uniformly distributed load. Davidson (2008) presented FE simulation techniques to predict the capacity of membrane retrofitted masonry wall. Crawford et al. (2009) presented a simple analytical model to predict the response of thin steel sheet retrofitted masonry wall using the conservation of energy approach.

Moradi et al. (2010) presented an analytical model for the masonry wall retrofitted using various materials and the analysis results corresponded well with the experimental results.

From the numerical simulation results of non-composite SCS panels under blast loading, it was found that the contribution of the front steel faceplate in the energy absorption of the SCS panels was insignificant. The front faceplate was separated from the concrete core, and the kinetic energy of the concrete core was mainly dissipated through the energy absorption of the rear steel faceplate, which was similar to the response of the catcher system. The simplified energy approach presented by Crawford et al. (2009) for the thin steel sheet retrofitted masonry wall was modified in this study and used to predict the response of non-composite SCS panels under blast loading.

9.1.1 Analytical model for the thin steel sheet catcher system

There are five assumptions in the analytical model of the thin steel sheet catcher system presented by Crawford et al. (2009):

- (a) The stress-strain relationship of steel is simplified into a bilinear relationship. Initial stress-strain relationship of the steel is defined by Young's modulus. After yielding, a plastic modulus is defined until the steel reached the fracture strain as shown in Figure 9.2;

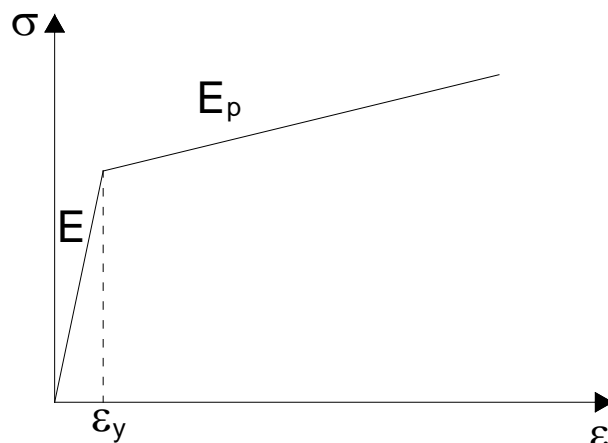


Figure 9.2: Assumed bilinear stress-strain curve for the steel used in the thin sheet catcher system.

- (b) The deformed shape of the thin steel sheet is simplified into a triangular shape with the maximum displacement at mid-span;
- (c) The velocity of the concrete masonry wall is determined based on rigid body mechanics,

$$v_{core} = \frac{I}{m_{core}} = \frac{I}{\rho_c t_c} \quad (9.1)$$

where I is the reflected blast impulse, m_{core} is the mass per unit area of the concrete masonry wall, ρ_c is the density of concrete masonry wall and t_c is the thickness of the concrete masonry wall;

- (d) The strain energy absorption capacity of the concrete masonry wall is ignored, and all the kinetic energy of the concrete masonry wall is dissipated by the thin steel sheet;
- (e) The strain in the thin steel sheet (rear faceplate) is uniformly distributed over its area and thickness at the maximum displacement.

For the thin steel sheet catcher system, the maximum displacement of the steel sheet can be determined by equating the kinetic energy of the concrete masonry wall to the strain energy of the steel sheet. The kinetic energy of the concrete masonry wall is given by,

$$K.E._{core} = \frac{1}{2} M_{core} v_{core}^2 \quad (9.2)$$

where M_{core} is the total mass of the concrete masonry wall and v_{core} is the velocity of the concrete masonry wall.

The strain energy per unit volume of the thin steel sheet is,

$$\eta = \int \sigma d\varepsilon = \frac{1}{2} [E_p \varepsilon^2 + 2(E - E_p) \varepsilon_y \varepsilon - (E - E_p) \varepsilon_y^2] \quad (9.3)$$

where σ is the stress, E is the Young's modulus of steel, E_p is the plastic modulus of steel, ε_y is the yield strain of steel. The strain energy of the thin steel sheet at the maximum displacement is given by,

$$\begin{aligned} I.E._{sheet} &= \int \eta dV = \frac{1}{2} B H_p L [E_p \varepsilon_{max}^2 + 2(E - E_p) \varepsilon_y \varepsilon_{max} - (E - E_p) \varepsilon_y^2] \\ &= \frac{1}{2} V_{sheet} [E_p \varepsilon_{max}^2 + 2(E - E_p) \varepsilon_y \varepsilon_{max} - (E - E_p) \varepsilon_y^2] \end{aligned} \quad (9.4)$$

where B and L is the height and the length of the steel sheet, respectively. H_p is the thickness of the steel sheet and V_{sheet} is the volume of the steel sheet.

Using energy equilibrium equation, the maximum strain of the steel sheet can be determined from the kinetic energy of the concrete masonry wall as,

$$\frac{1}{2}V_{sheet} \left[E_p \varepsilon_{max}^2 + 2(E - E_p) \varepsilon_y \varepsilon_{max} - (E - E_p) \varepsilon_y^2 \right] = \frac{1}{2} M_{core} v_{core}^2 \quad (9.5)$$

$$E_p \varepsilon_{max}^2 + 2(E - E_p) \varepsilon_{max} \varepsilon_y - \left[(E - E_p) \varepsilon_y^2 + \frac{M_{core} v_{core}^2}{V_{sheet}} \right] = 0$$

The maximum strain of the steel sheet can be determined by solving the quadratic equation (Eq. 9.5) as,

$$\varepsilon_{max} = \left[1 - \frac{E}{E_p} \right] \varepsilon_y + \sqrt{\left(\frac{E}{E_p} - 1 \right) \frac{E}{E_p} \varepsilon_y^2 + \frac{(\rho_c H_c) v_{core}^2}{E_p H_p}} \quad (9.6)$$

Assuming the triangular deformed shape of the steel sheet shown in Figure 9.3, the elongated length of the steel sheet is given as,

$$\frac{L_{new}}{2} = \sqrt{\left(\frac{L}{2} \right)^2 + \delta_{max}^2} \quad (9.7)$$

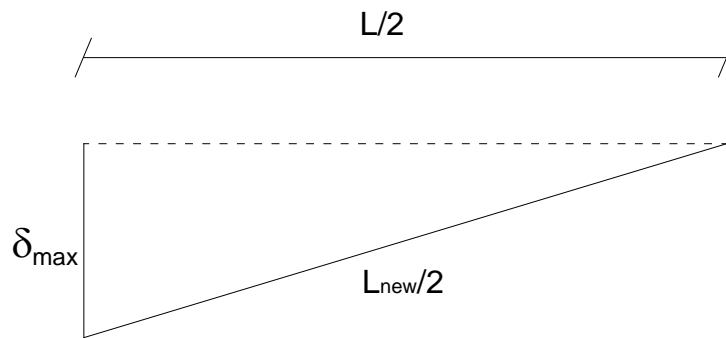


Figure 9.3: Triangular deformed shape of the steel sheet.

The strain of the steel sheet is given as,

$$\varepsilon_{max} = \frac{L_{new}/2 - L/2}{L/2} \quad (9.8)$$

By substituting Eq. 9.7 into Eq. 9.8, the maximum strain is related to the maximum displacement of the steel sheet by,

$$\varepsilon_{\max} = \sqrt{1 + \left(\frac{2\delta_{\max}}{L}\right)^2} - 1 \quad (9.9)$$

The maximum displacement of the steel sheet is given by,

$$\delta_{\max} = \frac{L}{2} \sqrt{(\varepsilon_{\max} + 1)^2 - 1} \quad (9.10)$$

9.1.2 Improved analytical model for non-composite SCS panels

For the simplified analytical model of the thin steel sheet catcher system (Crawford et al., 2009), the mass of the thin steel sheet is insignificant compared to the mass of the concrete masonry wall and thus it is ignored in the analysis. In non-composite SCS panels, the thickness of the rear faceplate was normally more than 10 mm, where the mass of the rear faceplate could have significant effects in the theoretical analysis. Therefore, in this study, the analytical model of the thin steel sheet catcher system was modified to include the mass of the rear faceplate in the analysis. The five assumptions used for the thin steel sheet catcher system were applied to the improved analytical model for non-composite SCS panels. The contribution of the front steel faceplate to the energy absorption mechanism was ignored to simplify the analysis.

The velocity of the concrete core is determined based on the rigid body mechanics,

$$v_{core} = \frac{I}{m_{core}} = \frac{I}{\rho_c t_c} \quad (9.11)$$

where I is the reflected blast impulse, m_{core} is the mass per unit area of the concrete core, ρ_c is the density of concrete core and t_c is the thickness of the concrete core.

The concrete core receives the momentum from the impulse loading and then strikes the rear faceplate. Both of them then move together at a new velocity,

$$v = \frac{m_{core} v_{core}}{m_{core} + m_{plate}} \quad (9.12)$$

where m_p is the mass per unit area of the rear faceplate. The total kinetic energy in the concrete core and the rear faceplate is,

$$K.E_{core+plate} = \frac{1}{2}(M_{core} + M_{plate})v^2 \quad (9.13)$$

where M_{plate} is the total mass of the rear faceplate. The strain energy of the rear faceplate can be determined based on Eq. 9.4. From the equilibrium of energy, the maximum strain of the rear faceplate can be determined as,

$$\varepsilon_{max} = \left[1 - \frac{E}{E_p}\right] \varepsilon_y + \sqrt{\left(\frac{E}{E_p} - 1\right) \frac{E}{E_p} \varepsilon_y^2 + \frac{(\rho_c H_c + \rho_t H_p) v^2}{E_p H_p}} \quad (9.14)$$

Based on the maximum strain of the rear faceplate, the maximum displacement of the rear faceplate can be determined using Eq.9.10.

9.2 Response of fully fixed non-composite SCS panels subjected to uniform blast impulse

In this section, the response of fully fixed non-composite SCS panels was investigated using the non-linear transient dynamic finite element software LS-DYNA. The simulation results were compared to the theoretical results of the improved analytical model for the non-composite SCS panel. The dimension of the full scale SCS panel is illustrated in Figure 9.4. The overall thickness of the SCS panel was 200 mm. The thickness of the concrete core and the steel faceplate was 180 mm and 10 mm, respectively. The length of the SCS panel between the flared ends was 3500 mm, and the height of the panel was 3500 mm. The angle of the flared ends was 30° and the length of the flared ends was 172 mm.

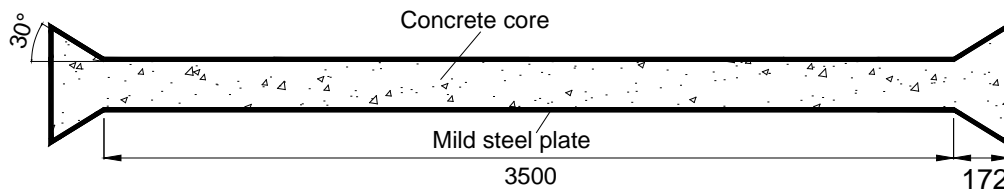


Figure 9.4: Geometry and dimension (in mm) of a full scale non-composite SCS panel.

The concrete core was modelled using constant stress solid elements, while the steel faceplates were modelled using Belytschko-Tsay shell elements. The mesh size for the concrete core and the steel faceplates was 20 mm and 40 mm, respectively. The Automatic-Surface-to-Surface contact algorithm was used to model the interaction between the steel faceplate and the concrete core. The dynamic coefficient of friction of 0.2 was defined for this contact interface.

The mild steel faceplates were assigned with a bilinear elasto-plastic stress-strain relationship using the Plastic Kinematic material model. Based on the tensile coupon test results in Chapter 5, the yield stress for the mild steel was 271 MPa. The plastic modulus of 230 MPa and the fracture strain of 0.25 were defined. The concrete core was modelled using the concrete material model Damage Release III (Mat. 72 R3) with a concrete compressive strength of 40 MPa. The hourglass control algorithm, Flanagan-Belytschko stiffness form with exact volume integration for solid elements (HG type 5), was used to control the hourglass energy in the concrete core. In the FE model, the strain rate effects of steel and concrete were ignored. The strain rate effects of steel were ignored so that the same stress-strain curve used in the FE model could be used in the theoretical analyses, therefore the validity of the analytical models could be evaluated. The solids elements and the shell elements at the flared ends were restrained against translational movement in the x, y and z directions to simulate a fully fixed support condition.

In the FE model, the blast loading was modelled by applying the reflected pressure time history uniformly over the front faceplate. The reflected pressure, time of arrival, positive phase duration and reflected impulse for various detonation scenarios obtained from the software ATBLAST are presented in Table 9.1. The reflected pressure time history was simplified into a triangular shape with a linear decay of reflected pressure in the FE model.

Table 9.1: Blast loading for various detonation scenarios obtained from ATBLAST.

Scenario	Arrival time (msec)	Peak reflected pressure (kPa)	Peak reflected impulse (kPa.msec)	Positive phase duration (msec)
100kg TNT@5m	2.48	6645	3717	1.12
250kg TNT@5m	1.95	14698	7650	1.04
400kg TNT@5m	1.74	21115	11164	1.06
500kg TNT@5m	1.66	24818	13384	1.08

Three categories of FE simulation were carried out to investigate the effects of different parameters on the response of non-composite SCS panels. The first parameter investigated was the effects of the increased blast loading on the response of SCS panels. The blast loading was increased from 100 kg TNT to 500 kg TNT at a standoff distance of 5 m as shown in Table 9.1. The geometry and the dimension of the SCS panels are illustrated in Figure 9.4.

Then, the effect of the rear faceplate thickness was evaluated by increasing the thickness of the rear faceplate from 10 mm to 16 mm and to 20 mm. The blast loading used was 250 kg TNT at a standoff distance of 5 m in these FE models. The thickness of the concrete core and the front faceplate remained at 180 mm and 10 mm, respectively. The last parameter studied was the effects of the thickness of the concrete core. The thickness of the concrete core considered in this study was 180 mm, 280 mm and 380 mm. The blast loading due to detonation of 250 kg TNT at a 5 m standoff distance was applied in these FE models and the thickness of the steel faceplates was 10 mm. The simulation results were compared to the results from the analytical model of the thin sheet catcher system and the improved analytical model of the non-composite SCS panels.

9.2.1 Parametric study 1: Effects of increased blast loading on the response of non-composite SCS panels

The responses of non-composite SCS panels under increased blast loading were found to be similar to each other. The panels deformation profile is exemplified by the SCS panel subjected to the blast loading of 250 kg TNT at a standoff distance of

5 m in Figure 9.5. The front faceplate moved together with the concrete core during the initial stage. The non-reinforced concrete core was severely damaged in the area adjacent to the flared ends, which implied possible shear failure of the concrete core at this zone. At about 0.01 s, the concrete core continued to move due to the acquired momentum, but the front faceplate had stopped moving. This caused the front faceplate to separate from the concrete core. The rear faceplate was pushed in the direction of blast load by the concrete core. The rear faceplate yielded at the mid-span and near the flared ends. At the maximum displacement, the concrete core along the span was severely damaged (with the maximum damage scalar parameter of 2 for the material model Damage Release III). The front faceplate had rebounded and moved in the opposite direction to the blast loading. From the simulation results, it was found that the maximum displacement of the rear faceplate increased as the blast loading increased, as shown in Table 9.2. It was also found that the ratio of the hourglass energy to the internal energy of the concrete core increased as the displacement increased.

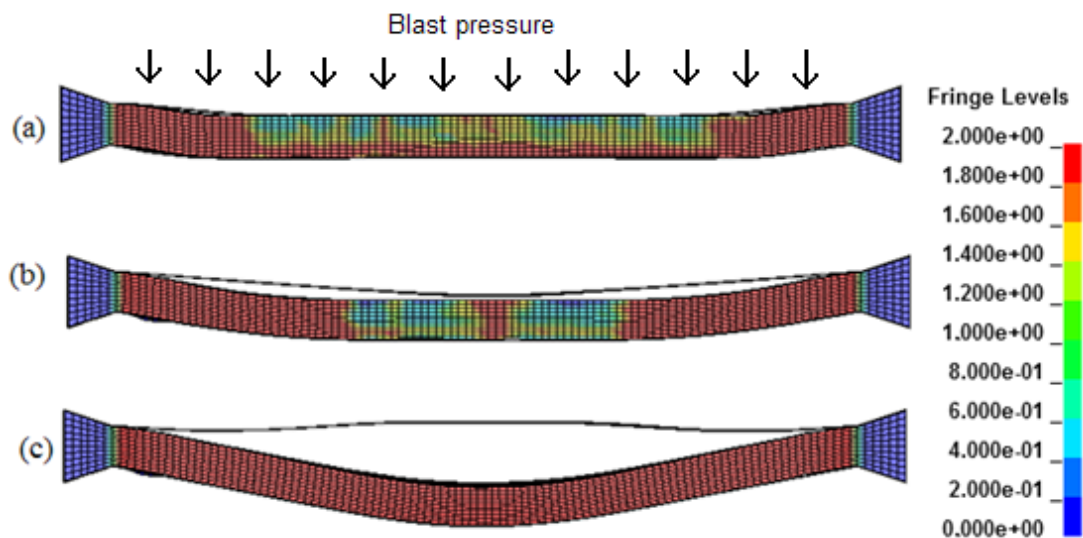


Figure 9.5: Deformation profile of a non-composite SCS panel subjected to blast loading of 250 kg TNT at a 5 m standoff distance: (a) at 0.005 s, (b) at 0.01 s and (c) at the maximum displacement.

Table 9.2: Maximum displacement of the rear faceplate and the hourglass energy ratio of the concrete core under various blast loading conditions.

Blast threat Scenario	Peak reflected impulse (kPa.msec)	Maximum displacement (mm)	Support rotation (°)	Hourglass energy ratio (%)
100kg TNT@5m	3717	134	4.4	9
250kg TNT@5m	7650	283	9.2	11
400kg TNT@5m	11164	432	13.9	17
500kg TNT@5m	13384	522	16.6	21

The strain energy partition in the non-composite SCS panel under various blast loading conditions is summarized in Table 9.3. The membrane stretching of the rear faceplate was the main energy dissipation mechanism, where at least 75% of the total energy was dissipated by the rear faceplate. It was found that a maximum of 25% of the total energy was dissipated by the concrete core and front faceplate. Generally, the percentage of the strain energy of the concrete core reduced as the blast loading increased. The strain energy of the concrete core was attributed to the energy dissipated when the concrete fractured. When the blast impulse was increased from 3717 kPa.msec to 7650 kPa.msec, the front faceplate showed plastic deformation and developed tensile membrane resistance. Therefore, the percentage of energy dissipated by the front faceplate increased from 2% to 10%. However, when the blast loading was further increased, the energy dissipated by the front faceplate remained at less than 10%.

Table 9.3: Strain energy partition in the non-composite SCS panel under increased blast loading condition.

Component	Partition of strain energy in the panel (%)			
	Impulse 3717 kPa.msec	Impulse 7650 kPa.msec	Impulse 11164 kPa.msec	Impulse 13384 kPa.msec
Rear plate	75	83	82	82
Concrete core	23	7	10	8
Front plate	2	10	8	10

The maximum displacements of the rear faceplate from numerical simulations were compared to the prediction of the analytical models for the thin sheet catcher system and the improved analytical model in Table 9.4. Both theoretical models overestimated the maximum displacement of the rear faceplate compared to the simulation results. The overestimation of the analytical models could be attributed to the assumption that all the kinetic energy was dissipated by the rear faceplate. The simulation results showed that about 20% of the kinetic energy was dissipated by the front faceplate and the concrete core (Table 9.3). When the blast loading increased, the percentage of difference between the simulation results and the theoretical predictions reduced.

The prediction of the improved analytical model corresponded better with the simulation results. Difference between the improved analytical model prediction and the FE simulation results was between 11% and 23%. As for the thin sheet catcher system analytical model, the difference was between 17% to 28%. Both simulation and analytical results showed that the maximum displacement of the rear faceplate increased linearly with the peak reflected impulse acting on the panel, as shown in Figure 9.6. Comparison between the simulation results and the theoretical predictions showed that the use of the improved analytical model was appropriate as it provided an improved but still conservative prediction of the maximum displacement of the rear faceplate under various blast loading conditions.

Table 9.4: A comparison between the maximum displacement of the rear faceplate predicted by the FE models and the results of analytical models under increased blast loading conditions.

Peak reflected impulse (kPa.msec)	Maximum FE displacement (mm)	Thin sheet catcher analytical model		Improved analytical model	
		Max displacement (mm)	% difference	Max displacement (mm)	% difference
3717	134	186	28	175	23
7650	283	365	22	341	17
11164	432	528	18	493	12
13384	522	632	17	590	11

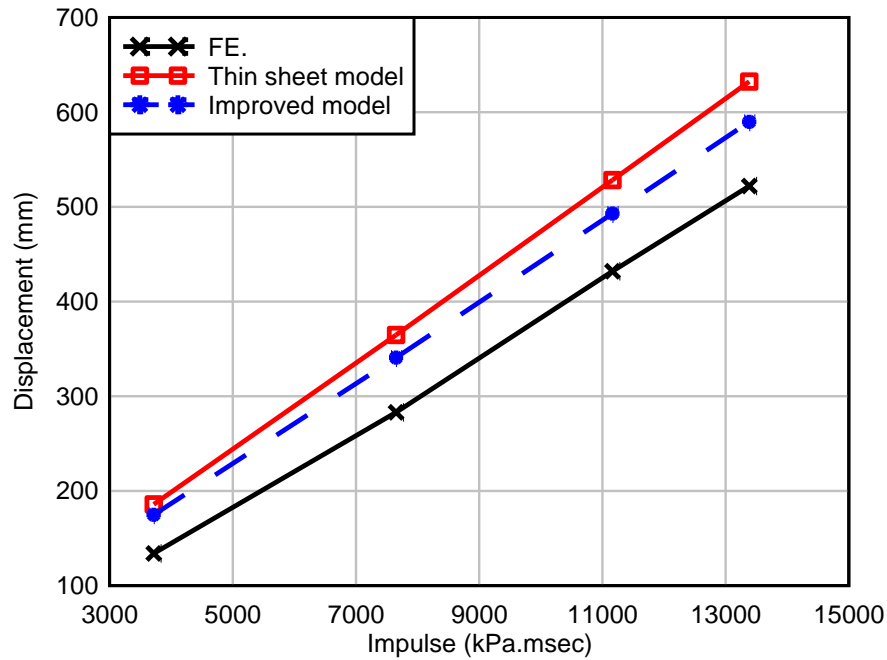


Figure 9.6: A comparison between the maximum displacement of the rear faceplate predicted by the FE models and the analytical models under increased blast loading conditions.

9.2.2 Parametric study 2: Effects of the rear faceplate thickness on the response of non-composite SCS panels

In this section, rear faceplates with varying thickness (10 mm, 16 mm and 20 mm) were studied. The thickness of the front faceplate and the concrete core were fixed at 10 mm and 180 mm, respectively. The reflected pressure time history due to detonation of 250 kg TNT at a 5 m standoff distance was applied uniformly onto the front faceplate in the FE models. The non-composite SCS panels with increased rear faceplate thickness appeared to respond in a similar fashion with the panel illustrated in Figure 9.5. The front faceplate was separated from the concrete core, the concrete core was severely damaged along the span and the rear faceplate yielded at the mid-span and near the flared ends.

The simulation results showed that the maximum displacement of the rear faceplate decreased as the thickness of the rear faceplate increased. When the thickness of the rear faceplate increased from 10 mm to 20 mm, the maximum displacement of the rear faceplate reduced by 32%, as shown in Table 9.5. The hourglass energy in the concrete core was less than 16% for all the rear faceplate thickness considered. The

kinetic energy in the SCS panels reduced proportionally to the additional mass when the thickness of the rear faceplate was increased.

Table 9.5: FE results for non-composite SCS panels with increased thickness of the rear faceplate.

Rear faceplate thickness (mm)	Maximum FE. displacement (mm)	Support rotation (°)	% reduction of maximum displacement	% of additional mass	% reduction of kinetic energy
10	283	9.2	-	-	-
16	223	7.3	21	7.5	7.4
20	192	6.3	32	12.4	12.7

Table 9.6 shows that the thickness of the rear faceplate had little effect on the strain energy partition in the non-composite SCS panels. The membrane stretching of the rear faceplate was the main energy dissipation mechanism, contributing a minimum of 80% of the total strain energy. According to Eq. 9.4, the strain energy in the rear faceplate is proportional to its thickness. When the blast loading remained constant, the maximum strain of the rear faceplate reduced as the thickness of the rear faceplate increased. This caused the reduction in the maximum displacement of the rear faceplate as the displacement was proportional to the maximum strain of the rear faceplate. In other words, the energy absorption capacity of the rear faceplate increased as its thickness increased. Therefore, the additional mass and the higher energy absorption capacity of the thicker rear faceplate caused a reduction of the maximum displacement of the rear faceplate under this blast loading condition.

Table 9.6: Strain energy partition in non-composite SCS panels with increased thickness of the rear faceplate.

Component	Partition of strain energy in the panel (%)		
	10 mm rear plate	16 mm rear plate	20 mm rear plate
Rear plate	83	85	81
Concrete core	10	10	15
Front plate	7	5	4

Figure 9.7 shows that both analytical models predicted higher maximum displacement of the rear faceplate compared to the simulation results. Table 9.7 shows that the percentage of difference between the simulation results and the thin sheet catcher system analysis results increased as the thickness of the rear faceplate increased. This was due to the mass of the rear faceplate was ignored in the analytical model of the thin sheet catcher system. In the improved analytical model, the additional mass of the rear faceplate was taken into consideration. Therefore, the percentage of difference was consistent at about 17%. This showed that the improved analytical model could provide reasonable prediction of the maximum displacement for the non-composite SCS panels with different rear faceplate thicknesses.

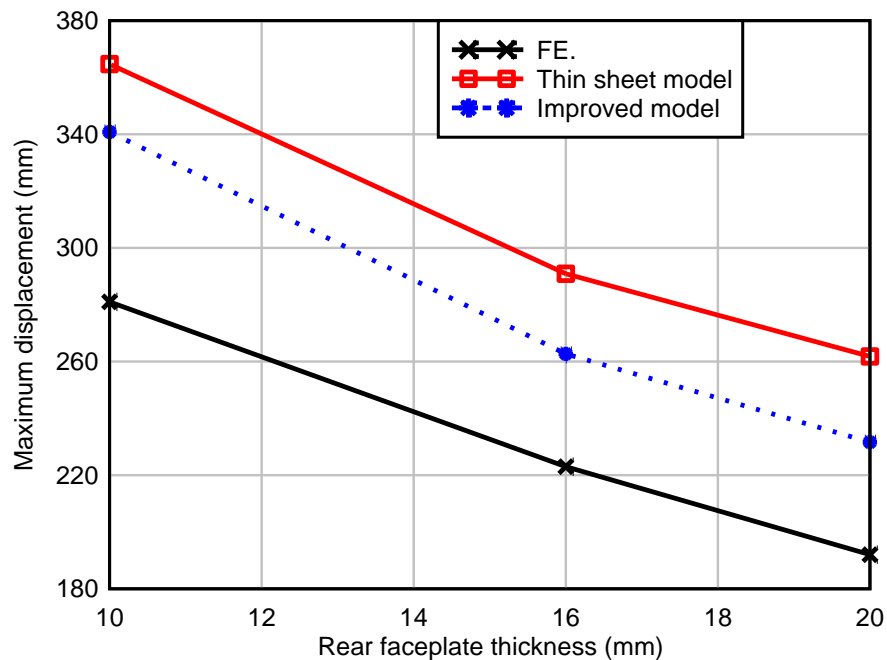


Figure 9.7: A comparison between the maximum displacement of the rear faceplate predicted by the FE models and the analytical models for the SCS panels with increased rear faceplate thickness.

Table 9.7: A comparison between the maximum displacement of the rear faceplate from the simulation results and the theoretical predictions for the SCS panels with increased rear faceplate thickness.

Rear faceplate thickness (mm)	Maximum FE displacement (mm)	Thin sheet catcher analytical model		Improved analytical model	
		Max displacement (mm)	% difference	Max displacement (mm)	% difference
10	283	365	22	341	17
16	223	291	23	263	15
20	192	262	27	232	17

9.2.3 Parametric study 3: Effects of the concrete core thickness on the response of non-composite SCS panels

In this study, the concrete core thickness was varied. The concrete core thicknesses of 180 mm, 280 mm and 380 mm were investigated. The thickness of the steel faceplate was 10 mm and the reflected pressure time history due to detonation of 250 kg TNT at a 5 m standoff distance was applied uniformly on the front faceplate. The response of non-composite SCS panels with increased concrete core thickness appeared to be similar to the response of panel illustrated in Figure 9.5. The front faceplate was separated from the concrete core and the rear faceplate yielded at mid-span and near the flared ends. However, damage on the concrete core was reduced as the thickness of the concrete core increased to 380 mm.

The maximum displacement of the rear faceplate decreased as the thickness of the concrete core increased. The maximum displacement of the rear faceplate was found to be reduced by 34% when the thickness of the concrete core increased by 200 mm, as shown in Table 9.8 . The hourglass energy in the concrete core was about 10% for the concrete core thicknesses considered in this study. Table 9.8 shows that the kinetic energy in the panel was reduced by almost 50% when the mass of the concrete core increased by almost two fold.

Table 9.8: FE results for non-composite SCS panels with increased concrete core thickness.

Concrete core thickness (mm)	Maximum FE. displacement (mm)	Support rotation (°)	% reduction of maximum displacement	% of additional mass	% reduction of kinetic energy
180	283	9.2	-	-	-
280	212	6.9	25	56	35
380	186	6.1	34	111	52

Table 9.9 summarizes the strain energy partition in the non-composite SCS panels when the concrete core thickness was increased. The membrane stretching of the rear faceplate was still the main energy dissipation mechanism. However, the percentage of strain energy in the concrete core increased significantly as the thickness of the concrete core increased. The energy dissipated by the concrete core increased from 10% to 36% when the thickness of the concrete core was increased from 180 mm to 380 mm. The energy dissipated by the front faceplate was insignificant (less than 7 %) and reduced as the thickness of the concrete core increased. The reduction in maximum displacement of the rear faceplate could be attributed to the additional mass and increased strain energy in the thicker concrete core.

Table 9.9: Strain energy partition in the non-composite SCS panel with increased concrete core thickness.

Component	Partition of strain energy in the panel (%)		
	180 mm concrete core	280 mm concrete core	380 mm concrete core
Rear plate	83	75	63
Concrete core	10	23	36
Front plate	7	2	1

Figure 9.8 shows that both analytical models predicted higher maximum displacement of the rear faceplate compared to the simulation results. Table 9.10 shows that the percentage of difference between the simulation results and the prediction of the analytical models increased as the thickness of the concrete core increased. This could be attributed to the increased energy dissipation by the concrete

core as the thickness of the concrete core increased in the numerical simulations. In the analytical models, the strain energy of the concrete core was ignored and it was assumed that all the energy was dissipated by the rear faceplate. Both analytical models predicted similar maximum displacement when the thickness of the concrete core increased to 380 mm. This implied that when the ratio of the mass of the concrete core over the mass of the rear faceplate exceeded 12, the mass of the rear faceplate could be ignored in the analysis. Comparison of the simulation results and the theoretical analysis showed that both analytical models' prediction were very conservative for the non-composite SCS panel with thick concrete core.

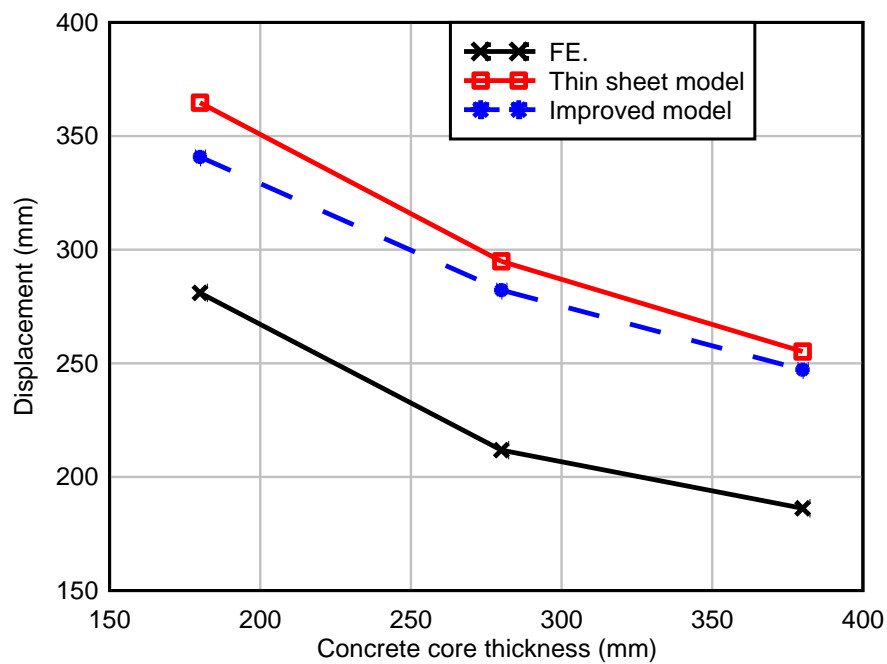


Figure 9.8: A comparison between the maximum displacement of the rear faceplate predicted by the FE models and analytical models for the SCS panels with increased concrete core thickness.

Table 9.10: A comparison between the maximum displacement of the rear faceplate from the simulation results and the theoretical predictions for the SCS panels with increased concrete core thickness.

Concrete core thickness (mm)	Maximum FE displacement (mm)	Thin sheet catcher analytical model		Improved analytical model	
		Max displacement (mm)	% difference	Max displacement (mm)	% difference
180	283	365	22	341	17
280	212	295	28	282	25
380	186	255	27	247	25

9.2.4 Summary for the response of non-composite SCS panels under fixed support condition

The response of fixed supported non-composite SCS panels under various blast loading conditions, rear faceplate and concrete core thicknesses had been investigated. It was found that the response of non-composite SCS panels under blast loading was similar to the catcher system. The membrane stretching of the rear faceplate was the main energy dissipation mechanism. For SCS panels with concrete core thickness less than 200 mm, simulation results showed that the rear faceplate dissipated about 80% of the total energy. When the thickness of the concrete core exceeded 200 mm, the concrete core contributed significantly to the energy absorption where it dissipated about 30% of the total energy.

The simulation results showed that the maximum displacement of the rear faceplate could be reduced by increasing the thickness of the rear faceplate and concrete core. Table 9.5 and Table 9.8 show that the FE model with 20 mm thick rear faceplate and 180 mm thick concrete core predicted similar maximum displacement with the FE model using 10 mm thick rear faceplate and 380 mm thick concrete core. This showed that increasing the thickness of the rear faceplate was more effective to control the maximum displacement of the rear faceplate compared to increasing the concrete core thickness.

Comparison of the simulation results and the results of the theoretical models showed that the improved analytical model could predict the maximum displacement of the non-composite SCS panels with reasonable accuracy when the thickness of concrete core was less than 200 mm. When the thickness of the concrete core exceeded 200 mm, the results of the improved analytical model were found to be very conservative.

9.3 Response of full scale protective barrier under non-uniform blast pressure

9.3.1 Design of the post

In the prototype barrier, the non-composite SCS panels were connected to the steel posts, which were penetrated into the ground at one end. The design of the penetration depth and the soil-post interaction were ignored in this study and it was assumed that the posts acted as cantilever beams. The post was composed of an I-beam with keyed connections, and bracings between the flanges and the web of the I-beam, as shown in Figure 9.9. The bracings were used to limit the local bending deformation of the rear flange due to the reaction force from the SCS panels. This local bending deformation would cause pull-out of the SCS panel from the keyed connection.

The depth of the post was determined based on the angle of inclination of the bracing and the keyed connections. To effectively restrain the in-plane movement of the SCS panel at the keyed connections and to prevent excessive local bending deformation of the rear flange, a 30° angle of inclination was chosen. Based on this angle of inclination, the required depth between the flanges was determined to be 600 mm for the SCS panel with 200 mm thickness. The thickness of the flanges was 25 mm, the thickness of the web was 16 mm, and the thickness of the plate used to form the keyed connections and bracings was 10 mm. The dimension of the post is illustrated in Figure 9.9 (b). The height of the post was 3500 mm and the void in the keyed connections was filled with 40 MPa concrete.

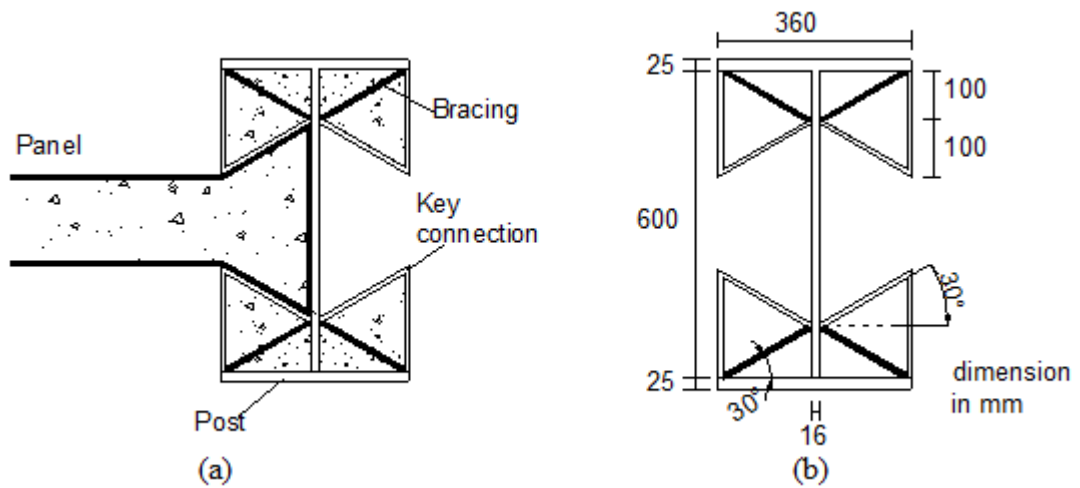


Figure 9.9: (a) Connection details between the non-composite SCS panel and the post, (b) geometry and dimension of the post.

Two types of steel post investigated in this study were: 1) steel posts constructed from mild steel plates (mild steel posts), and 2) steel posts utilizing high strength steel plates (high strength steel posts). The static yield stress of the mild steel was 271 MPa, obtained from the tensile coupon tests in Chapter 5. The plastic modulus of mild steel after yielding was 230 MPa. The static yield stress of high strength steel (Bisplate 80) was 690 MPa, obtained from Bisalloy Steels (2006) and the hardening effect after yielding was ignored. The fracture strain for the mild steel was 0.25 while the fracture strain for the high strength steel was assumed as 0.18. In this section, the strain rate effect of steel was considered based on Cormie et al. (2009), where the dynamic yield stress was 1.2 times of the static yield stress. Therefore, dynamic yield stress for mild steel and high strength steel was 325 MPa and 826 MPa, respectively.

9.3.2 FE modelling

Figure 9.10 shows the FE model of the protective barrier supported by steel posts. Three non-composite SCS panels were modelled. The middle panel was modelled using a finer mesh size of 25 mm. The two side panels were modelled using a mesh size of 50 mm. The posts were modelled in detail. The steel plates in the post were modelled using Belytschko-Tsay shell elements, while the concrete infill was modelled using constant stress solid elements.

The Automatic-Surface-to-Surface contact algorithm was used to define the interaction between the SCS panels and the keyed connections with a dynamic coefficient of friction of 0.2. The mild steel was modelled using the Plastic Kinematic material model with a dynamic yield stress of 325 MPa and a plastic modulus of 230 MPa. For the high strength steel, a dynamic yield stress of 828 MPa was defined in the Plastic Kinematic material model. The fracture strain of mild steel and high strength steel plates was 0.25 and 0.18, respectively. The concrete core along the span of SCS panels was modelled using the concrete material model Damage Release III (Mat. 72 R3). Concrete infill in the posts and at the flared ends of the SCS panels was modelled using the material model CSCM. Concrete compressive strength was 40 MPa and the strain rate effects of concrete were ignored. The Flanagan-Belytschko stiffness form with exact volume integration for solid elements (HG type 5) was used to control the hourglass energy in the concrete core.

The loading of various blast scenarios was generated by using the Load_Blast_Enhanced command. The inputs required in this loading command were the mass of the charge, height of burst, standoff distance between the charge and the target, type of blast source and the units used in the FE model. In this study, the charge was positioned on the ground surface, and the standoff distance was 5 m or 10 m from the mid-span of the middle panel. The type of blast source was hemispherical surface burst with the initial shock wave of the detonation was reflected and reinforced by the ground. Blast loading was applied to the front faceplates of the SCS panels and the front flange of the steel posts using the Blast_Segment_Set algorithm. The nodes at the bottom of the posts were restrained against translational and rotational degrees of freedom in x, y and z directions. Two posts at the far corner were restrained to move in the y direction (in-plane direction), to account for the continuity of the barrier structure beyond the three panels modelled in this study.

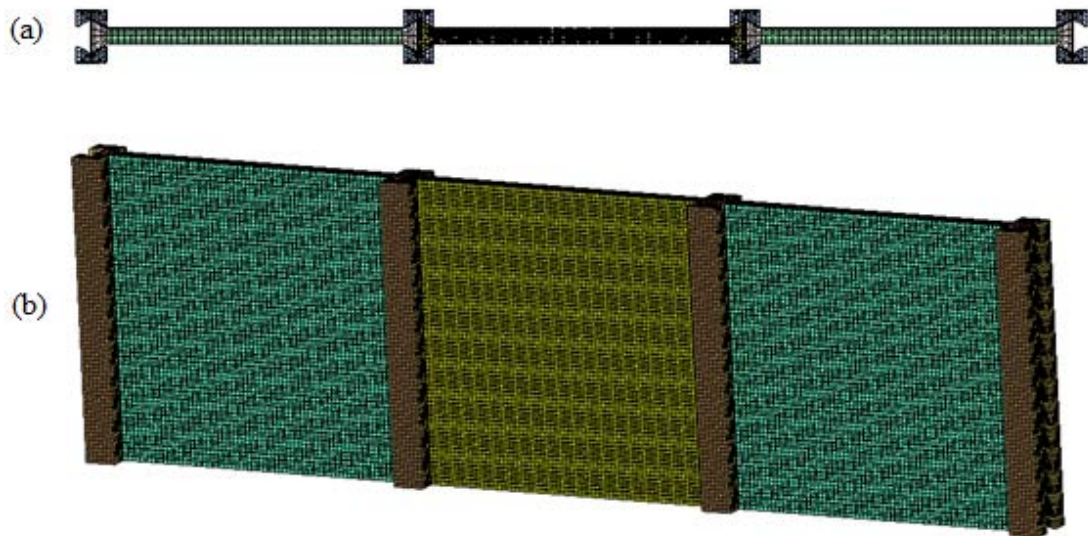


Figure 9.10: FE model of the barrier consists of non-composite SCS panels and posts
(a) top view, (b) isometric view.

9.3.3 FE results for the barrier with 200 mm thick non-composite SCS panels supported by posts

For the barrier supported by the mild steel posts, four blast loading scenarios considered were (1) 500 kg TNT at 10 m standoff distance, (2) 250 kg TNT at 5 m standoff distance, (3) 500 kg TNT at 5 m standoff distance and (4) 750 kg TNT at 5 m standoff distance. The corresponding scaled distances (Z) for these blast loading conditions were (1) $1.26 \text{ m/kg}^{1/3}$, (2) $0.79 \text{ m/kg}^{1/3}$, (3) $0.63 \text{ m/kg}^{1/3}$ and (4) $0.55 \text{ m/kg}^{1/3}$. When the scaled distance decreased, the reflected pressure on the barrier increased. The reflected pressure became highly non-uniform when the scaled distance was less than $0.8 \text{ m/kg}^{1/3}$ and the peak reflected pressure on the barrier was recorded near the bottom of the middle panel at the mid-span. This could be attributed to the position of the charge on the ground. The reflected pressures on the side panels were significantly lower than the middle panel.

The response of the barrier supported by the mild steel posts was similar when it was subjected to increased blast loading conditions. The response of the barrier was exemplified by the response of the middle panel and the mild steel posts shown in Figure 9.11. The barrier was subjected to the blast loading of 500 kg TNT at a 5 m

standoff distance. The middle panel and the mild steel posts connected to the middle panel showed the most severe deformation because the charge was positioned at 5 m or 10 m from the centre of the middle panel.

When subjected to blast loadings, the panels and the mild steel posts started to deform simultaneously. At the early stage, the extensive damage of the concrete core near the posts (Figure 9.11) could be attributed to the shear failure of the non-reinforced concrete core. Moderate damage was observed for the concrete infill in the posts and at the flared ends of the panels. As the displacement increased, the concrete core along the span of the middle panel was severely damaged and the front faceplate was separated from the concrete core. The rear faceplate was pushed in the direction of the blast loading by the concrete core and it started to yield at the flared ends and mid-span. At the maximum displacement, it was observed that no significant local bending deformation occurred at the rear flanges of the mild steel posts and the keyed connection was effective in restraining the in-plane displacement of the SCS panel. The in-plane displacement of the mild steel posts was less than 10 mm.

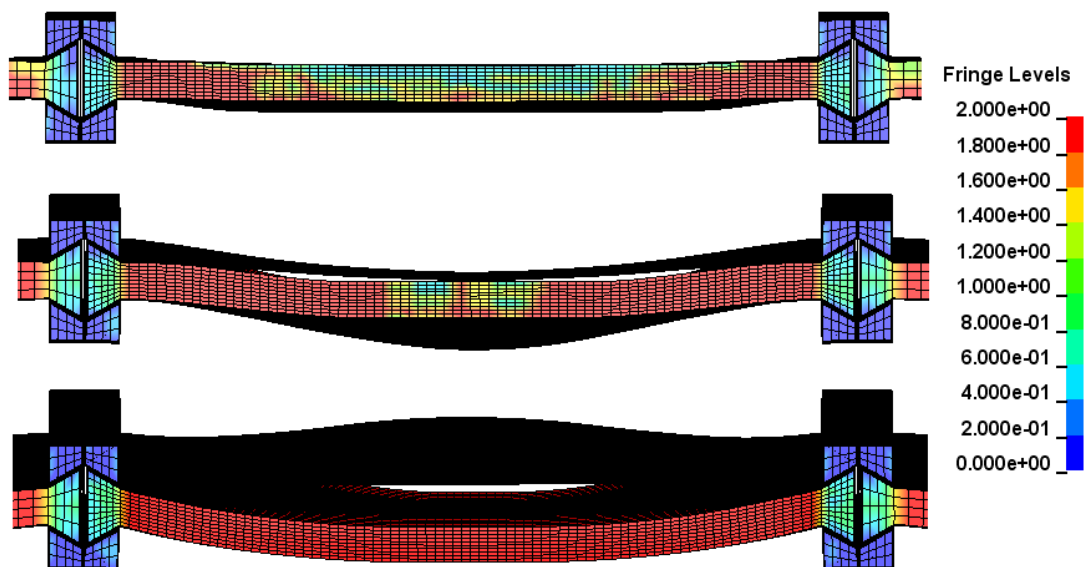


Figure 9.11: The response of a protective barrier with 200 mm thick non-composite SCS panels supported by mild steel posts under the blast loading of 500 kg TNT at a 5 m standoff distance.

Table 9.11 summarizes the peak displacement of the middle panel at mid-span and the maximum displacement of the mild steel post and the keyed connection. The peak displacement of the middle panel at mid-span was non-uniform, with the mid-height displacement showing lowest peak displacement. The peak displacement at the bottom of the middle panel was larger than the mid-height displacement due to the charge being positioned on the ground surface, and therefore generating higher blast pressure at the lower part of the panel. The middle panel showed highest peak displacement at the top (except for the barrier subjected to blast loading of 500 kg TNT at a 5 m standoff distance) due to the deflection of the mild steel posts. The rear faceplate yielded at the mid-span and the flared ends. When the blast loading increased, the plastic deformation of the rear faceplate was concentrated at the flared ends. The maximum support rotation of the middle panel was about 20° when the barrier was subjected to the blast loading of 750 kg TNT at a 5 m standoff distance.

For all the blast loading scenarios considered, the mild steel posts supporting the middle panel yielded at the base. When the barrier was subjected to the blast loading of 500 kg TNT at a 10 m standoff distance, the maximum support rotation of the mild steel post was 1.1° and the maximum strain of the shell elements adjacent to the base was about 0.06. The maximum support rotation of the mild steel post increased to 4.6° and the maximum strain approached to fracture strain of mild steel (0.25) when the blast loading was increased to 500 kg TNT at a 5 m standoff distance. As the blast loading was increased to 750 kg TNT at a 5 m standoff distance, the shell elements of the rear flange and the keyed connection near the base reached fracture strain and were eliminated from the simulation, as shown in Figure 9.12. The maximum support rotation of the keyed connection was 2.2° when the barrier was subjected to this blast loading condition. These results showed that the design of keyed connection was sufficient in providing axial restraint to the panels. The flexural failure of the posts was the critical design limit in the barrier supported by the posts.

Table 9.11: Deformation of the barrier with 200 mm thick SCS panels supported by mild steel posts under various blast loading conditions.

Blast threat Scenarios		Displacement of middle panel (mm)			Mild steel post		Keyed connection	
Standoff distance (m)	TNT mass (kg)	Bottom	Mid-height	Top	Displa. (mm)	Rotation (°)	Displa. (mm)	Rotation (°)
10	500	189	188	222	67	1.1	1.2	0.3
5	250	265	239	269	89	1.5	2.8	0.65
	500	465	415	449	284	4.6	5.3	1.2
	750	674	590	728	557	9.0	9.2	2.2

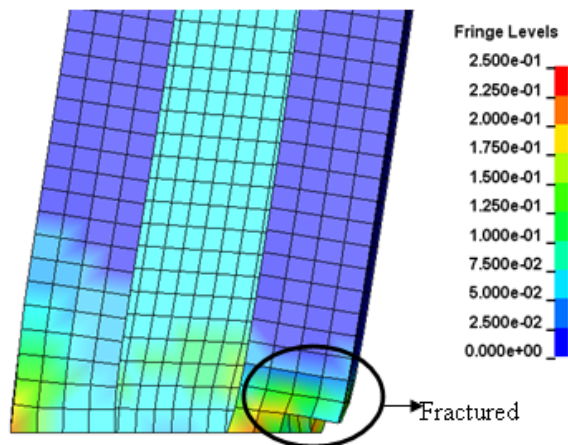


Figure 9.12: Fracture of the mild steel post at the base when the barrier was subjected to blast loading of 750 kg TNT at a standoff distance of 5 m.

Table 9.12 shows that a certain percentage of the kinetic energy of the panels being transferred to the posts for the barrier supported by the mild steel posts. The panels dissipated less than 50% of the kinetic energy in the panels for all the blast loading conditions considered. The balance of the kinetic energy of the panels was transferred and dissipated by the strain energy of the mild steel posts. These results showed that the post design had significant effects on the energy dissipation in the barrier. A large percentage of the kinetic energy of the panels (up to 70%) was transferred into the mild steel posts due to the panel-post interaction.

Table 9.12: Energy transferred from the SCS panels to the posts for 200 mm thick SCS panels supported by mild steel posts.

Blast threat Scenarios		Middle panel		Side panels	
Standoff distance (m)	TNT mass (kg)	Strain energy (%)	Energy transferred to the post (%)	Strain energy (%)	Energy transferred to the post (%)
10	500	39	61	43	57
5	250	46	54	41	59
	500	30	70	30	70
	750	33	67	33	67

There were five blast threat scenarios investigated for the barrier supported by the high strength steel posts. The first scenario was 500 kg TNT at a standoff distance of 10 m. The other four blast threat scenarios considered were 250 kg TNT, 500 kg TNT, 750 kg TNT and 1000 kg TNT at a 5 m standoff distance. The corresponding scaled distances (Z) for these blast loading conditions were (1) $1.26 \text{ m/kg}^{1/3}$, (2) $0.79 \text{ m/kg}^{1/3}$, (3) $0.63 \text{ m/kg}^{1/3}$, (4) $0.55 \text{ m/kg}^{1/3}$ and (5) $0.5 \text{ m/kg}^{1/3}$. The overall response of the barrier supported by the high strength steel posts under blast loading conditions was similar to the response of the barrier supported by the mild steel posts illustrated in Figure 9.11. The non-reinforced concrete core showed shear failure adjacent to the posts at the early stage, the front faceplate was separated from the concrete core and the rear faceplate yielded at the mid-span and the flared zone. As the blast loading increased, the plastic deformation on the rear faceplate concentrated at the flared zone. Table 9.13 summarizes the maximum displacement of the middle panel at mid-span and the maximum deformation of one of the posts connected to the middle panel.

The maximum displacement of the middle panel was recorded at the bottom of the panel at mid-span (except for the barrier under the blast scenario of 500 kg TNT at a 10 m standoff distance), followed by the top of the panel. This was different from the SCS panels supported by mild steel posts (Table 9.11), where the maximum displacement was recorded at the top of the panel. The deflection of the high strength steel post was lower than the mild steel post under the same blast loading condition,

causing a lower displacement at the top of the SCS panels. In addition, the maximum displacement of the panels supported by high strength steel posts was lower than the maximum displacement of the panel supported by mild steel posts.

Table 9.13: Deformation of the barrier with 200 mm thick SCS panels supported by high strength steel posts under various blast loading conditions.

Blast threat Scenarios		Displacement of middle panel (mm)			High strength steel post		Keyed connection	
Standoff distance (m)	TNT mass (kg)	Bottom	Mid-height	Top	Displa. (mm)	Rotation (°)	Displa. (mm)	Rotation (°)
10	500	174	174	214	36	0.6	1.1	0.3
5	250	254	228	251	36	0.6	1.3	0.3
	500	435	364	389	83	1.4	3.1	0.7
	750	610	495	530	179	2.9	5	1.2
	1000	794	641	751	430	7.0	7	1.6

Under the same displacement, the high strength steel posts have a higher energy dissipation capacity compared to the mild steel posts due to its higher flexural load capacity. Therefore, the maximum deformation of the high strength steel post was significantly lower than the mild steel post under the same blast loading condition. For instance, the mild steel post was fractured when the barrier was subjected to the blast loading of 750 kg TNT at a 5 m standoff distance, while the high strength steel post only showed support rotation of 2.8°. When the blast loading increased to 1000 kg TNT at a 5 m standoff distance, the high strength steel posts supporting the middle panel were fractured, similar to the fracture of mild steel post shown in Figure 9.12. The support rotation of the high strength steel post when it fractured was lower than the mild steel post due to a lower fracture strain of the high strength steel compared to the mild steel. Furthermore, the rear faceplate was fractured at the lower part of the flared ends when it reached support rotation of 24°, as shown in Figure 9.13.

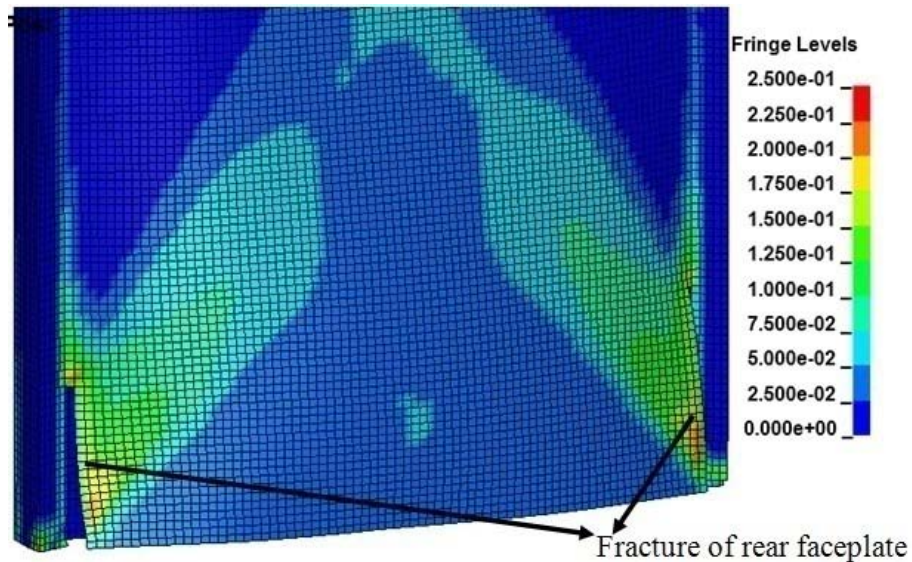


Figure 9.13: Fracture of the mild steel rear faceplate at the flared ends when the barrier supported by high strength steel posts was subjected to blast loading of 1000 kg TNT at a standoff distance of 5 m.

Table 9.14 shows a certain percentage of the kinetic energy of the panels being transferred to the posts for the barrier supported by the high strength steel posts. The middle panel dissipated about 70% of its kinetic energy, while the side panels dissipated about 55% of their kinetic energy through strain energy. The balance kinetic energy in the panels was transferred and dissipated by the strain energy of the posts. The percentage of the energy transferred from the panels to the posts was consistent for the blast loading in the range of 250 kg TNT to 1000 kg TNT at a 5 m standoff distance. These results showed that the non-composite SCS panels supported by the high strength steel posts were more effective in dissipating the kinetic energy of the panels compared to the panels supported by the mild steel posts (Table 9.12).

Table 9.14: Energy transferred from the SCS panels to the posts for 200 mm thick SCS panels supported by high strength steel posts.

Blast threat Scenarios		Middle panel		Side panels	
Standoff distance (m)	TNT mass (kg)	Strain energy (%)	Energy transferred to the post (%)	Strain energy (%)	Energy transferred to the post (%)
10	500	60	40	56	44
5	250	71	29	55	45
	500	78	22	57	43
	750	74	26	56	44
	1000	70	30	58	42

9.3.3.1 Effects of increased thickness of non-composite SCS panels on barrier performance

In this section, the effects of increased thickness of non-composite SCS panels on the performance of the barrier under various blast threat scenarios were investigated. The thickness of the panel was increased to 300 mm by increasing the thickness of the concrete core. The depth of the post was increased accordingly by increasing the depth of the web. The thickness of the steel plates in the post and keyed connection was remained the same with the post illustrated in Figure 9.9. Two types of steel plates used to construct the posts were the mild steel plate and high strength steel plate.

For the barrier with 300 mm thick SCS panels supported by mild steel posts, two blast threat scenarios considered were 500 kg TNT and 750 kg TNT at a 5 m standoff distance. The barrier with 300 mm thick SCS panels responded in a similar manner to the barrier with 200 mm thick SCS panel illustrated in Figure 9.11. By increasing the thickness of SCS panels, the maximum deformation of the panels and the posts were reduced. The deformation of the barrier with 300 mm thick SCS panels subjected to the increased blast loading is presented in Table 9.15. Compared to the deformation of the barrier with 200 mm thick SCS panels subjected to the same blast loading (Table 9.11), the 300 mm thick SCS panel could reduce the maximum

displacement of the middle panel and the mild steel post by up to 25% and 45%, respectively. The maximum displacement of the SCS panels was reduced due to the additional mass of concrete core causing the kinetic energy in the panels to reduce. The higher yield load of the posts (due to the increased depth of the posts) and reduced kinetic energy in the SCS panels both contributed to the lower deformation of the posts.

Table 9.15: Deformation of the barrier with 300 mm thick non-composite SCS panels supported by mild steel posts under various blast loading conditions.

Blast threat Scenarios		Displacement of middle panel (mm)			Post		Keyed connection	
Standoff distance (m)	TNT mass (kg)	Bottom	Mid-height	Top	Displa. (mm)	Rotation (°)	Displa. (mm)	Rotation (°)
5	500	374	342	375	154	2.5	4.4	1.0
	750	551	498	538	344	5.6	4.8	1.1

Table 9.16 shows the percentage of energy transferred from the 300 mm thick SCS panels to the posts for the barrier supported by the mild steel posts. The SCS panels only dissipated about 30% of the kinetic energy impinged on them. The balance kinetic energy of the panels was transferred and dissipated by the mild steel posts. This observation was similar to the barrier with 200 mm thick SCS panels supported by the mild steel posts shown in Table 9.12. These results showed that increasing the thickness of the SCS panels had no significant effect on the energy transfer phenomena in the panel-post interaction.

Table 9.16: Energy transferred from the SCS panels to the posts for the barrier with 300 mm thick SCS panels supported by mild steel posts.

Blast threat Scenarios		Middle panel		Side panels	
Standoff distance (m)	TNT mass (kg)	Strain energy (%)	Energy transferred to the post (%)	Strain energy (%)	Energy transferred to the post (%)
5	500	32	68	35	65
	750	28	72	32	68

The barrier with 300 mm thick SCS panels supported by high strength steel posts was subjected to three blast loading scenarios, namely (1) 500 kg TNT, (2) 750 kg TNT and (3) 1000 kg TNT, at a 5 m standoff distance. The deformation of the SCS panels and the high strength steel posts under increased blast loading is presented in Table 9.17. Comparing the response of the barrier with 300 mm thick SCS panels supported by different types of steel posts (Table 9.15 and Table 9.17), the deformation of the high strength steel post was approximately 70% lower than the mild steel post under the same blast loading condition. The maximum displacement of the panels supported by the high strength steel posts was slightly lower than the maximum displacement of the panels supported by mild steel posts.

Table 9.17: Deformation of the barrier with 300 mm thick SCS panels supported by high strength steel posts under various blast loading conditions.

Blast threat Scenario		Displacement of middle panel (mm)			Post		Keyed connection	
Standoff distance (m)	TNT mass (kg)	Bottom	Mid-height	Top	Displa. (mm)	Rotation (°)	Displa. (mm)	Rotation (°)
5	500	361	302	322	46	0.8	1.6	0.4
	750	501	411	485	79	1.3	2.4	0.6
	1000	646	517	546	153	2.5	5.9	1.4

Table 9.18 shows the percentage of energy transferred from the 300 mm thick panels to the posts for the barrier supported by the high strength steel posts. The middle panel dissipated about 80% of its kinetic energy, while the side panels dissipated about 60% of their kinetic energy. These results showed that the panels supported by high strength steel posts were more effective in dissipating the kinetic energy than the panels supported by mild steel posts (Table 9.16). In addition, the percentage of energy dissipated by the 300 mm thick panels supported by high strength steel posts was similar to the 200 mm thick panels supported by the high strength steel posts shown in Table 9.14. This showed that the thickness of SCS panels had no significant effect on the energy transfer phenomena in the panel-post interaction.

Table 9.18: Energy transferred from the SCS panels to the posts for the barrier with 300 mm thick SCS panels supported by high strength steel posts.

Blast threat Scenarios		Middle panel		Side panels	
Standoff distance (m)	TNT mass (kg)	Strain energy (%)	Energy transferred to the post (%)	Strain energy (%)	Energy transferred to the post (%)
5	500	78	22	62	38
	750	83	17	66	34
	1000	77	23	62	38

9.3.3.2 Summary for the non-composite SCS panels supported by posts

The failure modes identified for the barrier composed of the non-composite SCS panels and the steel posts were the flexural failure of the posts and the fracture of the rear faceplate near the flared ends under large deformation. The yield stress of the steel posts had significant effect on the deformation of the posts and the energy transfer mechanism in the panel-post interaction. High strength steel had a higher yield stress than mild steel, thus the energy absorption capacity of the high strength steel post was higher than the mild steel post under the same displacement. Higher energy absorption capacity of the high strength steel post caused its maximum displacement to be lower than the mild steel post under the same blast loading condition. The maximum support rotation of the high strength steel post when it fractured was lower than the mild steel post due to the lower fracture strain of high strength steel (0.18) compared to mild steel of 0.25.

A certain percentage of the kinetic energy of the panels was transferred onto the posts and dissipated by the strain energy of the posts due to panel-post interaction. The yield stress of the posts affected the percentage of kinetic energy of the panels being transferred into the posts. The simulation results showed that the panels dissipated a higher percentage of energy when they were supported by high strength steel posts compared to mild steel posts under the same blast loading condition. The thickness of the SCS panels had no significant effect on the energy transfer mechanism in the panel-post interaction. The maximum deformation of the panels

and the posts could be reduced by increasing the thickness of the SCS panel and the depth of the post.

For the barrier with mild steel posts, the simulation results showed that up to 70% of the kinetic energy of the panels was dissipated by the mild steel posts for the blast loading scenarios considered in this study (Table 9.12 and Table 9.16). For the barrier supported by high strength steel posts, the middle panel dissipated about 70% of its kinetic energy, while the side panels dissipated about 55% of their kinetic energy (Table 9.14 and Table 9.18).

These simulation results showed that the use of high strength steel posts had advantages over the mild steel posts in the barrier design. The high strength steel posts showed less deformation compared to the mild steel posts under the same blast loading condition. The non-composite SCS panels supported by high strength steel posts could dissipate energy more effectively than the panels supported by mild steel posts. However, it should be noted that the lower fracture strain of high strength steel will cause the high strength steel posts to fracture at a lower support rotation compared to the mild steel posts.

9.3.4 Theoretical analysis for non-composite SCS panels supported by posts

The maximum displacement of the non-composite SCS panels with fixed support condition was determined using the improved analytical model for non-composite SCS panels under various blast loading scenarios. The analytical results were compared to the FE simulation results for the middle panel supported by the steel posts. It should be noted that, all the kinetic energy of the panel was assumed to be dissipated by the strain energy of the rear faceplate in the improved analytical model. The energy transfer due to the panel-post interaction observed in the FE simulation was ignored in the theoretical analysis. In the FE model, the blast loading on the middle panel was non-uniform. The lower half of the panel was subjected to a higher blast loading due to the position of the charge on the ground level. In the theoretical analysis, it was assumed that the impulse was uniformly distributed on the panel. The equivalent uniform impulse for various blast loading scenarios on each components

of the barrier was determined using the Conwep program and the results is presented in Table 9.19. The equivalent uniform impulse for the middle panel was used in the improved analytical model to determine the theoretical maximum displacement of the rear faceplate.

Table 9.19: Equivalent uniform impulse on each components of the barrier determined using the Conwep program under various blast loading conditions.

Blast threat scenarios	Equivalent uniform impulse determined using Conwep (kPa.msec)		
	middle panel	middle post	side panel
500kg TNT/10m	4922	4719	4245
250kg TNT/5m	6260	5448	3943
500kg TNT/5m	10650	9042	6345
750kg TNT/5m	14550	12160	8403
1000kg TNT/5m	18100	15010	10330

The theoretical maximum displacement of 200 mm thick SCS panels was compared to the FE predicted maximum displacement of the middle panel supported by steel posts in Table 9.20. Table 9.21 shows the comparison between the results of the improved analytical model and the FE predicted maximum displacements for 300 mm thick SCS panels under various blast threat scenarios. The improved analytical model predicted slightly higher maximum displacement of the panels (for both 200 mm and 300 mm thick panels) compared to the FE simulation when the support rotation of the posts was less than 5°. When the support rotation of the posts exceeded 5°, the improved analytical model predicted a lower maximum displacement of the panel compared to the FE results.

Table 9.20: Theoretical maximum displacement of 200 mm thick non-composite SCS panel compared to the simulation results of the middle panel supported by steel posts under various blast loading conditions.

Types of post	Blast threat scenarios	Support rotation of post (°)	Maximum displacement of middle panel (mm)		% difference
			FE results	Improved analytical results	
Mild steel posts	500kg TNT/10m	1.1	222	223	0
	250kg TNT/5m	1.5	269	278	3
	500kg TNT/5m	4.6	465	465	0
	750kg TNT/5m	9.0	728	633	-15
High strength steel posts	500kg TNT/10m	0.6	214	223	4
	250kg TNT/5m	0.6	254	278	9
	500kg TNT/5m	1.4	435	465	6
	750kg TNT/5m	2.9	610	633	4
	1000kg TNT/5m	7.0	794	787	-1

Table 9.21: Theoretical maximum displacement of 300 mm thick non-composite SCS panel compared to the simulation results of the middle panel supported by steel posts under various blast loading conditions.

Types of post	Blast threat scenarios	Support rotation of post (°)	Maximum displacement of middle panel (mm)		% difference
			FE results	Improved analytical results	
Mild steel posts	500kg TNT/5m	2.5	375	385	3
	750kg TNT/5m	5.6	551	523	-5
High strength steel posts	500kg TNT/5m	0.8	361	385	6
	750kg TNT/5m	1.3	501	523	4
	1000kg TNT/5m	2.5	646	649	0

Comparison of the theoretical predictions and FE simulation results showed that the improved analytical model for the fix supported non-composite SCS panels could provide a conservative prediction of the maximum displacement of the SCS panels support by steel posts, when the support rotation of the post was less than 5° . The improved analytical model slightly overestimated the maximum displacement of the middle panel supported by the mild steel posts (less than 3%) while it overestimated the maximum displacement of the middle panel supported by high strength steel posts by about 10%. Therefore, the improved analytical model for fix supported non-composite SCS panels could be used as a simplified method to predict the maximum displacement of the non-composite SCS panels supported by steel posts, ignoring the energy transfer between the panel and the post.

9.3.5 Two degrees of freedom (2DOF) system for the barrier

In this section, two degrees of freedom system was modelled using non-linear transient dynamic commercial software Strand7 to predict the response of the barrier under various blast threat scenarios. The components of the barrier considered in the two degrees of freedom system was the post, half of the middle panel and half of the side panel as shown in Figure 9.14 (a). In the two degrees of freedom system, it was assumed that the reaction force of half of the middle panel and half of the side panel would be resisted by this post.

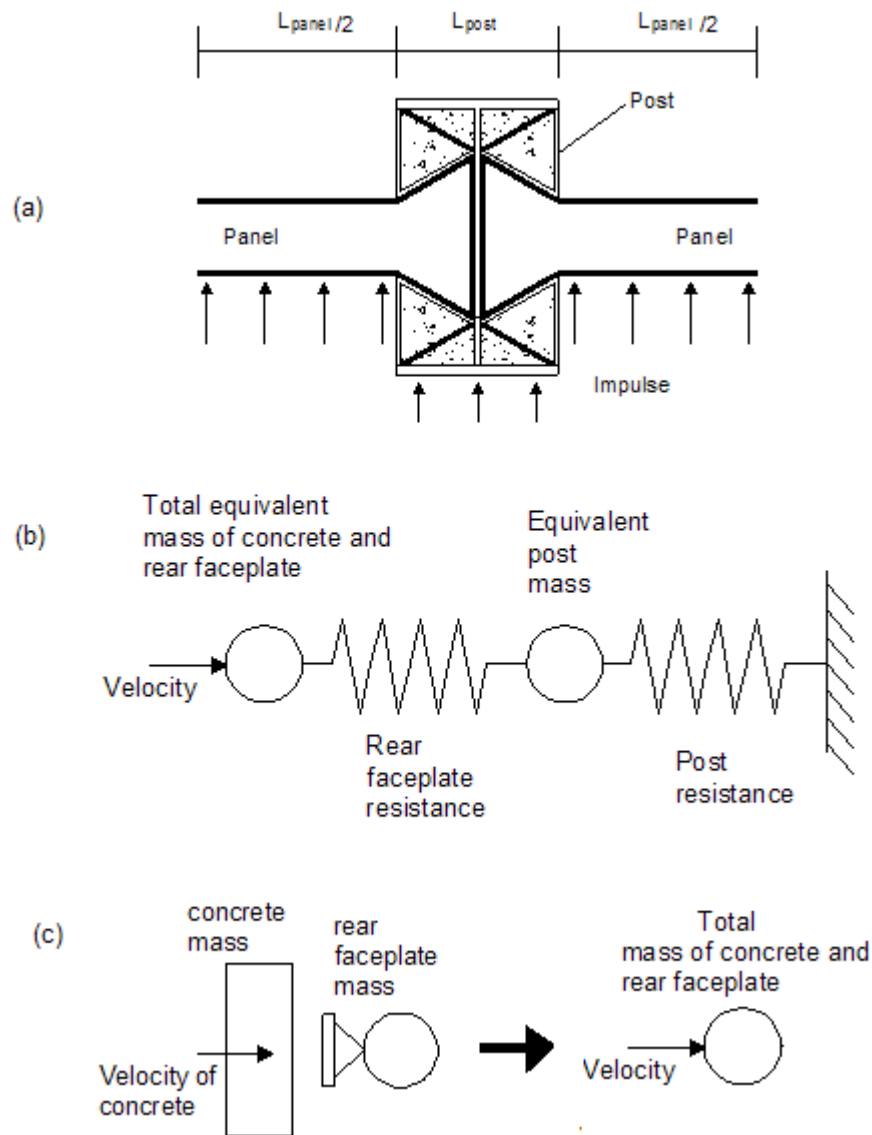


Figure 9.14: (a) The panels and the post of the barrier, (b) simplification of the barrier system into two degrees of freedom system, (c) determination of the velocity of panel.

Figure 9.14 (b) shows the simplification of the panels and the post into two degrees of freedom system. The mass of concrete cores and rear faceplates from both middle and side panels were combined into a single mass. The mass of the concrete core at the flared ends was ignored in the analysis. The total mass of the concrete core and the rear faceplate was scaled with a load mass factor (K_{LM}) to obtain the total equivalent mass used in the two degrees of freedom system. According to Dinan (2005), the load mass factor (K_{LM}) for structures under membrane response is 0.8. For the SCS panels with 200 mm thickness and 300 mm thickness, the total

equivalent mass of the concrete core and the rear faceplate was 5100 kg and 7350 kg, respectively.

When subjected to the blast loading, it was assumed that the concrete core was first impinged by the blast impulse (ignoring the front faceplate) and moved towards the mass of the rear faceplate with an initial velocity of the concrete core as illustrated in Figure 9.14 (c). The initial velocity of the concrete core is given by,

$$v_{core} = \frac{I}{m_{core}} = \frac{I}{\rho_c t_c} \quad (9.15)$$

where I is the blast impulse, m_{core} is the mass per unit area of the concrete core, ρ_c is the density of the concrete and t_c is the thickness of the concrete core. In this study, the blast impulse on the middle panel under various blast threat scenarios (Table 9.19) was used to determine the velocity of the concrete core for conservative reason.

Upon contact, the mass of the concrete core and the mass of the rear faceplate moved together with a new velocity given by,

$$v = \frac{m_{core} v_{core}}{m_{core} + m_{plate}} \quad (9.16)$$

where m_{plate} is the mass per unit area of the rear faceplate. The blast impulse on the post was ignored due to the assumption that the deformation of the post was mainly caused by the panel-post interaction. Table 9.22 presents the velocity of the concrete core and rear faceplate under various blast loading conditions.

Table 9.22: Velocity of the concrete core and rear faceplate upon contact under various blast loading conditions.

Blast threat scenarios	Impulse (kPa.msec)	Velocity on the concrete core and rear plate (m/s)	
		200 mm thick panel	300 m thick panel
500kg TNT/10m	4922	9.7	-
250kg TNT/5m	6260	12.1	-
500kg TNT/5m	10650	20.6	14.2
750kg TNT/5m	14550	28.1	19.4
1000kg TNT/5m	18100	34.9	24.1

The static resistance function of the rear faceplate was highly dependent on the stiffness of the axial restraint. Under semi-rigid axial restraint supports, the rear faceplate showed transient membrane response up to a large displacement before turning into a plastic membrane. For the steel plate supported by rigid axial restraint supports, the plate displayed plastic membrane response while the displacement was less than its thickness (Clarkson, 1956). During the transient membrane response, the load increased non-linearly, where the stiffness of the rear faceplate increased as the displacement increased. The load increased linearly with the displacement during the plastic membrane response. The commercial software Strand7 used in the modelling of the two degrees of freedom system had limitation in solving the resistance function with an increasing stiffness. It was also found that using the load-displacement relationship of the plastic membrane as the resistance function for the rear faceplate will yield erroneous prediction of the barrier response. To account for the effect of the transient membrane response, the static resistance function of the rear faceplate was defined as a plastic membrane response with a reduction factor (α). The resistance function for the rear faceplate used in this study was,

$$P = \alpha \frac{8\sigma_y A \delta_{\max}}{L} \quad (9.17)$$

where P is the total applied load, α is the reduction factor, σ_y is the yield stress of the rear faceplate, A is the cross section area of the rear faceplate, δ_{\max} is the displacement at mid-span, and L is the distance between the supports. Figure 9.15 (a) illustrates the resistance function for the rear faceplate used in this study.

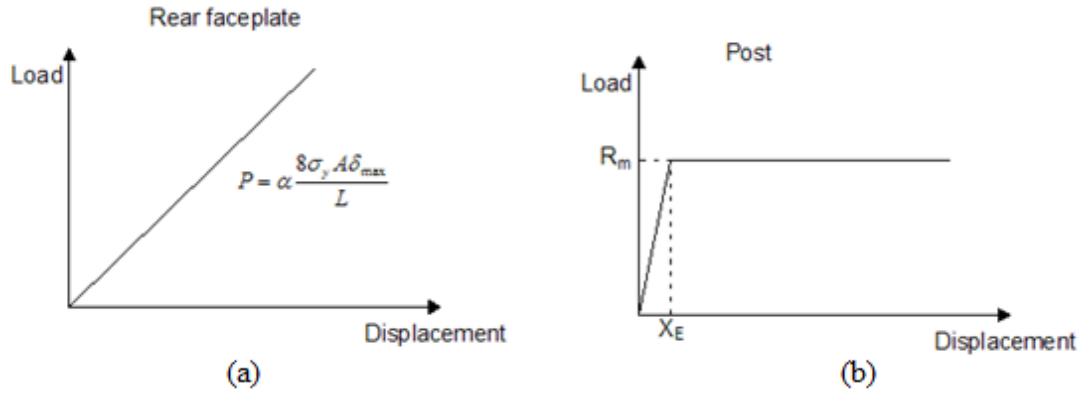


Figure 9.15: Static resistance functions: (a) the rear faceplate with a reduced plastic membrane response, (b) the elasto-plastic response of the post.

It was assumed that the post was subjected to a uniformly distributed load from the panels due to the panel-post interaction. The load mass factor (K_{LM}) for the post subjected to a uniformly distributed load under elastic response and plastic response was 0.65 and 0.66, respectively (Cormie et al. 2009). The load mass factor (K_{LM}) under plastic response of 0.66 was used for the post in this study. The equivalent mass of 650 mm depth post and 750 mm depth post are presented in Table 9.23. The elasto-plastic resistance function was defined for the post as shown in Figure 9.15 (b). The dynamic moment capacity, dynamic ultimate flexural capacity and elastic limit displacement for the mild steel post and high strength steel post is summarized in Table 9.23. The hardening effect of mild steel after yielding was ignored in the analysis.

Table 9.23: Properties of mild steel post and high strength steel post.

	Mild steel post		High strength steel post	
	650	750	650	750
Depth of the post (mm)	650	750	650	750
Total mass (kg)	2160	2200	2160	2200
Equivalent mass (kg)	1425	1452	1425	1452
Dynamic yield stress (MPa)	325	325	826	826
Moment of Inertia (mm ⁴)	3.05x10 ⁹	4.35 x10 ⁹	3.05x10 ⁹	4.35 x10 ⁹
Plastic section modulus (mm ³)	1.17x10 ⁷	1.43x10 ⁷	1.17x10 ⁷	1.43x10 ⁷
Dynamic moment capacity (kNm), M_p	3790	4640	9660	11800

Dynamic ultimate load capacity (kN), R_m	2170	2650	5550	6740
Elastic limit displacement (mm), X_E	19	16	49	42

The results of the two degrees of freedoms system were compared to the FE simulation results in Table 9.24. By changing the reduction factor, α , in the resistance function of the rear faceplate, the two degrees of freedom system could predict the response of the barrier under blast loading conditions. The results of the two degrees of freedom system was inconsistent compared to the FE simulation results. The difference between the results of the two degrees of freedom system and the FE simulation results was within 30% for most of the cases by using the proposed reduction factor. Figure 9.16 shows that the displacement time histories of the barrier predicted by the FE model and the two degrees of freedom system were similar under blast scenario of 250 kg TNT at a 5 m standoff distance. For the response of mild steel post, the two degrees of freedom system predicted similar peak displacement but at a later stage compared to the FE result. The factor α reduced as the deformation of the post increased (Table 9.24). For the barrier supported by mild steel posts, the reduction factor (α) was in the range of 0.4 to 0.6 when the support rotation of the post was less than 2° . When the support rotation of the mild steel post exceeded 2° , the factor was in between 0.2 to 0.4. For the barrier supported by high strength steel posts, the reduction factor of 0.8 could be used when the support rotation of the high strength steel post was less than 2° . The reduction factor for the resistance function of the rear faceplate was in the range of 0.5 to 0.8 when the support rotation of the high strength steel post exceeded 2° .

Table 9.24: A comparison between the maximum deformation of the barrier predicted by the FE models and two degrees of freedom (2DOF) system.

Type of steel post	Thickness of SCS panel (mm)	Blast threat scenarios	Factor (α)	Post support rotation ($^{\circ}$)	Panel displacement			Post displacement		
					FE (mm)	2DOF (mm)	(%) difference	FE (mm)	2DOF (mm)	(%) difference
Mild steel	200	500kg TNT/10m	0.6	1.1	67	54	-19	222	187	-16
		250kg TNT/5m	0.4	1.5	89	86	-3	269	277	3
		500kg TNT/5m	0.2	4.6	284	363	28	465	662	42
		750kg TNT/5m	0.2	9.0	557	823	48	728	941	29
	300	500kg TNT/5m	0.3	2.5	154	148	-4	375	447	19
		750kg TNT/5m	0.3	5.6	344	445	29	551	623	13
High strength steel	200	500kg TNT/10m	0.8	0.6	36	29	-19	214	163	-24
		250kg TNT/5m	0.8	0.6	36	36	0	254	204	-20
		500kg TNT/5m	0.8	1.4	83	87	5	435	350	-20
		750kg TNT/5m	0.5	2.9	179	197	10	610	588	-4
		1000kg TNT/5m	0.5	7.0	430	471	10	794	746	-6
	300	500kg TNT/5m	0.8	0.8	46	38	-17	361	283	-22
		750kg TNT/5m	0.8	1.3	79	80	1	501	387	-23
		1000kg TNT/5m	0.6	2.5	153	152	-1	646	548	-15

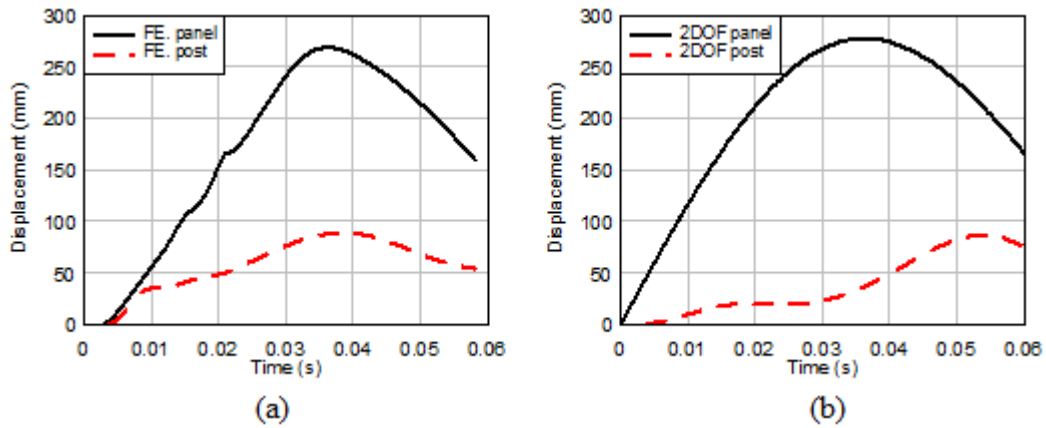


Figure 9.16: Displacement time histories of the middle panel and the post for the barrier supported by mild steel post under 250 kg TNT at a 5 m standoff distance, (a) FE simulation results and (b) two degrees of freedom system (2DOF).

These results showed that the resistance function of the rear faceplate was not consistent where it depended on the types of steel post (flexural yield load of the post) and the support rotation of the posts, as these factors had direct implication on the stiffness of axial restraint. High strength steel posts had a higher flexural yield load than mild steel posts, and the rear faceplate of the panel supported by high strength steel posts showed higher resistance (higher α factor) than the panels supported by mild steel posts when subjected to the same blast loading condition. When the deformation of post increased, the resistance of the rear faceplate decreased (lower α factor) for the panels supported by both mild steel posts and high strength steels posts. These results showed that, the rear faceplate could not achieve full capacity of the plastic membrane due to the deformation of the post. In order to use the two degrees of freedom system effectively in predicting the response of the barrier, more research is required to derive the resistance function of the rear faceplate as a function of the flexural yield load of the post and deformation of the post.

9.4 Comparison between the prototype barrier with non-composite SCS panel and the cantilever concrete blast wall

In this section, a cantilever concrete blast wall was designed to resist the blast threat scenario of 250 kg TNT at a 5 m standoff distance. The design of the concrete blast wall was compared to the performance of the barrier with non-composite SCS panels supported by mild steel posts subjected to the same blast loading condition.

The design of the concrete blast wall was carried out by following the design example in Cormie et al. (2009). The height of the concrete blast wall was 3.5 m. It was symmetrically reinforced using grade 460 steel for flexural reinforcement, and grade 250 steel for shear reinforcement. The reinforcement ratio of 1% (ρ_s) was chosen for the concrete blast wall and the concrete grade was 40 MPa. The density of the concrete was assumed as 2400 kg/m³. The peak reflected impulse on the concrete blast wall obtained from the ATBLAST was 7650 kPa.msec.

The dynamic design stress for the flexural reinforcement is given by Cormie et al. (2009) as,

$$\begin{aligned}
 f_d &= f_{dy} + (f_{du} - f_{dy})/4 \\
 &= 1.2f_y + (1.05f_u - 1.2f_y)/4 \\
 &= 1.2 \times 460 + (1.05 \times 550 - 1.2 \times 460)/4 \\
 &= 560 \text{ MPa}
 \end{aligned} \tag{9.18}$$

The ultimate resistance of the concrete blast wall is,

$$\begin{aligned}
 r_u &= \frac{2\rho_s f_{ds} d_c^2}{H^2} \\
 &= \frac{2 \times 0.01 \times 560 \times 10^6 d_c^2}{3.5^2} \\
 &= 914 \times 10^3 d_c^2 \text{ N/m}^2
 \end{aligned} \tag{9.19}$$

For protection category 2, the maximum displacement of the cantilever concrete blast wall is limited to,

$$X_m = H \tan 4^\circ = 3.5 \tan 4^\circ = 0.245 \text{ m} \tag{9.20}$$

The Young's modulus of the concrete and the steel was 28 GPa and 200 GPa, respectively. The ratio of Young's modulus of steel to concrete was 7.14. From Figure 5.8 in Mays and Smith (1995), the second moment of area of the concrete blast wall is,

$$I = 0.044bd_c^3$$

The elastic flexural stiffness of the concrete blast wall is,

$$\begin{aligned} K_E &= \frac{8EI}{H^4} \\ &= \frac{8 \times 28 \times 10^9 \times 0.044 \times 1 \times d_c^3}{3.5^4} \\ &= 65.7 \times 10^6 d_c^3 N/m^2 / m \end{aligned} \quad (9.21)$$

The maximum elastic displacement is,

$$X_E = \frac{r_u}{K_E} = \frac{914 \times 10^3 d_c^2}{65.7 \times 10^6 d_c^3} = \frac{13.9 \times 10^{-3}}{d_c} m \quad (9.22)$$

The basic impulse equation can be used to determine the required concrete depth,

$$\frac{I}{2K_{LM}m} = r_u \left(X_m - \frac{X_E}{2} \right) \quad (9.23)$$

where I is the impulse on the concrete blast wall, K_{LM} is the load mass factor, m is the mass per unit area of the wall, and X_m is the maximum displacement of the wall.

The load mass factor (K_{LM}) for the cantilever wall subjected to uniform loading is 0.66. By inputting all the information into Eq. 9.23, it becomes,

$$\frac{7650^2}{2 \times 0.66 \times 2400 \times d_c} = 914 \times 10^3 d_c^2 \left(0.245 - \frac{13.9 \times 10^{-3}}{2d_c} \right) \quad (9.24)$$

Solving the above equation give $d_c = 0.445$ m, therefore $d_c = 0.45$ m was chosen.

The flexural reinforcement required on each face is,

$$A_s = 0.01 \times 1000 \times 450 = 4500 mm^2 / m \quad (9.25)$$

Therefore, T25 bars were used at 100 mm centres of each face (4900 mm^2). The overall thickness of the concrete blast wall including the 40 mm concrete cover is,

$$D = 450 + 40 + 40 + 12.5 + 12.5 = 555\text{mm} \quad (9.26)$$

The ultimate shear stress at a distance $d_c = 0.45$ m from the support is given as,

$$\begin{aligned} v_u &= \frac{r_u(H - d_c)}{d_c} \\ &= \frac{914 \times 10^3 \times 0.45^2 (3.5 - 0.45)}{0.45} \\ &= 1.25\text{N} / \text{mm}^2 \end{aligned} \quad (9.27)$$

The shear capacity of the concrete was determined based on AS 3600 (Standards Australia, 2009),

$$v_c = \beta \left(\frac{A_s f_c}{bd_c} \right)^{1/3} \quad (9.28)$$

where β is 1.1 for members subjected to the bending and f_c is the concrete compressive strength. The shear capacity of the concrete was,

$$v_c = 1.1 \times \sqrt[3]{\frac{4900 \times 40}{1000 \times 450}} = 0.83\text{N} / \text{mm}^2 \quad (9.29)$$

The design shear stress is chosen from the maximum between $(v_u - v_c)$ and $0.85v_c$,

$$(v_u - v_c) = 1.25 - 0.83 = 0.42\text{N} / \text{mm}^2 < 0.85v_c = 0.85 \times 0.83 = 0.71\text{N} / \text{mm}^2 \quad (9.30)$$

The dynamic yield stress of the grade 250 shear reinforcement is,

$$f_{dy} = 1.1 \times 250 = 275\text{N} / \text{mm}^2 \quad (9.31)$$

The required area of stirrups of width $b = 100$ mm and spacing (s) of 300 mm was,

$$A_v = \frac{0.71 \times 100 \times 300}{275} = 77.5\text{mm}^2 \quad (9.32)$$

The shear reinforcement provided was R10 stirrups at 300 mm centres (78.6 mm^2). The design of diagonal bars at the support was ignored in this study. The detail of the reinforcement arrangement of the designed concrete blast wall is illustrated in Figure 9.17.

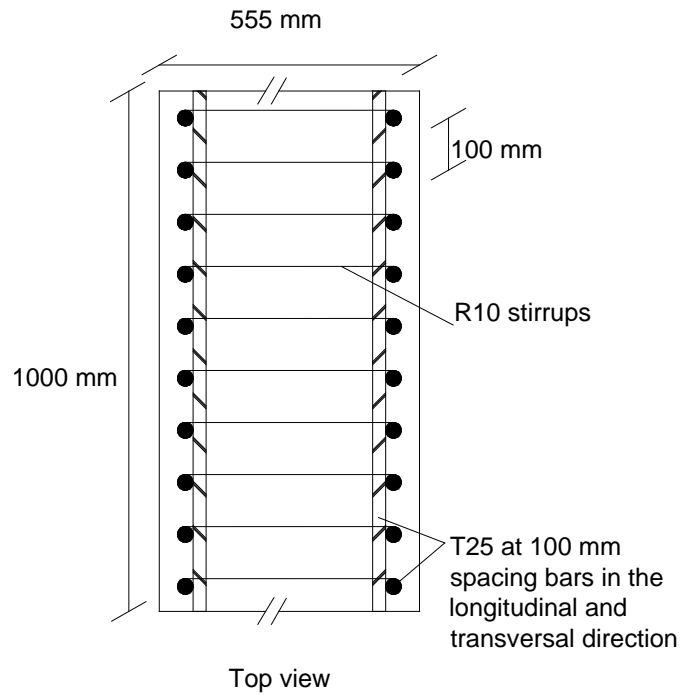


Figure 9.17: Reinforcement detail in the concrete blast wall designed to resist blast loading of 250 kg TNT at a 5 m standoff distance.

Table 9.25 shows the comparison between the reinforced concrete blast wall and the prototype barrier supported by mild steel posts when subjected to the blast loading of 250 kg TNT at a 5 m standoff distance. Using the barrier with non-composite SCS panels supported by mild steel posts, the wall thickness could be reduced significantly by about 60%. The volume of steel per metre wall width used in the construction of the both types of blast wall was compared, by ignoring the reinforcement amount in the base of the concrete blast wall and the posts in the prototype barrier. The steel amount in the concrete blast wall was 4% higher than the non-composite SCS panels used in this study.

Table 9.25: Comparison between the concrete blast wall and the barrier composed of non-composite SCS panels supported by mild steel posts under blast loading of 250 kg TNT at 5 m standoff distance.

	Cantilever concrete wall	SCS panel	% difference
Overall wall thickness (mm)	555	200	64
Volume of steel per unit wall length (m ³ /m)	0.073	0.07	4
Maximum displacement (mm)	245	269	-10

The maximum displacement of the concrete blast wall was about 10% lower than the displacement of the barrier with non-composite SCS panels obtained from the FE simulation. However, it should be noted that for the protection category two in the blast wall design, the maximum displacement of the wall is limited by the collapse of the wall under blast loading. The maximum displacement of the concrete blast wall is limited to 4 degrees support rotation (without tensile membrane action) to prevent catastrophe collapse (Cormie et al. 2009). From experimental and numerical investigations, the non-composite SCS panels showed the capacity to undergo large support rotation, more than 12° without collapsed. Even though the maximum displacement of the non-composite SCS panel was slightly higher than the concrete blast wall, the performance of the barrier with non-composite SCS panels still satisfied the performance requirement of protection category two.

From these results, it was found that the barrier with non-composite SCS panels is an economical alternative to the existing concrete blast wall design in terms of amount of concrete and steel used in the construction. In addition, the simple construction methods such as no shear connections in the panels, and easy connection between the panels and the posts, can further reduce the construction cost. Another advantage of the barrier with non-composite SCS panels is that it will not generate hazardous concrete fragments under blast loading conditions.

9.5 Conclusions

In this chapter, the response of non-composite SCS panels under fixed and post support conditions subjected to blast loading was investigated. Using the panels under fixed support condition, a parametric study was carried out to evaluate the effects of the thickness of the rear faceplate and the concrete core on the response of the non-composite SCS panels. For the panels under post support condition, two types of steel post investigated were the mild steel posts and the high strength steel posts. Several important observations are listed below:

- (a) The response of non-composite SCS panels under blast loading was similar to the thin sheet catcher system. Under fixed support condition, the rear faceplate dissipated about 80% of the kinetic energy in the panel through membrane stretching.
- (b) From the parametric study, the maximum displacement of the panel could be reduced by increasing the thickness of the rear faceplate and the concrete core. Increasing the thickness of the rear faceplate was more effective in reducing the maximum displacement of the panel compared to increasing the thickness of the concrete core. The simulation results showed that by increasing the thickness of the rear faceplate by 10 mm, it had the same effect as increasing the thickness of the concrete core by 200 mm for the panel under fixed support condition.
- (c) The analytical model of the thin sheet catcher system was improved by taking into account the mass of the rear faceplate in the analysis. The improved analytical model could predict the maximum displacement of the rear faceplate reasonably well for the non-composite SCS panels with the concrete core thickness of less than 200 mm. When the thickness of the concrete core exceeded 200 mm, the improved analytical model predicted a conservative maximum displacement of the rear faceplate.
- (d) For the non-composite SCS panels supported by steel posts, a certain percentage of kinetic energy of the panels was dissipated by the posts due to the interaction between the panels and the posts. The failure modes observed from the simulation results were the flexural failure of the post and fracture failure of the rear faceplate. The use of high strength steel posts in the barrier was beneficial as the high strength steel posts deformed less than the mild steel posts under the

same blast loading condition and the membrane stretching of the rear faceplate could be utilized effectively.

- (e) In this study, two degrees of freedom system was developed for the barrier supported by steel posts. The results of two degrees of freedom system showed that the resistance function of the rear faceplate was of prime important in order to predict the response of the barrier under blast loading. The rear faceplate could not develop full capacity of a plastic membrane due to deformation of the steel posts. The transient membrane resistance should be considered in the resistance function of the rear faceplate.
- (f) The prototype barrier with non-composite SCS panels is a viable alternative to the existing reinforced concrete blast wall. The prototype barrier have the potential of reducing the overall thickness of the blast wall, lower construction cost and higher safety feature where not hazardous concrete fragments will be generated compared to the reinforced concrete blast wall.

CHAPTER 10

CONCLUSIONS AND SUGGESTIONS FOR FUTURE WORKS

In this study, experimental investigations had been carried out on the stainless steel Grade 304 under medium strain rates and the axially restrained non-composite steel-concrete-steel (SCS) under quasi-static and impact loading conditions. Based on the experimental results of stainless steel under medium strain rates, new Cowper-Symonds coefficients were proposed. The experimental results of axially restrained non-composite SCS panels under quasi-static loading had been used to develop the static resistance function of the panels. The finite element (FE) modelling techniques for the non-composite SCS panels were validated against the impact test results of the panels.

Using the validated FE modelling techniques, the response of the barrier utilising non-composite SCS panels under blast loading had been investigated. It was found that the barrier utilising non-composite SCS panels has high energy dissipation capacity where it dissipates the blast energy by membrane stretching of the rear faceplate. The barrier utilising non-composite SCS panels is an economical alternative to the reinforced concrete blast wall in resisting close-in detonation of high explosives. The major findings and suggestions for future works for the experimental and numerical studies are presented in the following sections.

10.1 Strain rate effects for stainless steel Grade 304

The experimental results of Grade 304 stainless steel under medium strain rates were compared to the theoretical prediction using the existing Cowper-Symonds coefficients. The experimental results were significantly lower than the theoretical prediction. This could be attributed to differences in the stress level, prior work hardening, heat treatment condition and microstructure of the stainless steel

specimens used in this study. The use of existing Cowper Symonds coefficients will overestimate the yield stress and ultimate tensile strength of the stainless steel in the design.

Using the experimental data, new Cowper-Symonds coefficients for solution annealed stainless steel Grade 304 with fine grain size and 0.2% proof stress of 550 MPa were derived for strain rates in the range of 0.002 - 600 s⁻¹ at room temperature. The coefficients are different for the yield stress and the ultimate tensile strength due to different strain rate sensitivity observed in the tests. For the yield stress, the Cowper-Symonds coefficients are 14000 (*D*) and 3 (*q*), while they are 6000 (*D*) and 1.5 (*q*) for the ultimate tensile strength. It is recommended further experimental investigation to be carried out using the tensile split Hopkinson bar in order to study the strain rate effects of stainless steel 304 under strain rates greater than 600 s⁻¹.

10. 2 Static testing of axially restrained non-composite SCS panels

With the axial restraint, the non-composite SCS panels were able to develop tensile membrane resistance at large displacement, even though various failure modes had been observed during the flexural response. The tensile membrane resistance was significantly higher than the flexural load capacity of the non-composite SCS panels and the panels had very high ductility where they showed support rotation more than 15° without collapse.

The most effective method to increase the flexural load capacity of a SCS panel is by increasing the degree of interaction between the steel faceplates and the concrete core, especially by welding end caps to steel faceplates to form a fully enclosed SCS panel. The use of stainless steel faceplates in the non-composite SCS panel will increase the flexural load capacity compared to the panels with mild steel faceplates, due to the effects of significant strain hardening of stainless steel. The use of reinforcement in the concrete core slightly increases the flexural load capacity, while the infill material with a low compressive strength such as lightweight concrete will significantly reduce the flexural load capacity of the panels under static loading condition.

The stiffness of axial restraint has a significant effect on the development of tensile membrane resistance in the SCS panels. The stiffness of axial restraint on the panel was influenced by the stiffness of the axial restraint supports and the stiffness of the panel at flared end. Low axial restraint used in this study caused the tensile membrane resistance of the SCS panel developed at large mid-span displacement.

10. 3 Impact testing of axially restrained non-composite SCS panels

Generally, the response of axially restrained SCS panels under impact loading was similar to the static load-displacement relationship of the panels, where the panels showed the flexural resistance followed by the tensile membrane resistance under large displacement. The panels also showed inertial effects immediately after impact, and it lasted only for 1-2 milliseconds. The axially restrained non-composite SCS panels could withstand very large impact energy through the development of tensile membrane resistance in the steel faceplates. The possible failure modes identified in this study were the penetration of steel faceplate by the hard impactor under very large impact load, and the failure of the axial restraint on the panel. The failure of the axial restraint could be attributed to the damage of concrete infill at the flared end or the buckling of end plate.

From the impact test results, the lightweight concrete infill had no significant effect on the impact response of the axially restrained non-composite SCS panel. For the panels with non-reinforced concrete core, the flexural load capacity under impact loading condition was significantly lower than the static flexural load capacity due to the fracture of concrete core. For the panels with reinforced concrete core, the flexural load capacity under impact test was significantly higher than the static flexural load capacity. The use of reinforced concrete core, stainless steel faceplates and increased degree of interaction between the steel faceplates and the concrete core could reduce the maximum displacement of the panel up to 15%.

10. 4 Response of non-composite SCS panels subjected to blast loading

Using the validated FE modelling techniques, the response of non-composite SCS panels subjected to blast loading under fixed and post support conditions had been

investigated. The response of non-composite SCS panel under blast loading is similar to the thin sheet catcher system. Under fixed support condition, the rear faceplate dissipated about 80% of the kinetic energy in the panel through membrane stretching.

A certain percentage of kinetic energy of the panels was dissipated by the posts due to the interaction between the panels and the posts. The use of posts made of high strength steel plates in the barrier is beneficial as the posts deform less than the mild steel posts under the same blast loading condition and the membrane stretching of the rear faceplate could be utilized effectively. The failure modes observed from the simulation results were the flexural failure of the post and the fracture failure of the rear faceplate.

In this study, two degrees of freedom system was developed for the barrier supported by steel posts. The rear faceplate could not develop the full capacity of a plastic membrane due to the deformation of steel posts. The prototype barrier with non-composite SCS panels is a viable alternative to the existing reinforced concrete blast wall. The prototype barrier have the potential of reducing the overall thickness of the blast wall, lower construction cost and higher safety feature where not hazardous concrete fragments will be generated compared to the reinforced concrete blast wall.

It is acknowledged that the blast threat scenarios considered in the numerical simulation of the barrier utilising non-composite SCS panels are limited as the position of the charge is fixed at the mid-span of the panels. The response of the barrier when the explosive charge is positioned in front of the steel post or the quarter-span of the panels has not been studied due to the time constraint. It is recommended to carry out more numerical simulations to study the response of the barrier under these blast threat scenarios. Furthermore, physical testing of the barrier under blast loading should be conducted to verify the FE results before the barrier is utilised for protecting critical infrastructure facilities.

REFERENCES

- Andersson, R., Syk, M., Powell, J. and Magnusson, C. (2005). "Development of high strain rate equations for stainless steels." *Journal of Material Engineering and Performance* 14 (5), pp. 553-562.
- Baddoo, N.R. (2008). "Stainless steel in construction: A review of research, applications, challenges and opportunities." *Journal of Constructional Steel Research* 64 (11), pp. 1199-1206.
- Bangash, M. Y. H. (1993). *Impact and explosion: Structural analysis and design*, Boca Raton, FL, CRC Press.
- Beyer, M.E. (1986). "Blast loads behind vertical walls." *Proceedings of the 22nd explosives safety seminar*, Anaheim, CA: Department of Defence, Explosives Safety Board.
- Biggs, J.M. (1964). *Introduction to structural dynamics*, McGraw-Hill, New York.
- Bisalloy Steels (2006). *Bisplate Technical Manual*.
- Blazynski, T.Z. (1987). *Materials at High Strain Rates*, Elsevier Applied Science, pp.133-183.
- Borgers, J.B.W. and Vantomme, J. (2006). "Towards a parametric model of a planar blast wave created with detonating cord." *19th International Symposium on Military Aspects of Blast and Shock*, Calgary, Canada.
- Børvik, T., Hanssen, A.G., Langseth, M. and Olovsson, L. (2009) "Response of structures to planar blast loads – a finite element engineering approach." *Journal of Computers and Structures* 87, pp. 777-787.
- Brode, H.L. (1955). "Numerical simulation of spherical blast waves." *Journal of Applied Physics*, American Institute of Physics.
- Campbell, T.T., and Charlton, T.M. (1973). "Finite deformation of a fully fixed beam comprised of a non-linear material." *International Journal of Mechanical Sciences* 15, pp. 415-428.
- Cavill, B. and Rebentrost, M. (2006). "Ductal – a high performance material for resistance and impact." *Australian Journal of Structural Engineering* 7 (1), pp. 37-45.

- Chapman, T.C., Rose, T.A. and Smith, P.D. (1995). "Blast wave simulation using AutoDyn2D: A parametric study." *International Journal of Impact Engineering* 16 (5), pp. 777-787.
- Clarkson, J. (1956). "A new approach to the design of plates to withstand lateral pressure." *Trans. I.N.A.* 98, pp. 443-463.
- Comité Euro-International du Béton (1993). CEB-FIP model code. Redwood Books, Trowbridge, Wiltshire, United Kingdom.
- Cormie, D., Mays, G., and Smith, P.D. (2009). *Blast effects on buildings* 2nd edition, Thomas Telford.
- Coughlin, A.M., Musselman, E.S., Schokker, A.J. and Linzell, D.G. (2010). "Behavior of portable fiber reinforced concrete vehicle barriers subjected to blasts from contact charges." *International Journal of Impact Engineering* 37, pp. 521-529.
- Crawford, J.E., and Lan, S. (2006). "Blast barrier design and Testing." 2006 Structures Congress, St Louis, Missouri, USA.
- Crawford, J., Wu, Y., Torres, L. and Lan, S. (2009). "Design methods for enhancing the blast resistance of masonry walls and windows with thin panel catcher systems." 8th International Conference on Shock & Impact loads on Structures, December 2-4, 2009, Adelaide, Australia.
- Cunat, P.J. (2000). "Stainless steel properties for structural automotive applications." *Proceedings of Metal Bulletin International Automotive Materials Conference*, Cologne.
- Dancygier, A.N., Yankelevsky, D.Z. and Jaegermann, C. (2007). "Response of high performance concrete plates to impact of non-deforming projectiles." *International Journal of Impact Engineering* 34 (5), pp. 1768-1779.
- Davidson, J.S., Porter, J.R., Dinan, R.J., Hammons, M.I. and Connells, J.D. (2004). "Explosive testing of polymer retrofit masonry walls." *Journal of Performance of Constructed Facilities* 18 (2), pp. 100-106.
- Davidson, J. (2008). *Advanced computational dynamics simulation of protective structures research*. AFRL-RX-TY-TR-2008-4610.
- Euro Inox and The Steel Construction Institute (2006). *Design Manual for Structural Stainless Steel* Third Edition,

- Det Norske Veritas (2010). Recommended Practice DNV-RP-C204, Design Against Accidental Loads.
- Dinan, R.J. (2005). Blast resistant steel stud wall design, PhD thesis, University of Missouri-Columbia.
- Di Sarno, L., Elnashai, A. S. and. Nethercot, D. A. (2003). "Seismic performance assessment of stainless steel frames." *Journal of Constructional Steel Research* 59(10), pp. 1289-1319.
- Eibl, J. (1998). "Concrete structures under impact and impulsive loading." Synthesis report bulletin, D'Information No. 187.
- Farnam, Y., Mohammadi, S., Shekarchi, M. (2010). "Experimental and numerical investigations of low velocity impact behaviour of high-performance fiber-reinforced cement based composite." *International Journal of Impact Engineering* 37(2), pp. 220-229.
- Federal Highway Administration. (2007a). Users manual for LS_DYNA concrete material model 159. Publication No. FHWA-HRT-05-062.
- Federal Highway Administration. (2007b). Evaluation of LS-DYNA concrete material model 159, Publication No. FHWA-HRT-05-063.
- Fernie, R., and Warrior, N.A. (2002). "Impact test rig for high strain rate tensile and compressive testing of composite materials." *Strain* (2002), pp. 69-73.
- Forrestal, M.J. and Sagartz, M.J. (1978). "Elastic-plastic response of 304 stainless steel beams to impulse loads." *Journal of Applied Mechanics* 45, pp. 685-687.
- Foundoukus, N. and Chapman, J.C. (2008). "Finite element analysis of steel-concrete-steel sandwich beams." *Journal of Constructional Steel Research* 64, pp. 947-96.
- Gamble, W.L. and Park, R. (2000). Reinforced Concrete slabs 2nd Edition, John Wiley and Sons.
- Gardner, L. (2005). "The use of stainless steel in structures" *Progress in Structural Engineering and Materials* (7), pp. 45-55.
- Hallquist, J.O. (2010). LS-DYNA keyword user's manual, Volume 1, Version 971. Livermore Software Technology Corporation (LSTC).
- Harding, J., Wood, E.O. and Campbell, J.D. (1960). "Tensile testing of material at impact rates of strain." *Journal of Mechanical Science* 2, pp. 88-96.

- Haythornthwaite, R.M. (1957). "Beams with full end fixity." *Engineering* 183, pp. 110-112.
- Heng, L., Kennedy, L.J., and Mays, G.C. (1995). "Blast resistance of fully enclosed steel-concrete-steel sandwich panels." 7th International Symposium on Interaction of Effect of Munitions with Structures, Mannheim, Germany.
- Hodge Jr., P.G. (1974). "Post-yield behaviour of a beam with partial end fixity." *International Journal of Mechanical Sciences* 16, pp. 385-388.
- Hulton, F.G. (2010). "The development of Protective walls." 21st International Symposium on Military Aspects of Blast and Shock, Jerusalem, Israel.
- Itoh, Y., Liu, C. and Kusama, R. (2007). "Modelling and simulation of collisions of heavy trucks with concrete barriers." *Journal of Transportation Engineering*, August 2007, pp. 462-468.
- Izzuddin, B.A. (2005). "A simplified model for axially restrained beams subjected to extreme loading." *International Journal of Steel Structures* 5, pp. 421-429.
- Jeong, Y.J. (2008). "Simplified model to predict partial-interactive structural performance of steel-concrete composite slabs." *Journal of Constructional Steel Research* 64, pp. 238-246.
- Jones, N. (1973). "Influence of in-plane displacement at the boundaries of rigid-plastic beams and plates." *International Journal of Mechanical Sciences* 15, pp.547-561.
- Jones, N. (1989). *Structural Impact*, Cambridge University Press.
- Jones, N. (1995). "Quasi-static analysis of structural impact damage." *Journal of Construction Steel Research* 33, pp.151-177.
- Krauthammer, T. (1999). "Blast-resistant structural concrete and steel connections." *International Journal of Impact Engineering* 22, pp. 887-910.
- Lan, S., Crawford, J. and Xin, X. (2006). "Development of Shallow Footing Anti-ram Bollard System Through Modelling and Testing." *Proceedings of the 1st International Conference on Analysis and Design of Structures against Explosive and Impact Loads*, Tianjin, China, 15-17 September 2006.
- Lan, S., Lok, T.S., and Heng, L. (2005). "Composite structural panels subjected to explosive loading." *Journal of Construction and Building Materials* 19, pp. 387-395.

- Langdon, G.S., and Schleyer, G.K. (2005a). "Deformation and failure of profiled stainless steel blast wall panels. Part I: experimental investigation." *International Journal of Impact Engineering* 31 (4), pp. 341-369.
- Langdon, G.S., and Schleyer, G.K. (2005b). "Deformation and failure of profiled stainless steel blast wall panels. Part II: analytical modelling considerations." *International Journal of Impact Engineering* 31 (4), pp. 371-399.
- Langdon, G.S., and Schleyer, G.K. (2006). "Deformation and failure of profiled stainless steel blast wall panels. Part III: finite element simulations and overall summary." *International Journal of Impact Engineering* 32 (6), pp. 988-1012.
- Lee, W.S. and Lin, C.F. (2001). "Impact properties and microstructure evolution of 304L stainless steel." *Material Science and Engineering A* (308), pp. 124-135.
- Lee, S.C., Soheli, K.M.A. and Liew, J.Y.R. (2008). "Numerical simulation of ultra-lightweight steel-concrete-steel sandwich composite panels subjected to impact." *Proceedings of the Ninth International Conference on Computational Structures Technology*, Civil-comp Press, Stirlingshire, Scotland.
- Li, Q.M., Reid, S.R., Wen, H.M., and Telford, A.R. (2005). "Local impact effects of hard missiles on concrete targets." *International Journal of Impact Engineering* 32, pp. 224-284.
- Liew, J.Y. R., and Soheli, K.M.A. (2009). "Lightweight steel-concrete-steel sandwich system with J-hook connectors." *Journal of Engineering Structures* 31(5), pp. 1166-1178.
- Liew, J.Y. R., Soheli, K.M.A. and Koh, C.G. (2009). "Impact tests on steel-concrete-steel sandwich beams with lightweight concrete core." *Journal of Engineering Structures* 31(9), pp. 2045-2059.
- Louca, L.A. and Boh, J.W. (2004). "Analysis and design of profiled blast wall." *Research Report 146*, Imperial College London.
- Lu, J.P., Anderson, J.G. and Christo, F.C. (2003). "Detonation and blast wave modelling of explosions in air." *Australia Symposium on Combustion & the 8th Australia Flames Days*, pp. 1-5.
- Malvar, L.J., Crawford, J.E., Wesevich, J.W. and Simons, D. (1997). "A plasticity concrete material model for DYNA3D." *International Journal of Impact Engineering* 19 (9-10), pp. 847-873.

- Malvar, L.J. and Ross, C.A. (1998). "Review of strain rate effects for concrete in tension." *ACI Materials Journal* 95 (6), pp. 735-739.
- Marais, S.T., Tait, R.B., Cloete, T.J. and Nurick, G.N. (2004). "Material testing at high strain rate using the split Hopkinson pressure bar." *Latin American Journal of Solids and Structures* 1, pp. 319-339.
- Millard, S.G., Molyneaux, T.C.K., Barnett, S.J. and Gao, X. (2010). "Dynamic enhancement of blast-resistance ultra high performance fibre-reinforced concrete under flexural and shear loading." *International Journal of Impact Engineering* 37(4), pp. 405-413.
- Moradi, L.G., Dinan, R.J., Bewick, B.T., Davidson, J.S. (2010). Resistance of concrete masonry walls with membrane catcher systems subjected to blast loading. AFRL-RX-TY-TP-2010-0090.
- Mursi, M. and Uy, B. (2004). "Strength of slender concrete filled high strength steel box columns." *Journal of Constructional Steel Research* 6 (12), pp. 1825-1848.
- Mutalib, A.A. and Hao, H. (2010). "Development of P-I diagrams for FRP strengthened RC columns." *International Journal of Impact Engineering* 38 (5), pp. 290-304.
- Narayanan, R., Roberts, T.M. and Naji, F.J. (1994). *Design Guide for Steel-Concrete-Steel Sandwich Construction: Vol. 1: General Principles and Rules for Basic Elements*, The Steel Construction Institute, UK.
- Ngo, T., Mendis, P., Gupta, A. and Ramsay, J. (2007). "Blast loading and blast effects on structures – An overview." *Electronic Journal of Structural Engineering Special Issue: Loading on structures*, pp. 76-91.
- Ngo, T., Mendis, P., and Krauthammer, T. (2007). "Behaviour of ultra-high strength prestressed concrete panels subjected to blast loading." *Journal of Structural Engineering* 133 (11), pp. 1582-1590.
- Nicholas, T. (1981). "Tensile testing of material at high rates of strain." *Experimental Mechanics* 21 (5), pp. 177-185.
- Nili, M. and Afroughsabet, V. (2010). "Combined effect of silica fume and steel fibers on the impact resistance and mechanical properties of concrete." *International Journal of Impact Engineering* 37(8), pp. 879-886.

- Nystrom, U. and Gylltoft, K. (2011). "Comparative numerical studies of projectile impacts on plain and steel-fibre reinforced concrete." *International Journal of Impact Engineering* 38(2-3), pp. 95-105.
- Oduyemi, T.O.S., and Wrigth, H.D. (1989). "An experimental investigation into the behaviour of double-skin sandwich beams." *Journal of Constructional Steel Research* 14(3), pp. 197-220.
- Oehlers, D.J. and Bradford, M.A. (1995). *Composite Steel and concrete structural members Fundamental Behaviour*, Pergamon.
- Park, R. (1964). "Tensile membrane behaviour of uniformly loaded rectangular reinforced concrete slabs with fully restrained edges." *Magazine of Concrete Research* 16 (46), pp. 39-44.
- Peixinho N. (2006). "Determination of crash-relevant material properties of stainless steel alloy and constitutive equations." *Journal of Physics IV France* 134, pp. 243-249.
- Pérez-Quiroz, J.T., Terán, J., Herrera, M.J., Martínez, M. and Genescá, J. (2008). "Assessment of stainless steel reinforcement for concrete structures rehabilitation." *Journal of Constructional Steel Research* 64 (11), pp. 1317 – 1324.
- Rasmussen, K. (2001). "Full-range stress-strain curves for stainless steel alloys." *Research Report No. R811*, The University of Sydney.
- Remennikov, A.M. and Rose, T.A. (2005). "Modelling blast loads on buildings in complex city geometries." *Journal Computers and Structures* 83(27), pp. 2197-2205.
- Remennikov, A.M. and Rose, T.A. (2007). "Predicting the effectiveness of blast wall barriers using neural networks." *International Journal of Impact Engineering* 34, pp. 1907-1923.
- Remennikov, A.M., Kong, S.Y., and Uy, B. (2009). "Response of rigid polyurethane foam-filled steel hollow columns under low velocity impact." 8th *International Conference on Shock & Impact Loads on Structures*, Adelaide, Australia, pp. 513-520.
- Remennikov, A.M., Kong, S.Y. and Uy, B. (2009). "Simulation of impulsive loading on columns using an inflatable airbag technique." 8th *International Conference*

- on Shock & Impact Loads on Structures, 2-4 December 2009, Adelaide, Australia.
- Remennikov, A., Kong, S.Y. and Uy, B. (2010 a). "Static and dynamic behaviour of non-composite steel-concrete-steel protective panels under large deformation." 4th International Conference on Steel & Composite Structures, 23-23 July 2010, Sydney, Australia.
- Remennikov, A., Kong, S.Y. and Uy, B. (2010b). "Impact resistance of non-composite axially restrained steel-concrete-steel sandwich panels." The 5th Civil Engineering Conference in the Asian Region and Australasian Structural Engineering Conference 2010, 8-12 August 2010, Sydney, Australia.
- Remennikov, A.M., Kong, S.Y. and Uy, B. (2011). "The Response of Foam- and Concrete-Filled Square Steel Tubes under Low Velocity Impact Loading." *Journal of Performance of Constructed Facilities (ASCE)* 25 (5), pp. 373-381.
- Ren, Z. and Vesenjak, M. (2005). "Computational and experimental crash analysis of the road safety barrier." *Engineering Failure Analysis* 12, pp. 963-973.
- Ritzel, D. V. (2009). Short course: The Basics of blast physics and damage.
- Ronalds, B.F. (1990). "Membrane action in the beam mechanism." *Journal of Strain Analysis* 25(4), pp. 241-253.
- Rose, T.A., Smith, P.D. and Mays, G.C. (1995). "The effectiveness of walls designed for the protection of structures against air blast from high explosives." *Proceedings of the Institution of Civil Engineers, Structures & Building* 110, pp. 78-85.
- Rose, T.A., Smith, P.D. and Mays, G.C. (1997). "Design charts relating to protection of structures against airblast from high explosives." *Proceedings of the Institution of Civil Engineers, Structures & Building* 123, pp. 186-192.
- Rose, T.A., Smith, P.D. and Mays, G.C. (1998). "Protection of structures against airblast using barriers of limited robustness." *Proceedings of the Institution of Civil Engineers, Structures & Building* 128, pp. 167-176
- Rose, T.A. and Smith, P.D. (2002). "Influence of the principal geometrical parameters of straight city streets on positive and negative phase blast wave impulses." *International Journal of Impact Engineering* 27, pp. 359-376.
- Rose, T.A. (2003). "Air3d User's Guide" RCMS, Cranfield University, U.K.

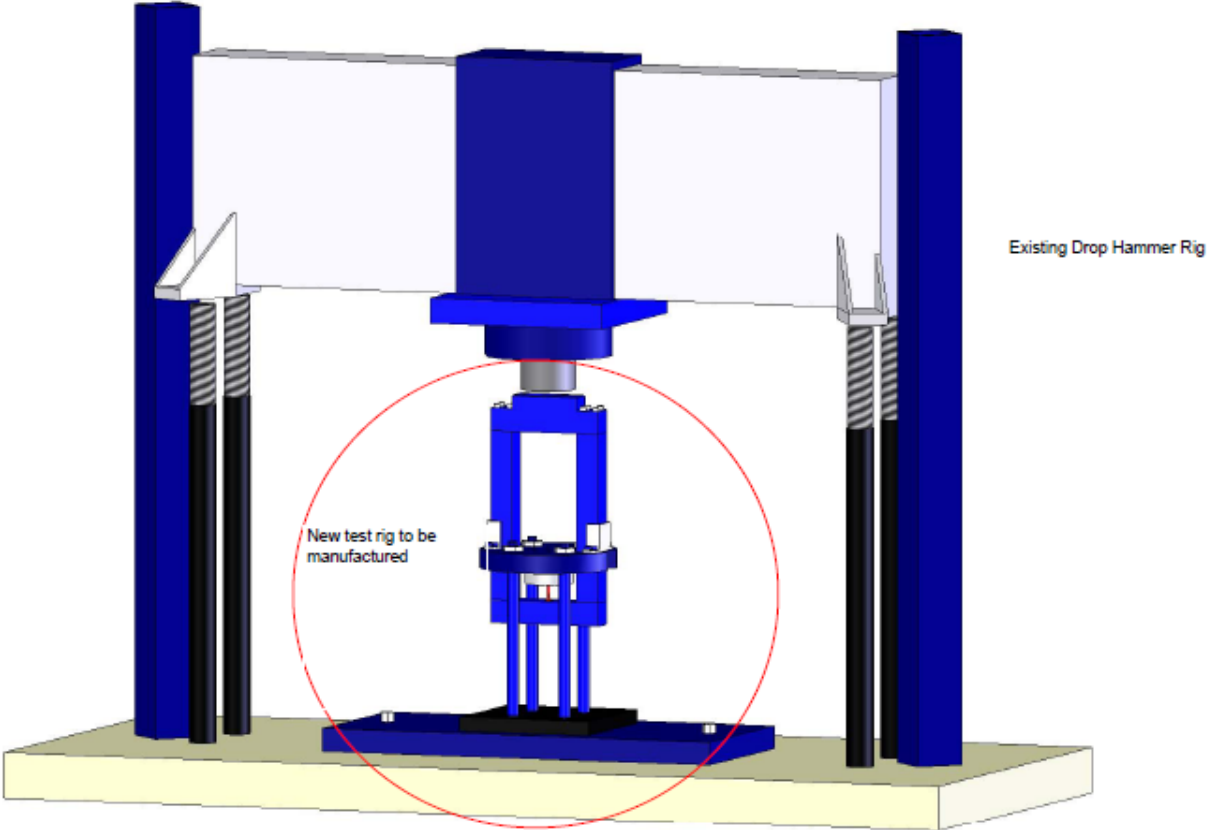
- Roufegarinejad, A., Uy, B. and Bradford, M.A. (2004). "Behaviour and design of concrete filled steel columns utilising stainless steel cross-sections under combined action." 18th Australia Conference on Mechanics of Structures and Materials, Perth, Australia.
- Salim, H.A., Hoemann, J. and Dinan, R.J. (2008). Ductile thin sheets for blast retrofit. AFRL-RX-TY-TP-2008-4532.
- Schleyer, G.K., Lowak, M.J., Polcyn, M.A. and Langdon, G.S. (2007). "Experimental investigation of blast wall panels under shock pressure loading." International Journal of Impact Engineering 34, pp. 1095-1118.
- Schwer, L.E. and Malvar, L.J. (2005). "Simplified concrete modelling with *MAT_CONCRETE_DAMAGE_REL3." JRI LS-DYNA USER WEEK 2005.
- Shanmugam, N.E., Kumar, G. and Thevendran, V. (2002). "Finite element modelling of double skin composite slabs." Finite Element in Analysis and Design 38, pp. 579-599.
- Shanmugam, N.E., and Kumar, G. (2005). "Behaviour of double skin composite slabs-an experimental study." Journal of Steel Structures 5, pp. 431-440.
- Shi, Y., Hao, H. and Li, Z.X. (2008). "Numerical derivation of pressure-impulse diagrams for prediction of RC column damage to blast loads." International Journal of Impact Engineering 35, pp. 1213-1227.
- Smith, P. D., Whalen, G. P., Feng, L. J. and Rose, T. A. (2001). "Blast loading on buildings from explosions in city streets." Proceedings of the Institution of Civil Engineers, Structures & Building 146(1), pp. 47-55.
- Smith, P.D. (2010). "Blast walls for structural protection against high explosive threats: A review." International Journal of Protective Structures 1 (1), pp. 67-84.
- Standards Australia, (2007). AS 1391-2007 Metallic materials-Tensile testing at ambient temperature, Standards Australia.
- Standards Australia, (2009). AS 3600-2009 Concrete structures, Standards Australia.
- Steichen, J.M. (1971). "High strain rate mechanical properties of type 304 stainless steel and nickel 200." HEDL-TME71-145, Hanford Engineering Development Laboratory, Richland Wash.


- Steichen, J.M. (1973). "High strain rate tensile properties of AISI type 304 stainless steel." *Transaction of ASME Journal of Engineering materials and technology*, pp. 182-185.
- Terry, P. and Tholen, M. (2006). "Security barrier design." *Practice Periodical on Structural Design and Construction*, ASCE, pp. 105-111.
- Timoshenko, S.P. and Woinowsky-Kriger, S. (1959). *Theory of plates and shells International student second edition*. McGRAW-HILL BOOK COMPACNY, INC.
- U.S. Department of the Army (1990). *Structures to Resist the Effects of Accidental Explosions*, Technical Manual 5-1300.
- Uy, B. (2008). "Stability and ductility of high performance steel sections with concrete infill." *Journal of Constructional Steel Research* 64 (7-8), pp. 748-754.
- Uy, B. (2006). "Behaviour and design of high performance steel sections with concrete infill subjected to abnormal loading." *The 19th Australasian Conference on the Mechanics of Structures and Materials*, Christchurch, New Zealand, pp.127-132.
- Uy, B. and Remennikov, A. (2007). "Behaviour of high performance steel sections subjected to impact loads." *5th International Conference on Advances in Steel Structures*, Singapore, pp. 929-934.
- Wright, H.D., Oduyemi, T.O.S., and Evans, H.R. (1991). "The experimental behaviour of double skin composite elements." *Journal of Constructional Steel Research* 19(2), pp. 97-110.
- Wu, C., Oehlers, D.J., Rebentrost, M., Leach, J., and Whittaker, A.S. (2009). "Blast testing of ultra-high performance fibre and FRP-retrofitted concrete slabs." *Engineering structures* 31 (9), pp. 2060-2069.
- Xie, M., Foundoukus, N., and Chapman, J.C. (2007). "Static tests on steel-concrete-steel sandwich beams." *Journal of Constructional Steel Research* 63, pp. 735-750.
- Young, A.G. (1959). "Ship plating loaded beyond the elastic limit." *Trans. I.N.A.* 101, pp. 143-165.

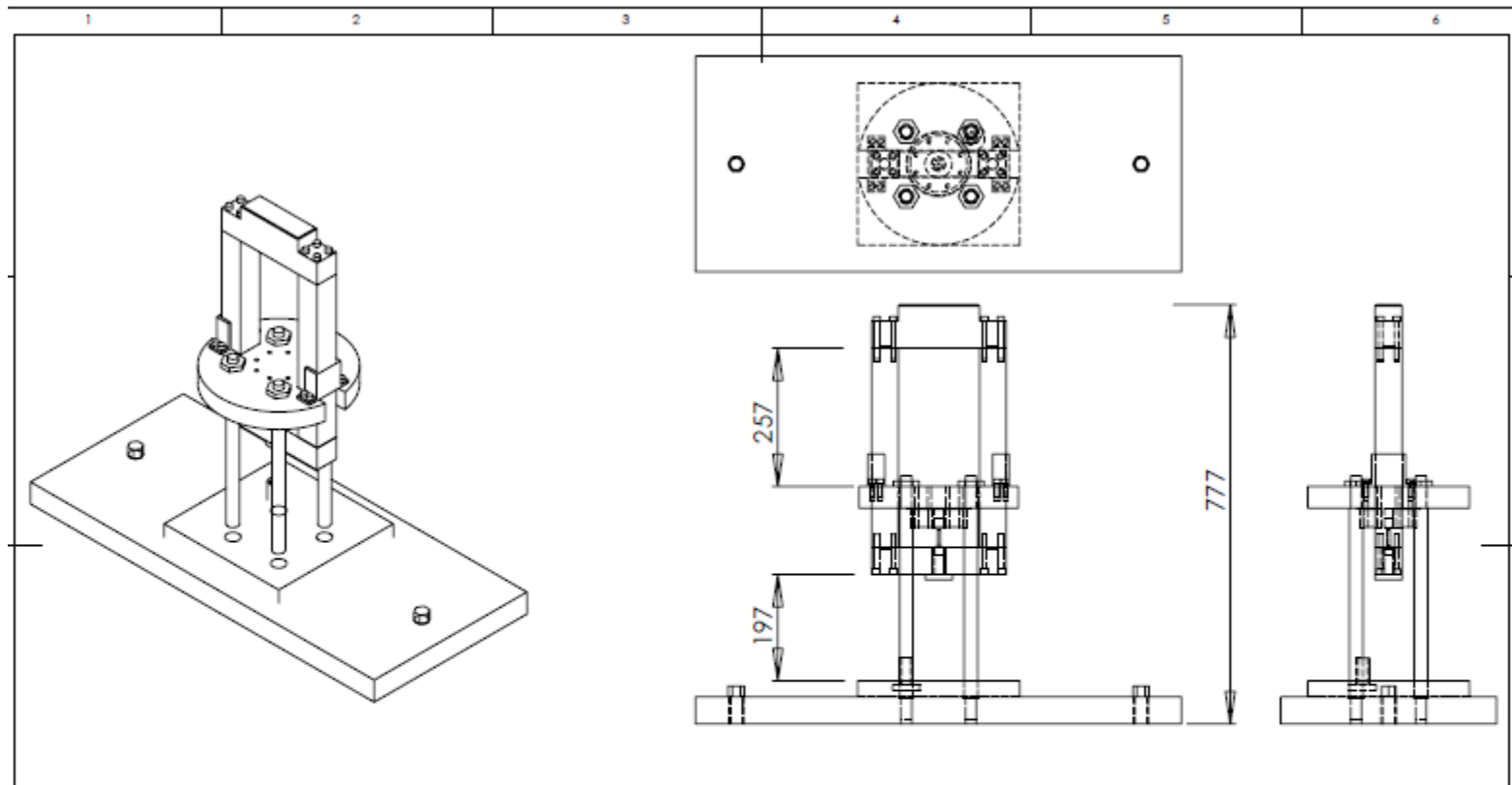
- Young, B., and Coyle, N. (2002). "Resistance of Bi-steel to in-contact and close-proximity high explosive detonations." 17th International Symposium on Military Aspects of Blast and Shock, Lac Vegas, Nevada, USA.
- Yousuf, M., Uy, B., Remennikov, A. and Tao, Z. (2009). "Experimental behaviour of concrete-filled stainless steel tubular columns under impact loading." 8th International Conference on Shock & Impact Loads on Structures, Adelaide, Australia, pp. 761-768.
- Zabotkin, K., O'Toole, B. and Trabia, M. (2003). "Identification of the dynamic tensile properties of metals under moderate strain rates." 16th ASCE Engineering Mechanics Conference.
- Zhang, M.H., Shim, V.P.W., Lu, G., and Chew, C.W. (2005). "Resistance of high-strength concrete to projectile impact." International Journal of Impact Engineering 31 (7), pp. 825-841.
- Zhou, X.Q. and Hao, H. (2008). "Prediction of airblast loads on structures behind a protective barrier." International Journal of Impact Engineering 35, pp. 363-375.

APPENDIX A:
DRAWINGS OF THE INSTRUMENTED FALLING
WEIGHT IMPACT (IFWI) TEST RIG

Impact Tensile Test Rig

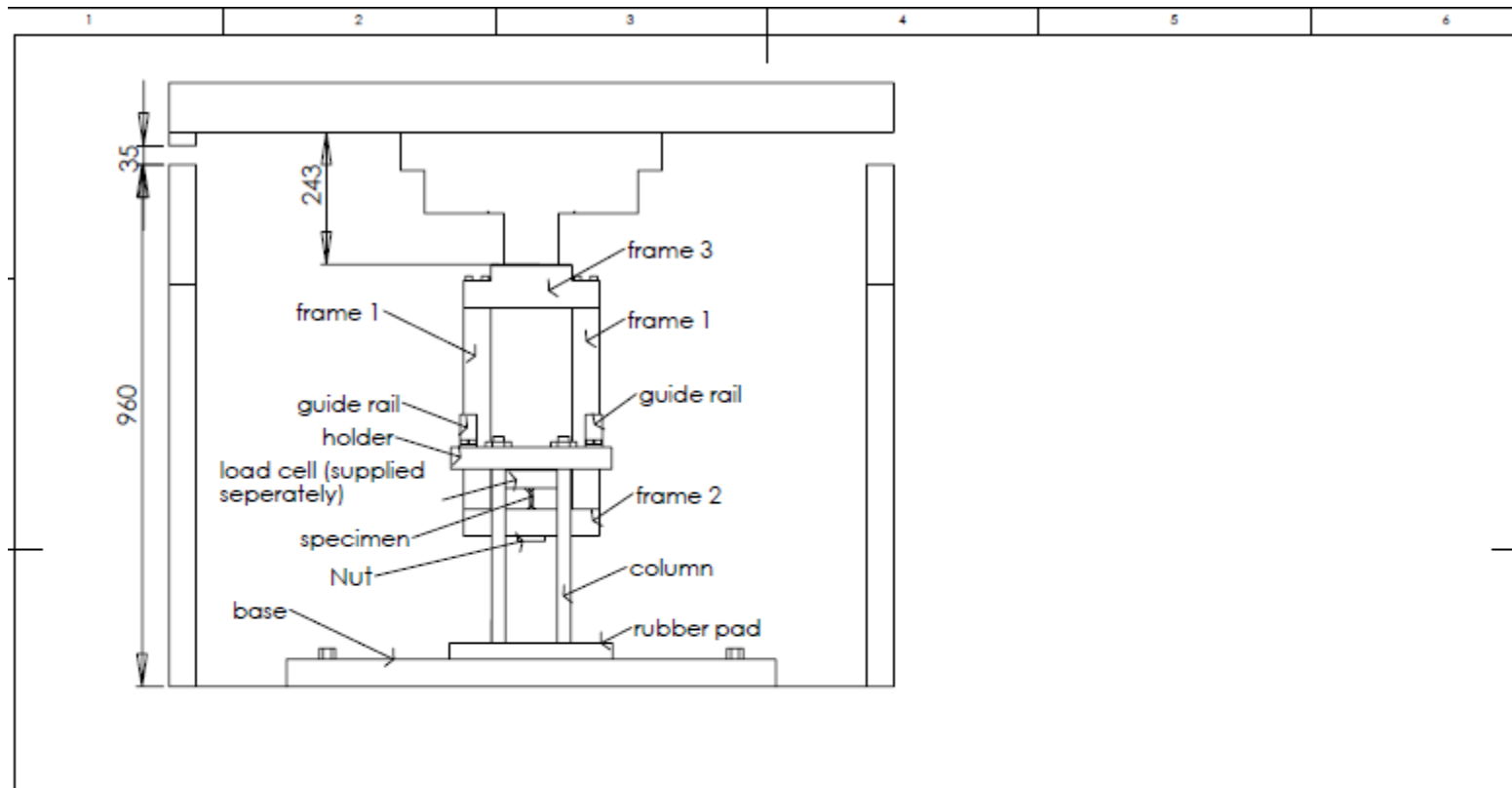


 SolidWorks Student License
Academic Use Only



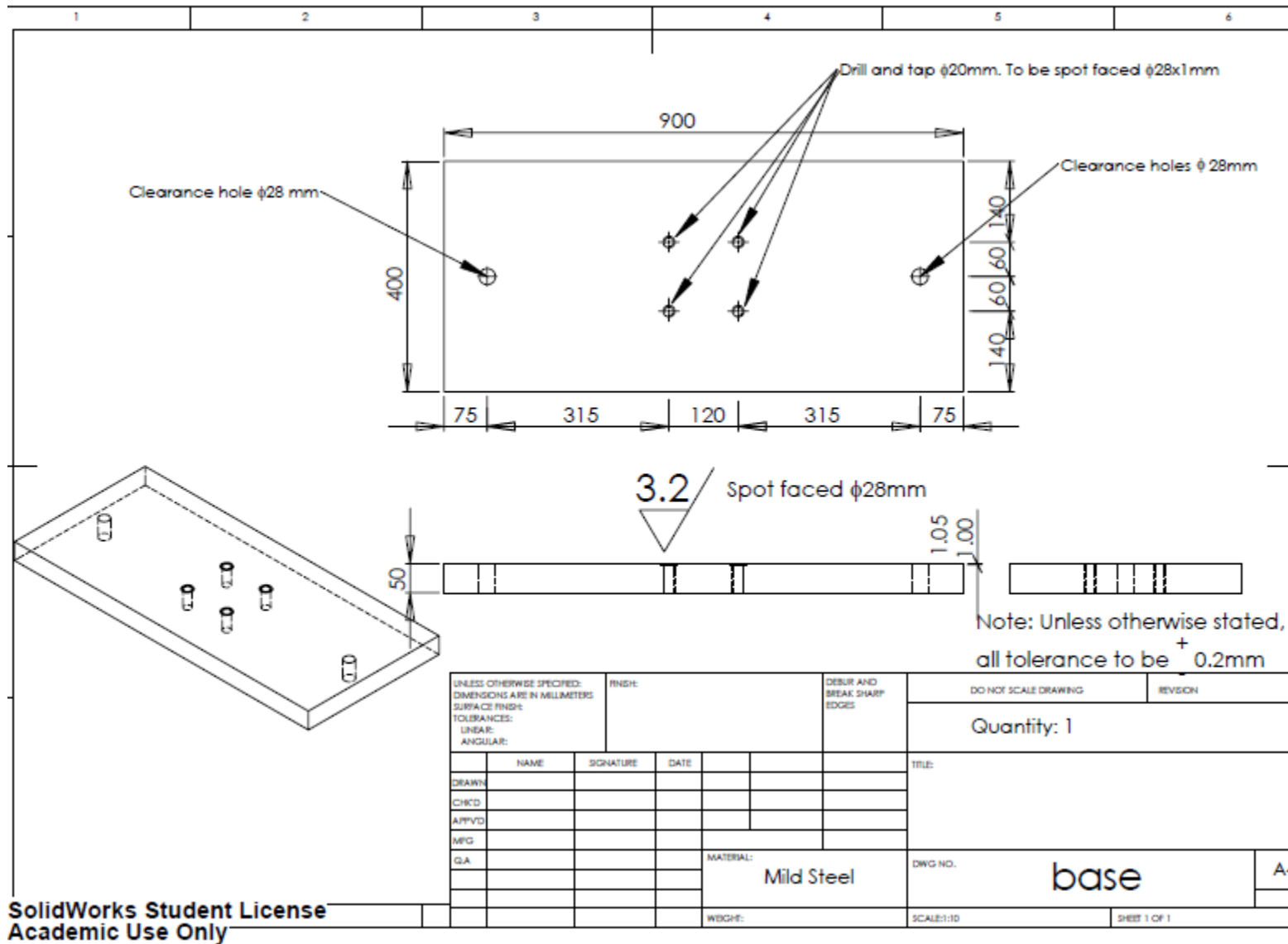
UNLESS OTHERWISE SPECIFIED: DIMENSIONS ARE IN MILLIMETERS SURFACE FINISH: TOLERANCES: LINEAR: ANGULAR:			FINISH:		DEBUR AND BREAK SHARP EDGES		DO NOT SCALE DRAWING		REVISION	
									TITLE:	
DRAWN:			NAME		SIGNATURE		DATE			
CHKD:										
APPVD:										
MFG:										
QA:									MATERIAL:	
									DWG NO.	
									Assem test rig	
									A4	
									WEIGHT:	
									SCALE:1:10	
									SHEET 1 OF 2	

SolidWorks Student License
Academic Use Only

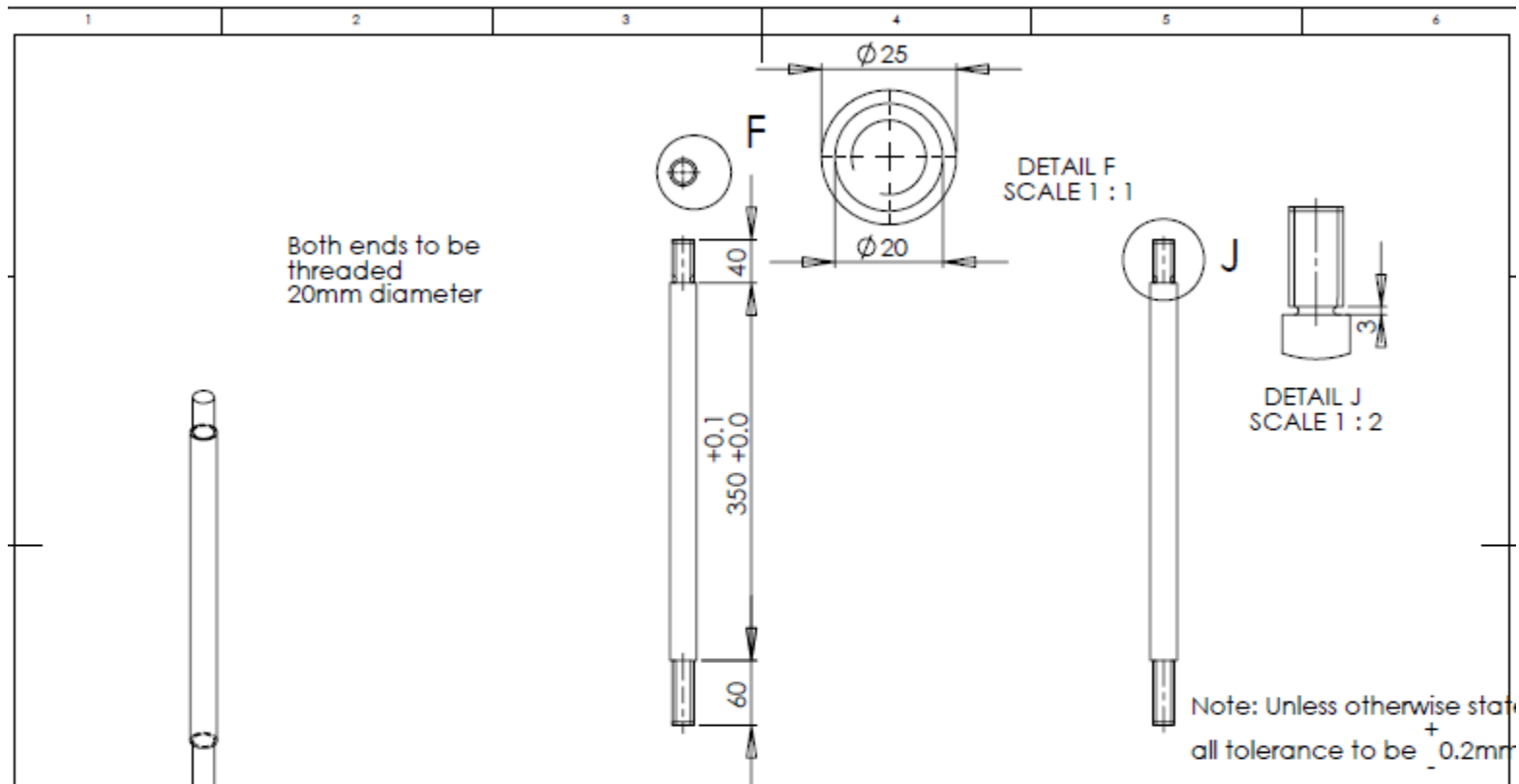


UNLESS OTHERWISE SPECIFIED: DIMENSIONS ARE IN MILLIMETERS SURFACE FINISH: TOLERANCES: LINEAR: ANGULAR:		FINISH:		DEBUR AND BREAK SHARP EDGES		DO NOT SCALE DRAWING		REVISION	
DRAWN		NAME		SIGNATURE		DATE		TITLE:	
CHKD									
APPVD									
MFG									
G.A.						MATERIAL:		DWG NO. Assem test rig	
								A4	
						WEIGH:		SCALE:1:10	
								SHEET 2 OF 2	

SolidWorks Student License
Academic Use Only

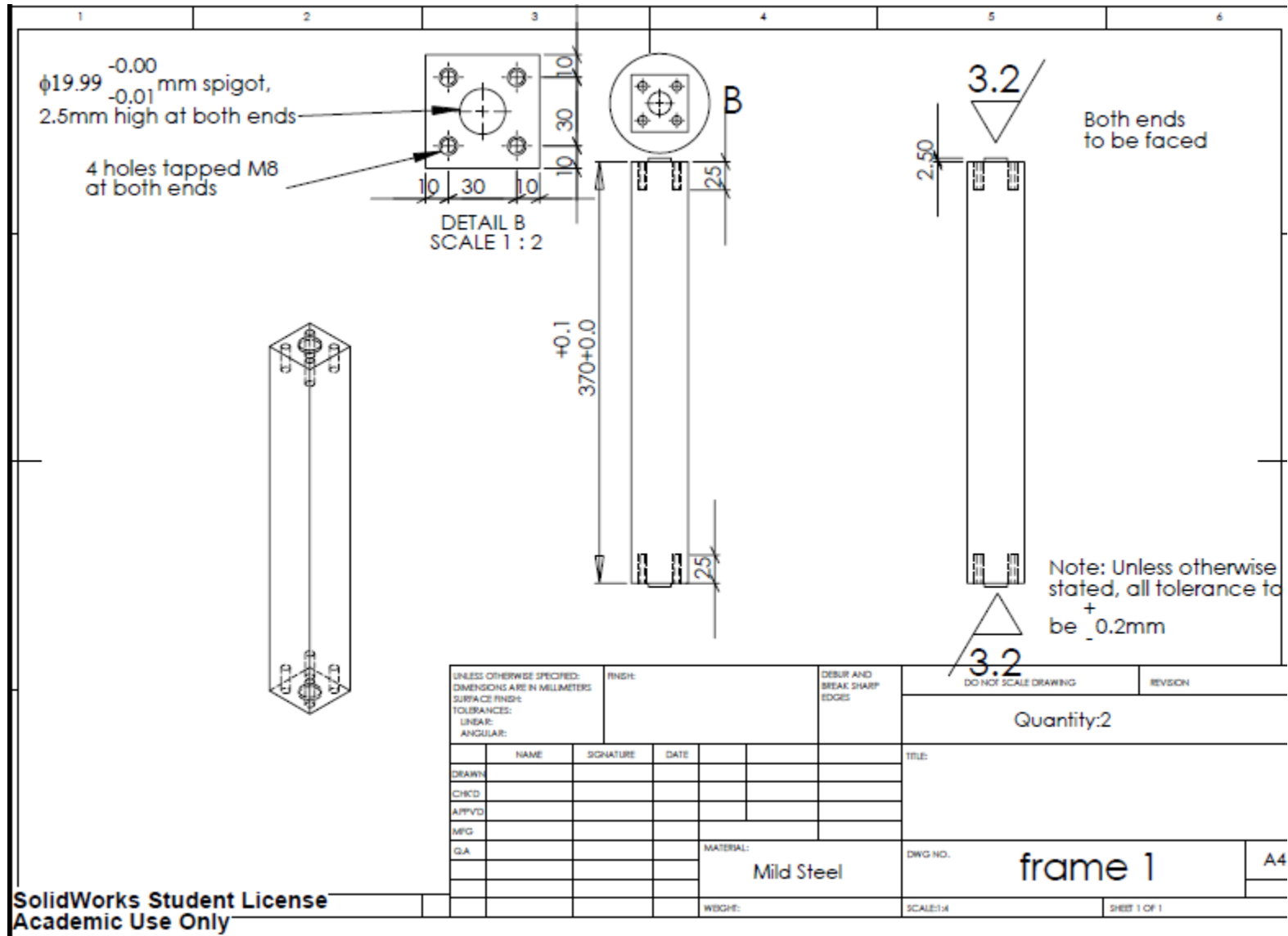


SolidWorks Student License
Academic Use Only

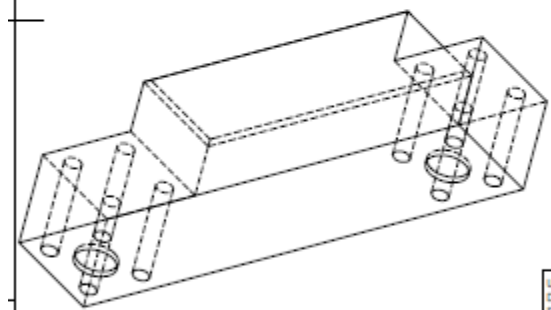
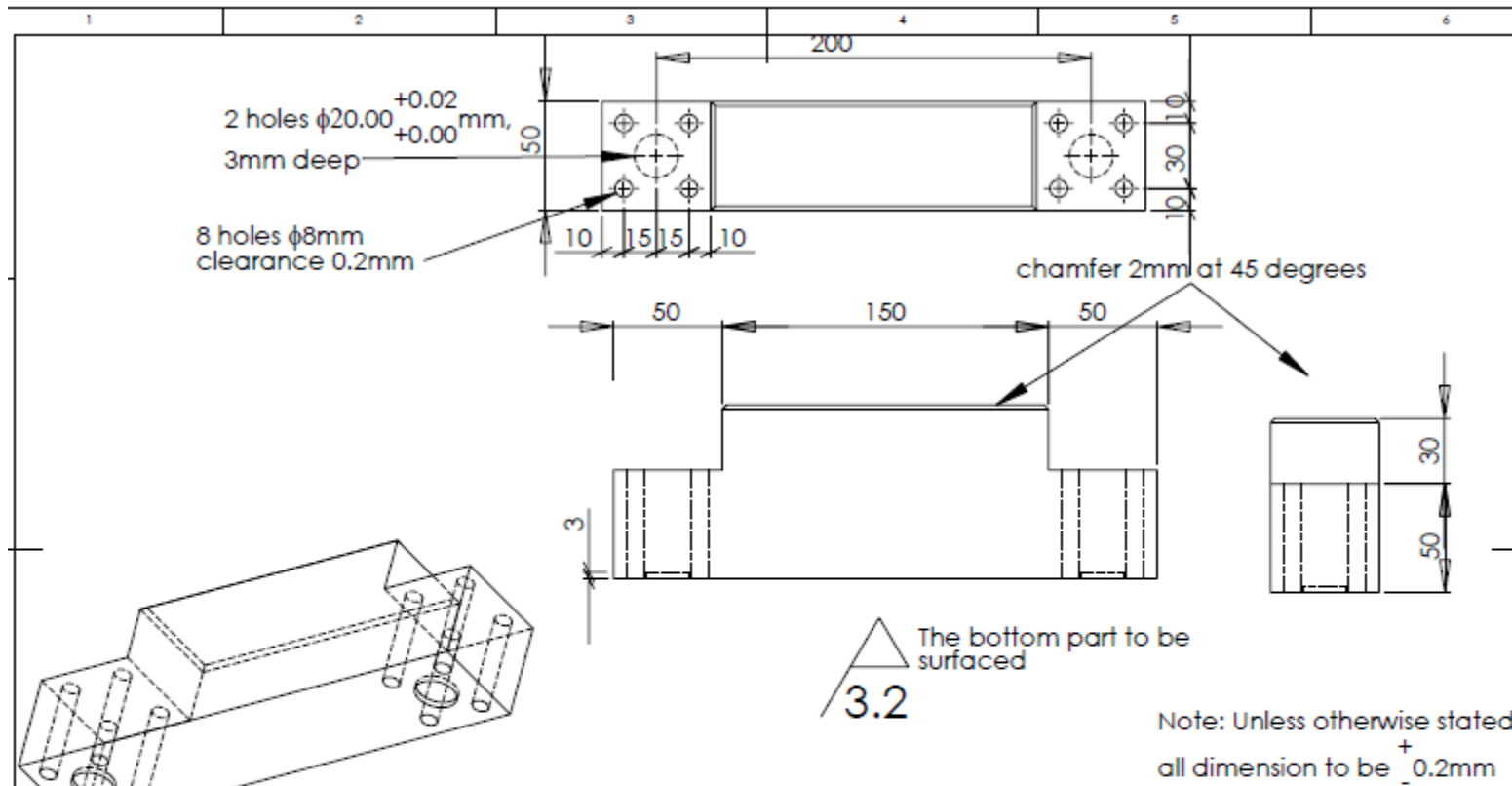


UNLESS OTHERWISE SPECIFIED: DIMENSIONS ARE IN MILLIMETERS SURFACE FINISH: TOLERANCES: LINEAR: ANGULAR:		FINISH:	DEBUR AND BREAK SHARP EDGES		DO NOT SCALE DRAWING	REVISION
					Quantity:4	
NAME	SIGNATURE	DATE			TITLE:	
DRAWN						
CHKD.						
APPVD						
MFG						
G.A.			MATERIAL: Mild Steel		DWG NO.	column
			SCALE:1:5		A4	
			SHEET 1 OF 1			

SolidWorks Student License
Academic Use Only

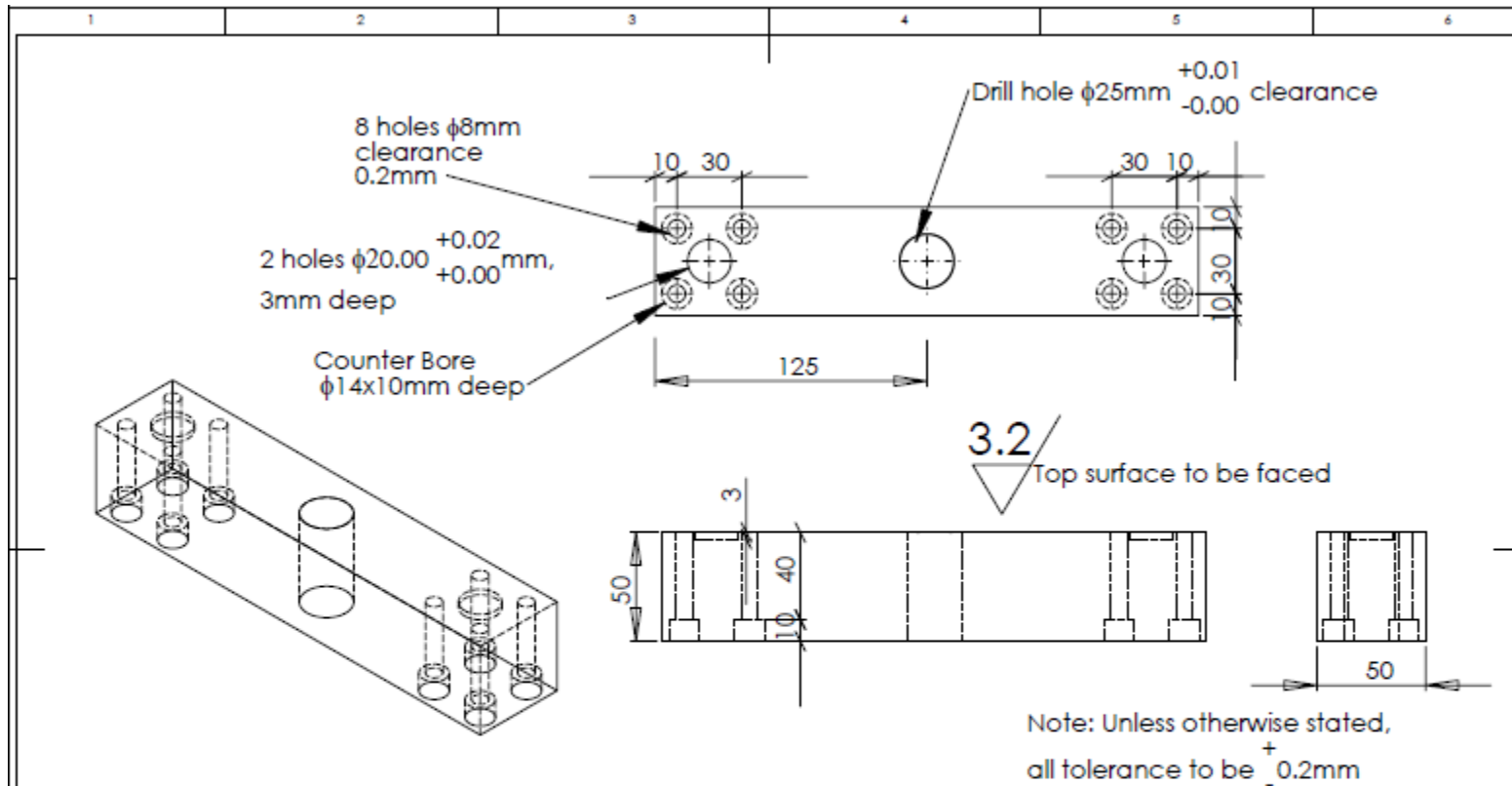


SolidWorks Student License
Academic Use Only



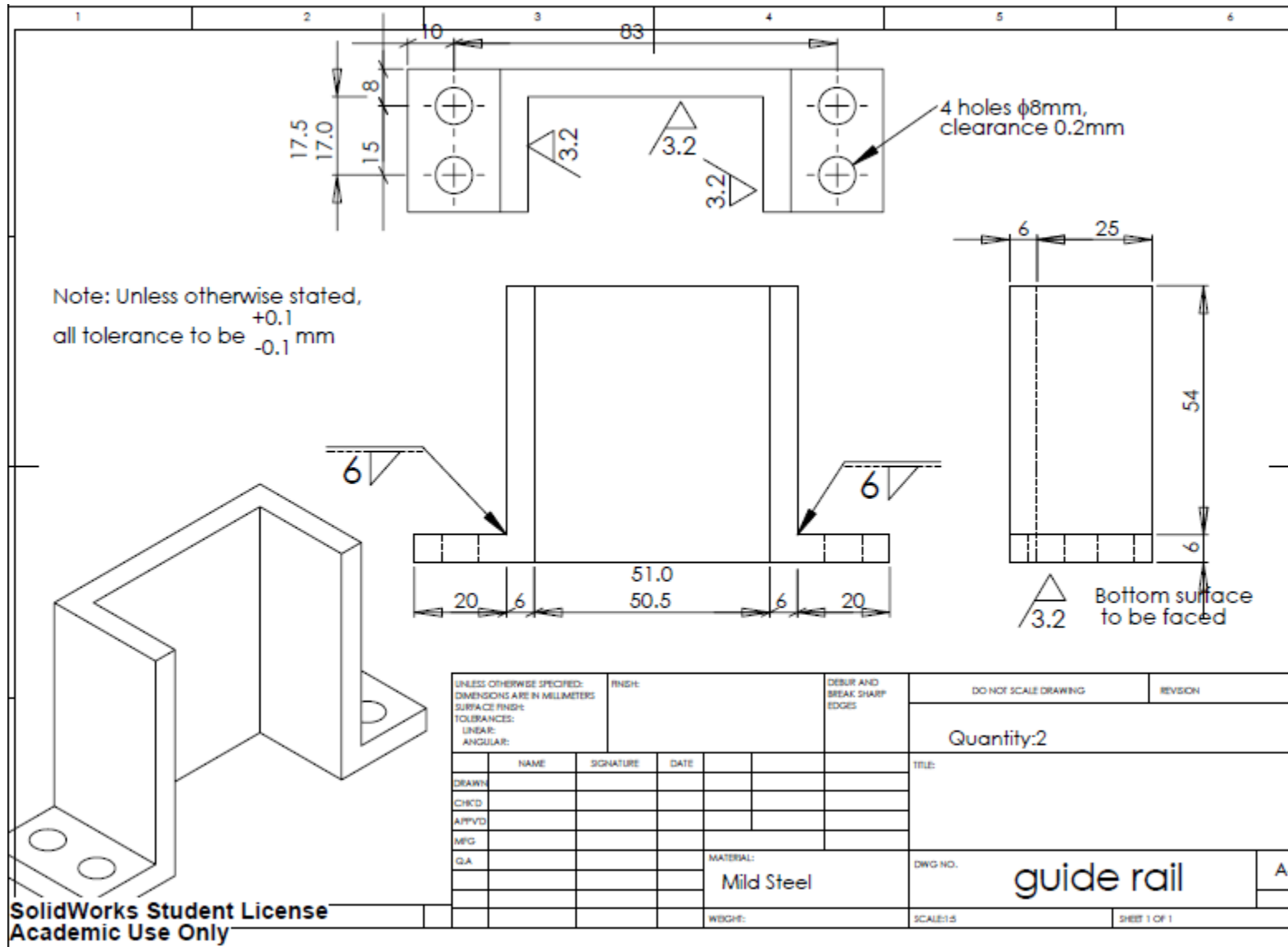
UNLESS OTHERWISE SPECIFIED: DIMENSIONS ARE IN MILLIMETERS		FINISH:		DEBUR AND BREAK SHARP EDGES		DO NOT SCALE DRAWING		REVISION	
SURFACE FINISH:						Quantity:1			
TOLERANCES:									
LINEAR:									
ANGULAR:									
NAME	SIGNATURE	DATE				TITLE:			
DRAWN									
CHKD.									
APPVD									
MFG									
G.A.									
					MATERIAL:		DWG NO.		A4
					High Strength steel		frame 3		
					WGCH:		SCALE:1:2.5		SHEET 1 OF 1

SolidWorks Student License
Academic Use Only

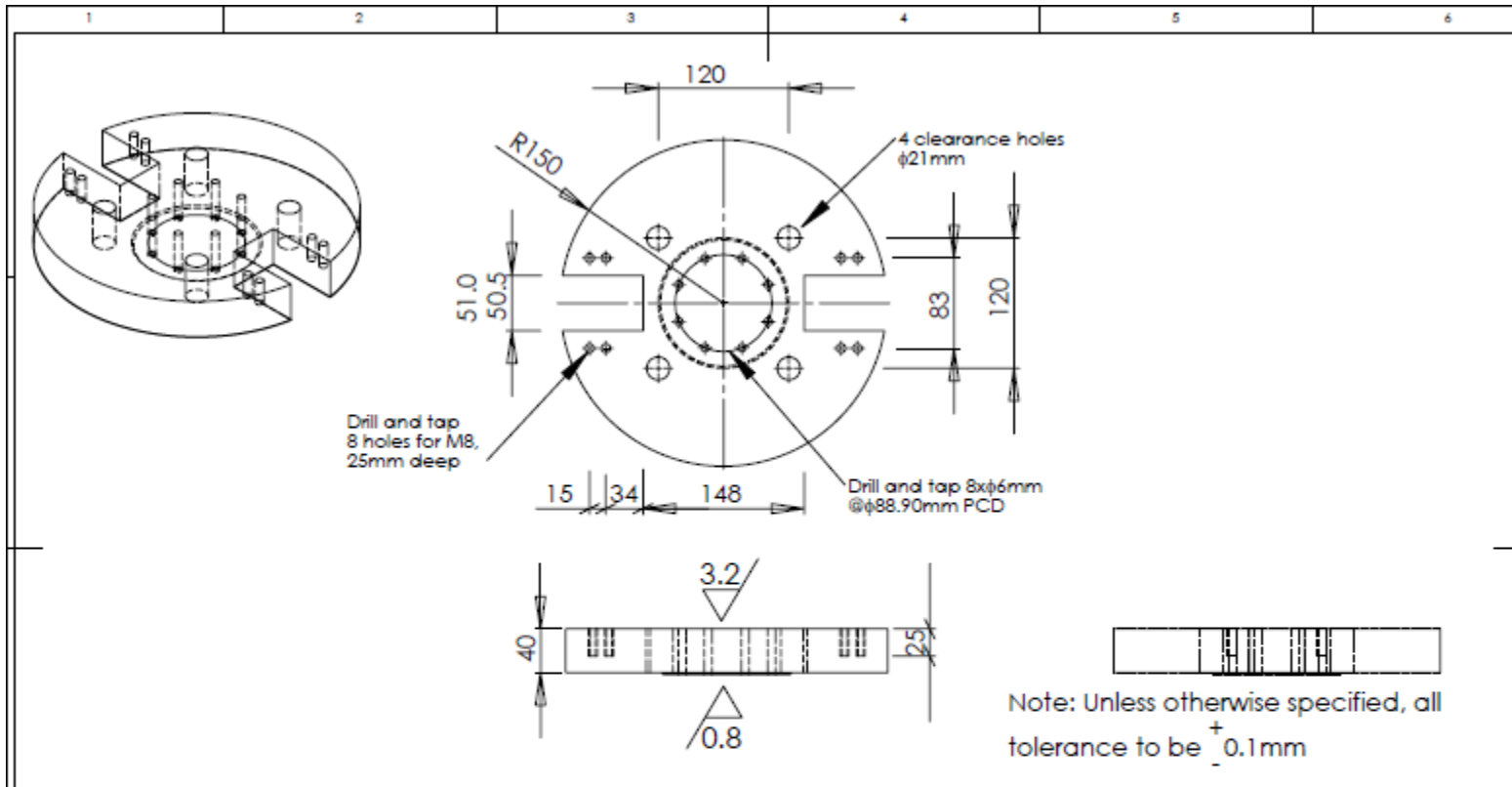


UNLESS OTHERWISE SPECIFIED: DIMENSIONS ARE IN MILLIMETERS SURFACE FINISH: TOLERANCES: LINEAR: ANGULAR:				FINISH:	DEBUR AND BREAK SHARP EDGES	DO NOT SCALE DRAWING	REVISION
						Quantity:1	
						TITLE:	
NAME	SIGNATURE	DATE					
DRAWN							
CHKD							
APPVD							
MFG							
QA							
					MATERIAL:	DWG NO.	
					High Strength Steel	frame2	A4
					WEIGHT:	SCALE:1:2.5	SHEET 1 OF 1

SolidWorks Student License
Academic Use Only

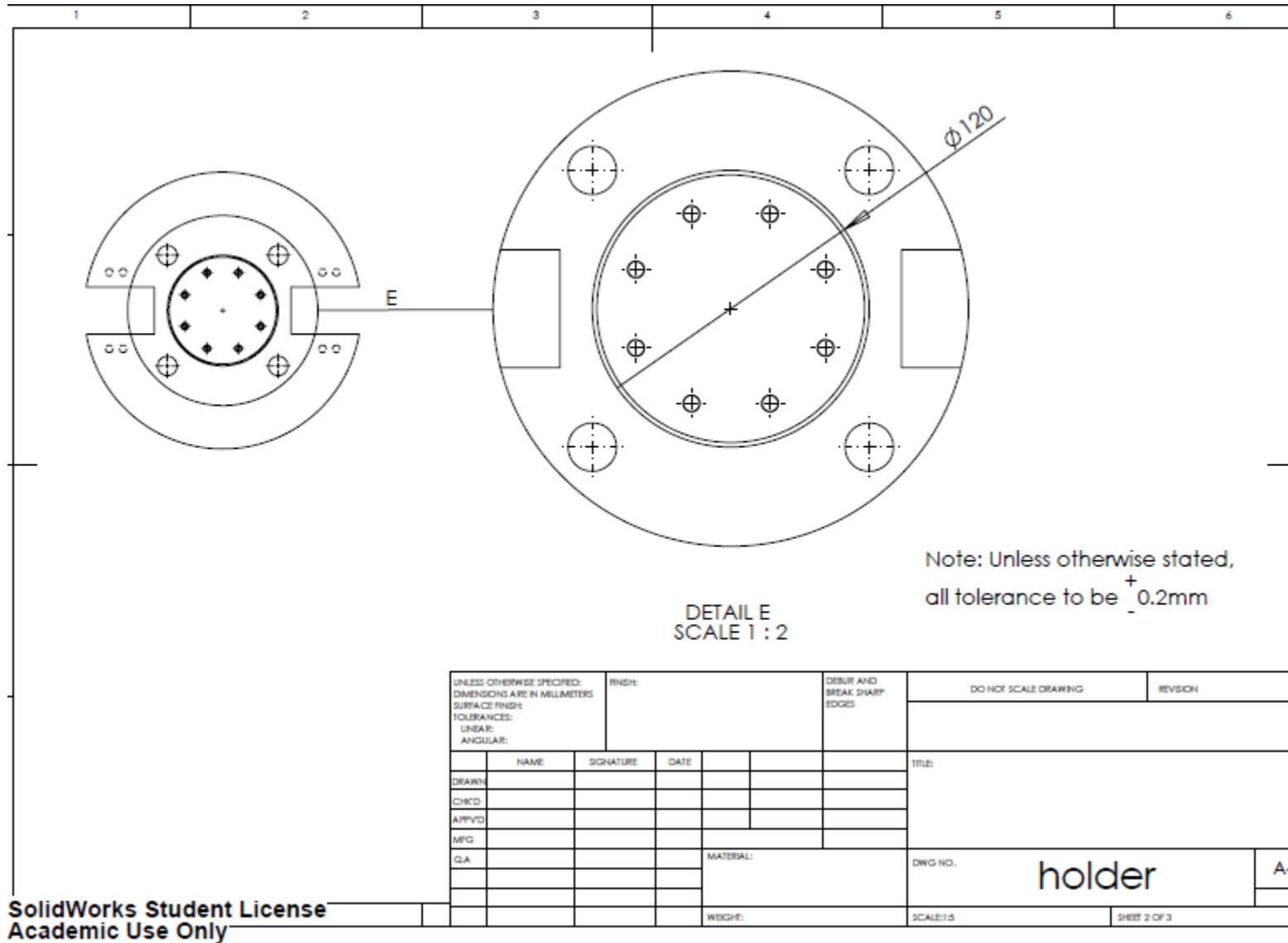


SolidWorks Student License
Academic Use Only



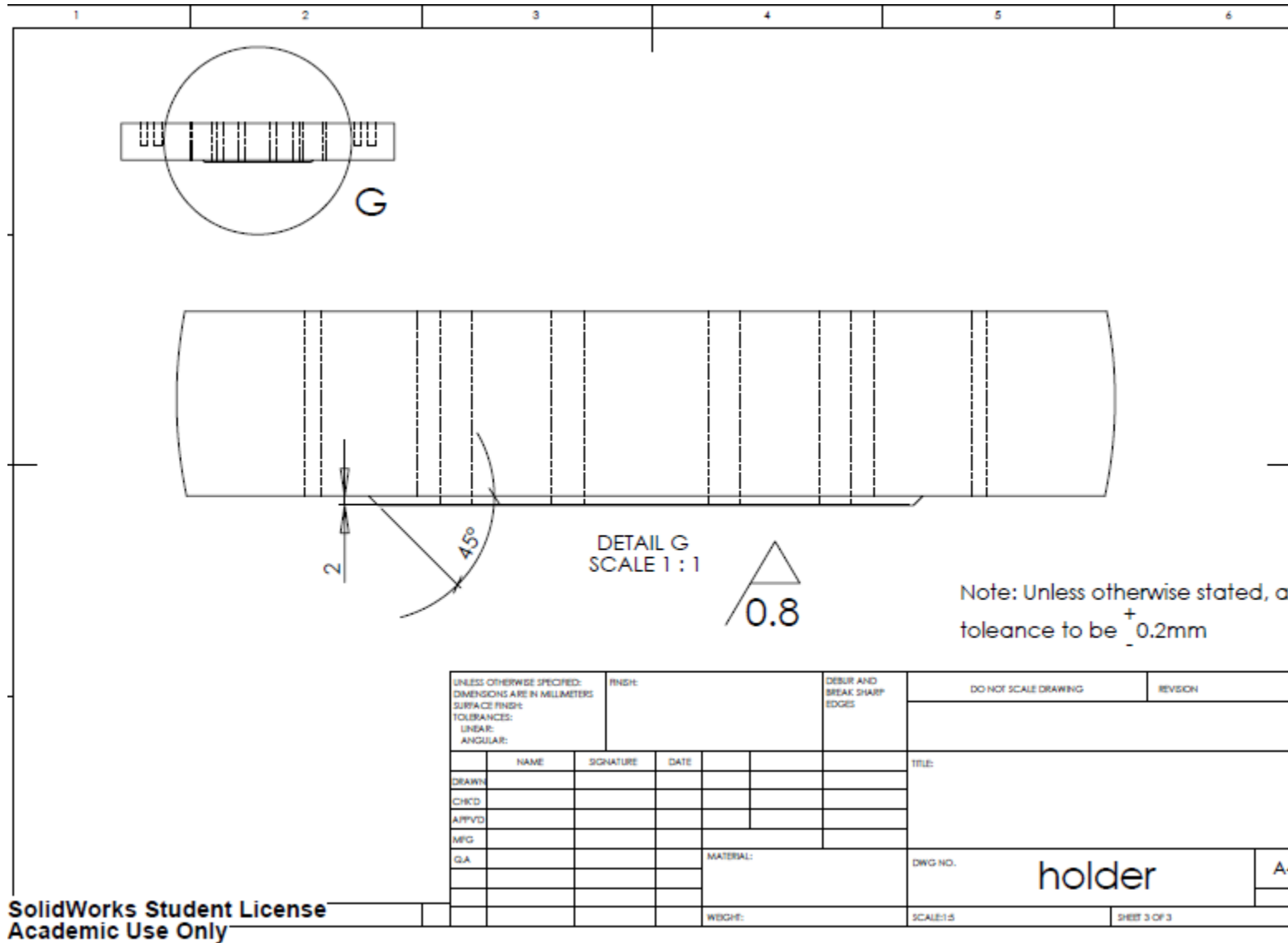
UNLESS OTHERWISE SPECIFIED: DIMENSIONS ARE IN MILLIMETERS SURFACE FINISH: TOLERANCES: LINEAR: ANGULAR:				FINISH:	DEBUR AND BREAK SHARP EDGES	DO NOT SCALE DRAWING	REVISION
						Quantity:1	
						TITLE:	
DRAWN	NAME	SIGNATURE	DATE				
CHKD							
APPVD							
MFG							
QA					MATERIAL:	DWG NO.	
					Mild Steel	holder	A4
					WEIGHT:	SCALE:1:5	SHEET 1 OF 3

SolidWorks Student License
Academic Use Only



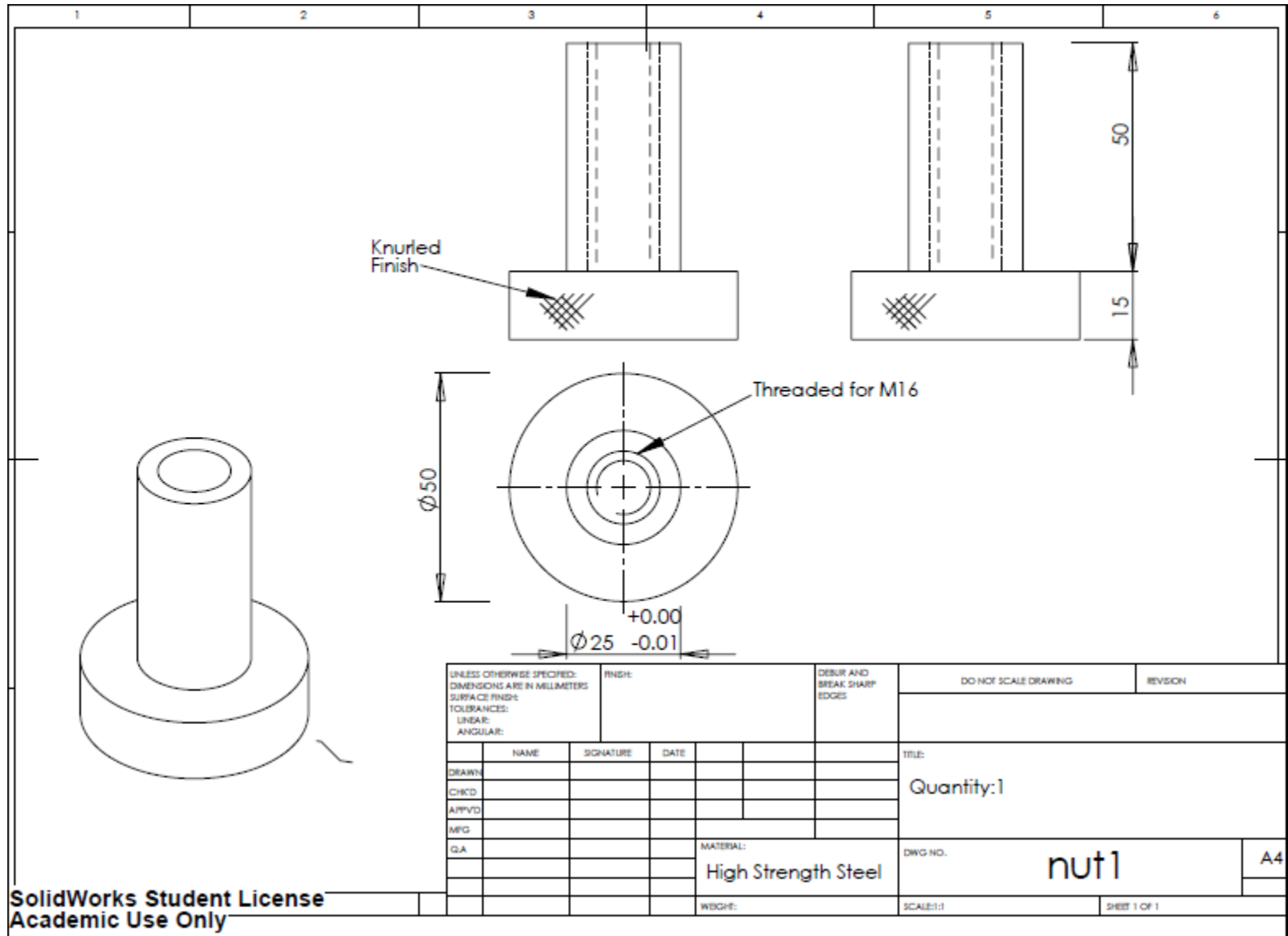
UNLESS OTHERWISE SPECIFIED: DIMENSIONS ARE IN MILLIMETERS SURFACE FINISH: TOLERANCES: LINEAR: ANGULAR:		FINISH:	DEBUR AND BREAK SHARP EDGES	DO NOT SCALE DRAWING	REVISION
NAME	SIGNATURE	DATE		TITLE:	
DRAWN					
CHKD					
APPVD					
MFG					
QA			MATERIAL:	DWG NO.	holder
					A4
			WEIGHT:	SCALE:1:5	SHEET 2 OF 3

SolidWorks Student License
Academic Use Only



UNLESS OTHERWISE SPECIFIED: DIMENSIONS ARE IN MILLIMETERS SURFACE FINISH: TOLERANCES: LINEAR: ANGULAR:		FINISH:		DEBUR AND BREAK SHARP EDGES		DO NOT SCALE DRAWING		REVISION	
DRAWN:		NAME		SIGNATURE		DATE		TITLE:	
CHKD:									
APPVD:									
MFG:									
QA:						MATERIAL:		DWG NO. holder A4	
						WEIGHT:		SCALE:1:5 SHEET 3 OF 3	

SolidWorks Student License
Academic Use Only



SolidWorks Student License
Academic Use Only